2006

Search for multi-photon signatures of a Higgs boson in ppbar collisions at sqrt(s) = 1.96 TeV

Oleksiy Vladimirovich Atramentov
Iowa State University

Search for multi-photon signatures of a Higgs boson in ppbar collisions at sqrt(s) = 1.96 TeV

by

Oleksiy Vladimirovich Atramentov

A doctorate dissertation submitted to the graduate faculty

in partial fulfillment of the requirements for the degree of

DOCTOR OF PHILOSOPHY

Major: Physics

Program of Study Committee:
John Hauptman (Major Professor)
Marshall Luban
Vasant Honavar
Marzia Rosatti
James Vary

Iowa State University

Ames, Iowa

2006

Graduate College

Iowa State University

This is to certify that the Doctoral dissertation of

Oleksiy Vladimirovich Atramentov

has met the dissertation requirements of Iowa State University

Signature was redacted for privacy.

Major Professor

Signature was redacted for privacy.

For the Major Program

To my parents Nataliya A. Babenko and Vladimir A. Atramentov

and in the memory of my late grandfather Alexey Stepanovich Babenko.

TABLE OF CONTENTS

LIST OF TABLES

LIST OF FIGURES

1 INTRODUCTION

Children are such curious creatures. They explore, question, and wonder, and by doing so, learn. From the moment of birth, likely even before, humans are drawn to new things. When we are curious about something new, we want to explore it. And while exploring we discover. By turning the light switch on and off over and over again, the toddler is learning about cause and effect. By pouring water into a dozen different-shaped containers and on the floor and over clothes, the 4-year-old is learning pre-concepts of mass and volume.

Around the the age of 4-5 a child learns to adopt tools for a more sophisticated exploration. A set of screwdrivers discovered earlier in grandfather's drawer is used for a disassembly and total annihilation of father's watches discovered earlier in parents' bedroom. The experience of exploration, while not always pleasurable, is certainly a rewarding experience. And the urge stays with you for all your life.

As we grow older the questions turn to areas where fewer and fewer people know the answer. And one day we realize that we just reached the horizon. And that is when we decide to take charge and find an answer. Yet, this time we need a much bigger magnifying glass and something more than a set of screwdrivers.

High energy particle physics is the area of physics that tries to find answers to some of the most fundamental questions – what are the elementary constituents of the world and how are they related to each other?, what are the origins of the underlying structure, and finally, the most difficult question, WHY is this structure the way it is?

All that we know about elementary particles has been formed into the so-called Standard Model of elementary particles. The model is mathematically elegant and incorporates all particles that we have observed. Unfortunately, one ingredient is still missing – massiveness of electroweak bosons[1] – W and Z. These bosons, while weighing as much as Zr nucleus[2], are intimately related to a photon which is massless.

One of the possible ways to fix this [gross] inconsistency is to introduce a hypothetical particle that gives mass to W and Z through its interaction with them. The corresponding mechanism of [electroweak] symmetry breaking has been first proposed by Peter Higgs and the corresponding particle is referred to as the "higgs boson" or just the "higgs". Properties of the higgs are well understood and its decay modes are being actively searched for at the particle colliders. Although various indirect studies point to its presence, the direct searches turned out to be negative.

A number of more complex and more realistic theoretical models exist. And because of the different particle content, predictions of the observation of the higgs (or whatever particle plays its role) can differ (sometimes drastically) from those of the Standard Model higgs.

Although the most promising discovery channel of the Standard Model higgs is through its decay to two b quarks, very interesting scenaria exist in other models. The decay of higgs into two photons is probably the most fascinating of them. The Higgs only couples to particles with mass so, since it does not interact directly with photons, its $\gamma\gamma$ decay must be induced by electroweak symmetry breaking

---

[1] "Electroweak" and "boson" are a jargon that refers to some properties of mathematical entities under certain symmetry transformations.

[2] Atomic number of Zirconium is 40 – a wee less than two iron nuclei.

effects. The decay proceeds mainly through intermediate states involving $W^{\pm}$ bosons and t quarks, and thus is very sensitive to the manner in which the electroweak symmetry is broken.

There are many interesting and well-motivated theories that predict an enhanced decay rate into the $\gamma\gamma$ channel. And in these cases, non-standard search strategies must be employed to either find this higgs boson or rule out its existence in the kinematically accessible mass range.

An experimental approach to a discovery of particles as heavy as the W boson, top quark [1], or higgs, is through high energy collisions, collisions where a pair of particles like electrons or protons have been accelerated to a total energy high enough to produce particle of interest[2].

The present study describes a novel search for traces of a higgs boson in the events that contain three or more photons. This experimental study is performed with the DØ detector (Sec. 4) at the world's highest energy particle accelerator – the Tevatron collider. For more than a decade the Tevatron collider has been leading the the energy frontier and in 1995 it brought about the discovery of the top quark, the heaviest of the known fundamental particles.

Theoretical calculations [1] predict that at almost 2 TeV of center of mass energy provided by the Tevatron one would start detecting multi-photon signatures of the higgs boson. The underlying mechanism is unique in a way that it could not have been realized at previous experiments either because the energy in the collisions was not enough to create the two higgs particles involved in the production

---

[1]Top quark weighs almost as much as a nucleus of gold.

[2]Remember Einstein's relation between energy and mass?

mechanism, and/or the colliding particles was not "right"[1]. At the previous run of the Tevatron (Run I) the rate of the collisions was not high enough to produce a statistically significant number of signal events.

This thesis comprises nine chapters. In the current chapter we provide a brief description of the Standard Model of elementary particles (Sec. 1.1), we outline the limitations of the Standard Model (Sec. 1.2), and proceed with the description of the newly developed theoretical ideas that motivate the present study (Chapter 2).

In Chapters 3 and 4 we describe the apparatus that made this search possible – the DØ detector and the Tevatron collider. In Chapter 5 we outline the algorithms used to reconstruct various detector objects that are further used for more elaborate object definitions[2]

The core of this analysis lies with the photon identification to which we dedicate a separate Chapter 6.

One of the critical quantities in almost all analyses is the statistics of available data, i.e. integrated luminosity. It is this quantity that relates the number of observed events to a production rate of the sough-after signal. We chose to estimate the integrated luminosity ourselves from a well-understood sample of $Z \rightarrow e^+e^-$ decays. The corresponding study is presented in Chapter 7.

In this study we chose to minimize reliance on the theoretical modeling of backgrounds that we obtain from data samples. The estimation of various processes that produce multi-photon events, and,

---

[1] As will be seen in Sec. 2 in order for this process to occur colliding paritcles should be quarks with the same sign but different charges, i.e. process almost exclusive to $p\bar{p}$ colliders.

[2] "Object", is another jargon word that stands for a physical particle the way it is seen by the detector.

thus, the background to a higgs signal, is presented in Chapter 8. We observe good agreement of data with all expected backgrounds. Further, we introduce additional constraints on the event sample which reduces the number of observed events to zero with 0.5 events expected from all background sources.

Having not observed an anticipated higgs signal we perform 95% CL exclusion of the higgs masses for various parameters of the model. The results are presented in Sec. 8.8 and summarized in Chapter 9.

In the Apprendixes we provide Event Displays of interesting events – $3\gamma + X$ (App. A), $2e + \gamma + X$ (App. B), $3e$ (App. C), and $2\gamma^{CC} + \gamma^{EC} + X$(App. D). We decided to include events with two central (CC) photons and one forward (EC) photon because they exhibit some very interesting features that we felt obliged to share with the reader.

1.1 The Standard Model

The *Standard Model* (SM) of Particle Physics is the current theory of elementary particles along with the interactions that act between them (except gravity). The SM is a quantum theory of fields (QFT), which arises from combining quantum mechanics with special relativity. The SM includes most of the current understanding of the laws of physics, and has been verified experimentally to a high level of accuracy.

Nevertheless, the theory is incomplete. The SM contains many free parameters that cannot be derived from first principles. The higgs boson, which is considered to be the last remaining piece to the SM, has not been experimentally detected yet. Furthermore, gravity is not included in the SM. The following give an overview of the SM [2; 3; 4; 5; 6; 7].

1.1.1 Quarks and Leptons

In the SM the fundamental particles that make up ordinary matter are divided into two groups: *quarks* and *leptons* (Fig. 1). Both quarks and leptons are *fermions* since they are spin-$\frac{1}{2}$ particles, and therefore obey Fermi-Dirac statistics. As indicated in Fig. 1, quarks and leptons are each arranged in three generations, containing particles of similar properties but differing in mass. For each particle there exists an associated anti-particle.

There are six different flavors of quarks, labeled (in order of increasing mass) *up*, *down*, *strange*, *charm*, *bottom*, and *top*. Quarks are never observed as single particles (see Chapter 1.1.2.3), and they carry fractional electrical charges[1] of $+\frac{2}{3}$ or $-\frac{1}{3}$. Quarks form bound states called *hadrons* by either combining three quarks into *baryons*, or by pairing a quark with an antiquark into *mesons*. Protons (made up of two up-quarks and one down-quark) and neutrons (made up of two down-quarks and one up-quark) are the most common examples of baryons. Pions ($\pi^{0,\pm}$) and Kaons ($K^{\pm}$, K^0, $\bar{K}^0$) are the most common types of mesons.

There are three different flavors of charged leptons carrying a charge of -1: *electron* (e^-), *muon* (μ^-), and *tau* (τ^-). While electrons exist in all atoms, muons and taus can only be observed in energetic processes like cosmic ray showers, or in high energy particle collisions. There are three neutral leptons, called *neutrinos* (ν), each corresponding to a charged lepton: ν_e, ν_μ, and ν_τ. Neutrinos interact extraordinarily weakly with matter, and their masses are negligibly small.

---

[1] All charges are given in units of the absolute value of the electron charge, 1.602×10^{-19} Coulombs.

Leptons spin = 1/2			Quarks spin = 1/2		
Flavor	Mass GeV/c^2	Electric charge	Flavor	Approx. Mass GeV/c^2	Electric charge
ν_e electron neutrino	$<1\times10^{-8}$	0	u up	0.003	2/3
e electron	0.000511	−1	d down	0.006	−1/3
ν_μ muon neutrino	<0.0002	0	c charm	1.3	2/3
μ muon	0.106	−1	s strange	0.1	−1/3
ν_τ tau neutrino	<0.02	0	t top	175	2/3
τ tau	1.7771	−1	b bottom	4.3	−1/3

Fig. 1: Properties of fermion particles: quarks and leptons. Spin is given in units of $\hbar$, electric charge is given in units of the absolute value of the electron charge.

Property \ Interaction	Gravitational	Weak (Electroweak)	Electromagnetic (Electroweak)	Strong: Fundamental	Strong: Residual
Acts on:	Mass – Energy	Flavor	Electric Charge	Color Charge	See Residual Strong Interaction Note
Particles experiencing:	All	Quarks, Leptons	Electrically charged	Quarks, Gluons	Hadrons
Particles mediating:	Graviton (not yet observed)	W^+ W^- Z^0	γ	Gluons	Mesons
Strength relative to electromagnetic for two u quarks at: 10^{-18} m	10^{-41}	0.8	1	25	Not applicable to quarks
Strength relative to electromagnetic for two u quarks at: 3×10^{-17} m	10^{-41}	10^{-4}	1	60	
Strength relative to electromagnetic for two protons in nucleus	10^{-36}	10^{-7}	1	Not applicable to hadrons	20

Fig. 2: Fundamental forces and their properties.

1.1.2 Interactions

One of the most fundamental insights in theoretical physics is that interactions are dictated by symmetry principles. In QFT, interactions manifest themselves by imposing symmetry conditions on the quantum fields representing the respective interactions. Using the framework of Lagrangian field theory, the Lagrangian of the theory is required to be invariant under a group of local phase changes (*local gauge invariance*). A local phase depends on space and time in a completely arbitrary way. In order to ensure gauge invariance of such a Lagrangian, gauge fields are introduced. These gauge fields lead to spin-1 bosons that are the mediators of the interactions (except gravity).

Four types of interactions are currently known (in order of decreasing strength): strong, electromagnetic, weak, and gravitational. Fig. 2 summarizes the basic properties of the four interactions. The following is a brief summary of the interactions that have been incorporated into the SM.

1.1.2.1 Electromagnetic Interaction

Historically, the electromagnetic interaction was the first to be formulated in the framework of a calculable (*renormalizable*) QFT by Tomonaga, Feynman, and Schwinger in the 1940s (Nobel Prize in 1965). *Quantum Electrodynamics* (QED) describes the electromagnetic interaction by requiring gauge invariance under U(1) group transformations. U(1) denotes a group of unitary one-dimensional matrices, describing space-time dependent rotations in a complex plane. The requirement of gauge invariance gives rise to the photon field and the *photons* as the corresponding mediator of the electromagnetic interaction. Because the photon is massless the interaction has infinite range. The photon couples to all particles that carry electrical charge, like quarks and charged leptons. The strength of the interaction is proportional to the magnitude of the dimensionless *fine structure coupling constant*:

$$\alpha_{EM} = \frac{e^2}{4\pi} \approx \frac{1}{137}. \tag{1.1}$$

1.1.2.2 Weak Interaction

The weak interaction is most prominent in *beta decays* and associated radioactivity:

$$n \rightarrow p + e^- + \bar{\nu}_e \tag{1.2}$$

$$p \rightarrow n + e^+ + \nu_e. \tag{1.3}$$

The range of the interaction is short due to the high mass of the mediating gauge bosons ($W^{\pm}$, Z^0) [8]:

$$m_{W^{\pm}} = 80.425 \pm 0.038\ GeV \tag{1.4}$$

$$m_{Z^0} = 91.1876 \pm 0.0021\ GeV. \tag{1.5}$$

A QFT combining the electromagnetic with the weak interaction was first developed by Glashow, Weinberg, and Salam (*GWS theory*, Noble Prize in 1979). Later 't Hooft and Veltman were able to prove that the theory is renormalizable (Nobel Prize in 1999). Electroweak theory combines a U(1) group with an SU(2) group, and requires invariance under SU(2)⊗U(1) transformations. SU(n) describes groups of special[1] unitary $n \times n$ matrices. Local gauge invariance under SU(2) group transformations introduces three massless spin-1 gauge bosons W^+, W^-, and W^0. Adding the U(1) group introduces another gauge boson called B^0. The W^0 and B^0 mix quantum mechanically to give rise to the experimentally observed photon (γ) and Z^0:

$$\gamma = W^0 \sin\theta_W + B^0 \cos\theta_W \tag{1.6}$$

$$Z^0 = W^0 \cos\theta_W - B^0 \sin\theta_W. \tag{1.7}$$

where θ_W is called the *weak mixing angle* or *Weinberg angle*. As opposed to QED, the underlying group of the electroweak theory is *non-Abelian* since not all the generators of the group commute with each other.

---

[1] The determinant of the matrices must be 1.

Up to this point the electroweak theory is very simple and elegant. Yet it is incomplete, since all particles of the theory are massless. Additionally, mass terms cannot be introduced into the Lagrangian describing the system, since this would destroy the local gauge invariance of the Lagrangian. This problem is resolved by the *higgs mechanism*, which introduces *spontaneous symmetry breaking* of the higgs scalar field potential, thereby giving mass to the gauge bosons (W and Z) and the quarks and leptons.

1.1.2.3 Strong Interaction

Quantum Chromo Dynamics (QCD) is the QFT describing the strong interaction. It is based on an SU(3) gauge field, which leads to 8 mediating massless gauge bosons called *gluons*. Quarks carry a new type of "charge" called *color*. Each (anti)quark can carry a (anti)red, (anti)green, or (anti)blue color charge. Gluons carry a combination of a color and anticolor charge. As carriers of the color charge, gluons can couple to each other. This derives from the non-Abelian character of the gauge theory. Quarks and gluons are collectively referred to as *partons*.

One interesting feature of QCD is that the strength of the strong coupling increases with decreasing energy scale, i.e. at low energies and long distances the interaction becomes too strong to be treated within the framework of perturbation theory. This leads to *confinement*, which assumes that all objects carrying color can never be found as free particles in nature and that they are confined into color-neutral composite hadrons. The quarks that combine into baryons or mesons are referred to as *valence quarks*, and they constantly interact with each other by exchanging gluons. Since gluons can couple to each other, they can emit more gluons that can further split into virtual quark-antiquark pairs called *sea quarks*.

Experimentally quarks and gluons are observed as *jets* of color-neutral hadrons. This means that if a single parton emerges from a particle collision, gluons will be radiated which subsequently produce quark-antiquark pairs to form a *parton shower*. Ultimately the partons combine into a jet of hadrons moving in the direction close to that of the original parton. This final step is called *hadronization*.

The strong coupling constant, α_s, can be expressed to leading-log[1] in Q^2 by:

$$\alpha_s(Q^2) = \frac{12\pi}{(11c - 2n_f)\log(\frac{Q^2}{\Lambda^2})}, \tag{1.8}$$

where Q expresses the magnitude of the momentum transferred in the interaction, n_f indicates the number of quark flavors (6 in the SM), and c is the number of quark colors (3 in the SM). Λ is the QCD scale parameter, defined as:

$$\Lambda^2 = \mu_R^2 \exp\frac{-12\pi}{(11c - 2n_f)\alpha_s(\mu_R^2)}. \tag{1.9}$$

The parameter μ_R introduces an arbitrary renormalization scale to regulate divergences in the perturbative calculation of α_s. Equation 1.8 shows that the strength of the strong coupling decreases with increasing momentum transfer Q^2. Therefore, quarks and gluons are *asymptotically free* when probed at high energies. Theoretical work on asymptotic freedom by Gross, Politzer, and Wilczek was rewarded with the 2004 Nobel Prize. On the other hand, as Q^2 approaches Λ, the coupling becomes large and perturbative calculations are no longer possible.

---

[1]The term "leading-log" is used to indicate an all-orders calculation in which only the leading logarithm terms are retained.

1.1.3 EWSB

The electroweak theory is based on the realization that the quantum of light, the photon, and the quanta of β decay, the $W^{\pm}$ bosons, are intimately related. Just as isospin, asymetry of strong interactions, identifies the neutron and proton as partners, a new symmetry, weak isospin, identifies an electron and its neutrino as partners.

The electroweak symmetry is far from exact. The W and Z bosons are among the heaviest known elementary particles, while the photon is the lightest, though they are related by this symmetry. Similarly, the neutrino and the electron can hardly be confused, even though they are partners.

How is the electroweak symmetry broken? Magnetic field, for example, applied to an atom breaks its rotational symmetry. Or heating up a crystal until it melts breaks the discrete symmetry of the latice. The theory requires that electroweak symmetry be broken in similar, yet in a more intricate form. Without the electroweak symmetry breaking (EWSB), the $W^{\pm}$ and Z, and all the quarks and leptons would be massless. If any progress is to be made in understanding these masses, the source of EWSB must be discovered. It is one of the core questions in high-energy physics.

Mathematically there are several ways to break the electroweak symmetry, however not all of them are appealing from the perspective of physical intuition.

In one approach, a number of scalar particles are introduced. Some of these particles are absorbed by the W and Z bosons thus giving them mass. The remaining appear as new particles. In the simplest realization just one such particle – the higgs boson.

A second possibility, called supersymmetry, predicts the existence of many new particles, among them a number of scalars like the higgs boson. While there is no direct evidence for the supersymmetry

there is strong theoretical motivation for it. There is also some supporting circumstantial evidence from extrapolating the electroweak and strong couplings to high energies, where the three couplings coalesce – if supersymmetry effects are included – as they should if there is a unification of these forces at high energy (grand unification).

A third possibility, referred to as strongly coupled EWSB, introduces no new particles but requires that their role is played by new features of strong interaction. The corresponding theory is commonly referred to as technicolor.

1.1.4 The Standard Model higgs

The simplest form of EMSB is realized with a doublet of complex scalar fields of which as single neutral scalar particle, the Higgs boson, remains after symmetry breaking.

At hadron colliders, Higgs bosons can be produced via four different production mechanisms:

- gluon fusion, $gg \rightarrow H$, which is mediated at lowest order by a heavy quark loop;
- vector boson fusion (VBF), $qq \rightarrow qqH$;
- associated production of a Higgs boson with weak gauge bosons, $qq \rightarrow W/ZH$ (Higgs Strahlung, Drell-Yan like production);
- associated Higgs boson production with heavy quarks, $gg, qq \rightarrow ttH$, $gg, qq \rightarrow bbH$ (and $gb \rightarrow bH$).

The lowest order production cross sections for the four different processes are shown in Fig. 3 for the Tevatron collider as a function of the Higgs boson mass. The dominant production mode is the gluon-fusion process. In the low mass region it amounts at leading order to about 20% of the gluon-

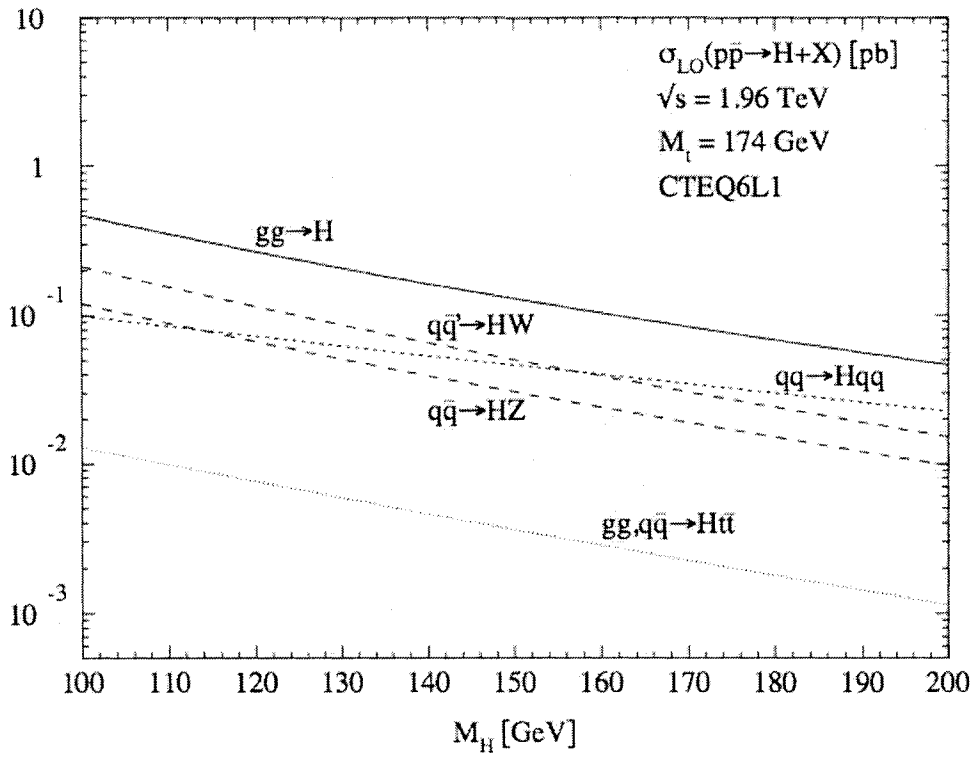

Fig. 3: Leading order production cross sections for a Standard Model Higgs boson as a function of the Higgs boson mass at 1.96 TeV at the Tevatron $p\bar{p}$ collider. In the cross section calculation the CTEQ6L1 structure function parametrization has been used.

fusion cross section, whereas it reaches the same level for masses around 800 GeV/c^2. At theTevatron $p\bar{p}$ collider, the contribution of the associated W/ZH production mode is also important and Higgs boson searches heavily exploit this production mode.

The most relevant decays of the SM Higgs boson [9; 10] are summarised in Fig. 4. For masses below about 130 GeV/c^2, decays to fermion pairs dominate, of which the decay $H \rightarrow b\bar{b}$ has the largest branching ratio.Decays to $\tau^+\tau^-$, $c\bar{c}$ and gluon pairs (via loops) contribute less than 10%. For such low masses the decay width is less than 10 MeV/c^2. For larger masses the W^+W^- and ZZ final states dominate and the decay width rises rapidly, reaching about 1 GeV at $m_h = 200$ GeV/c^2 and even 100 GeV/c^2 at mh0 = 500 GeV/c^2.

The direct search at the e^+e^- collider LEP has led to a lower bound on its mass of 114.4 GeV/c^2 [11]. Indirectly, high precision electroweak data constrain the mass of the Higgs boson via their sensitivity to loop corrections. Assuming the overall validity of the Standard Model, a global fit [12] to all electroweak data leads to $m_h = 114^{+69}_{?45}$ GeV/c^2. On the basis of the present theoretical knowledge, the Higgs sector in the Standard Model remains largely unconstrained. While there is no direct prediction for the mass of the Higgs boson, an upper limit of ≈ 1 TeV/c^2 can be inferred from unitarity arguments [13].

Further constraints can be derived under the assumption that the Standard Model is valid only up to a cutoff energy scale Λ, beyond which new physics becomes relevant. Requiring that the electroweak vacuum is stable and that the Standard Model remains perturbative allows to set upper and lower bounds on the Higgs boson mass[14; 15]. For a cutoff scale of the order of the Planck mass, the Higgs boson mass is required to be in the range $130 < m_h < 190$ GeV/c^2. If new physics appears at lower mass

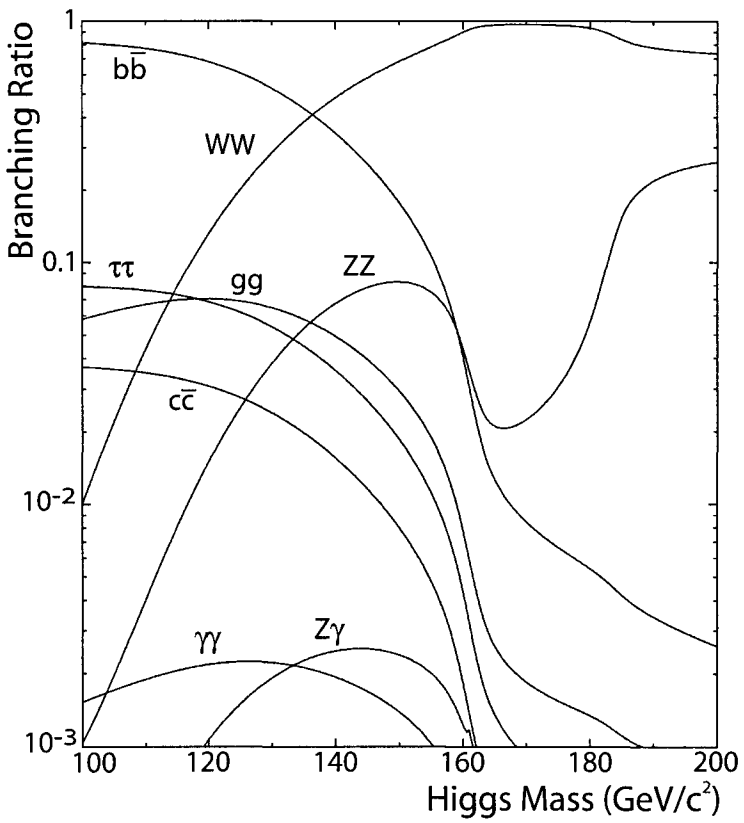

Fig. 4: Branching ratios of SM higgs boson. In the models with richer parameter content branching ratios can differ drastically from those in the SM.

scales, the bound becomes weaker, e.g., for $\Lambda = 1\text{TeV/c}^2$ the Higgs boson mass is constrained to be in the range $50 < m_h < 800\ \text{GeV/c}^2$.

Fig. 5 illustrates upper bounds, obtained by the Tevatron experiments CDF and DØ for the cross sections of event topologies motivated by Higgs boson production in the SM. The curves in the upper part represent the 95% CL experimnetal limits; the curves in the lower part are the SM predictions [16].

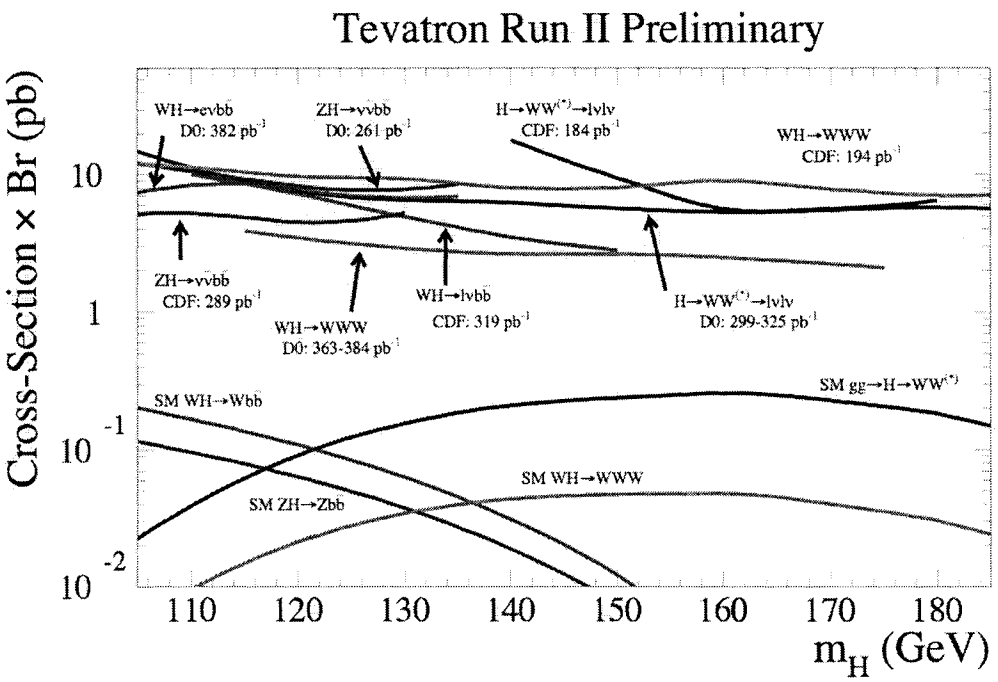

Fig. 5: Upper bounds, obtained by the Tevatron experiments CDF and DØ, for the cross sections of event topologies motivated by Higgs boson production in the SM. The curves in the upper part represent the 95% CL experimnetal limits; the curves in the lower part are the SM predictions.

For a more extensive review of Higgs mass limits in individual modes reader can see, e.g., [17] and references therein.

1.2 Limitations of the Standard Model

The Standard Model has been tested up to a very high precision. The accuracy of its predictions corresponds to experimental data mostly even much better than one percent. All Standard Model particles, except for the higgs boson, have been discovered experimentally. Nevertheless the Standard Model leaves some open questions, some of which are discussed below. They should be answered within a new theory of elementary particle physics.

- The Standard Model depends on at least 19 arbitrary parameters whose values are chosen to fit the experimental data: the values of the electromagnetic, the weak and the strong coupling constant, the mass of the six quarks and the three massive leptons, the four parameters of the Cabbibo-Kobayashi-Maskawa matrix[1], the mass of one of the electroweak bosons ($W^{\pm}$ or Z), the higgs boson massm_h and the parameter θ for the strong CP violation.
- The mechanism of the electroweak symmetry breaking is still unclear. In the Standard Model it is accomplished in an ad hoc fashion by the introduction of a scalar higgs field in the theory. In nature the symmetry breaking may well be realized in a different manner.
- In Grand Unified Theories (GUTs) the known electromagnetic, weak and strong forces are combined into a single theory. At the energy scale of $M_{GUT} \approx 10^{16}$ GeV/c^2 these forces are equally

[1]The Cabbibo-Kobayashi-Maskawa matrix relates the quark mass eigenstates and the weak eigenstates. The four parameters are three mixing angles and one phase.

strong. The difference between the weak energy scale $M_W \approx 10^2$ GeV/c^2 and the GUT energy scale is huge. This is already a powerful clue for physics beyond the Standard Model and is known as the hierarchy problem.

- The Standard Model higgs field requires a non-vanishing vacuum expectation value at the minimum of its potential. From measurements of the properties of weak interactions, m_H^2 is roughly of the order of (100 GeV/c^2)^2. However, m_H^2 receives large quantum corrections from the virtual effects of every particle which couples to the higgs field. When the Standard Model is embedded into a larger theory involving a high-energy scale, an ultraviolet momentum cutoff Λ_{UV} is used to regulate these loop integrals. The quantum corrections to m_H^2 are in the order of Λ_{UV}^2 . If Λ_{UV} is of the order of the Planck scale $M_P = 1.2 \cdot 10^{19}$ GeV/c^2, the quantum corrections to m_H^2 are some 30 orders of magnitude larger than the aimed-for value. The quantum corrections to the higgs mass need an incredible fine-tuning in the Standard Model to cancel the quadratic divergences.

- The couplings of the Standard Model are not constant, but a function of the energy. The strong and weak coupling g_s decrease with energy, while g' on the contrary increases, so it is possible that they become equal at some energy scale. When extrapolating the measured couplings up to a high energy scale, the unification at a single point is not possible within the Standard Model.

2 THEORETICAL MOTIVATION OF THE STUDY

The Standard Model describes our world at the presently attainable energies. Nevertheless, it is hard to hide a frustration about our ignorance on the mass generation mechanism. The spontaneous symmetry breaking mechanism requires a single doublet of complex scalar fields. But does the Nature follow this minimalistic version or does it require a multi-Higgs sector?

In a more general framework where the parameter content of the theory is much reacher one may expect deviations from the SM predictions in the form of drastic changes in the Higgs boson discovery signatures. One such example is the so-called "fermiophobic" Higgs boson, which has suppressed couplings to all fermions. It may arise in a variety of models, see e.g. [18]. A variation of this theme is the Higgs boson in certain top-color models, which may couple only to heavy quarks [19]. Some even more exotic possibilities have been suggested in the context of theories with large extra dimensions [20]. Finally, in the minimal supersimmetric Standard Model (MSSM), the width into $b\bar{b}$ pairs can be suppressed due to 1-loop supersymmetry (SUSY) corrections, thus enhancing the branching ratios of a light Higgs boson into more exotic signatures [21; 22]. In all these cases, the higgs boson decays to photon pairs are mediated through a W or a heavy quark loop and dominate for $m_h < 100$ GeV/c^2 [23].

Experimental searches for fermiophobic higgs (h_f) at LEP and the Tevatron has been negative so far. Mass limits have been set in a benchmark model which assumes that the coupling $h_f VV$ ($V \equiv W^{\pm}, Z$) has the same strength as in the Standard Model and that all fermion BR's are exactly zero. Lower bounds of the order $m_h > 105$ GeV/c^2 have been obtained by LEP collaborations OPAL [24], DELPHI [25],

ALEPH [26], and L3 [27], utilizing channel $e^+e^- \rightarrow h_f Z$, $h_f \rightarrow \gamma\gamma$. At the Tevatron Run I, the limits on m_{h_f} from the DØ and CDF collaborations are respectively 78.5 GeV [28] and 82 GeV [29] at 95% C.L., using the mechanism $qq' \rightarrow V^* h_f V$, $h_f \rightarrow \gamma\gamma$, with the dominant contribution coming from $V = W^{\pm}$. For an integrated luminosity of 2 fb^{-1}, Run II will extend the coverage of m_{h_f} in the benchmark model slightly beyond that of LEP [30; 31]. In addition, Run II will be sensitive to the region $110 < m_{h_f} < 160$ GeV/c^2 and BR($h_f \rightarrow \gamma\gamma$) > 4% which could not be probed at LEP. A preliminary search in the inclusive $2\gamma + X$ channel has been performed with 190 pb^{-1} of Run II data [32].

However, the $h_f VV$ coupling in a specific model could be suppressed relative to the $h_{SM}VV$ coupling by a mixing angle, leading to a weakening of the above mass limits. If this suppression were quite severe ($h_f VV / h_{SM}VV < 0.1$) a very light h_f ($m_{h_f} \ll 100$ GeV/c^2) would have eluded the searches at LEP and the Tevatron Run I in production mechanisms which rely upon the $h_f VV$ coupling. Therefore it is of interest to consider other production mechanisms for h_f which may allow observable rates if the $h_f VV$ coupling is suppressed. Since the couplings $h_f VV$ and $h_f VH$ (where H is another Higgs boson in the model) are complementary, two LEP collaborations, i.e. OPAL [24] and DELPHI [25], also searched for fermiophobic Higgs bosons in the channel $e^+e^- \rightarrow A^0 h_f$, and ruled out the region $m_A + m_{h_f} < 160$ GeV/c^2. However, a very light $m_{h_f} < 50$ GeV/c^2 is still possible if m_A is sufficiently heavy.

An alternative production mechanism which also depends on the complementary $h_f VH$ coupling is the process $qq' \rightarrow V^* \rightarrow h_f V$. Such a mechanism is exclusive to hadron colliders, and can offer promising rates at the Tevatron Run II provided that $H^{\pm}$ in not too far above its present mass bound $m_{H^{\pm}} > 90$ GeV/c^2 [33; 34; 35]. In fermiophobic models the decay $H^{\pm} \rightarrow h_f W^{(*)}$ can have a larger BR than the conventional decays $H^{\pm} \rightarrow tb, \tau\nu$ which leads to double h_f production.

In this study we perform a search for the inclusive production of multi-photon (3γ's or 4γ's) final states through the mechanism:

$$p\bar{p} \rightarrow h_f H^{\pm} \rightarrow h_f h_f W^{\pm} \rightarrow \gamma\gamma\gamma(\gamma) + X \tag{2.1}$$

In the 2HDM the multi-photon signature arises in the parameter space $m_{h_f} < 90$ GeV, $m_{H^{\pm}} < 200$ GeV, and $\tan\beta > 1$. In this region, BR($h_f \rightarrow \gamma\gamma$) ≈ 1 and BR($H^{\pm} \rightarrow h_f W^{\pm}$)$\rightarrow$1, leading to a 4γ + leptons or jets signature. The multi-photon signature has the added virtue of essentially negligible background, in contrast to the conventional searches for single h_f production in the channels $\gamma\gamma + V$ and $\gamma\gamma + X$. In [35] was shown that the multi-photon signal can be observed in a large fraction of the $m_{h_f} \times m_{H^{\pm}}$ plane at the Tevatron RUN II. In fact, at 95% C.L. the RUN II will be able to exclude Higgs masses up to $m_{H^{\pm}} < 270$ GeV for very light m_{h_f} , or $m_{h_f} < 100$ GeV for $m_H^{\pm} \approx 100$ GeV. For a complete information reader is referred to the bibliography referenced in this chapter and references therein. At this point we proceed to the experimental portion of this thesis which is the primary purpose of the present study.

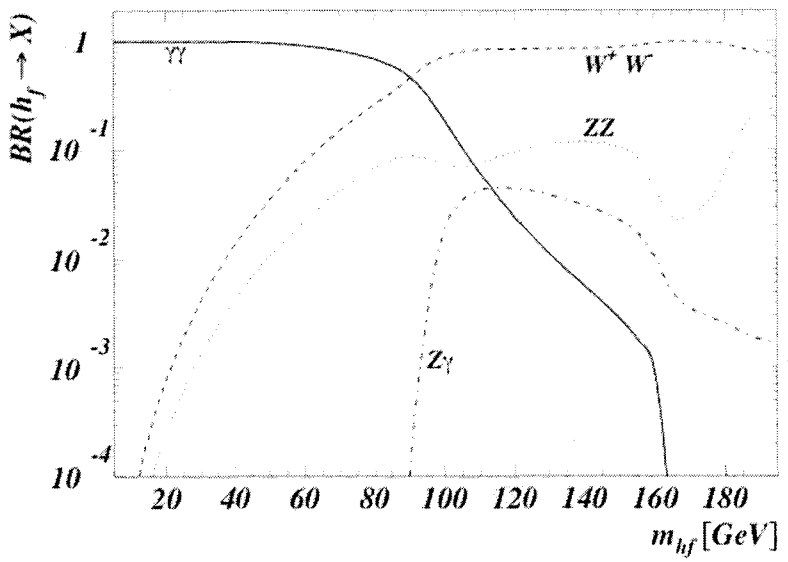

Fig. 6: Branching ratios of the largest decaymodes of afermiophobic higgs boson assuming exact fermiophobia at tree-level. The branching ratio into $\gamma\gamma$ equals the W^*W^* mode for $m \approx 90$ GeV/c^2 and drops to 20% for $m = 100$ GeV/c^2.

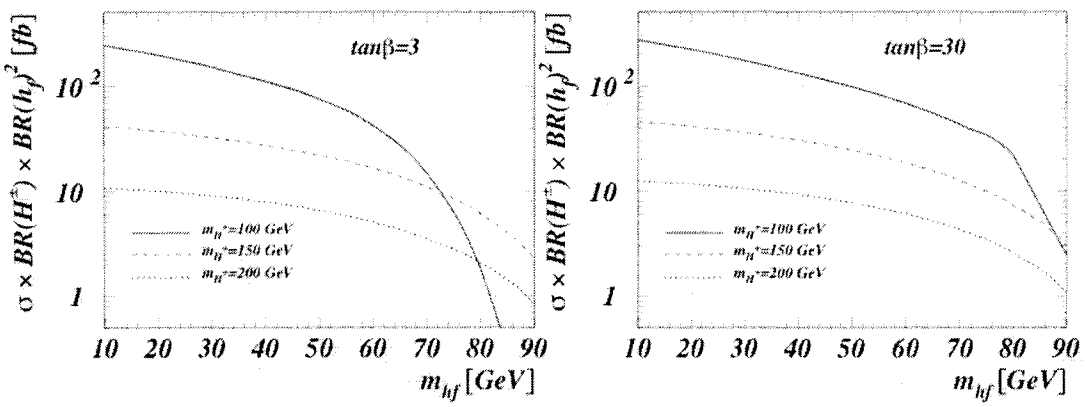

Fig. 7: Total production cross sections times branching ratios of $h_f \to \gamma\gamma$ and $H^{\pm} \to W^{\pm} h_f \to 4\gamma + W$ before cuts at the Tevatron RunII in femtobarns. The values of $\tan\beta$ and $m_{H^{\pm}}$ are as indicated in the figure.

3 THE FERMILAB ACCELERATORS

Fermi National Accelerator Laboratory (FNAL, or Fermilab) hosts the world's highest energy proton-antiproton collider, the *Tevatron*. In this chapter we describe the chain of accelerators that is necessary to achieve a center-of-mass collision energy of 1.96 TeV.

The Tevatron's operation started in 1987 and by the year 1989 its mission to provide the highest possible center-of-mass energy proton-antiproton collisions was achieved. These collisions, unlike any that have occurred since very shortly after the birth of the universe, were recorded by the two detectors DØ and CDF. During the Run I physics program (1992-1996), the Tevatron ran with 1.8 TeV collision energy and delivered luminosity to each of its two collider detectors of nearly 130 pb^{-1}. Currently the Run II physics program in under way, with the collider that has been upgraded to deliver both a higher center-of-mass energy (1.98 TeV) and much higher luminosity. This is the highest energy accelerator complex in the world, and will remain the energy frontier until the completion of the Large Hadron Collider (LHC) at CERN that will start its operation in the middle of 2008.

As with most high energy accelerators the Tevatron complex accelerates particles in several stages[36; 37; 38]. These accelerator components, schematically shown in Fig. 8, are crucial to achieve desired energies and instantaneous luminosities. They are as follows:

- A Cocroft-Walton pre-accelerator;
- Linear Accelerator: the LINAC;

- The Booster Synchrotron;
- The Main Injector;
- The Anti-proton source;
- The Debuncher, Accumulator;
- The Recycler;
- The Tevatron Ring Synchrotron.

3.1 The Pre-accelerator

The purpose of the pre-accelerator is to produce negatively charged hydrogen ions (H^-) with an energy of 750 keV, which are then transferred into the Linac. The reason for producing negatively charged ions becomes clear at later stages of acceleration and accumulation of protons – "The Booster". With this charge it is easier to inject a new portion of protons and not worry about Coulomb spread of the beam.

Hydrogen gas (H_2) enters a magnetron surface-plasma source (Fig. 9). Due to the electric field between the anode (positively charged) and cathode (negatively charged), the electrons are stripped away from the hydrogen atoms to create a plasma. The positively charged hydrogen ions then strike the surface of the cathode to collect extra electrons and form negatively charged hydrogen ions. The H^- ions are extracted through the anode aperture with an electric field of 18 kV applied by the extractor plate (Fig. 9).

A commercial Cockcroft-Walton Generator produces a 750 kV potential differential by charging capacitors in parallel from an AC voltage source and discharging them in series, via diodes [1]. The Cockcroft-Walton Generator is used to further accelerate the H^- ions to an energy of 750 keV.

After exiting the Cockcroft-Walton device the H^- ions travel through a transfer line. Before entering into the Linac the continuous stream of H^- ions passes through a single gap radio frequency (RF) cavity which bunches the beam at the RF frequency of the Linac (201.24 MHz).

3.2 The Linac

The Linac receives bunches of 750 keV H^- ions from the pre-accelerator and accelerates them further to an energy of 400 MeV using RF cavities (Fig. 10). The RF cavities are contained within a collection of steel tanks which are holding a sequence of drift tubes separated from each other by gaps. In order to accelerate H^- ions, the cavities are designed in such a way that particles traveling in the gaps experience an acceleration, while particles traveling in the drift tubes are shielded from the RF.

After passing through the Linac, bunches of 400 MeV H^- ions are transferred into the Booster.

3.3 The Booster

The Booster is the first synchrotron in the chain of accelerators. It consists of a sequence of dipole and quadrupole magnets and 17 RF cavities arranged in a circle with a diameter of 151 m. The Booster accelerates protons to an energy of 8 GeV.

It is easier to merge negatively charged H^- ions coming from the Linac with protons (H^+ ions) circulating in the Booster due to their opposite charge. Therefore the two beams are merged with the

---

[1] The maximum voltage is limited by how much the air can "stand off" before sparking.

help of dipole magnets, and the electrons are stripped from the H^- ions by letting the combined beam pass through a carbon foil.

Once the Booster is filled with proton bunches, the RF cavities provide an acceleration up to 8 GeV. At the same time the field strength in the dipole magnets is ramped up accordingly in order to maintain a constant radius for the circulating particles. Once the protons have reached an energy of 8 GeV they are transferred into the Main Injector.

3.4 The Main Injector

The Main Injector is a circular synchrotron with a diameter of 1 km. It can accelerate both protons (coming from the Booster) and antiprotons (coming from the Antiproton Source) from 8 GeV to 150 GeV before injecting them into the Tevatron. It also delivers 120 GeV protons to the Antiproton Source.

3.5 The Antiproton Source

The Antiproton Source consists of three major components: the *Target Station*, the *Debuncher*, and the *Accumulator*. In the first step the Target Station receives 120 GeV protons from the Main Injector and diverts them onto a Nickel Target. This produces a shower of secondary particles (including antiprotons) at many different angles and with a large spread in particle momentum. A Lithium lens and bending magnets are used to focus the beam and remove positively charged particles (Fig. 11). A process called *stochastic cooling* is used in both the Debuncher and Accumulator in order to reduce the spread in momentum and position of the antiprotons and thereby "cooling" them.

Both the Debuncher and Accumulator are located in a rounded-triangle shaped tunnel with a circumference of about 51 m. Antiprotons coming from the Target Station are transferred into the Debuncher where the momentum spread of the particles is reduced. It is technically very challenging to accumulate

a large quantity of antiprotons. On average, for every 1 million protons that hit the Nickel target, only about 20 antiprotons can be gathered. Therefore the Accumulator stores antiprotons until a sufficient amount has been generated that can be transferred into the Main Injector. The Accumulator must be capable of storing antiprotons over many hours.

3.6 The Tevatron

The Tevatron is the final stage in the sequence of proton and antiproton acceleration. It has a diameter of 2 km and uses superconducting magnets which operate at liquid helium temperature providing magnetic fields of up to 4 Tesla. Protons and antiprotons are accelerated to 980 GeV, leading to a center-of-mass collision energy of 1.96 TeV.

Protons and antiprotons travel in groups of particles (*bunches*) in opposite directions while sharing the same beam pipe. A full revolution (*turn*) takes $\approx$21 μs. The Tevatron injects 36 bunches of both protons and antiprotons for each store. A three fold symmetry is imposed by separating the 36 bunches into three superbunches. Overall, this leads to a time structure where bunches of protons and antiprotons (*live bunch crossings* or *zero bias events*) collide at 1.7 MHz [39].

3.7 Luminosity and Cross Section

Luminosity $\mathcal{L}$ is a measure of the particle flux per unit area and per unit time ($cm^{-2}s^{-1}$). In a collider experiment such as DØ, the luminosity gives an indication of how many proton-antiproton crossings occur in a given time and area. The luminosity is determined by measuring the rate of inelastic proton-antiproton scatterings for each bunch crossing, using scintillator arrays located near the beam pipe. These measurements are normalized to the expected (from previous measurements at lower $\sqrt{s}$) inelastic cross sections [40; 41].

The cross section σ is a measure of the interaction probability per unit flux. Cross sections are usually expressed in *barns*, where 1 barn = 10^{-24} cm^2.

The number of times a given process occurs, N, is proportional to $\mathcal{L}$ and σ:

$$N = \sigma \cdot \int \mathcal{L}\, dt, \tag{3.1}$$

where $\int \mathcal{L}\, dt$ is called *integrated luminosity*. Fig. 12 shows the integrated luminosity profile of the Tevatron, covering the data taking period from April 2002 through December 2005. A total integrated luminosity of 833 pb^{-1} was used for the result presented in this analysis.

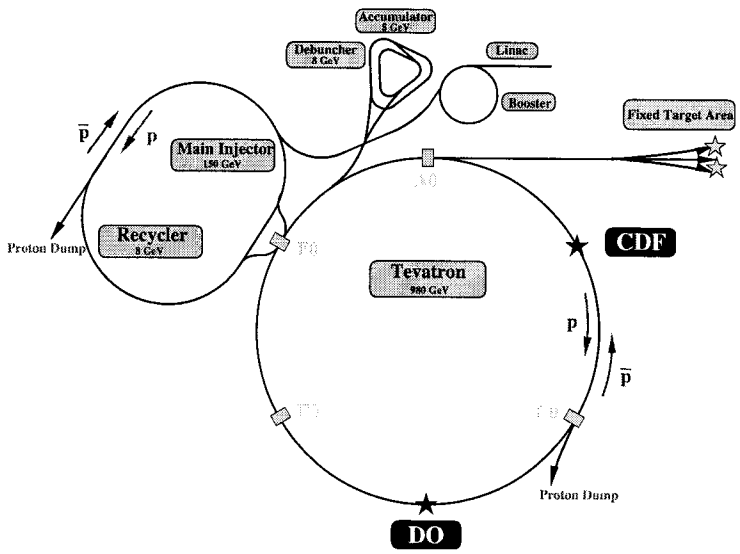

Fig. 8: Schematic view of the Fermilab accelerator chain.

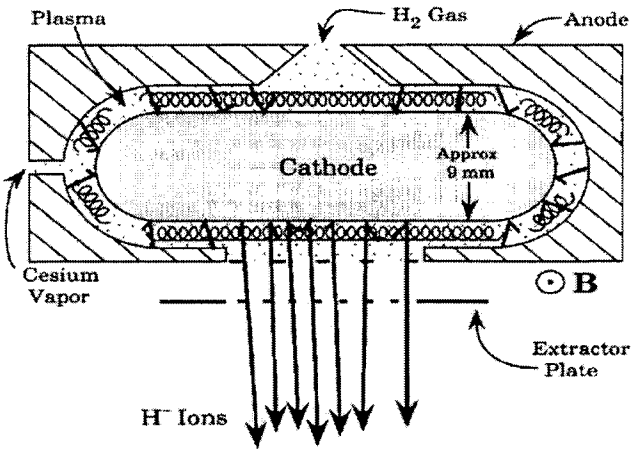

Fig. 9: Schematic view of magnetron operation for the hydrogen ion source.

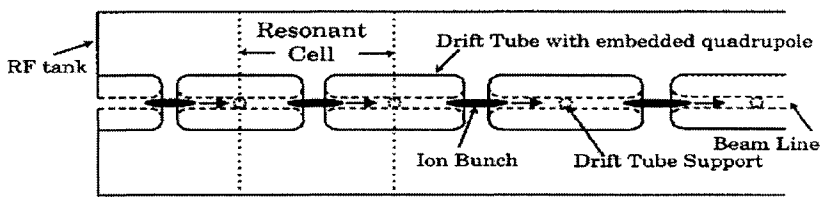

Fig. 10: Schematic of Linac RF cavity.

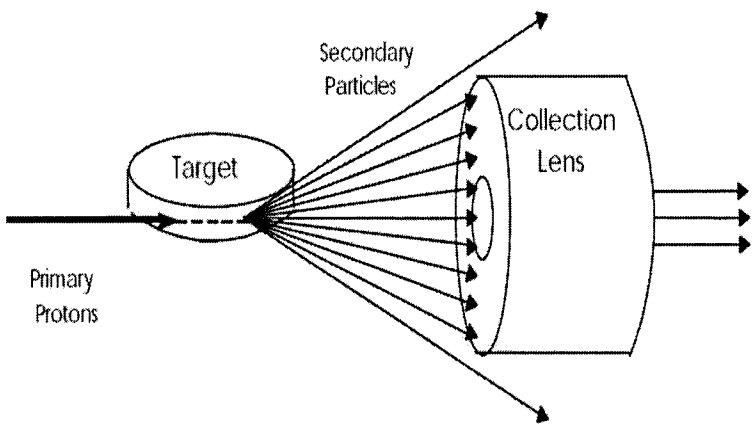

Fig. 11: Simplified drawing of anti-proton production with nickel target and lithium lens.

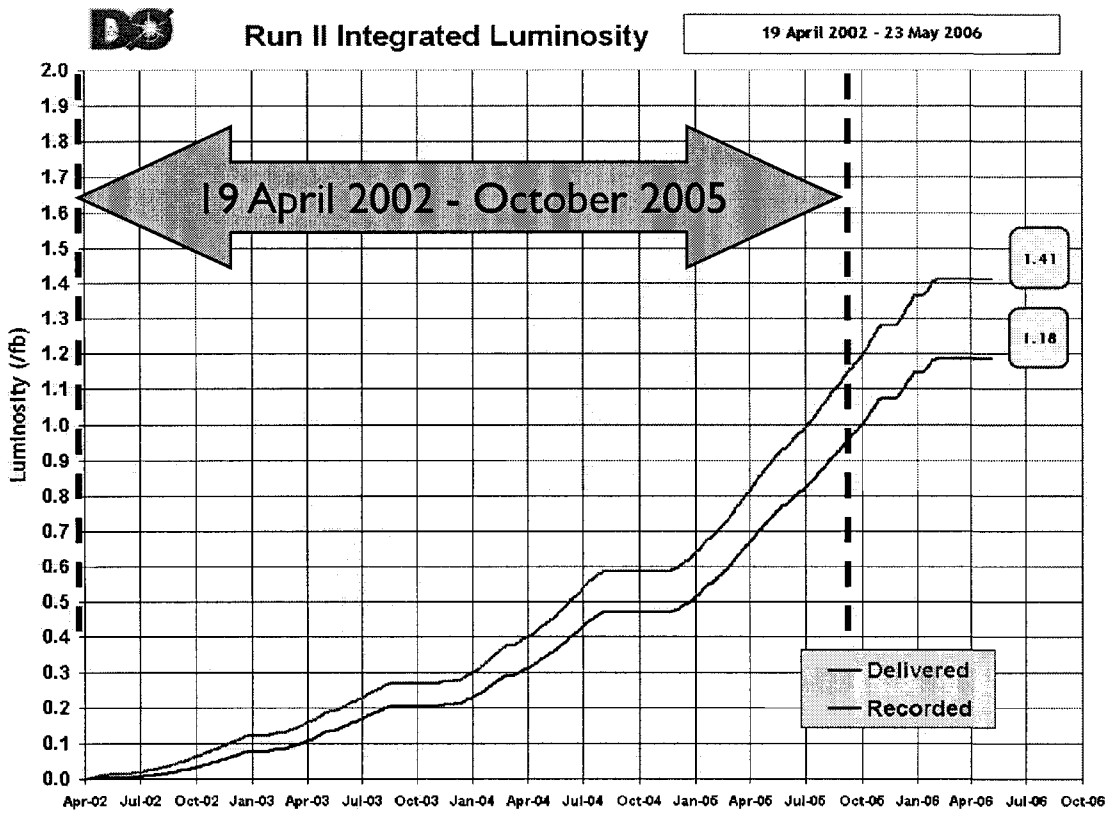

Fig. 12: Tevatron integrated luminosity delivered to DØ (April 2002 - October 2005). The arrow indicates the period during which the data for this analysis were recorded.

4 THE DØ DETECTOR

We provide an overview of the DØ detector which is built around one of the interaction regions where protons and antiprotons collide. The data used in this analysis were recorded with the DØ detector during the data taking period known as Run II, which officially began in March 2001.

The DØ detector [42; 43] has a magnetic central-tracking system, consisting of a silicon microstrip tracker (SMT) and a central fiber tracker (CFT), both located within a 2 Tesla superconducting solenoid (Fig. 13). Central and forward preshower detectors are located outside of the superconducting coil. A liquid-argon/uranium calorimeter has a central section (CC) covering pseudorapidities $|\eta|$ up to ≈ 1, and two end calorimeters (EC) extending coverage to $|\eta| \approx 4$, all three housed in separate cryostats. A muon system resides beyond the calorimeters, and consists of a layer of tracking detectors and scintillation trigger counters before 1.8 Tesla toroids, followed by two more similar layers after the toroids. Luminosity is measured using plastic scintillator arrays located in front of the EC cryostats. The three-tiered trigger and data acquisition systems are designed to accommodate the high luminosities of Run II.

Although a full description of the DØ detector is given in this chapter, the elements that are most relevant for the analysis presented in this dissertation are the calorimeter (Chapter 4.4) and tracking system (Chapter 4.2).

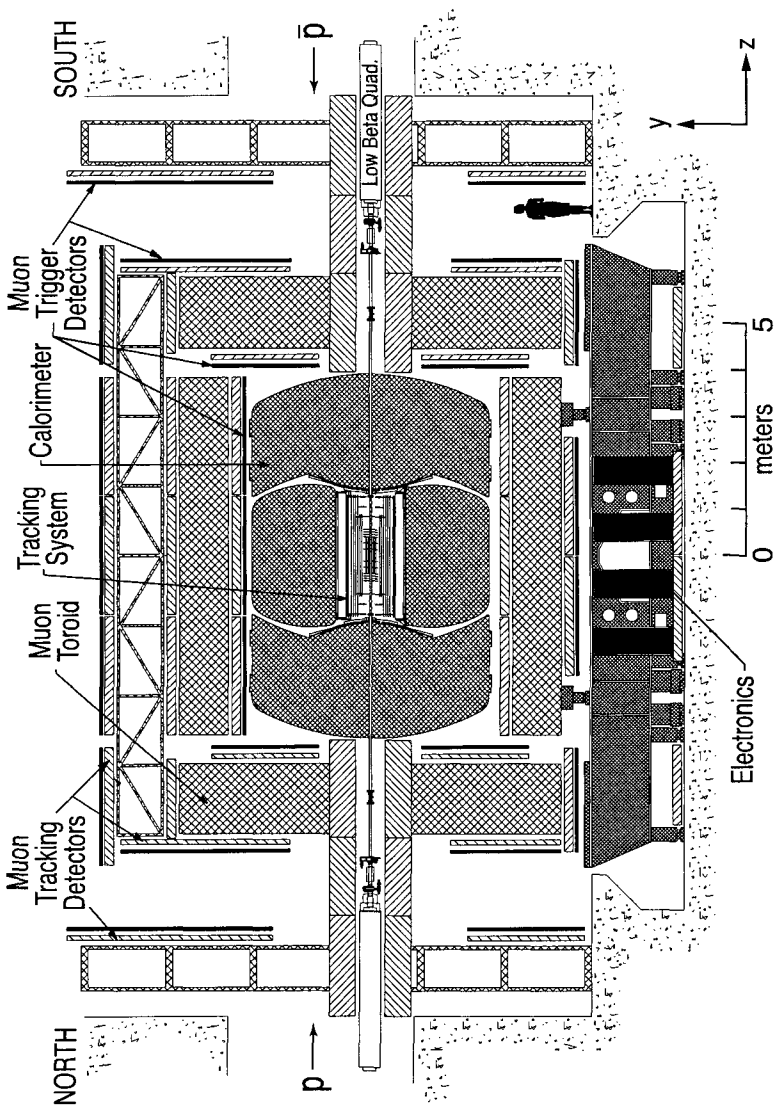

Fig. 13: Schematic view of the Run II DØ detector.

4.1 Coordinate Systems

The coordinate system used for the DØ detector is right-handed. It has the positive z-axis aligned with the direction in which the protons travel, and the positive y-axis pointing upwards.

In most cases cylindrical coordinates are used (z, ϕ, θ). ϕ is the azimuthal angle in the plane perpendicular to the beam (z-axis), where ϕ=0 coincides with the positive x-axis. θ is the polar angle relative to the positive z-axis.

Since the colliding protons and antiprotons can exhibit a significant net boost along the z-axis, it is suitable to choose a polar angle quantity that is invariant under relativistic transformations. Therefore, it is often more convenient to use pseudorapidity η instead of the polar angle θ:

$$\eta = -ln \cdot \left[tan \frac{\theta}{2} \right] \tag{4.1}$$

The pseudorapidity approximates the true rapidity,

$$y = \frac{1}{2} \cdot ln \left[\frac{E + p_z}{E - p_z} \right] \tag{4.2}$$

in the limit of $m \ll E$ (where m is the invariant mass $m^2 = E^2 - p^2$). The term "forward" is used to describe regions at $|\eta| > 1.1$.

In many cases some of the products of a proton-antiproton collisions escape along the beam pipe, which makes it difficult to measure momentum components along the z-axis accurately. Therefore it

is more convenient to use the momentum vector projected onto a plane perpendicular to the beam axis (*transverse momentum*):

$$p_T = p \cdot sin\theta. \tag{4.3}$$

In a similar fashion *transverse energy* is defined as

$$E_T = E \cdot sin\theta. \tag{4.4}$$

Unless stated otherwise, the four-momentum vectors for objects observed in the calorimeter are calculated using calorimeter energies.

4.2 Central Tracking System

The central tracking system measures the position and momentum of tracks resulting from the paths of charged particles. It is also essential in measuring the position of the primary interaction vertex with high accuracy, which subsequently allows good measurement of lepton p_T, jet E_T and missing transverse energy ($\not\!\!E_T$). It can also detect the presence of b-quarks through the measurement of displaced vertices.

The Central Tracking System consists of the silicon microstrip tracker (SMT), the central fiber tracker (CFT) and the superconducting solenoid (Fig. 14). Combining information from both SMT and CFT, the primary vertex resolution is approximately 35 μm along the beamline. Jets originating from the decay of b-quarks can be measured with an impact parameter resolution of less than 15 μm in the $r-\phi$ plane.

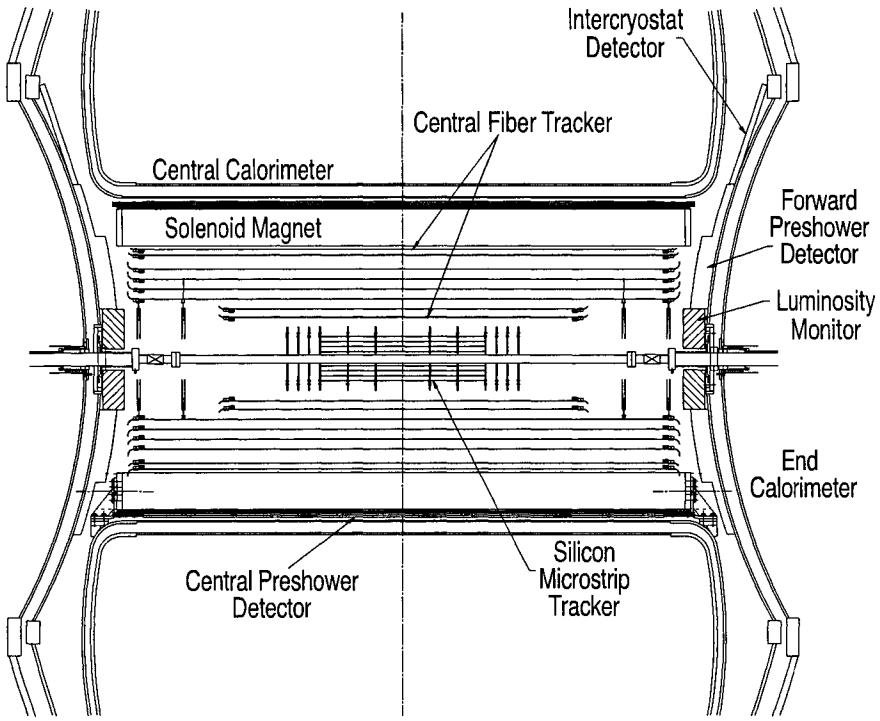

Fig. 14: The DØ central tracking system with solenoid, preshower detectors, luminosity monitor, and calorimeter.

4.2.1 Silicon Microstrip Tracker

In order to be able to detect the paths of charged particles emerging from a proton-antiproton collision, the SMT [44] uses wafers of silicon with a thickness of 300 μm. When a charged particle passes through a positive-negative ($p-n$) junction in silicon, it produces electron-hole pairs that can be separated by an applied voltage. The charge which is collected can then be stored in capacitors and later read-out and digitized. The SMT contains approximately 800,000 individual channels. Fig. 15 shows the design of a basic silicon detector unit (*ladder*).

The SMT is designed in such a way that tracks of charged particles are perpendicular to detector material over a large range of η values. The structure of the device is mostly dictated by the fact that the interaction region is spread out with respect to the center of the detector ($\sigma \approx 25$ cm). This lead to a design of barrel modules combined with disks in the center and larger disks in the forward region (Fig. 16). The SMT has six barrels along the z-axis, each containing four detector layers with a maximal outer radius of 10.5 cm. There are twelve small diameter double-sided "F" disks and four large diameter single-sided "H" disks to cover the far forward region ($|\eta| <3$). The F-disks are at $|z|$ = 12.5, 38.2, 43.1 and 53.1 cm. The centers of the H-disks are located at $|z|$ = 100.4, 121.0 cm.

4.2.2 Central Fiber Tracker

The Central Fiber Tracker (CFT) [45] is located between the SMT and the edge of the solenoid magnet. The purpose of the CFT is to improve the detection of charged particle tracks within $|\eta| < 2$. It consists of approximately 70,000 scintillating fibers mounted on eight concentric support cylinders with inner and outer radii of 20 and 52 cm, respectively. Each cylinder carries two layers of fibers running parallel to the beampipe (*axial layers*), and two layers of fibers oriented at small angles of $\pm 3^\circ$ (*stereo*

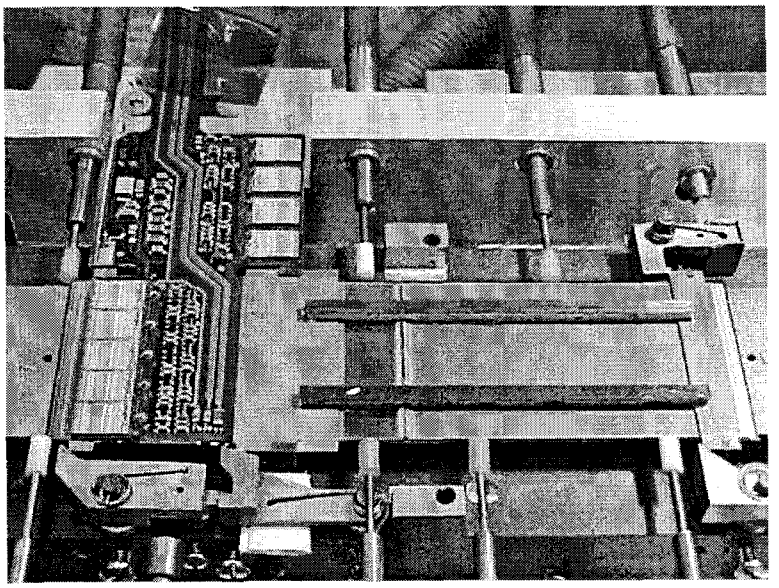

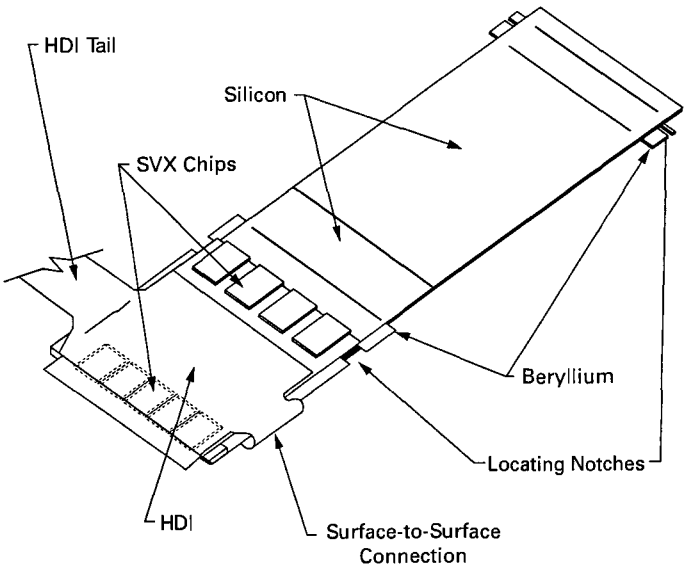

Fig. 15: Drawing of a silicon ladder (bottom) and a photon of a double sided ladder during assembly of the silicon onto the High Density Interconnect, HDI (up).

layers) (Fig. 17). The scintillating fibers have a diameter of 835 μm and are composed of a scintillating core surrounded by a layer with a high index of refraction, which leads to total internal refraction.

Charged particles passing through a scintillating fiber excite the molecules in the fiber which subsequently release photons in the yellow-green part of the visible light spectrum as they relax to their ground states. Clear fiber waveguides carry the scintillation light to visible light photon counters (VLPCs) that convert the light into electrical signals. The VLPCs are silicon avalanche photodetectors that operate at liquid helium temperature in order to reduce the background due to electronic noise.

4.2.3 Solenoid

The superconducting solenoid significantly improves the capabilities of the DØ detector since it allows measuring the momentum of charged tracks. The location and physical size of the solenoid are constrained by the available space between the inner tracking system and the vacuum vessel of the central calorimeter. The magnet has a length of 2.73 m and a diameter of 1.42 m and provides uniform field of 2 T (20 kG) [1] over most of the region covered by the inner tracking system (Fig. 18). Fig. 19 shows a perspective view of the solenoid inside the central calorimeter with its chimney and control dewar.

---

[1] After winter '06 shutdown magnetic filed was lowered down to 1.93 T due to failure of the solenoid to hold its nominal current. Although the cause was never determined, failure in grounding was suspected. Fortunately, this 5% change in the curvature of the particle trajectories can be neglected in comparison to the other uncertainties.

4.3 Preshower Detectors

The preshower detectors [46; 47] are designed to improve the identification of electrons and photons, and to correct for their upstream energy losses during offline event reconstruction. Due to their fast response time, the preshower detectors can also be used for Level 1 triggering.

Scintillators are used to measure both the position and energy of charged particles. In contrast to the scintillators used in the CFT, the preshower scintillators are triangular shaped (Fig. 20). This arranges scintillator layers without creating any dead space and thereby improves the accuracy of position measurements. The center of each scintillator carries a wavelength-shifting fiber which collects the light created by passing charged particles. The light is transmitted via clear fibers to VLPCs for readout.

4.3.1 Central Preshower Detector

The Central Preshower Detector (CPS) is located in the 5 cm gap between the solenoid and the central calorimeter, covering the region $|\eta| < 1.3$ (Fig. 14). It consists of a layer of lead radiator which has a thickness corresponding to approximately one radiation-length (X_0), followed by three layers of triangular scintillator strips. The scintillating layers are arranged in an axial-u-v geometry, with a u stereo angle of 23.8° and a v stereo angle of 24.0°. Each layer has a total number of 2,560 readout channels.

4.3.2 Forward Preshower Detector

The two Forward Preshower Detectors (FPS) are attached to the faces of the end calorimeters and cover a region of $1.5 < |\eta| < 2.5$ (Fig. 14). Each detector consists of an upstream double layer of scintillator strips (minimum ionizing particle layers, or MIP layers), followed by a lead-stainless-steel absorber layer, and another double layer of scintillator strips behind it (shower layers).

4.4 Calorimeter

The main purpose of the calorimeter system is to measure the position and energy deposits from electrons, photons, and jets. In addition, by imposing transverse energy balance in an event, it can also detect the presence of neutrinos.

The calorimeter system consists of a central calorimeter (CC) covering $|\eta| < 1.2$ and two end calorimeters (EC), covering $1.3 < |\eta| < 4.5$ (Fig. 21). Each of the calorimeters has an electromagnetic section, followed by fine and coarse hadronic sections (FH and CH, respectively). Since liquid argon is used as the active medium, all calorimeters are contained within cryostats. Different types of materials are used for absorber plates:

- 3 mm (4 mm) plates of depleted uranium for the CC (EC) electromagnetic sections.
- 6 mm plates of uranium-niobium (2%) for the fine hadronic sections.
- 46.5 mm plates of copper (stainless steel) for the CC (EC) coarse hadronic sections.

A typical calorimeter cell is shown in Fig. 22. Each cell consists of a grounded absorber plate and a signal board maintained at a positive high voltage of typically 2 kV. The 2.3 mm gap between the absorber plate and signal board is filled with liquid argon. The calorimeter cells are arranged to form pseudo-projective towers (Fig. 23). In order to measure the energy of electromagnetically interacting objects, the calorimeter takes advantage of the electromagnetic shower process. For example, an incoming high-energy electron will emit bremsstrahlung photons when passing through the dense absorber material. The emitted photons will subsequently convert into electron-positron pairs. The shower will continue until low energy photons start interacting via Compton and photoelectric effects

and the electrons/positrons via ionization. At each stage of the electromagnetic shower, charged particles are ionizing the liquid argon. The high voltage between the absorber plates and signal boards is then used to collect the ionization charges to measure the energy in the shower. Note, that there are gaps between ϕ-modules of the central calorimeter. This leads to the fringing of the electric field and thus longer trajectories of the ions close to the ϕ-boundaries. In order to reduce noise that comes from the particles that do not belong to an triggered event a charge collection time is gated by the readout electronics. These, together with absence of charge collection at these boundaries, leads to significant charge energy mis-measurement of the shower in the vicinity of the ϕ-cracks[1].

Hadronic showers are induced by the interaction between hadronic particles and the nuclei of the absorber material via the strong nuclear force. Secondary hadronic particles then further interact via inelastic nucleus collisions till their energy falls below a threshold. Typical transverse sizes of hadronic showers are of the order of 10 cm.

The space in between the central and end calorimeters ($1.1 < |\eta| < 1.4$) is referred to as the inter-cryostat region (ICR). In order to be able to measure the energies of particles that pass through this gap in the calorimeter coverage, additional detectors are used. Calorimeter cells called massless gaps (MG) are installed before the first layer of uranium inside of the central and end cryostats. Additionally, a ring of scintillator tiles mounted to the exterior surface of the end cryostats comprises the intercryostat detector (ICD).

Fig. 24 shows the different calorimeter detection layers for a given η value [48].

---

[1] See corresponding section on photon and electron reconstruction efficiencies.

4.5 Muon System

Due to their large mass and long lifetime, muons pass through the calorimeter by depositing only a small amount of energy ($\approx$ 2.5 GeV) via ionization. Therefore, the outermost subdetector is dedicated to the detection of muons (Fig. 25). The muon system is separated into central and forward detectors. A 1.9 T iron toroid magnet is used for muon momentum measurements.

Proportional Drift Tubes (PDT), Mini Drift Tubes (MDT), and scintillators are the main detection elements used in the muon system. Drift tubes collect the ionization charges created by muons passing through a gas mixture onto high voltage wires. Correlating the arrival times of ionization charges from different drift tubes with the beam crossing time allows extrapolation of the path of muons as they pass through the detector. Scintillators are mainly used for their good timing resolution ($\approx$ 4 ns) which allows this to trigger on muons.

The central muon system [49] covers the region of $|\eta| < 1.0$ and is referred to as the Wide Angle Muon System (WAMUS). It consists of three PDT layers, with the first layer (A layer) in between the toroid magnet and the calorimeter, and two more layers (B and C layers) after the toroid magnet. Additional layers of scintillators before the A layer and covering the outside of the muon system allow the rejection of cosmic rays by using spatial and precise timing measurements . The forward muon system [50] covers the region of $1.0 < |\eta| < 2.0$ and is referred to as the Forward Angle Muon System (FAMUS). It consists of three MDT layers and scintillators, with the first layer (A layer) before the toroid magnet, and two more layers (B and C layers) after the toroid magnet.

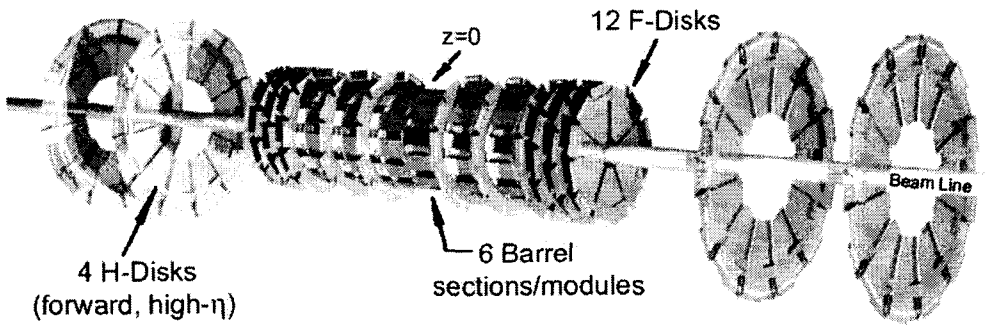

Fig. 16: SMT disk and barrel design.

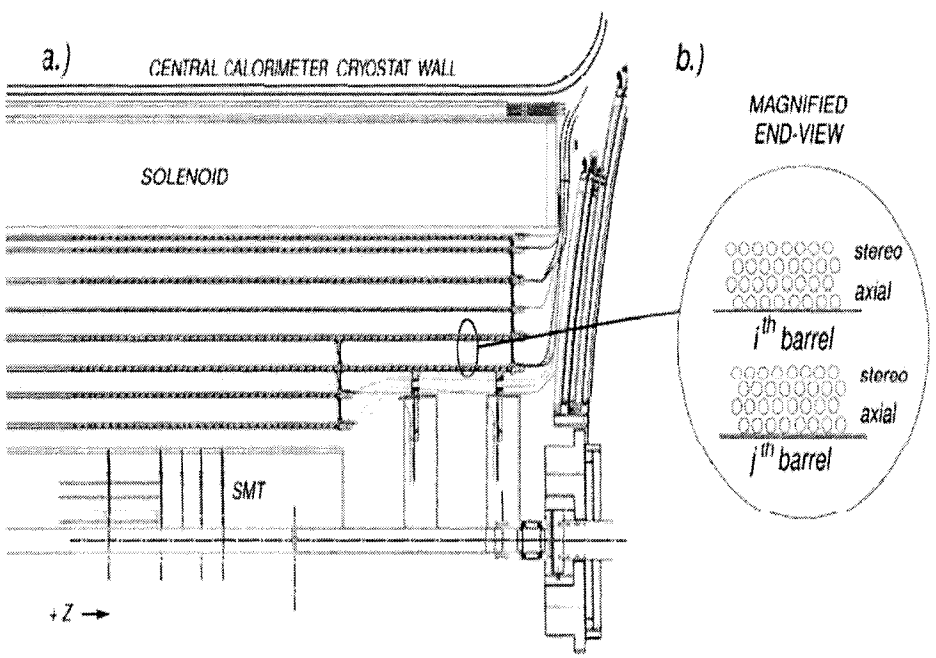

Fig. 17: a) Location of the Central Fiber Tracker (CFT). b) Closeup view of axial and stereo layers.

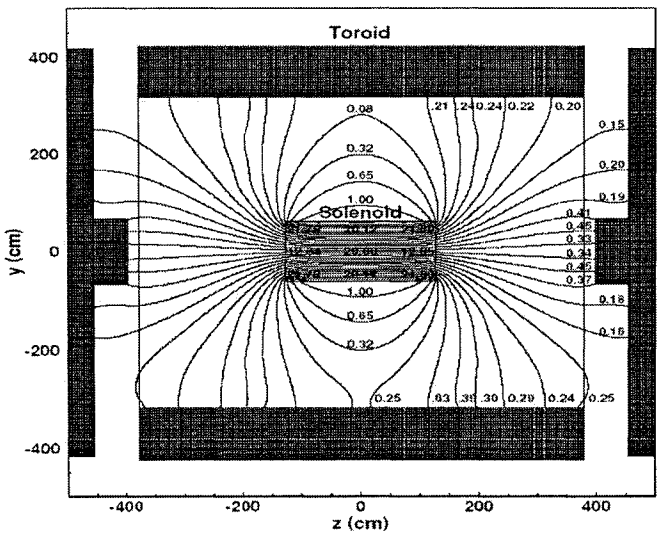

Fig. 18: $y-z$ view of the DØ magnetic field with both the toroid and solenoid magnets at full current. Numbers are in kG (10 kG = 1 T).

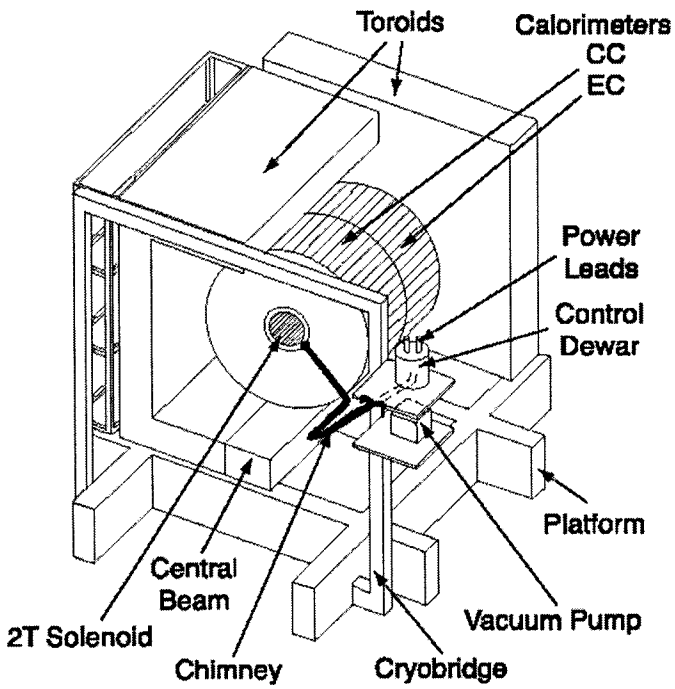

Fig. 19: Perspective view of the solenoid inside the central calorimeter.

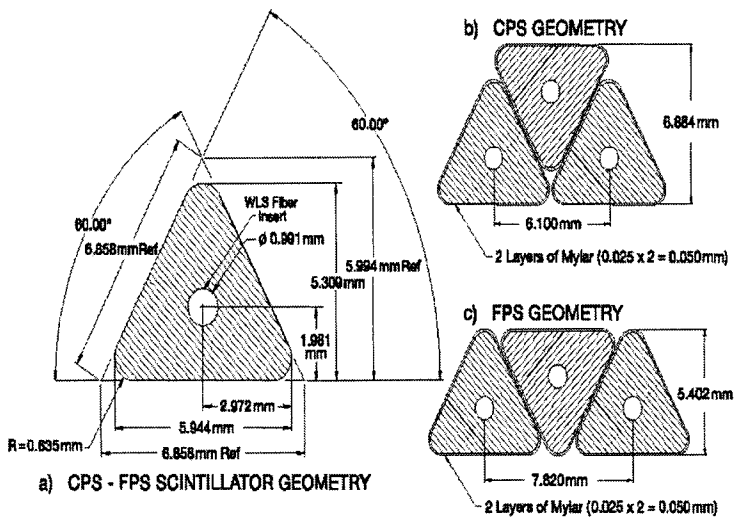

Fig. 20: Cross section and layout geometry of CPS and FPS scintillator strips.

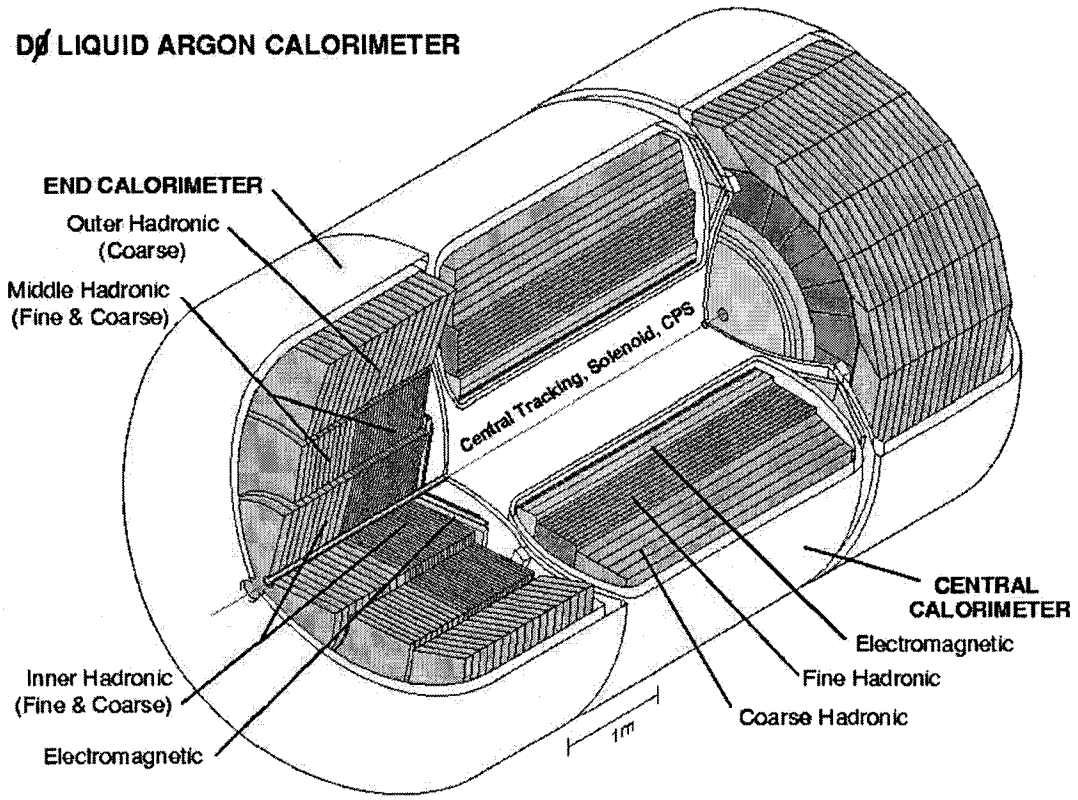

Fig. 21: Isometric view of the central and two end calorimeters.

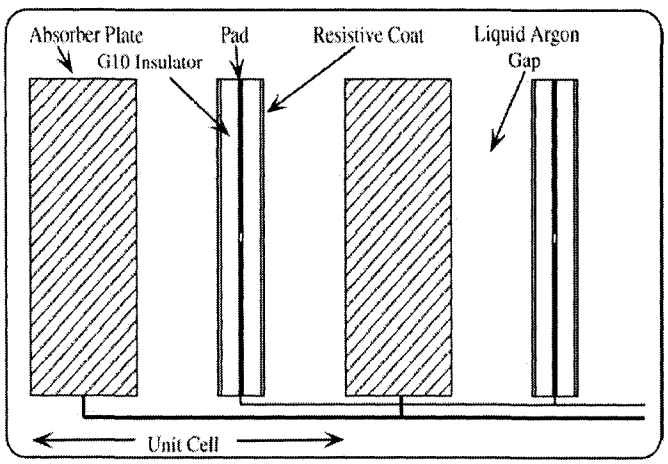

Fig. 22: Schematic view of two calorimeter cells.

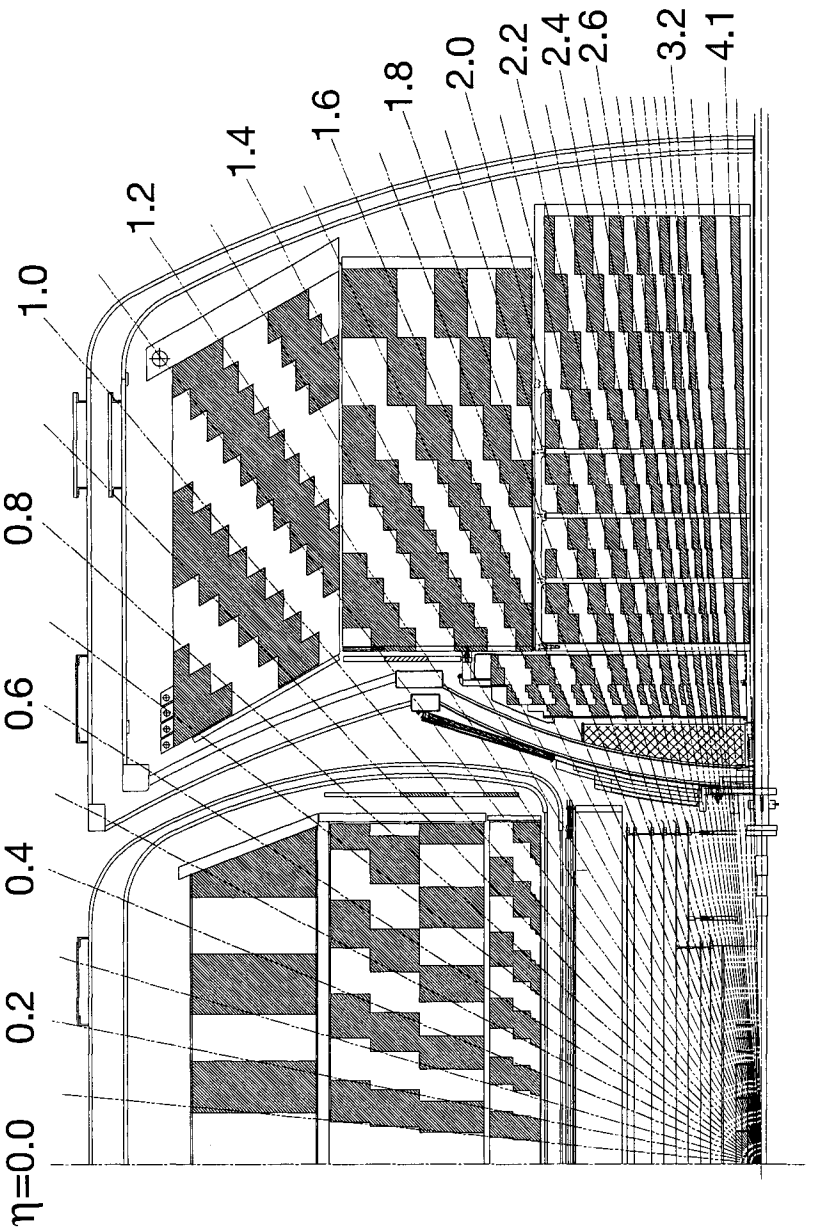

Fig. 23: Schematic view showing the calorimeter segmentation pattern. The shading pattern indicates cells for signal readout. The radial lines show the detector pseudo-rapidity intervals.

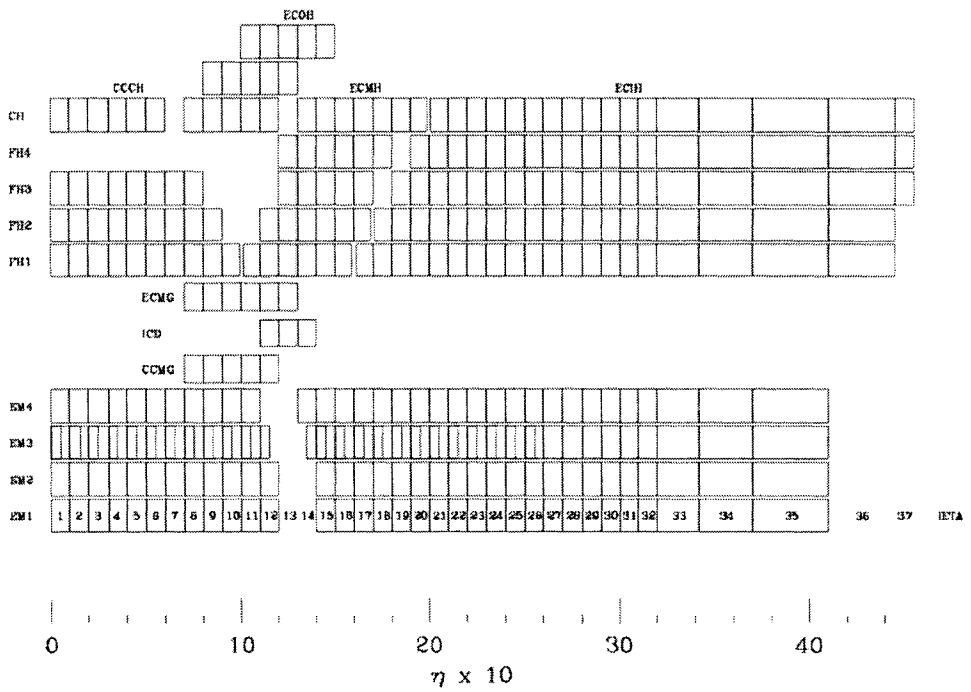

Fig. 24: Schematic view of different calorimeter detection layers vs η.

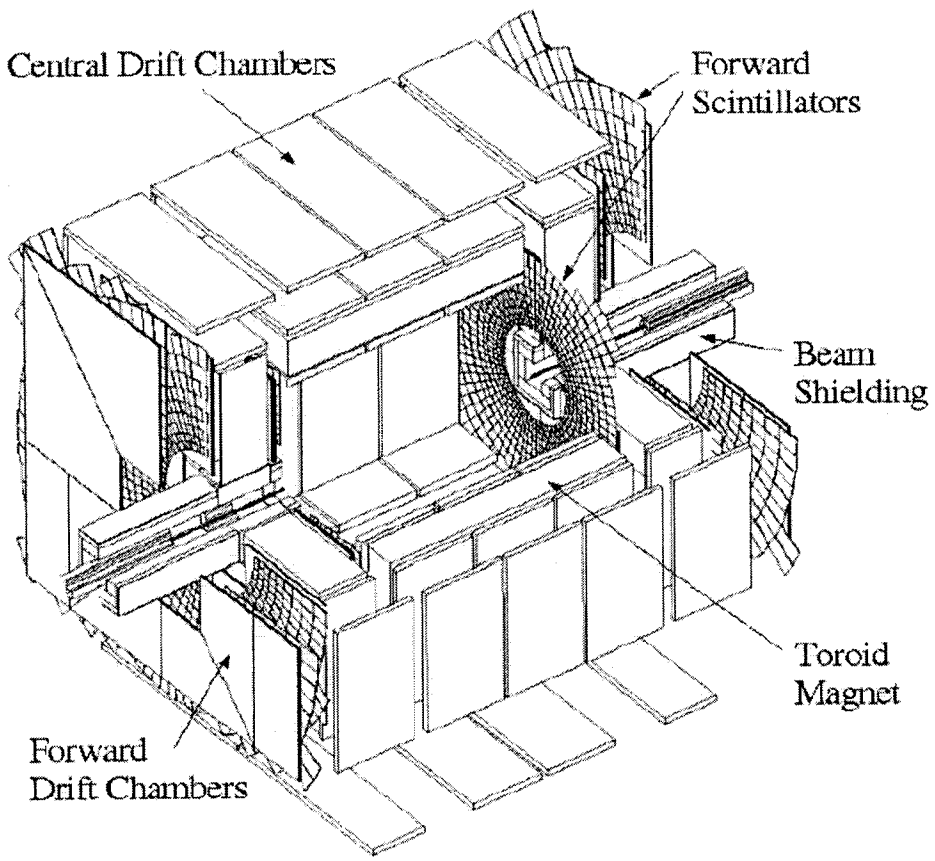

Fig. 25: The DØ muon system.

5 OFFLINE EVENT RECONSTRUCTION

The DØ detector is designed to detect and identify remnants of proton-antiproton collisions. Particles that are produced in these collisions interact with the detector and records of these interactions are stored as the raw data. To study the physics of particle interactions it is necessary to reconstruct kinematic properties of the particles that emerged from the original interaction. This reconstruction is done by means of a software program called d0reco [51] in C++ programming language.

The d0reco program is comprised of many software packages. Individual packages are responsible for a single reconstruction task, be it reconstruction of the electromagnetic cluster calculation of covariance matrix associated with it. Event reconstruction from the raw data is very CPU intensive task. A significant fraction of reconstruction time is spent in the track reconstruction phase. It is understandable – with thousands of SMT and CFT hits even clever track reconstruction algorithms (see next section) suffer from combinatorics of hits, let alone brute force track reconstruction which is merely impossible to use. It takes on average 2-4 minutes to reconstruct an event. With more than two billion recorded events the only way to reconstruct this quantity of data is by using computer farms.

As our knoweldge of the detector improves and reconstruction software becomes more elaborate and sophisticated new versions of d0reco appear, organized by the version number. The data used in this analysis was reconstructed using p17.x versions of d0reco. I should stress that d0reco is the result of work of many people over many years, and in this section only an overview of the basic concepts of particle reconstruction is presented.

5.1 Track Reconstruction

Charged prticles passing through the DØ SMT and CFT detectors deposit energy in many layers. These localized depositions are called hits. In addition to the hits from high-momentum charged particles traversing the detector (which are of primary interest for most of New Phenomena analyses), there are also hits from the low momentum tracks from jets, tracks from secondary collisions in the event, tracks from particles interacting with the beam pipe, and random electronic noise. For any event, there are many such hits in the tracking detectors which make the reconstruction of tracks difficult.

5.1.1 Tracking Algorithms

Several different algorithms have been used to reconstruct tracks in the DØ detector. Algorithms are chosen for each analysis based on unique requirements. The most common algorithm, used in this analysis for the study of efficiencies, is now a combination of the AA track algorithm [52] and the Hough transformation algorithm (HTF) [53]. Each is run separately and to generate a list of track candidates and then the two lists are combined, and duplicates are removed. After that, the final fitting is done.

The AA track algorithm starts by generating a pool of track candidates using the hits in the SMT. The algorithm selects all sets of three hits which lie along a path originating from a beam spot. It then extrapolates the path of the track outward to either the next layer of the SMT or to the CFT to calculate the location where the track would have crossed the next layer. The algorithm checks whether there is a hit near that location, and then extrapolates to the next layer, and repeats the procedure. At each layer a χ^2 of hits with respect to the track is calculated and the hit becomes associated to the track if its χ^2 is less than a certain value. If there is no hit in the layer, the algorithm continues and records a "miss" for this track. At the end of this procedure, a list of tracks is produced along with hits, misses, and χ^2-s.

Next, a list of vertices is constructed from tracks propagated back to the beam axis. These vertices are used to look at the track candidates that only have CFT hits. The same extrapolation procedure is used but starting in the CFT with the constraint that tracks originated at one of the vertices. CFT-only tracks have been used in several analyses and provide higher efficiency, although at some expense of resolution.

The trajectory of a charged particle in a uniform magnetic field is a helix. Its x-y projection, i.e. perpendicular to the magnetic field, is a circle and can be parametrized by three quantities: its curvature, impact parameter, and direction at the point of closest approach. The HTF algorithm operates in this parameter space. Each pair of hits corresponds to a point in this space. Further, hits that reside in the same bins are considered to correspond to the same track.

The separate lists from two AA and HTF algorithms are combined into one list and sorted by the number of hits, fewest misses, and lowest χ^2, in that order. The best tracks are kept and the rest are examined. These track are retained if they share not more then 2/3 of the hits of a good track or the number of unique hits is greater than three.

Still there is some inefficiency built into track reconstruction to make it robust. For energetic charged particles one can recover a significant fraction of lost tracks by using so-called Hits On the Road (HOR) algorithm [54]. HOR is a tracking algorithm design to recover lost tracks produced by energetic particles. This algorithm will be described in more detail later in this paper.

5.2 Primary Vertex Reconstruction

The primary vertex is critical for reconstruction of jets, b-jets, electrons, photons, and missing transverse energy. Once a list of tracks and a list of vertices have been found, the primary vertex can be

selected [55]. From these tracks, an initial selection is performed to exclude tracks with high impact parameter significance with respect to the beam line. These tracks can come from particles with a long lifetime, and therefore decaying away from the primary vertex. All the remaining tracks after the above selection are fitted to a single vertex, and the track with the highest χ^2 is rejected. Then this procedure is repeated for the remaining tracks, until those that remain all have χ^2 less than 10. In this case a primary vertex is found. The entire process is repeated on the remainder of the tracks to find and reconstruct any remaining primary vertices. After all primary vertices are identified, the secondary vertex finding is performed to reconstruct the decay positions of long lived particles.

5.3 Electromagnetic Object Reconstruction

The first step in the reconstruction of EM objects in DØ is the readout of the nearly 55,000 calorimeter channels (readout cells). The calorimeter readout is "zero-suppressed", meaning that only energies above pedestal and noise are read out. Zero-suppression is quantified as a ratio of the measured energy above the pedestal to the mean width of the noise (σ) in that channel. The suppression used is 2.5σ which means that the measured energy above the pedestal must be 2.5 times larger than the noise in the channel that is being read out. Also, due to liquid argon contamination, noise in depleted uranium, and deficiencies in the readout electronics, cells with unusually high energy can appear affecting the reconstruction. To mark these cells and prevent their usage, an algorithm called "NADA" [56] has been specifically designed for this purpose. The resulting calorimeter cells, with the same η and ϕ are grouped together to form towers[1]. Despite NADA and other event quality guards, we discovered a

[1] A calorimeter readout tower has $\delta\eta \times \delta\phi$ size of 0.1×0.1 zand a trigger tower is of the size 0.2×0.2 in $\delta\eta \times \delta\phi$.

certain fraction of events with an excess of perfectly isolated photons. We performed a global search for such objects and excluded regions in the calorimeter for certain run ranges where abnormality of deposition of electromagnetic energy was statistically significant. See 8.2.2 [57] for more details.

The showers from electron and photons are very similar: clusters of energy deposited in the adjacent cells of the EM calorimeter. Hence reconstruction of these objects is performed with the same algorithm. Reconstruction of EM object is handled by the EMReco component of d0reco. There are three different clustering algorithms available: the Nearest Neighbors (NN), Simple Cone (Scone), and the CellNN algorithms. For this analysis we use only scone algorithm since it provides better robustness in the energy regime of interest (E> 15 GeV) and backgrounds that are dominated by direct photons.

An EM tower consists of four EM layers and the first hadronic layer. The most energetic tower is selected. Then, a cluster is formed from the towers within $\Delta R = \sqrt{\Delta\eta^2 + \Delta\phi^2} = 0.4$. Clusters are allowed to be within $\Delta R = 0.3$ of each other. In the End Caps (EC) the algorithm uses a 10 cm window instead of 0.4 in ΔR. Among all reconstructed clusters, genuine EM showers are expected to pass crude selection criteria imposed by d0reco:

- the cluster must have a minimum transverse energy of 1.5 GeV
- the cluster should be relatively narrow which is enforced by requiring that more than 40% of its energy be contained in the central most energetic tower

- the cluster must have at least 90% of its energy deposited in the electromagnetic layers of the calorimeter. This fraction is defined as a ratio of cluster energy deposited only in the EM section of the calorimeter to the total energy (including FH1)[1]
- the cluster is required to be isolated in (η, ϕ) space, with the isolation is defined as fraction of EM energy outside of the smaller cone with $\Delta R > 0.2$, i.e.:

$$iso = \frac{E_{EM}(R \in [0.2, 0.4])}{E_{EM}(R \in [0.0, 0.2])} < 0.2. \tag{5.1}$$

The clusters that pass these criteria are selected as electron/photon candidates. For each such candidate, the centroid of the cluster is computed by weighting positions of the cells with the logarithm of the energy in the cluster at the third layer of the calorimeter (EM3). This layer is the most finely segmented in $\Delta\eta \times \Delta\phi = 0.05 \times 0.05$. The shower position together with the primary vertex is used to calculate the direction of the 4-momentum of the particle.

---

[1]Note, that with this definition a jet can lead to a reconstructed EM object.

6 PHOTON IDENTIFICATION

The present work heavily depends on our reliable understanding of photons in the DØ detector. But what do we really imply by the term "understanding"? Resisting a temptation of going into philosophical intricacies of this notion we resort to a more practical side – we ask, how should we select a detector photon so that we maximize our discovery potential. The answer to this question hinges on two quantities – ε_γ and ε_{bkg}, signal and background efficiencies, respectively. Here, by the background we mean hadronic jets and electrons that mimic photons due to various inefficiencies and limited resolution.

The probability that a jet will have most of its energy fragmented into all-neutral component (except neutrons), and hence EM, is very small. However, an enormous jet production cross section makes such backgrounds a real problem and thus requires clever algorithms to suppress them. Large backgrounds are not the only problem in photon identification.

We don't really know what a real photon looks like in our detector. As opposed to electrons for which nature has blessed us with a Z-boson resonance decaying into electron-positron pair and thus an unbiased source of electrons, photon pairs can not be separated from a comparable hadronic background based on their invariant mass. A sole reliance on the detector simulation (MC) is a trojan horse and a potential recipe for disaster if not treated carefully. In order to study photons we choose the approach described in the next section.

6.1 Approach

Electrons and photons have very similar and well understood interactions with detector materials. Because of the similarity in the shower formation we choose to treat photons like electrons without tracks. Since it is as close as we can get to the real photons we choose such selection variables that describe electrons well and for which there is no significant discrepancy between electrons and photons in the MC. In other words, we trust that our MC faithfully models *differences* between photons and electrons.

Then, we obtain difference between electrons in Data and in MC as well as difference between photons and electrons in MC and apply these two scaling factors to photon MC for proper comparison with the experimental data.

Yet, there remains a difference in signature that photons and electrons leave in the tracker and that can not be neglected. An electron leaves a track most of the time, and a photon, on the other hand, converts with a trace reconstructed as a track some fraction of a time. Thus, it makes sense to obtain the above mentioned scaling factors from the variables that do not contain track-verification. As far as the effect of conversions is concerned, it is appears to be not so trivial a task and is covered in [58]. The basic idea is to vary amount of material in the tracker and estimate the corresponding variation of the photon reconstruction efficiency. It was found [58] that amount of material was within 20%, and we assigned a conservative uncertainty of 3%.

6.2 Nomenclature

Before we proceed we believe it would be helpful to list definitions and various abriviations used throughout the rest of this study:

- MC – Monte Carlo detector or event simulation
- EM loose $\equiv$ EM – reconstructed calorimeter cluster with more than 90% of the electromagnetic fraction and less than 20% of isolation (see below)
- CC– Central Calorimeter
- EC – End Cap Calorimter
- fiducial – region of the detector far from inactive or highly nonlinear regions
- id=10, ± 11 – redundant, now this definition is absorbed into EM loose
- η – pseudorapidity (see Sec. 4.1) quantity related to the polar angle as $\eta = -ln \tan\theta/2$
- ΔR – metric in $\{\eta, \phi\}$ space, $\Delta R = \sqrt{(\Delta\eta)^2 + (\Delta\phi)^2}$
- emfr – electromagnetic faction of the shower (see Sec. 5.3)
- iso – isolation of electromagnetic shower (see Equation 5.1)
- sigphi – energy weighted rms of EM towers that make up given EM cluster
- prbtrk – χ^2-probability of a track to be matched to EM cluster, with $\chi^2 \equiv (\delta z/\sigma_z)^2 + (\delta\phi/\sigma_\phi)^2$, which is close to unity for an electron and almost zero for a background. An electron is said to have a track-match if trkprb>0.001

- H-Matrix(n)– covariance matrix for associated with an object in the EM calorimeter that uses n variables
- Lhood(8) – electron likelihood probability constructed from the distributions of 8 variables for electrons (P^i_{sig}) and for the background (P^i_{bkg}):

$$Lhood = \frac{\prod P^i_{sig}}{\prod P^i_{sig} + \prod P^i_{bkg}} \tag{6.1}$$

- CSG – Common Samples Group – a group responsible for centralized processing of DØ data
- CAF/CAFE – Common Analysis Format
- skim – a subset of data that was preselected with specific triggers or objects in the event
- highpt – having high transverse momentum
- EMMU – refers to a skim that contains events with one EM cluster and one muon candidate
- QCD – refers to a skim with events selected with jet triggers
- p17.xx.yy– a version of DØ reconstruction software applied on a given sample
- JT – in trigger names refers to a Jet Trigger
- 15JT – 15 GeV in trigger total (EM+Hadronic) towers
- CJT(i,j) – Central Jet trigger
- CFT – Central Fiber Tracker
- CPS – Central PreShower detector

- MB/ZB – Minimum/Zero Bias refers to events recorded in data and added to MC in order to simulate ambient hadronic activity in the detector

6.3 Identification Samples

In order to identify the best selection variables and choose optimal cuts we need the following objects: electrons, photons, and EM-like jets both in Data and in MC. Also, various single particle MC with additional amount of material to study effets of photon conversion. The following object sources were chosen:

- 2EMhighpt CSG skim – source of electrons in Data
- QCD CSG skim – source of EM-like jets in Data
- EMMU CSG skim – source of EM-like jets in Data
- Z→ee MC with overlaid MB
- direct photon MC ($\gamma + jet$) with overlaid MB
- $jet + jet$ MC enriched with EM-jets with overlaid MB
- single particle γ, e, π^0, and η MC with default material description
- single particle γ, e, π^0, and η MC with $0.1X_0$, $0.2X_0$, $0.3X_0$, $0.5X_0$, and $1.0X_0$ of extra uranium placed in front of the tracker[1].

---

[1]Placing extra material on the beampipe simulates a worst case scenario where conversion happens early enough to have a reconstructed track.

All data samples were reconstructed with p17.06.03, the version that contains the latest description of the material distribution in the tracker as well as other important improvements.

MC samples were reconstructed with the same version of d0reco. All MC samples (except single particle) were fixed with p17.08.05 version of the fixer. This version mainly concerns a description of the hadronic energy and improved description of EM-jets.

All study samples were converted into the cafe trees using p18.03.00 CAFE package. These trees reside in the common Photon-ID area /rooms/light hosted by enlightened-clued0.fnal.gov.

6.3.1 Data Electrons

As a source of electron candidates we use Z→ee events found in 2EMhightpt Common Sample skim. Dataset definition for fixed caf trees is CSG_CAF_2EMhighpt_v3. This skim requires an event to have at least two EM objects with id = 10 or ±11 and p_T above 15 GeV/c. Then, we use so-called tag-and-probe method to select electrons free from trigger bias. One of these candidates – the tag – is required to pass stringent cuts to improve the purity of the sample and be matched to a fired trigger while the other candidate – the probe – is required to pass the cuts relevant to the efficiency to be determined.

Tags satisfy these requirements:

- reconstructed with simple cone algorithm[1] with id = 10 or ±11
- EM fraction > 0.90
- isolation <0.15

---

[1]From now on we will assume that all EM objects in this study were reconstructed with Simple Cone algorithm, as opposed to CellNN that might be studied elsewhere.

- Lhood(8)>0.85
- H-Matrix(7) < 12 (CC)
- H-Matrix(8) < 20 (EC)
- spatial track probability greater then 0.01
- single-electron trigger within $\Delta R < 0.4$
- either in CC or in EC ($|\eta| < 2.5$)
- in η fiducial
- primary vertex within $\pm$ 60 cm
- $p_T > 25$ GeV

And a probe is defined as an EM object that passes a set of base ("**loose EM**") cuts plus a set of cuts under study:

- id = 10 or ± 11
- EM fraction > 0.90
- isolation < 0.15
- either in CC or in EC ($|\eta| < 2.5$)
- in η fiducial
- cuts under study

Further, we choose only events that fired at least one trigger from a set of predefined single-EM triggers. The trigger selection is identical to the one that we use in our analysis and we refer the reader to the corresponding section (Sec. 8.2.1). It is important to require that a tag electron is matched to a fired trigger. Mainly because if we don't require the tag to be matched to a trigger then there would be a fraction of electrons that has already been purified by the trigger selection which is in its turn tighter than EM loose definition. This will be reflected in a certain overestimation of the reconstruction efficiency.

6.3.2 MC Electrons

For a sample of electrons we use Drell-Yan $\gamma^*/Z \rightarrow$ee MC events with request id's given below:

- $m_{inv} \in [15GeV, 60GeV]$: 24270, 24269,
- $m_{inv} \in [60GeV, 130GeV]$: 24559, 23092, 23091, 23090, 24557, 24558,
- $m_{inv} \in [130GeV, 250GeV]$: 24047.

These samples were generated with the overlay of detector noise and ambient hadronic activity taken from data (so-called raw2sim overlay). They can be accessed in sam using the following name mask:

- `CSG_CAF-MCv1-${reqid}` - CAFE trees,
- `req-id-${reqid}-tmb-good-fix.p17.08.02`.

Reconstructed EM clusters were required to be within 0.3 in ΔR from the generator level electrons. Tag and probe are defined in the same way it is done for the real electrons except for the trigger and event quality requirements.

6.3.3 MC Photons

As a source of MC photons we use prompt photon events. These are full Pythia $2 \rightarrow 2$ processes with a direct photon in the final state. Corresponding dataset definition mask `req-id-$reqid -tmb-good-genuine`. With the following request ids:

- $p_{T\,min} \in [\ 5GeV/c, 980GeV/c]$: 28789, 28790
- $p_{T\,min} \in [\ 10GeV/c, 980GeV/c]$: 28787, 28788
- $p_{T\,min} \in [\ 20GeV/c, 980GeV/c]$: 28755, 28776
- $p_{T\,min} \in [\ 40GeV/c, 980GeV/c]$: 28777, 28778
- $p_{T\,min} \in [\ 80GeV/c, 980GeV/c]$: 28779, 28780
- $p_{T\,min} \in [980GeV/c, 1600GeV/c]$: 28781, 28782

They were processed with p17.09.01 version of d0reco and further transformed into CAFE trees with the help of p18.04.00 version of d0correct. Events in these samples have to satisfy the following requirements:

- at least one loose EM object (id = 10, ± 11, p_T>10 GeV, $|\eta|$<2.5, iso<0.15, and emfr>0.90)
- EM object should be separated from all (isGood() && !isEM()) jets by 0.9 in ΔR
- event should contain at least one such jet
- in these jets, leading jet should be above 15 GeV and trailing jet, if any, - below 10 GeV
- corrected missing transverse energy should be below 10 GeV
- primary vertex should be within $\pm$ 60 cm

- EM cluster should be opposite to the leading jet – $|\phi_{EM} - \phi_{lead\_jet} - \pi| < \pi/9$,
- matched MCpart photon should not come from any hadron.

One should be aware of certain bias in the sample that contains components with different turn-on curves. For some discussion see Sec. 6.3.6.

6.3.4 Data EM-jets

6.3.4.1 Jet triggered sample

Fake photon candidates were selected in a way similar to that used before [59]. We study fake photons in a di-jet sample where one jet with large fraction of its energy carried by neutral particles while the other has fired a jet trigger. A complication arises from $\gamma + jet$ events whose content is sizable with the number of $fake + jet$ events. The latter forms an irreducible background since topologically these two processes are almost indistinguishable. Therefore, we estimate expected fraction of $\gamma + jet$ events from event generator and apply it to the $fake + jet$ sample.

Common Sample QCD p17 skim was used to select EM-jets. Events were selected based on firing of either of the following single jet triggers:

- JT_15TT
- JT_25TT_NG
- JT_45TT
- JT_65TT
- JT_95TT

In these events we identify EM objects:

- id = 10 or ± 11
- iso<0.15
- emfr>0.90
- $|\eta| < 1.1$
- in η fiducial
- separated from any jet which is (isGood()&&!isEM()) by $\Delta R < 0.9$
- p_T>10 GeV

These events were selected in such a way that the EM objects contain some fraction of electrons and direct photons. These would lead to the overestimation of the fake rate if not properly accounted for. A sizable fraction of electrons that come from copious decays of W bosons can be removed by vetoing on neutrino momentum, i.e. a cut on missing transverse energy:

- $\not\!\!E_T < 10$ GeV

As far as direct photons are concerned we need to trust MC for a reliable subtraction. Especially we need to reliably model the fraction of direct photons in our sample of "fake" photon candidates. γ+jet final states, although difficult to model, have a better description than events with higher multiplicities of jets. Therefore, we choose to select only those events that have an energetic jet recoiled from an EM object and low energy secondary jets. These requirements are as follows:

- at least one jet that is (isGood()&&!isEM()) and is separated from the EM cluster by $\Delta R > 0.9$

- $p_t^{leading} > 15$ GeV
- $|(\phi^{leading} - \phi^{EM}) - \pi| < \pi/9$
- $p_t^{next} < 10$ GeV

6.3.4.2 Muon triggered sample

In this work we do not provide details of a study of a photon fake rate performed on a sample of events with EM-like jets triggered by a muon from a jet. This approach has been superficially addressed and we did not observe any significant deviation in the shape of the p_T distributions of EM-jets that would have been a clear indication of an unacceptable bias coming from jet triggers.

6.3.5 MC EM-jets

EM-jet events are QCD events where a quark or a gluon has fluctuated into a jet with a leading EM component[1]. The probability of such a fluctuation is very low, approximately a few percent. This makes statistically significant sample difficult to obtain with approximately 5 sec/evt spent in simulation and reconstruction phases.

In order to collect enough statistics we preselected such jets at the generator level, i.e. we accepted only those particle level jets that have a leading neutral component. Preselection efficiency for all p_T bins is shown in Tab. Table II.

6.3.6 On the bias in a sample with different turn-on components

Note, that the requirement of ϕ separation introduces additional bias close to the boundary of the minimal p_T with which the sample was generated. One of the possible reasons of this bias could be the

---

[1] I.e. such jets that pass EM loose cuts.

Table I: Single Jet triggers used to select events with fake photon candidates.

Trigger	L1	L2	L3
JT_15TT	CJT(2,3)	none	SCJET_8(15)
JT_25TT_NG	CJT(2,5)	none	SCJET_8(25)
JT_45TT	CJT(2,5)	none	SCJET_8(45)
JT_65TT	CJT(3,5)	L2Jet(1,20)	SCJET_8(65)
JT_95TT	none	none	none

L1 Triggers

CJT(n, E_T^{cut})	n global trigger towers with $E_T > E_T^{cut}$ GeV

L2 Triggers

L2Jet(1,20)	one L2 Jet candidate with $E_T > 20$ GeV

L3 Triggers

SCJET_8(E_T^{cut})	one L3 jet with $\|\eta\| < 3.0$ and $E_T > E_T^{cut}$ GeV

p_T	preselection efficiency	cross section, mb
5-10:	0.0496	7.587E+00
10-20:	0.0442	5.799E-01
20-30:	0.0477	2.835E-02
30-40:	0.0476	4.100E-03
40-60:	0.0484	1.207E-03
60-80:	0.0357	1.444E-04
80-120:	0.0281	3.625E-05
120-160:	0.0219	3.221E-06
160-320:	0.0158	6.359E-07

Table II: Statistics of the preselected EM-jets. This is a more efficient set of preselection cuts. Here, the column in the middle can be read as a probability of a quark or a gluon to fluctuate into object that will be reconstructed as loose EM cluster.

following. When we are studying direct photons with p_T less than the threshold value, the photon plus leading jet system become unbalanced in p_T and therefore the event, most certainly, contains additional soft jet(s). Now, this difference should be compensated by another jet. This, so-called trailing jet has no where to go but along the direction of the direct photon. The consequences of this can lead to serious misrepresetation of efficiencies. Same happens when we study fake rates in EM+jet events triggered by several triggers with different p_T thresholds.

Fig. 26 illustrates several efficiencies for a set of cuts defined further obtained from samples with different ${p_T}^{min}$ thresholds. These samples were generated with requirement that p_T of either direct photon or jet should be at least ${p_T}^{min}$.

6.3.7 Single particle MC

A set of events complementary to the above samples is single particle MC. We have generated single γ, e, π^0, and η events. Distributions are flat in pseudorapidity and generated at the following energies: 5, 10, 20, 35, 45, 65, 85 , 105, 135, 165, and 225. In addition to these samples, the same number of events with additional material (uranium) at the beam pipe ($0.1X_0$, $0.2X_0$, $0.3X_0$, $0.5X_0$, $0.7X_0$, and $1.0X_0$) was generated in order to assess effects of unaccounted material in the tracker on the photon efficiency. Since reco does not properly handle MC events without a reconstructed vertex, we "reco"-ed output of d0sim with a locally built version of reco where we force the MC vertex to be a primary one at the reconstruction phase.

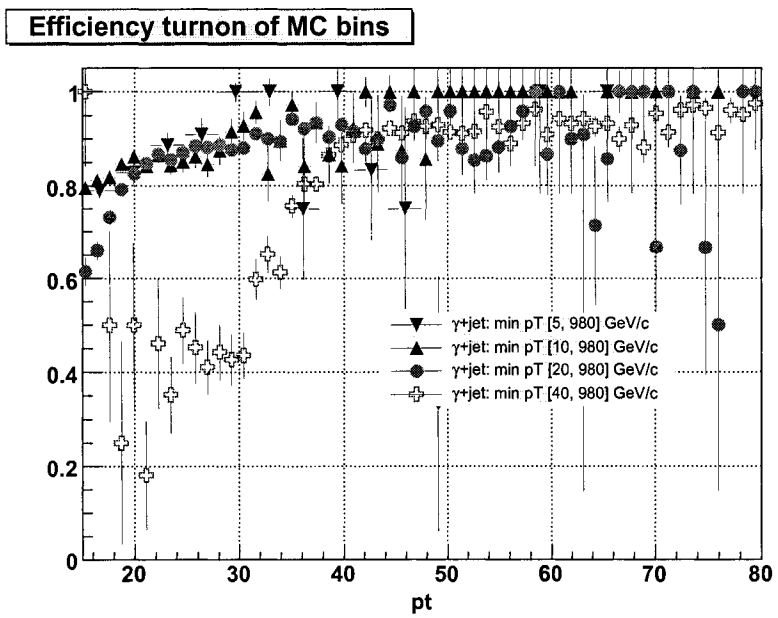

Fig. 26: Effect of the MC p_T cut-off on the photon reconstruction efficiency.

6.4 Indentification Variables

In Figs. Fig. 27- Fig. 32 we demostrate distributions of the following variables for electrons from the decays of Z bosons in the Data and the MC, fake photons from the QCD sample, and photons from the direct photon MC:

- **iso**, calorimeter isolation in the ring $\Delta R \in [0.2, 0.4]$,
- **emfr**, fraction of energy in the EM part of the calorimeter,
- **prbtrk**, spatial match χ^2 probability of a track associated with EM object,
- **IsoHC4**, scalar sum of tracks with $\Delta R \in [0.05, 0.4]$ with EM object direction as measured at the third layer of EM calorimeter. Note, that there are additional requirements on tracks: ${p_T}^{min} > 0.4 GeV/c$ and $|z_{vtx} - z_{trk}^{dca}| < 1.0$ cm,
- **IsoHC7**, same but with larger outer cone: $\Delta R \in [0.05, 0.7]$,
- **cps_rms(cps_sq_rms)**, energy (squared) weighted RMS of the re-mapped CPS cluster[1]
- **sigphi(sigz)**, (EM Cluster Width)^2 in $r \times \phi (r \times z)$ space in the third layer of the EM calorimeter,
- **floorE[i]**, fractional energy deposited in the i^{th} layer of the EM calorimeter.
- **floorE12**, ration of fractional energies - **floorE[1]/floorE[2]**.
- **hmx7**, a χ^2-like[2] function that was calculated using H-matrix trained on electron MC as an error matrix [62].

---

[1]For more details see Sec. 6.4.2 or the original document [60].

[2]The variables used to construct covariance matrix, in general, are not normally distributed and thus this function does not follow the χ^2 distribution exactly [61].

As seen from these distributions almost all variables have good agreement between the Data and the MC for electrons. Exception is sigz in CC. It is a known problem that has eluded previous attempts to resolve.. Recently we [63] attempted to see if there was any obvious correlation between the Data-MC discrepancy and the position of the shower in the detector. We did not observe any significant dependencies on the following:

- centrality of electrons: $|z_{vtx}| < 20$ cm vs $|z_{vtx}| > 50$ cm,
- small/large impact angles: for $|z_{vtx}| > 50$ cm - $z \times \eta_d < 0$ vs $z \times \eta_d > 0$,
- same as above for near/away η_d boundaries,
- near/away ϕ-cracks.

Although not the most rigorous, these studies suggest that the problem, whatever it is, might be residing at a more fundamental level. And the fact that we see this disagreement should encourage us to go after the source and make our MC better overall.

Except for *sigz* in CC, all others quantities can potentially be used as selection variables for photon identification. Figs. Fig. 33- Fig. 36 illustrate efficiency of a cut as a function of the cut value in CC and EC. For example, on Fig. 33 for $emfr > 0.98$ efficiency is approximately 0.95. These efficiencies are computed with respect to the EM loose selection.

A first step towards the optimization of cuts is to pick a cut value which maximizes $S/\sqrt{B}$. If $C = S/\sqrt{B}$ is significance of preselection cuts (i.e. EM loose) and S and B are the number of signal photons and fakes, respectively, then for the new set of cuts significance will be:

$$\tilde{C} = \frac{\tilde{S}}{\sqrt{\tilde{B}}} = \frac{\varepsilon_\gamma S}{\sqrt{\varepsilon_j B}} = \frac{\varepsilon_\gamma}{\sqrt{\varepsilon_j}} \cdot C \tag{6.2}$$

Here ε_γ and ε_j is a reconstruction efficiency of direct-photon MC and fake rate in Data, respectively. Figs. Fig. 37- Fig. 40 demostrate ratio $\frac{\varepsilon_\gamma}{\sqrt{\varepsilon_j}}$ as a function of a cut value. Note that floorE[i] variables do not provide noticable background suppression and will not be considered further. Also, it should be pointed out that maxima will have to be relaxed when we combine the cut variables. This is mainly due to certain degree of correlation between various quantities. Table III illustrates relaxed cuts along with their performance that will be further used to seed photon definition.

Variable/Cut	S	B
emfr>0.97	0.99	0.66
iso<0.07	0.97	0.37
IsoHC4<2.00	0.95	0.24
IsoHC7<3.00	0.90	0.20
sigphi<14.0	0.95	0.28
cps_rms<0.003	0.86	0.30
cps_sq_rms<0.002	0.85	0.25
flrE[1]/flr[2]<3.00	0.90	0.60

Table III: "Seed" cuts along with their performances for CC.

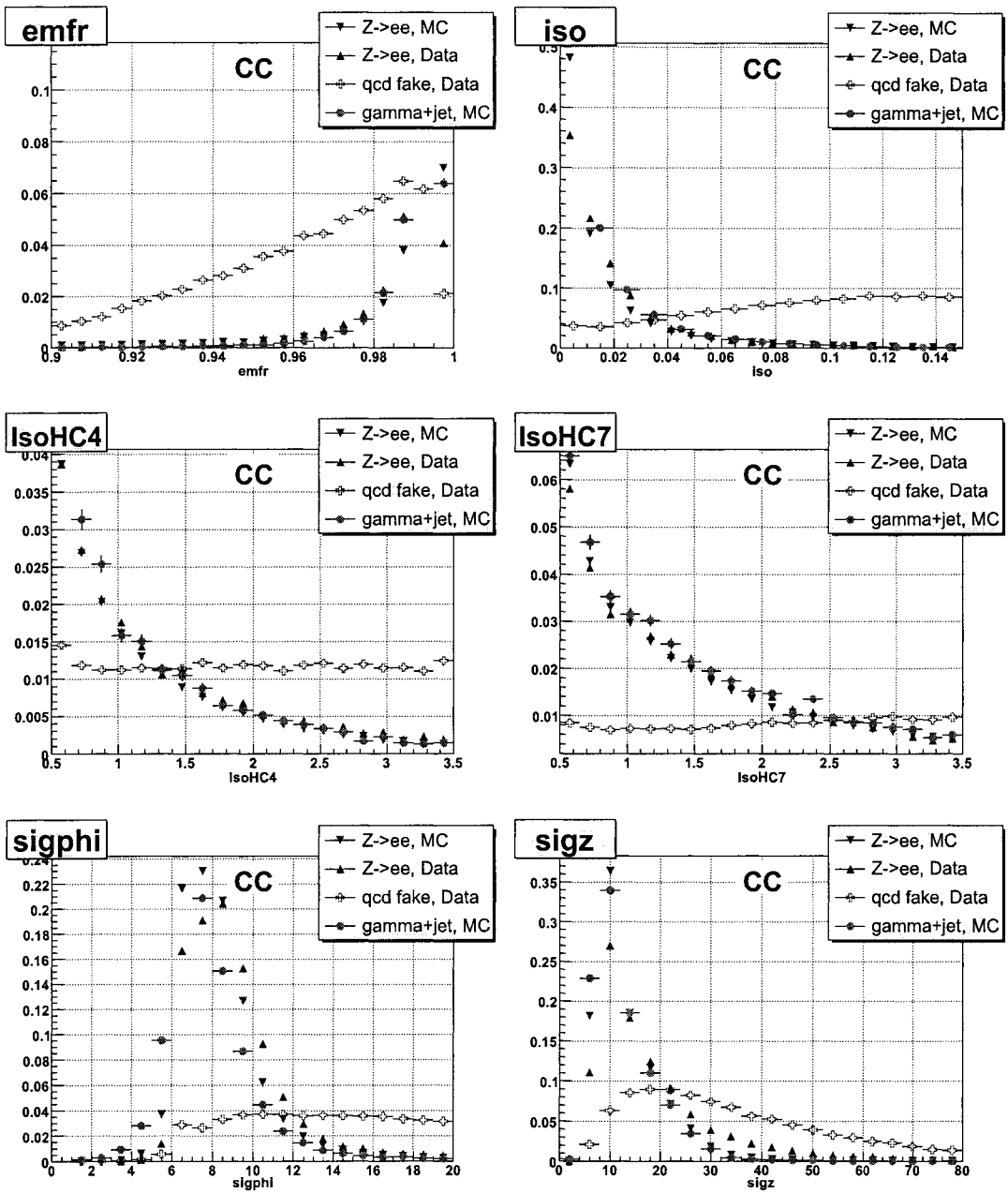

Fig. 27: Distribution of EM fraction, isolation, track isolation in hollow cones [0.05,0.4] and [0.05,0.7], square of energy weighted widths of EM shower at EM3.

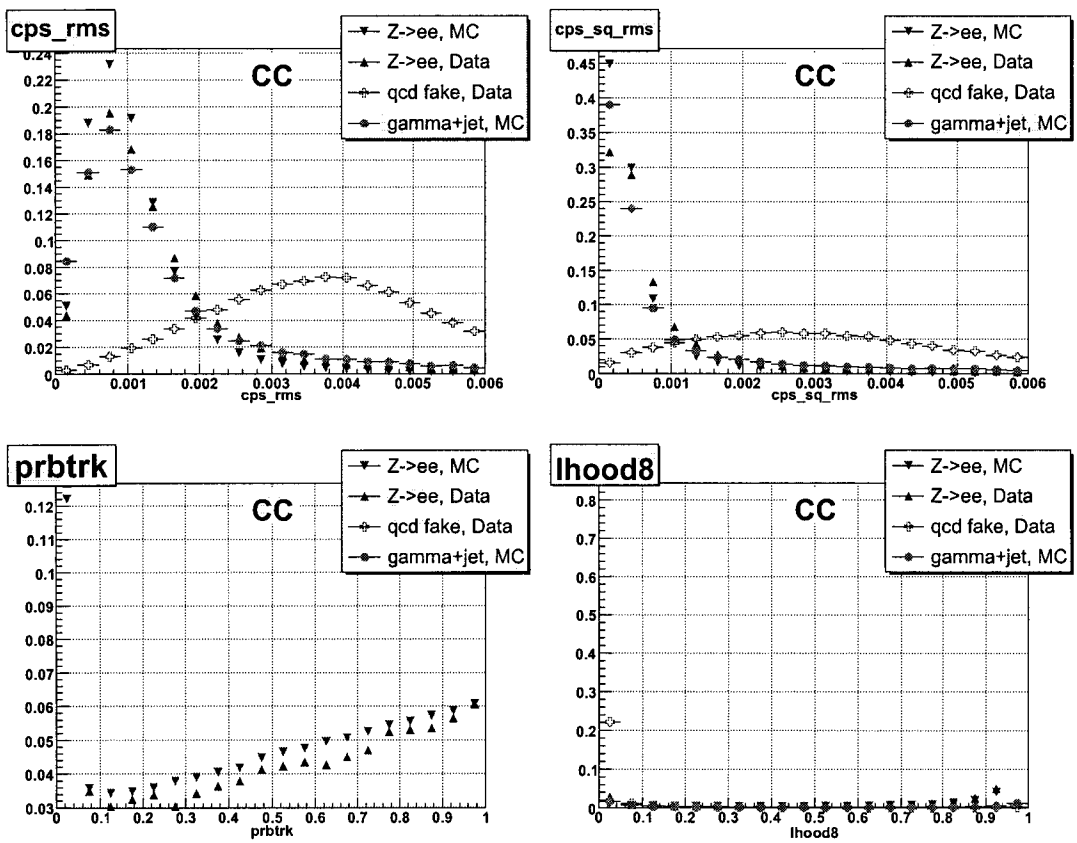

Fig. 28: Distribution of energy weighted and energy squared-weighted rms of cps clusters, probability of spacial track match, and electron likelihood.

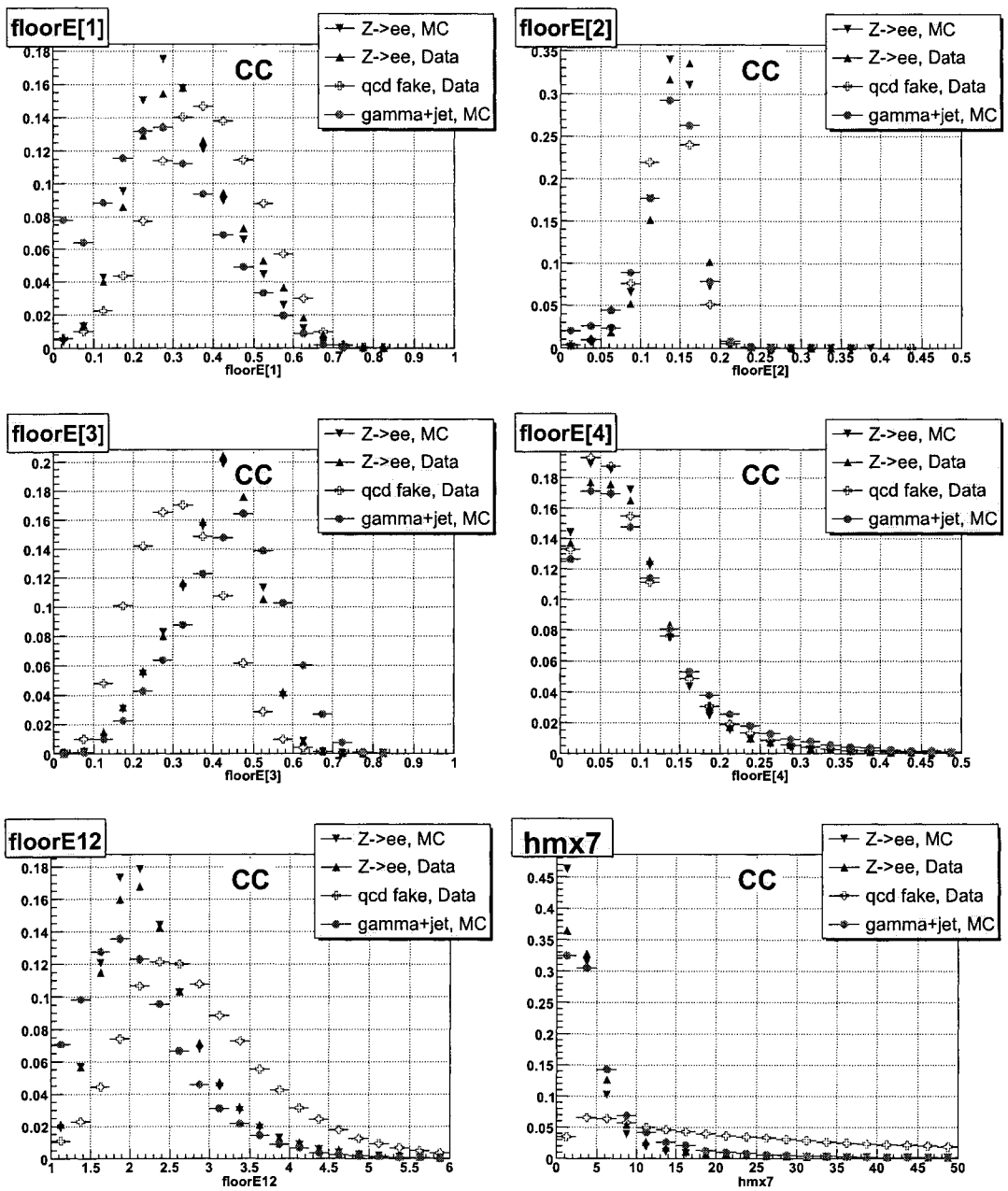

Fig. 29: Distribution of fractional energies at four layers of EM calorimeter and distribution of ratio of energies deposited at the first layer of the EM calorimeter to the second.

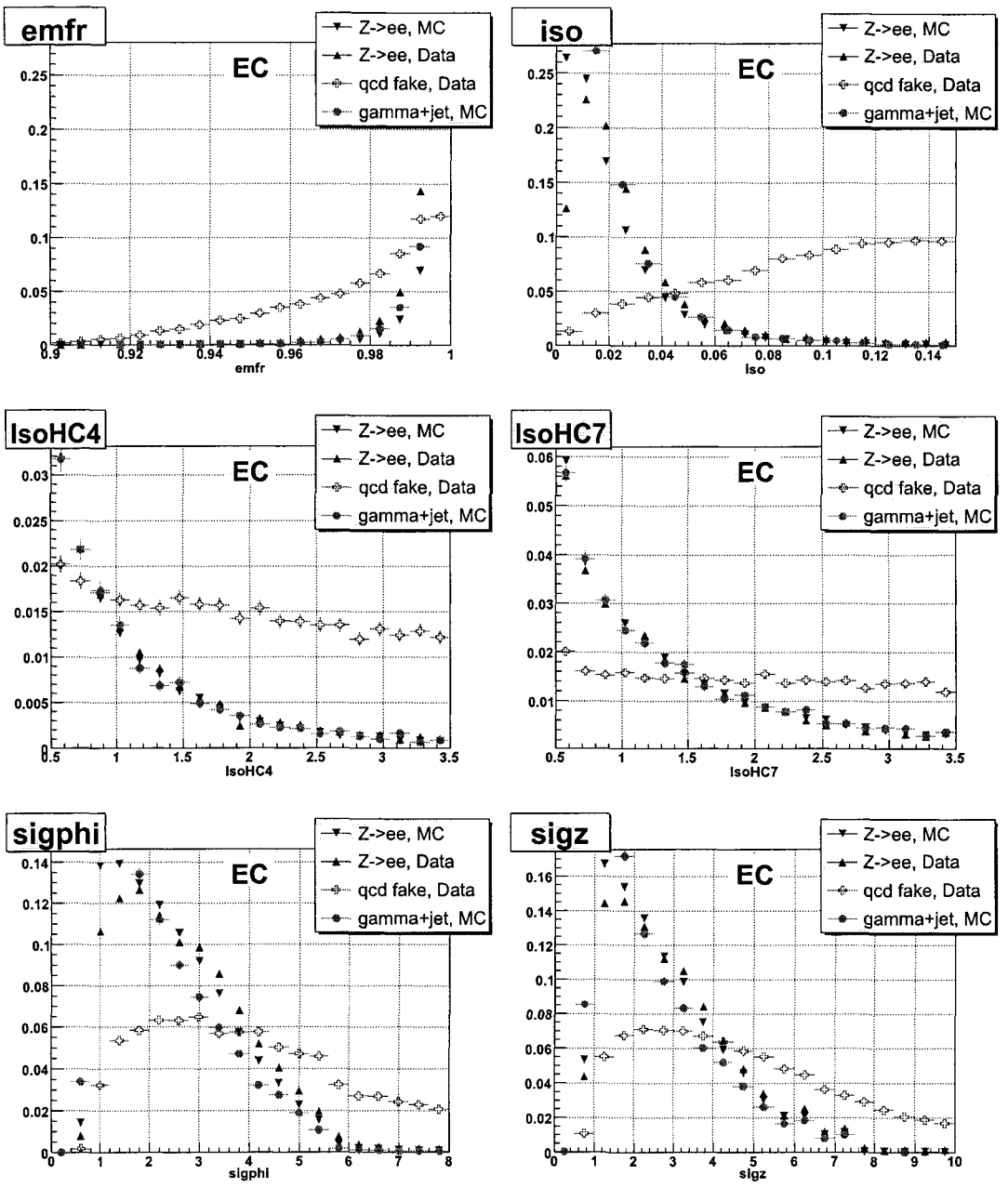

Fig. 30: Distribution of EM fraction, isolation, track isolation in hollow cones [0.05,0.4] and [0.05,0.7], square of energy weighted widths of EM shower at EM3.

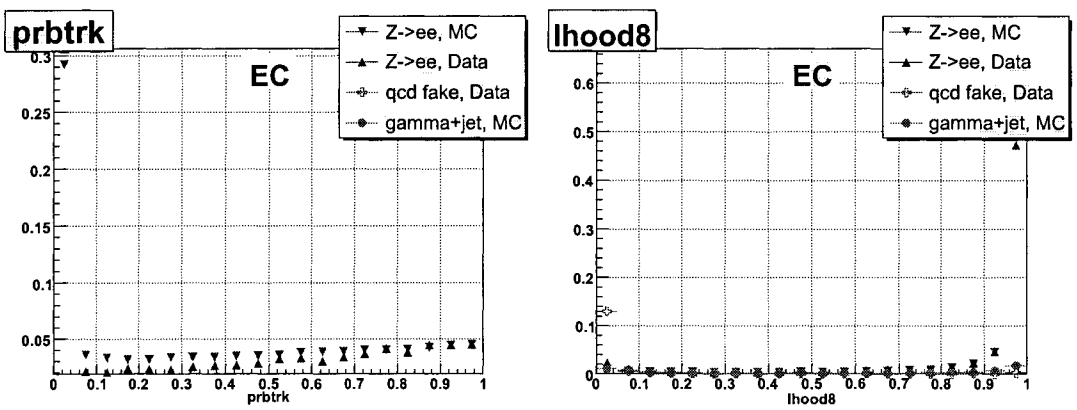

Fig. 31: Distribution of probability of spatial track match and lhood8.

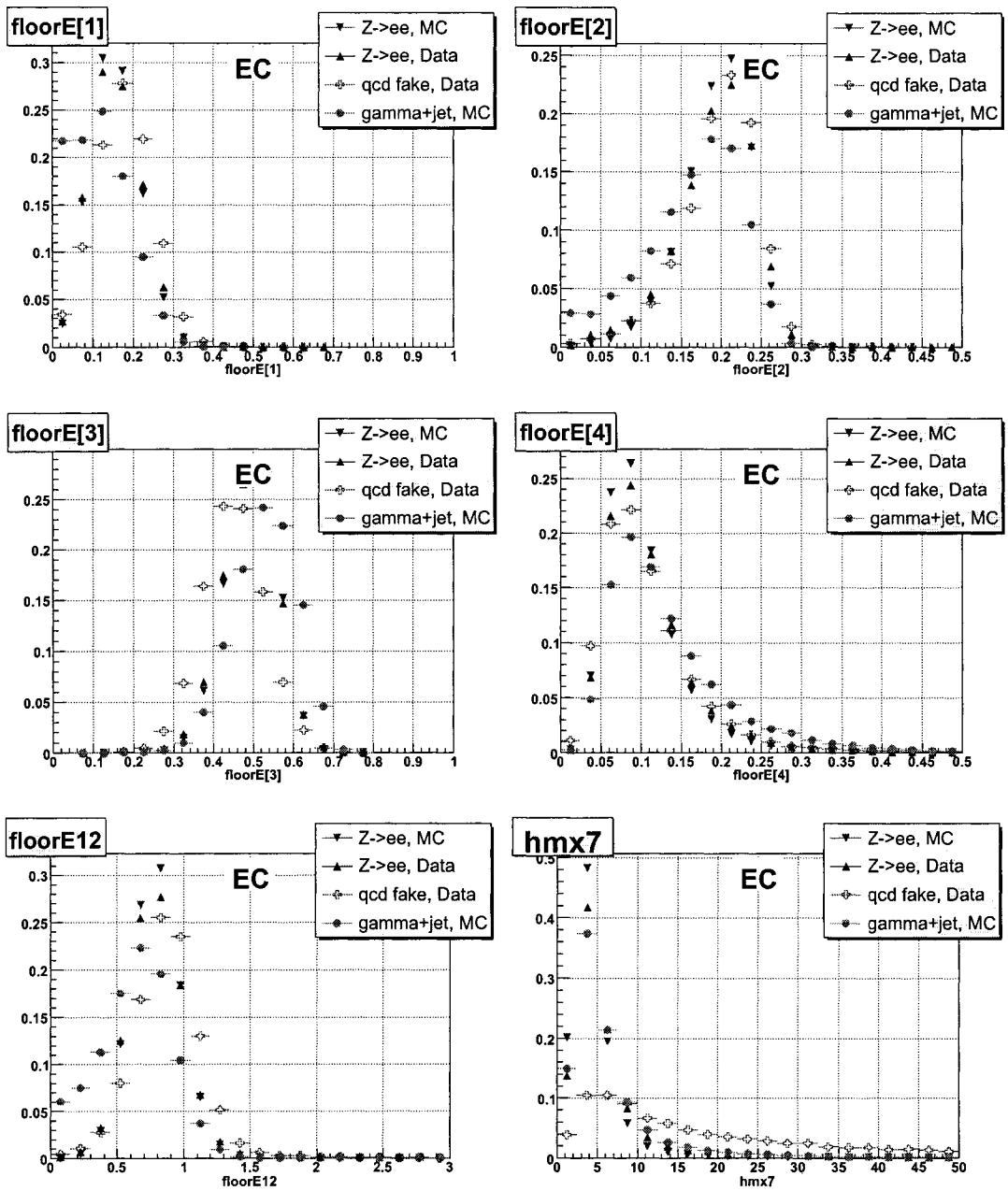

Fig. 32: Distribution of fractional energies at four layers of EM calorimeter and distribution of ratio of energies deposited at the first layer of the EM calorimeter to the second.

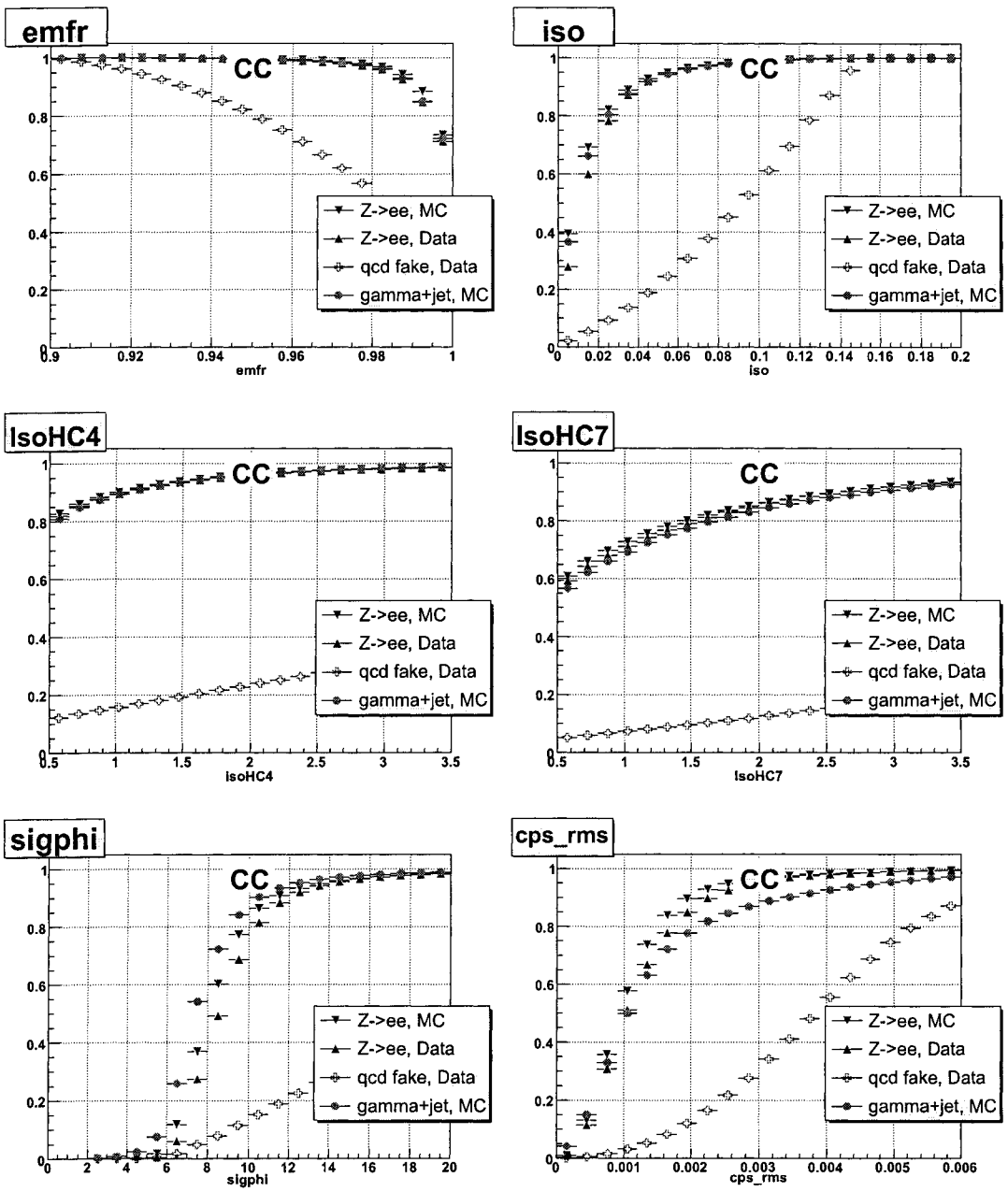

Fig. 33: Efficiency vs cut on emfr, iso, IsoHC4, IsoHC7, sigphi, cps_rms, or cps_sq_rms.

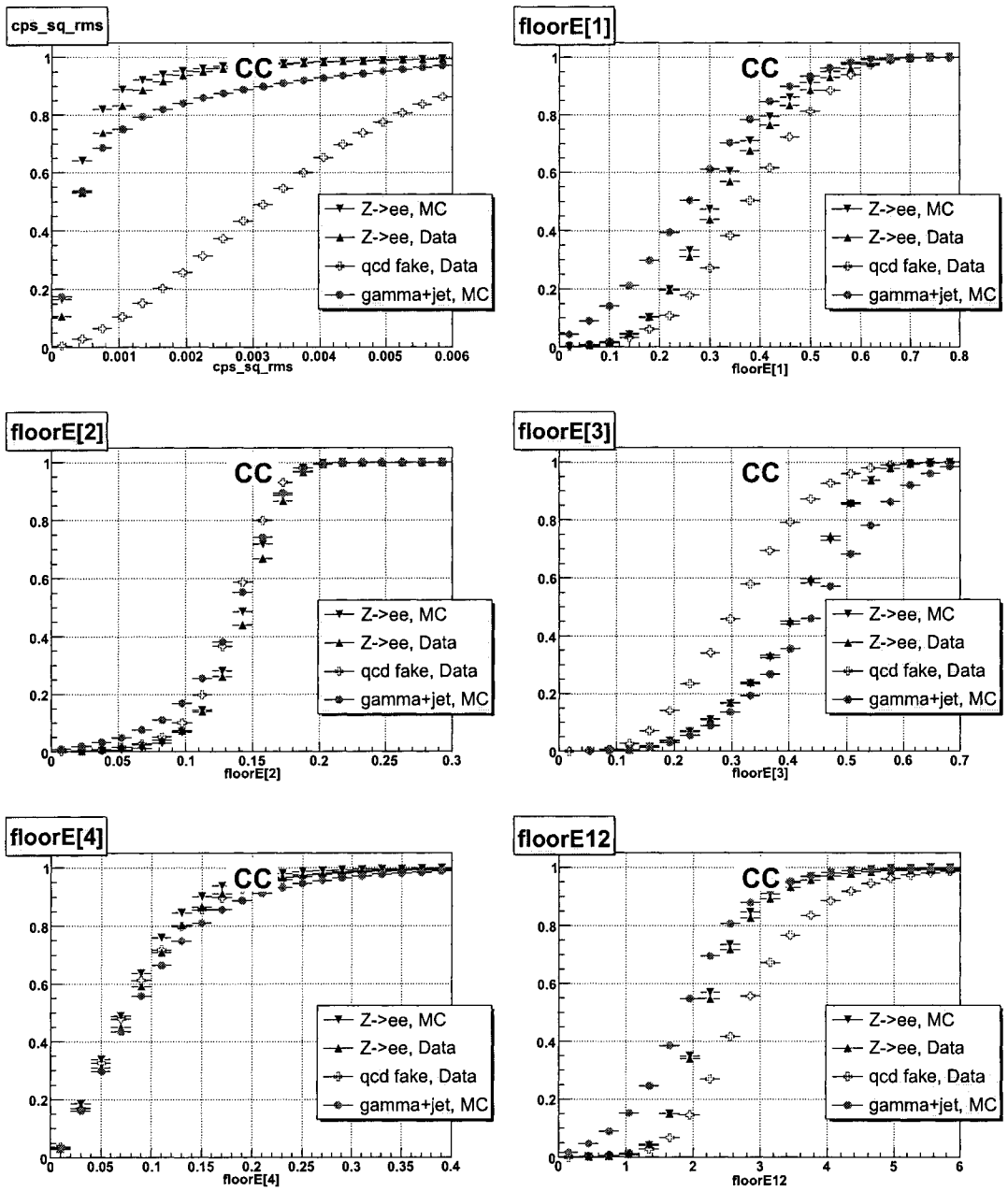

Fig. 34: Efficiency vs cut on hmx7, floorE[i], or floor12.

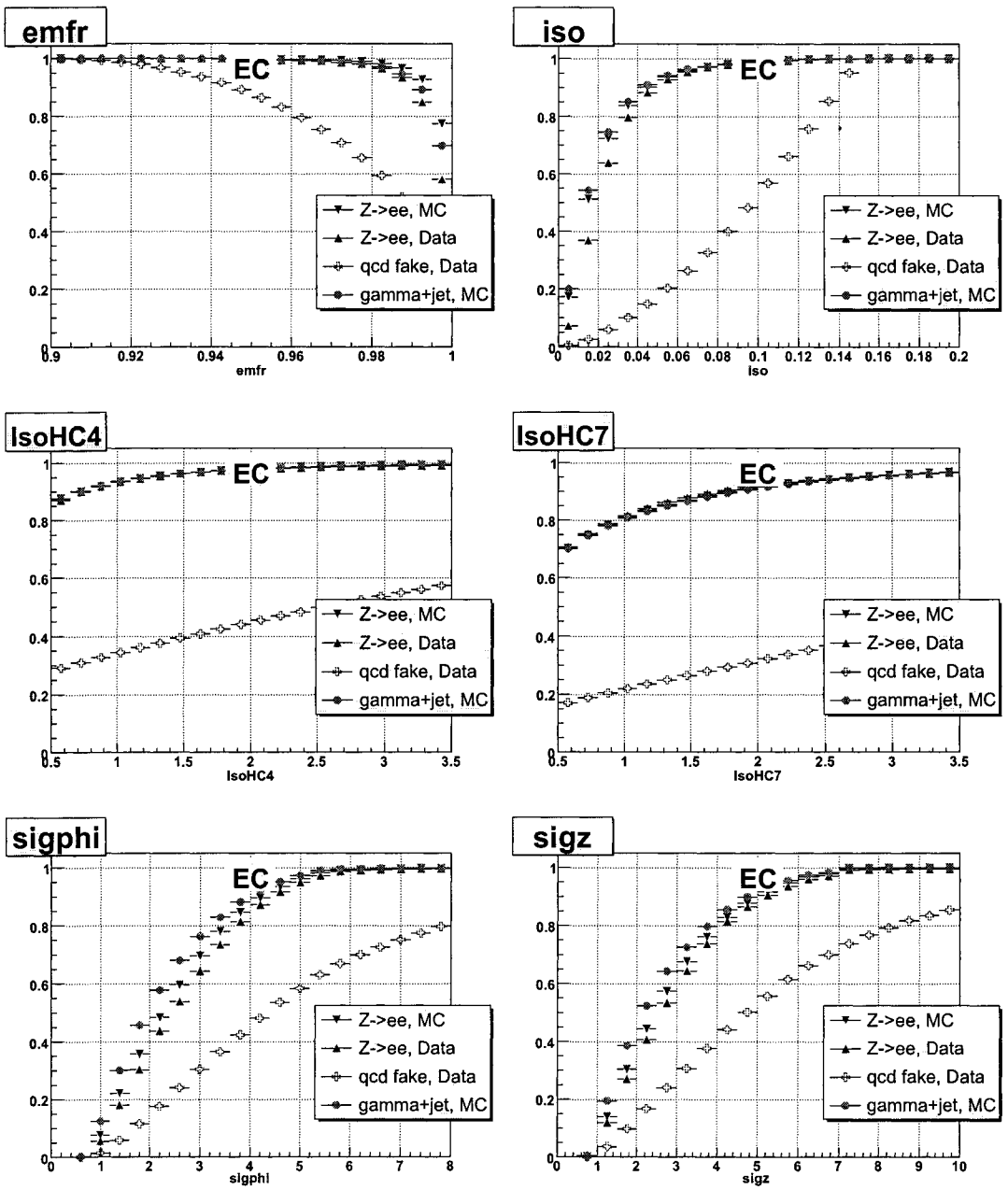

Fig. 35: Efficiency vs cut on emfr, iso, IsoHC4, IsoHC7, sigphi, cps_rms, or cps_sq_rms.

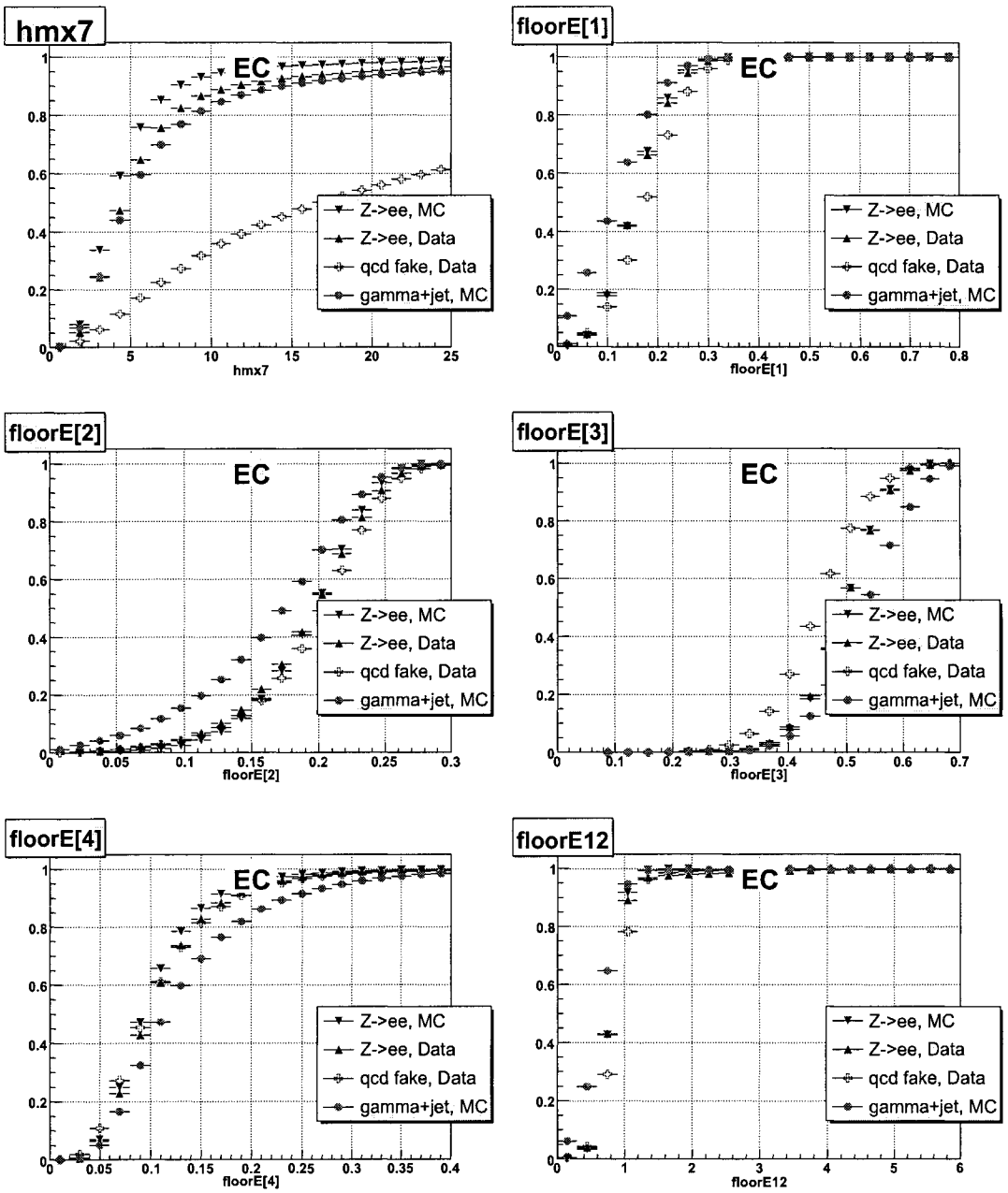

Fig. 36: Efficiency vs cut on hmx7, floorE[i], or floor12.

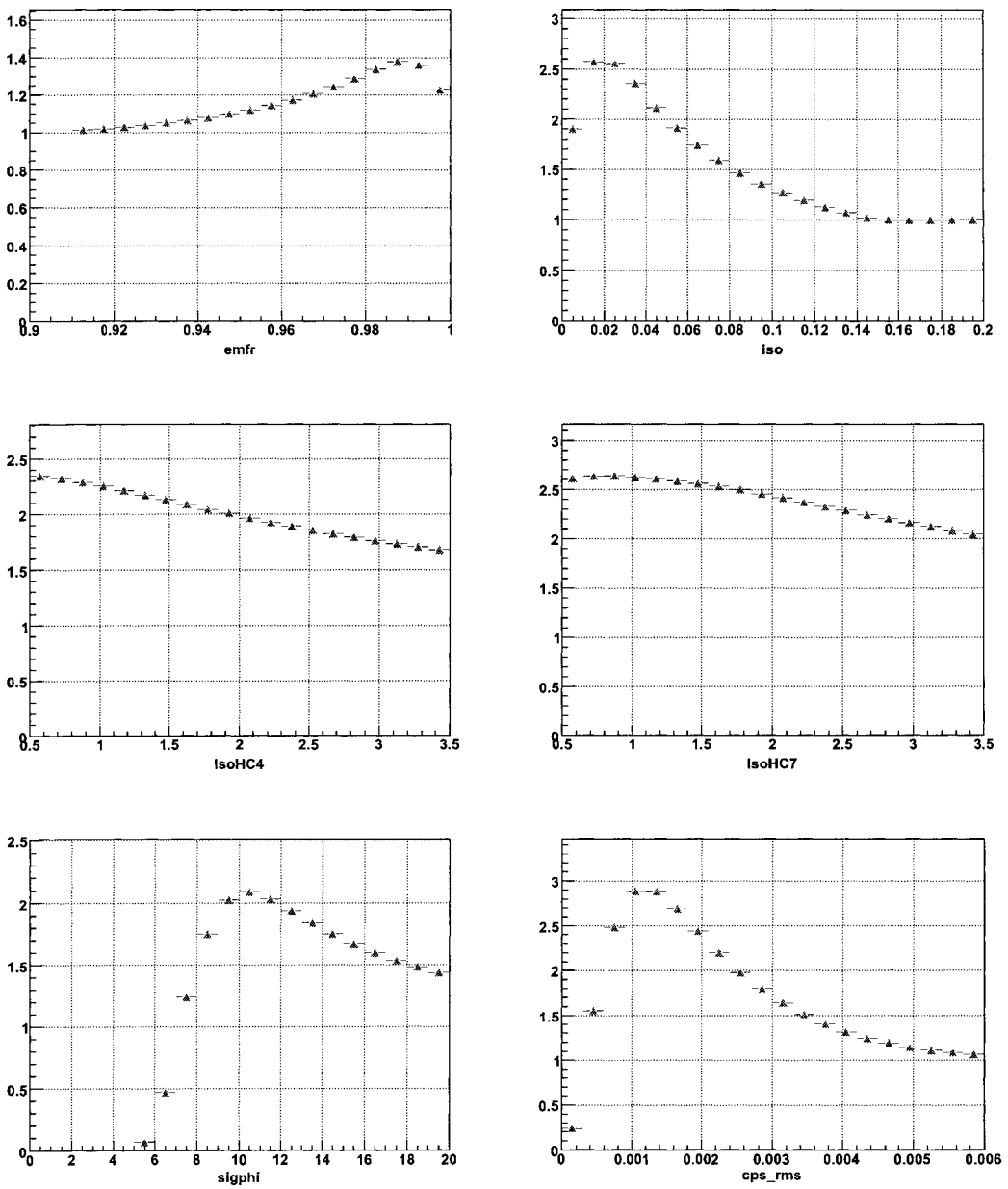

Fig. 37: Change in significance ($\varepsilon_\gamma/\sqrt{\varepsilon_j}$) vs cut on emfr, iso, IsoHC4, IsoHC7, sigphi, cps_rms, or cps_sq_rms in CC.

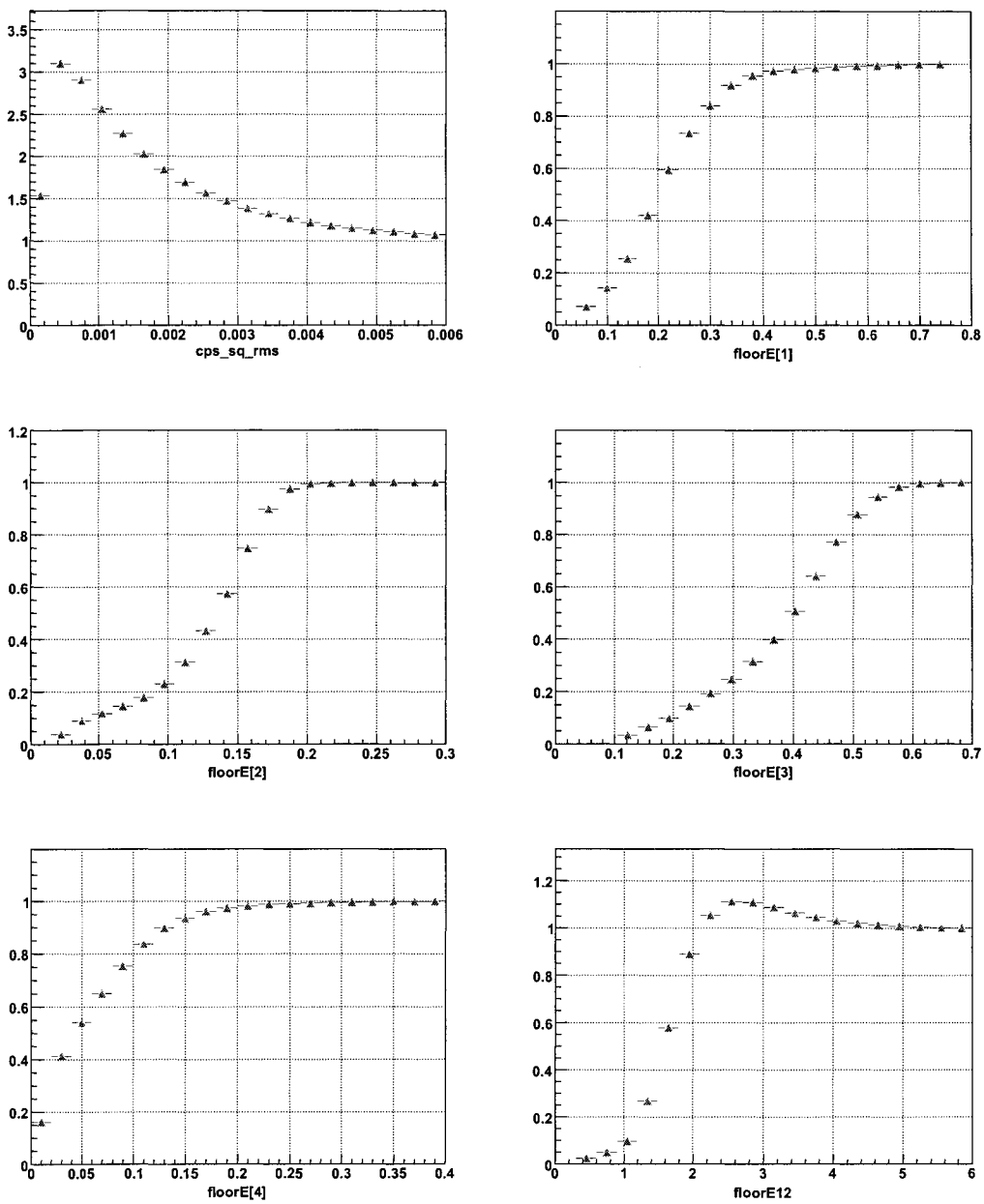

Fig. 38: Change in significance ($\varepsilon_\gamma/\sqrt{\varepsilon_j}$) vs cut on hmx7, floorE[i], or floor12 in CC.

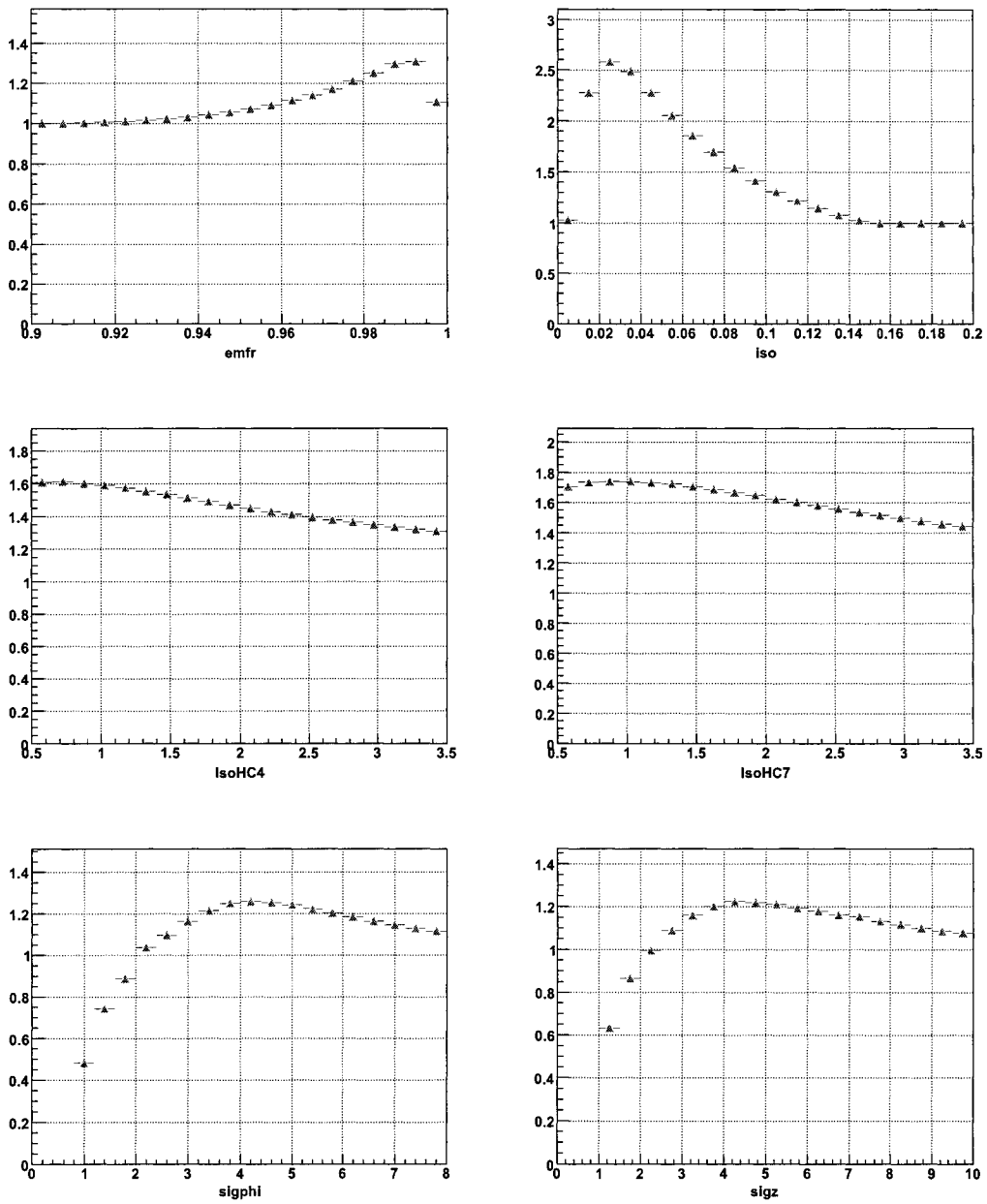

Fig. 39: Change in significance ($\varepsilon_\gamma/\sqrt{\varepsilon_j}$) vs cut on emfr, iso, IsoHC4, IsoHC7, sigphi, cps_rms, or cps_sq_rmsin EC.

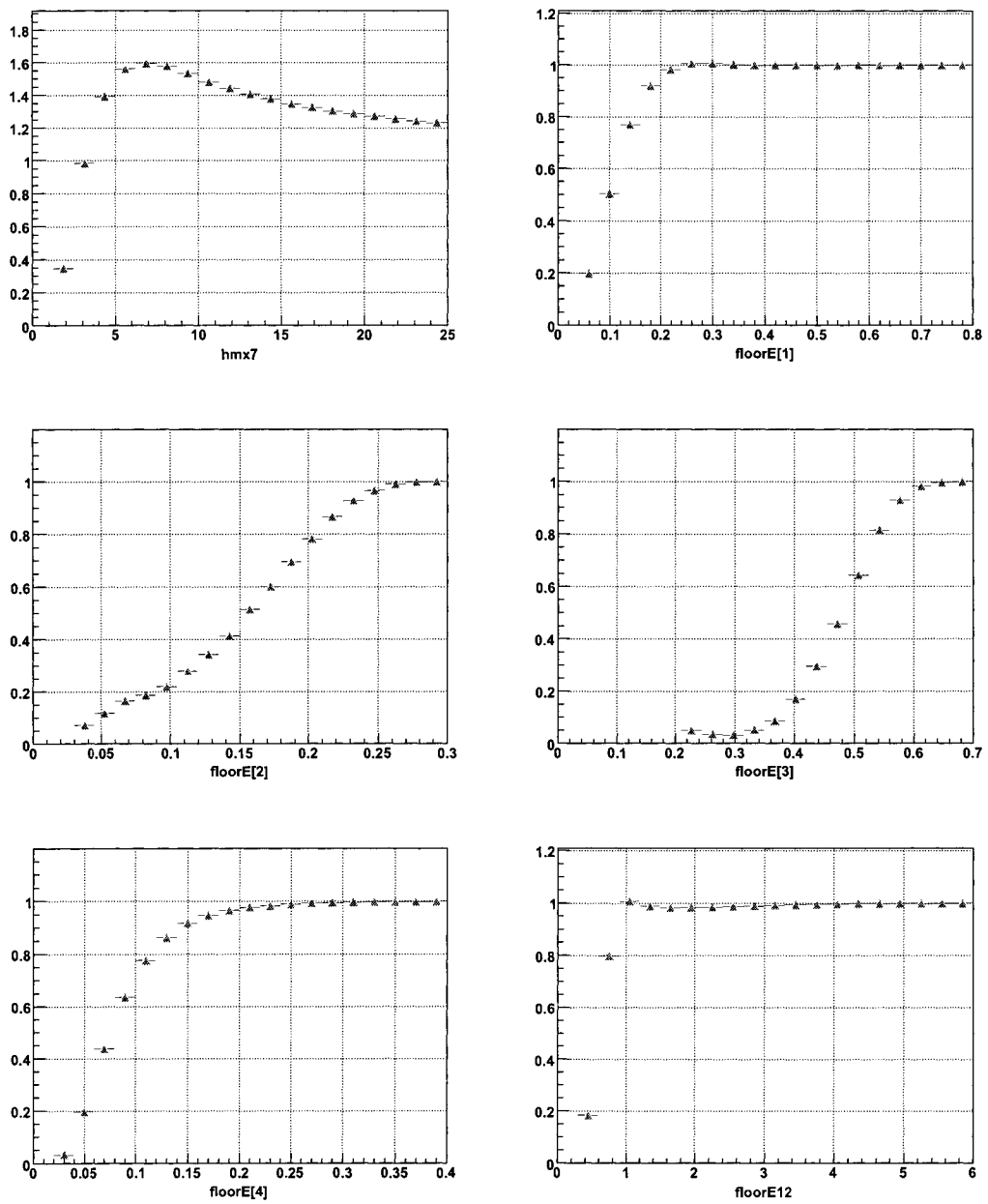

Fig. 40: Change in significance ($\varepsilon_\gamma/\sqrt{\varepsilon_j}$) vs cut on hmx7, floorE[i], or floor12 in EC.

6.4.1 Hits on the Road

In order to make track-finding task time-efficient, the track reconstruction algorithm at DØ had to adopt certain shortcuts, resulting in track reconstruction inefficiencies that lead to electrons misidentified as photons, a background that can not be neglected in some analyses.

In this chapter we approach the problem of recovery of electrons that lost their tracks. We do so by examining hit patterns in the tracker along the hypothetical trajectories[1] that a charged particle that created EM cluster under consideration could have traveled.

Description of the Method

For each calormieter EM object we define a road that describes a trajectory of a charged particle that originated in the primary vertex of the event and which has a transverse energy of the considered EM object (Fig. 41). Due to the ambiguity in the charge of EM object we define two such roads. We refer to these roads as a "Positive" or "Negative" road depending on the sign of a track's curvature. We count the number of fired CFT fibers or SMT pixels that are within 4σ of the road. The resolution in each layer of CFT and each ladder of SMT is measured in $Z \rightarrow ee$ sample. Due to geometry of the SMT detector, maximum number of hits depends on orientation of a track. Thus, we normalize the observed number of SMT hits by the maximum possible number of hits for a given track orientation.

If the EM object has no matched central preshower (CPS) stereo cluster [64], we use the 3d floor coordinates to define the roads. However, if a CPS cluster is matched to the EM object, we define roads using the CPS cluster's coordinates. Utilizing the CPS cluster improves the resolution of the hit

---

[1]Due to a prior ambiguity in the sign of the charge of the particle we examine hits along "positive" and "negative" trajectories, thus plural.

matching to the roads (see Fig. 42). We use di-EM and di-jet samples to study the contribution of random noise to the hits from real and fake electrons. In order to minimize effects of the energetic recoil jets, we study hits in the direction parametrized by where we do not expect significant activity in the tracker. For electrons we choose $\phi_{noise} = (\phi^{EM1} + \phi^{EM2})/2$ and $\eta_{noise} = (\eta^{EM1} + \eta^{EM2})/2$

Electrons and fakes have different distributions of hits found in the roads associated with the EM objects. In Fig. 43 we present the distribution of the number of hits for CFT Axial, CFT Stereo and SMT layers produced by the electrons (blue) and from random noise (red) . Distributions of the number of hits for the fakes are shown on Fig. 44. Qualitatively they are similar to the ones for random noise.

We define probabilities P_e and P_γ for an EM object to be an electron or a photon:

$$\begin{aligned} P_e(n) &= \frac{\sum_{i=0}^{i=n} N_e(i)}{\sum_{i=0}^{i=24} N_e(i)} \\ P_\gamma(n) &= \frac{1 - \sum_{i=n}^{i=24} N_\gamma(i)}{\sum_{i=0}^{i=24} N_\gamma(i)} \end{aligned} \tag{6.3}$$

Here, N_e and N_γ are the distributions of total number of hits shown in the Fig. 43 and Fig. 44 and n is a total number of SMT and CFT hits on the road. From normalized distributions in the last histogram of Fig. 43 (shown in Fig. 45) we construct an electron/photon discriminant D shown in Fig. 46 and defined as follows:

$$D(n) = \frac{P_e(n)}{P_e(n) + P_\gamma(n)} \tag{6.4}$$

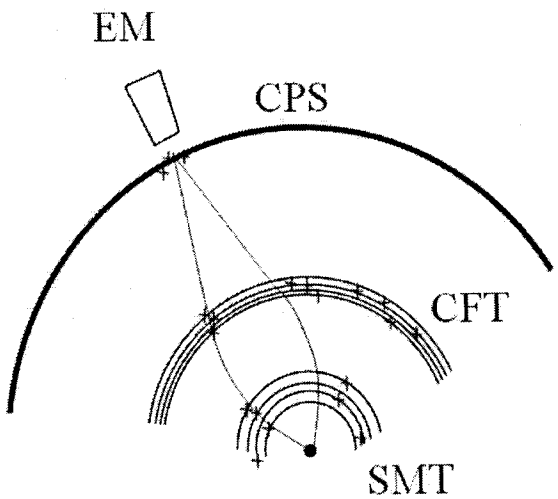

Fig. 41: "Positive" and "negative" roads.

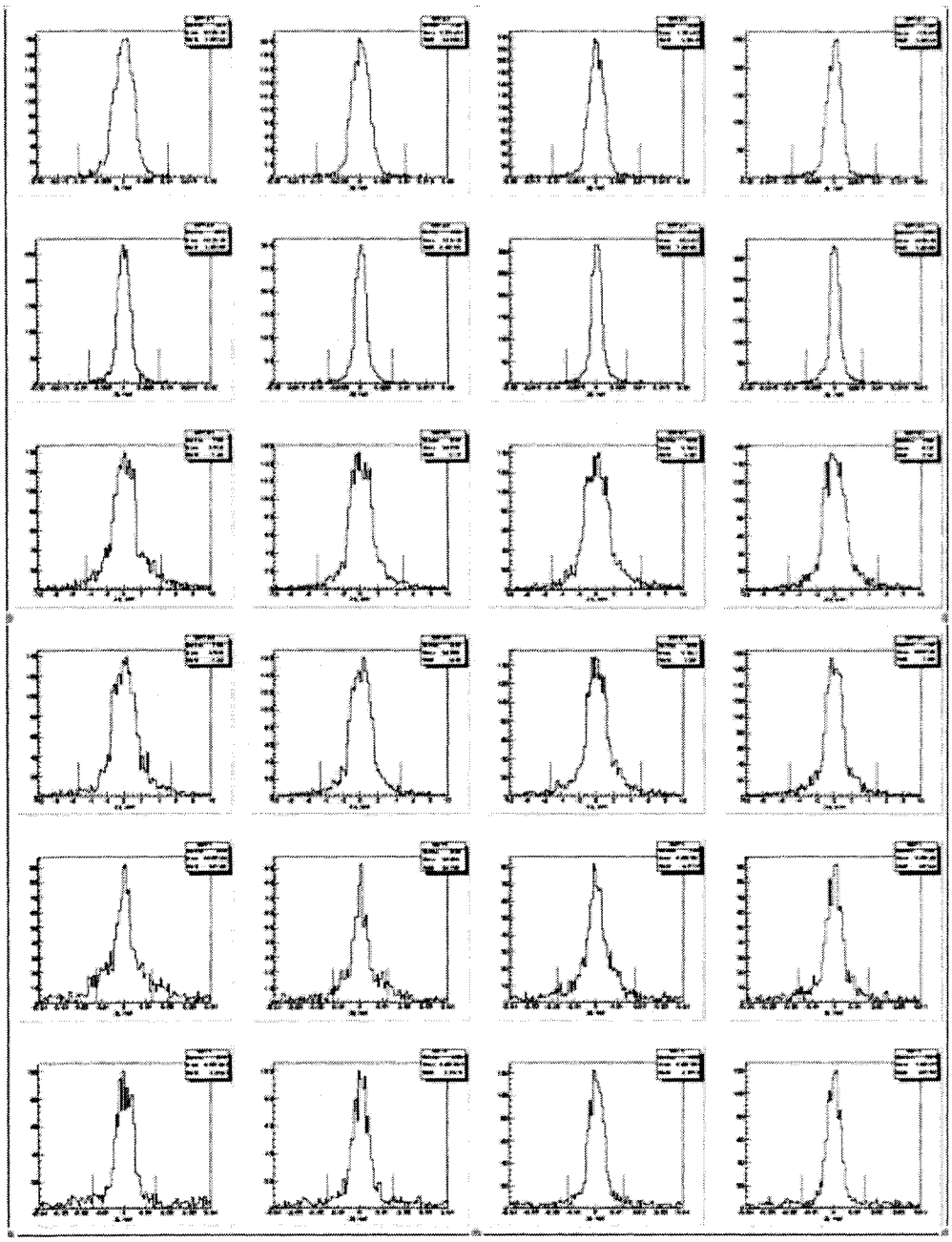

Fig. 42: Distribution of CFT Axial (upper eight), Stereo (middle eight), and SMT (lower eight) hits produced by electrons for roads matched to the most energetic CPS cluster associated with the electron.

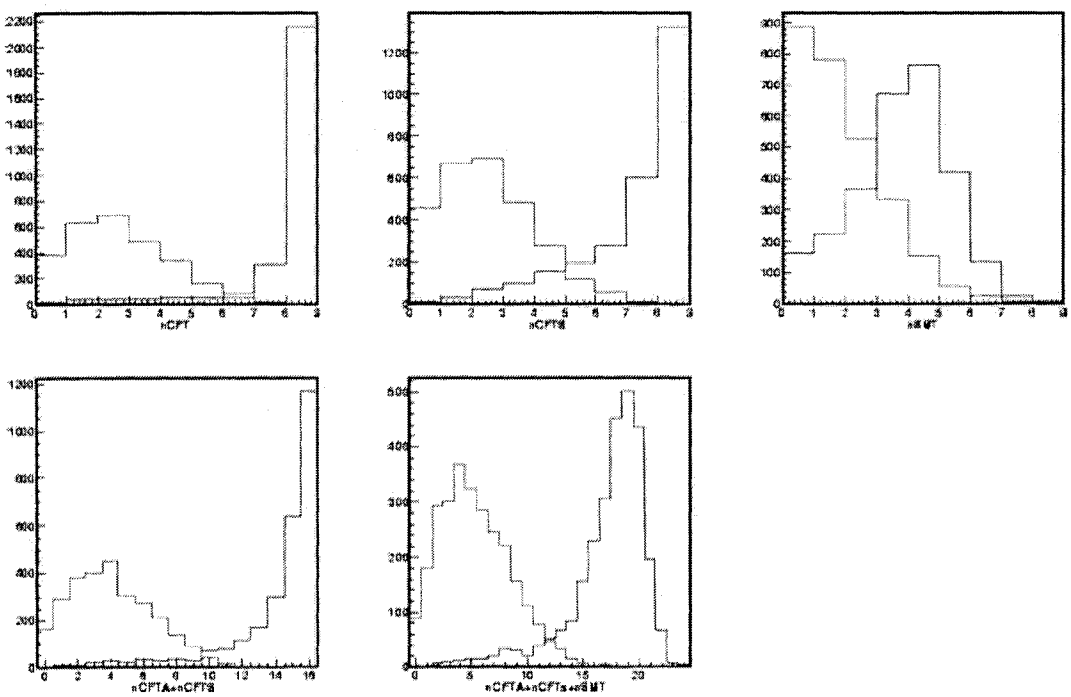

Fig. 43: Distribution of the number of hits produced by electrons (blue) and random noise (red).

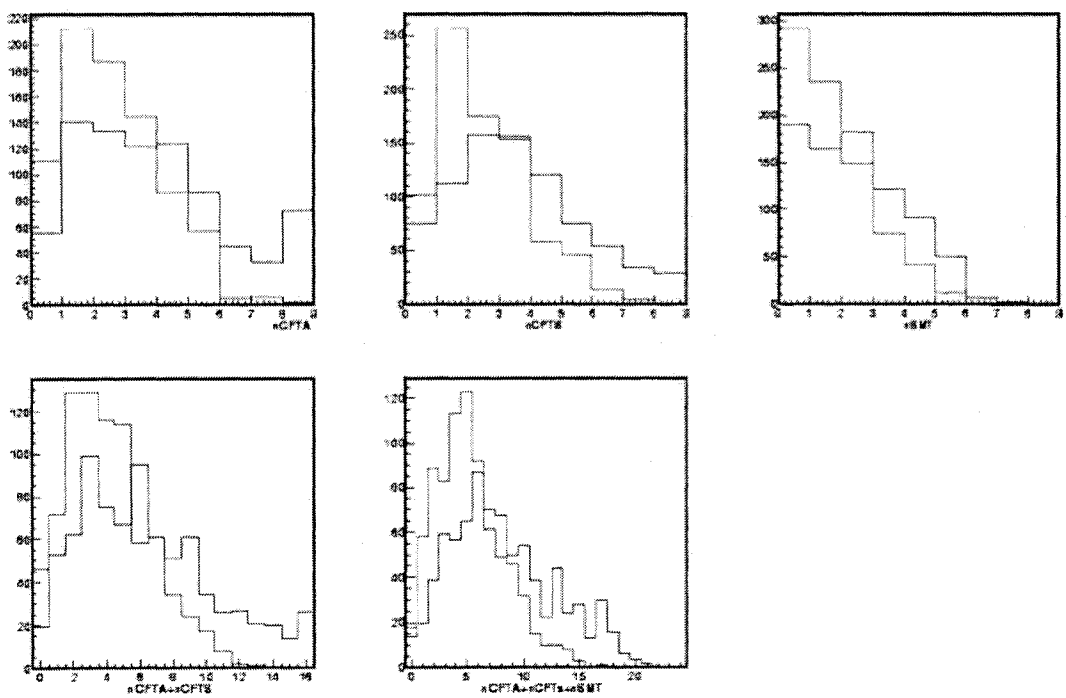

Fig. 44: Distribution of the number of hits produced by fake electrons (blue) and random noise (red).

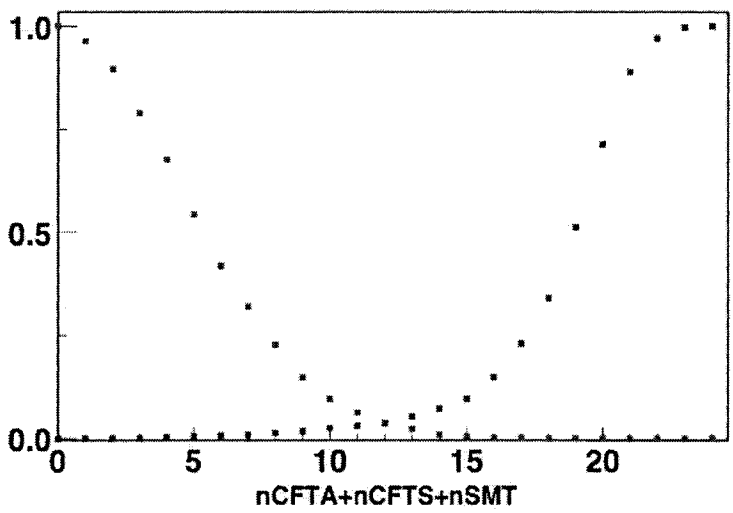

Fig. 45: Probability of an EM object with certain total number of hits to be an electron (blue) or a fake(red).

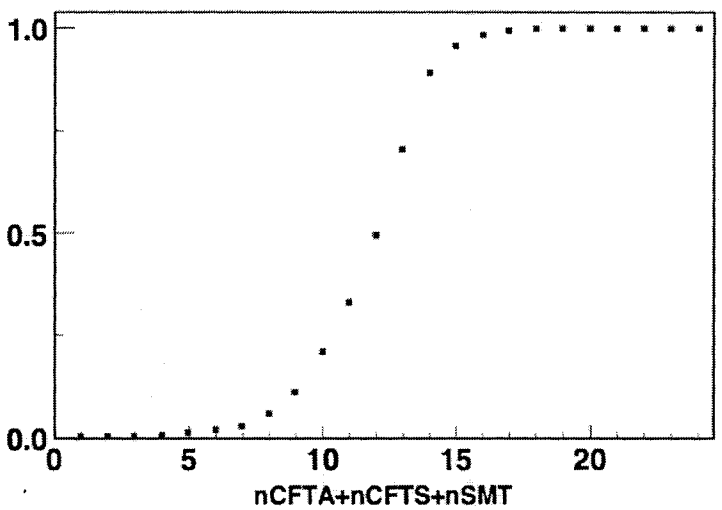

Fig. 46: A discriminant between an electron and a fake as a function of the total number of hits.

6.4.2 CPS clusters

Preshower quantities, constructed from hit strips within windows about the calorimeter position, have been developed for the purpose of gaining more discrimination between photons and EM-like jets. The variables selected for photon identification are both dependent on the squared difference between the preshower position in ϕ and the position of the electromagnetic cluster at the third floor of the calorimeter. In the first variable (referred to as `cps_rms`), this difference is weighted by the strip energies (in GeV). This variable discriminates against clusters which leave a wide deposition of energy in the preshower, as opposed to a very well constrained deposition from a true photon or an electron. In the second variable (referred to as `cps_sq_rms`), the square of the phi difference is weighted by the energy squared. This variable tends to discriminate against energy depositions in the preshower which have multiple peaks, such as from π^0's in which one photon undergoes an early conversion and leaves multiple peaks in the preshower layer. In both cases, these quantities are calculated for each layer (where the two stereo layers have been unmapped using the primary vertex and calorimeter position), and then summed. The proposed cuts and further details can be found in [60].

There is currently a discrepancy between the data and Monte Carlo for both of these variables. The problem is that the tail in the data for both variables is much longer than in the Monte Carlo. The root of these disagreements may involve a few separate issues (data quality, luminosity dependence, pedestal variation), but the most notable is the way in which the central preshower data is modeled in the Monte Carlo. The main concern is that the saturation in the preshower is not done on an individual basis for each strip. Instead it is set to a fixed value based on the average from all the strips in the CPS. There is also the issue of dead channels and channels that have little dynamic range. Efforts are being made

to understand these discrepancies and to modify the Monte Carlo description appropriately[1]. This will help the Monte Carlo more accurately reflect the performance of the real detector.

---

[1]It was recently observed that there are two potential reasons for Data/MC discrepancy. The first one - dead channels are not simulated in MC, and the second one - it appears that there is some CPS/Cal missalighnment that could have been caused by the distortion of the shape of CPS detector. Further study is underway.

6.5 Photon Purity

Just as any sample of isolated photons contains a certain fraction of QCD jets almost any sample of fake photons inevitably contains a fraction of "pure" photons[1]. The fraction of the photon events in the selected sample can be defined as the ratio:

$$P = \frac{N^{\gamma}}{N^{\gamma} + N^{jet}} \tag{6.5}$$

where N^{γ} (N^{jet}) is the number of single photons (EM-jets) that passed certain selection criteria.

At present, we estimate the content of direct photons, i.e. purity, in the sample of EM objects that pass photon-id cuts by means of MC. In general, it depends on the underlying physics and therefore we study purity on the sample of di-jet events very similar to those from which we obtain fake photons.

An important note is in order here. When computing purity using equation Equation 6.5 one should make sure that gamma+jet and EM-jet samples are statistically equivalent, i.e.:

$$N^{\gamma} = \varepsilon^{\gamma} \cdot A \cdot L \tag{6.6}$$

$$N^{jet} = \varepsilon^{jet} \cdot A \cdot L \tag{6.7}$$

which, in other words, means that same number of picobarns were generated for MC samples of photons and fakes.

---

[1] Although photons can be produced copiously within jets in this note we consider only those that are isolated from reconstructed jets.

Dependencies of the direct photon purities on p_T are shown in Fig. 47. The photon fractions were fitted by the functional form

$$P_f = 1/(1 + a\ (p_T{}^{\gamma})^b) \tag{6.8}$$

We have chosen this form because we expect the data to be a sum of two falling cross sections (photons and jets) with their ratio having roughly the form $a(p_T)^b$ (compared with formula (Equation 6.5)).

The source of the purity uncertainty here is the quadratic sum of the statistical uncertainty of the fit and the systematic uncertainty (that is $\approx 4-10\%$ for various $p_T{}^{\gamma}$) caused by the usage of two additional fit functions, $1 - exp[a + bp_T]$ and $a + b\ log(p_T)$. An additional source of the systematic uncertainty can be a fragmentation model realized in a MC event generator.

Yet another method to estimate purity is from shapes of `cps_rms` distributions by means of template method (similarly to ANN). For self-sufficiency let's remind ourselves of the idea behind the template method. The idea is to find an optimal fit of the distribution of some variable in the data with the sum of the distributions of this variable in signal and background MC samples. Then, at the optimal point, the normalized weight at the signal distribution correspond to the purity of the data sample.

In this study the energy weighted width of the cps cluster (`cps_rms`) has been chosen to construct templates from MC samples of gamma+jet and EM-jet[1]. Then, these distributions were stretched by the coefficient obtained from the comparison of the distributions for electrons in the Data and the MC (

[1]Note that the tempalte variable should not be used to select photon candidates.

6.5). Further, sample of fake photon candidates (6.3.4.1) was fitted with the normalized sum of stretched distributions of `cps_rms`. Normalized weight at the photon distribution that gives optimal fit is plotted as a function of transverse momentum of photon candidate (6.5).

It seems that with the proper Data/MC scaling (see Sec. 6.4.2) purity obtained in this manner is quite similar to the one obtained exclusively from the MC.

A more extensive study of purities along with photon and EM-jet energy scales can be found in [65].

6.6 Photon Definition

For our analysis we choose the following cuts:

- emfr > 0.97
- iso < 0.07
- IsoHC[0.05,0.4] < 2.0 GeV/c,
- sigphi^2 < 14.0 cm^2,
- prbtrk(w/o E/p) < 0.001,
- $|\eta_{det}| < 1.1$,
- in_eta_fiducial,
- p_T > 15 GeV/c;

and although we do not use photons with $|\eta| > 1.1$ we still provide selection for the EC:

- emfr > 0.97
- iso < 0.07

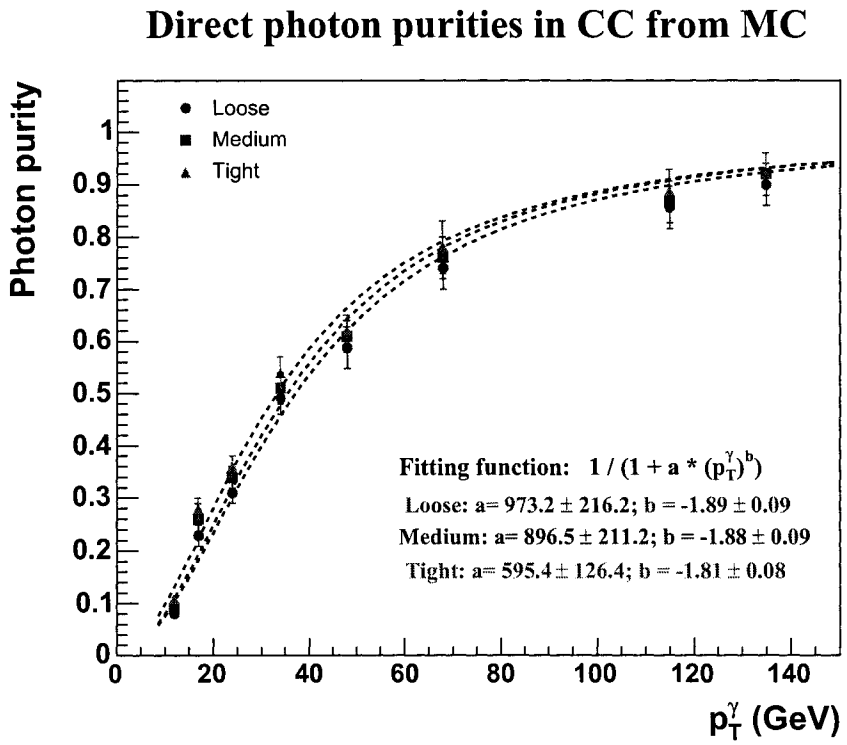

Fig. 47: Purity for several photon definitions in CC. This analysis is using "Core" which "Medium" on this Figure.

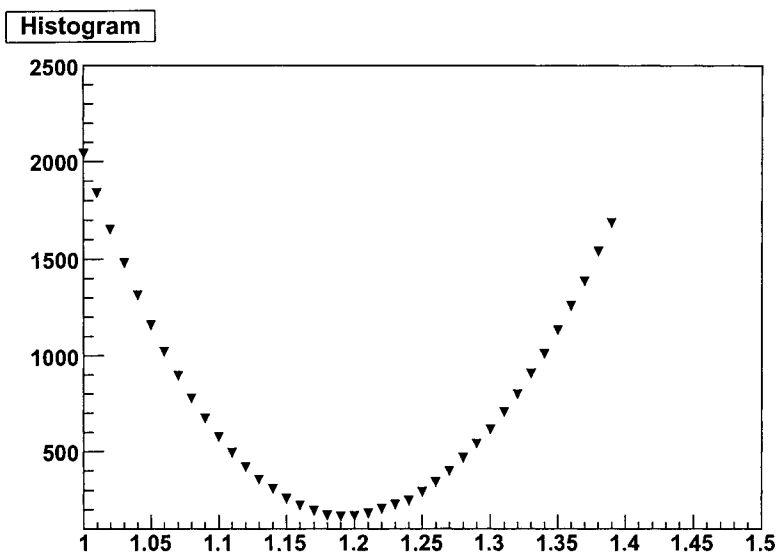

(a) Value of the χ^2 fit of `cps_rms` electron distribution in the Data to the stretched one in the MC plotted as a function of the streching coefficient. Optimal fit corresponds to $\approx$1.19

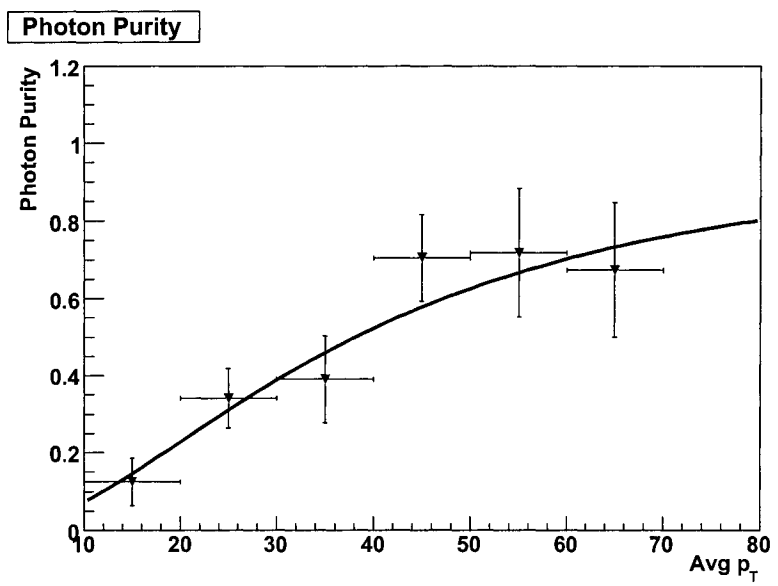

(b) Purity as a function of p_T of the photon candidate in data (triangles) and in MC (line).

- IsoHC[0.05,0.4] < 2.0 GeV/c,
- sigphi $< 2.74 \cdot |\eta_{det}|^2 - 16.3 \cdot |\eta_{det}| + 25.0$,
- sigz $< 5.96 \cdot |\eta_{det}|^2 - 30.6 \cdot |\eta_{det}| + 40.7$,
- prbtrk(w/o E/p) < 0.001,
- $1.5 < |\eta_{det}| < 2.5$,
- in_eta_fiducial,
- $p_T > 15$ GeV/c.

6.7 Efficiencies

Efficiency is defined as a fraction of objects that pass corresponding selection. For photons, photon-like jets, and for "single-particles" it is defined as a ratio of a number of objects that pass selection criteria to the total number of objects in the original sample. An exception is electrons that come from decays of Z. There, one has to be very careful. One easily can bias his/her study sample due to trigger or a correlation between two electrons. We use so-called "tag-and-probe" method that is mostly unaffected by these biases. A good description of the method is found in [66].

6.7.1 Data/MC scaling

In this section we determine Data/MC scaling factor on electrons for a set of core cuts which are defined as follows:

- emfr > 0.97
- iso < 0.07

- IsoHC[0.05,0.4] < 2.0 GeV/c,
- sigphi^2 < 14.0 cm^2,
- $|\eta_{det}|$ < 1.1,y
- in_eta_fiducial,
- p_T > 15 GeV/c;

Fig. 48 illustrates distribution of electron reconstruction efficiency in Data and MC as a function of p_T in the CC. Agreement is good, in general. However, there is some suspicious structure in the efficiency below 30 GeV/c in both Data and in MC. It is unlikely a real physical effect. In the next few paragraphs we will try to discuss possible causes of such behaviour and quantify its consequences.

Fig. 49 illustrates a 2D histogram of invariant mass vs p_T. Each p_T bin of this histogram is used to calculate numerator (or denumenator) in the efficiency by fitting Z distribution. The rightmost figures, (b) and (d), are the close-ups of the questionable p_T region. From these distributions it appears that D/Y proces was not properly represented in this MC sample. Also, there is a 60 GeV/c^2 cutoff on the invariant mass. In these figures we see that, aside from different backgrounds, these distributions have certain structure in the lower shoulder of the Z peak. This structure affects efficiency estimation.

The next set of figures Fig. 50- Fig. 55 illustrates different p_T slices of invariant mass distributions of electrons in Data and MC in the CC region fitted with the `emid` tools [66]. Clearly, in the low-p_T bins fitting fails. It fails because we do not properly describe structure of the signal, e.g. Fig. 49 and Fig. 52. This structure is a result of a superposition of two effects. The first one is a kinematical cut-off of electron p_T and the second one is the p_T-dependence of invariant mass of D/Y pair. The latter can be

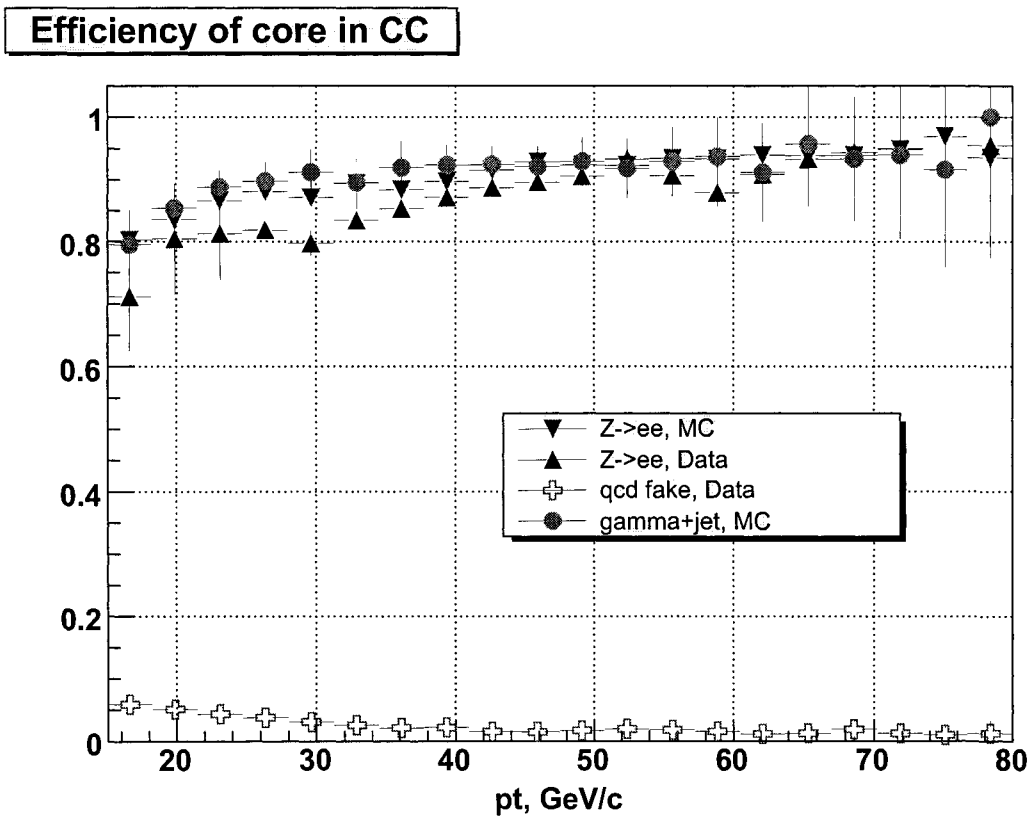

Fig. 48: Efficiency of core cuts for electrons in the CC as a function of p_T. Note, there is no track-matching requirement.

seen as a migration of a bump across the Z peak as we icrease p_T of the probe electron. This hypothesis is partially confirmed by the fact that when we narrow the window in which electrons are counted from $[80\ GeV/c^2, 110\ GeV/c^2]$ down to $[85\ GeV/c^2, 97\ GeV/c^2]$ the dip becomes smaller.

Now, suppose, we do not properly model our signal and still want to use `Voigt()` function for the signal and the exponent for the background. In this case the following happens. Since the righthand side point of the background is effectively fixed at zero at approximately 110-120 GeV/c^2 (for p_T bins in question) inclusion of a part of the signal into background would raise the slope of the green curve (background hypothesis) and therefore introduce an over-subtruction of the background. We estimate that this introduces an additional 2% uncertainty. Thus, we assign additional 2% uncertainty to both Data and MC efficiency and add it in quadrature to the errors of the fit.

Another (remote) possibility of such structure might be improperly implemented trigger matching. To test this possibility we studied efficiencies that were obtained with individual triggers and did not observe any change of p_T structure. Also, for consistency, we compared our results with the output of anothe certification package, `em_cert`. We observe similar behavior.

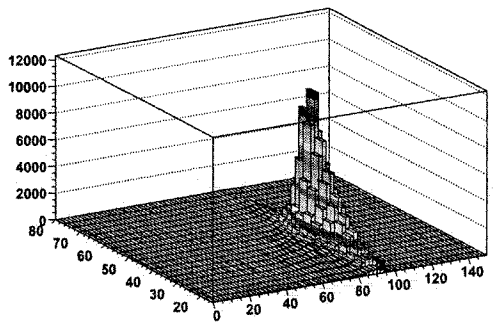

(a) m_{inv} vs p_T, MC.

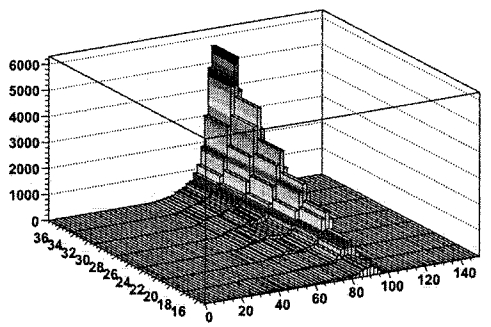

(b) Region of data dip, MC.

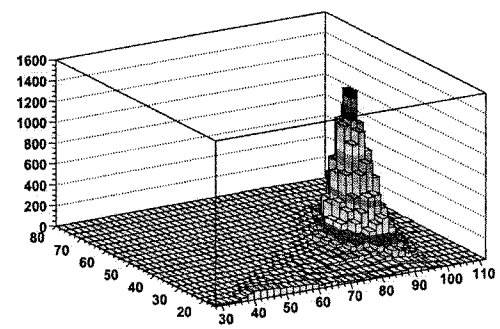

(c) m_{inv} vs p_T, Data.

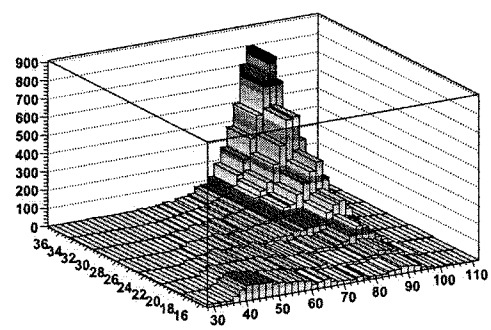

(d) Region of data dip, Data.

Fig. 49: Distribution of m_{inv} vs p_T for electrons in the Data and the MC. Number of entries inder the Z-peak in each p_T bin is used for estimation of efficiency in the corresponding bin. Note that in data background has different turn-on curve and therefore, in general, requires variable fitting limits and p_T-dependent background.

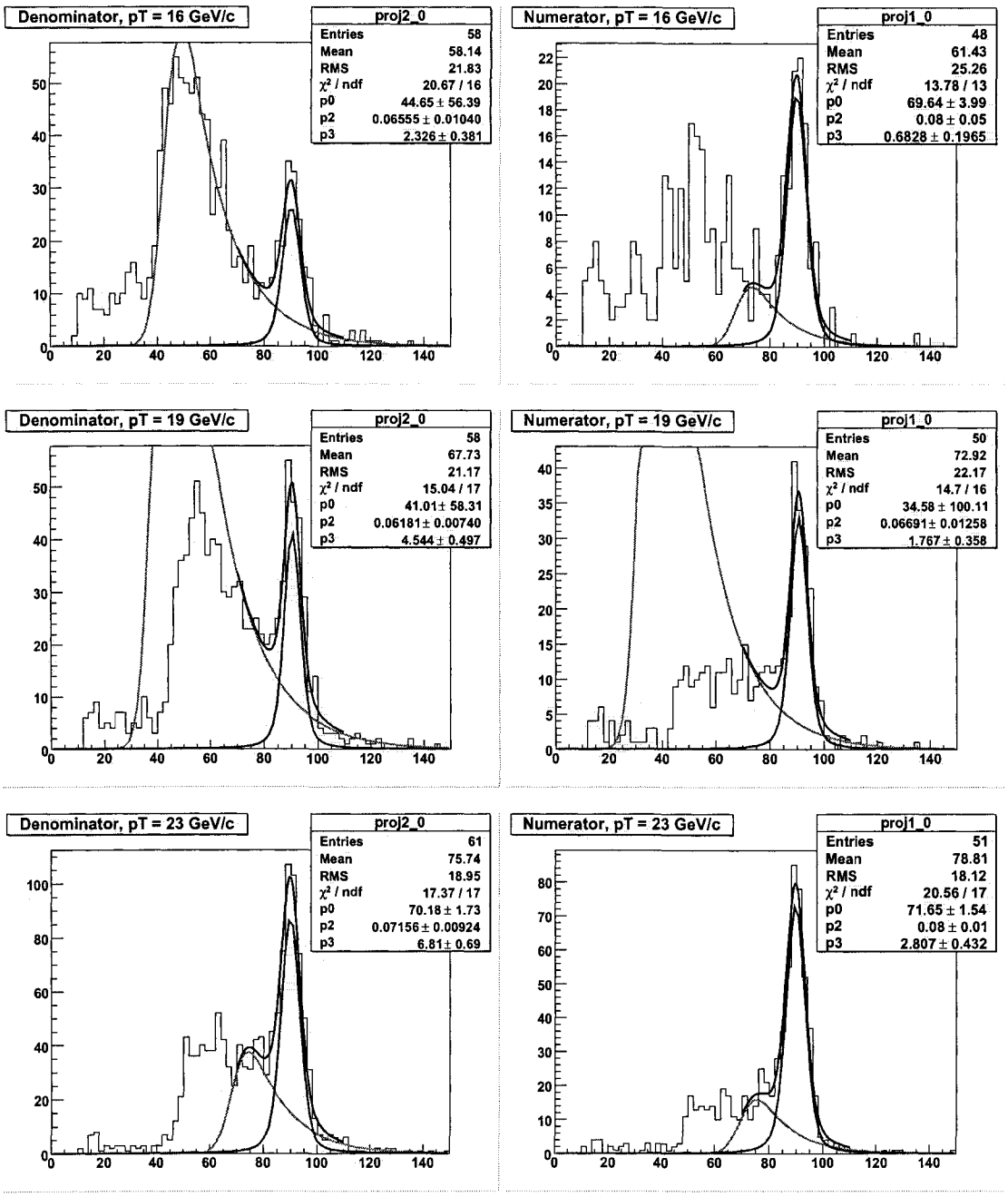

Fig. 50: Fits of 16-23 GeV/c p_T slices for CC electrons in Data.

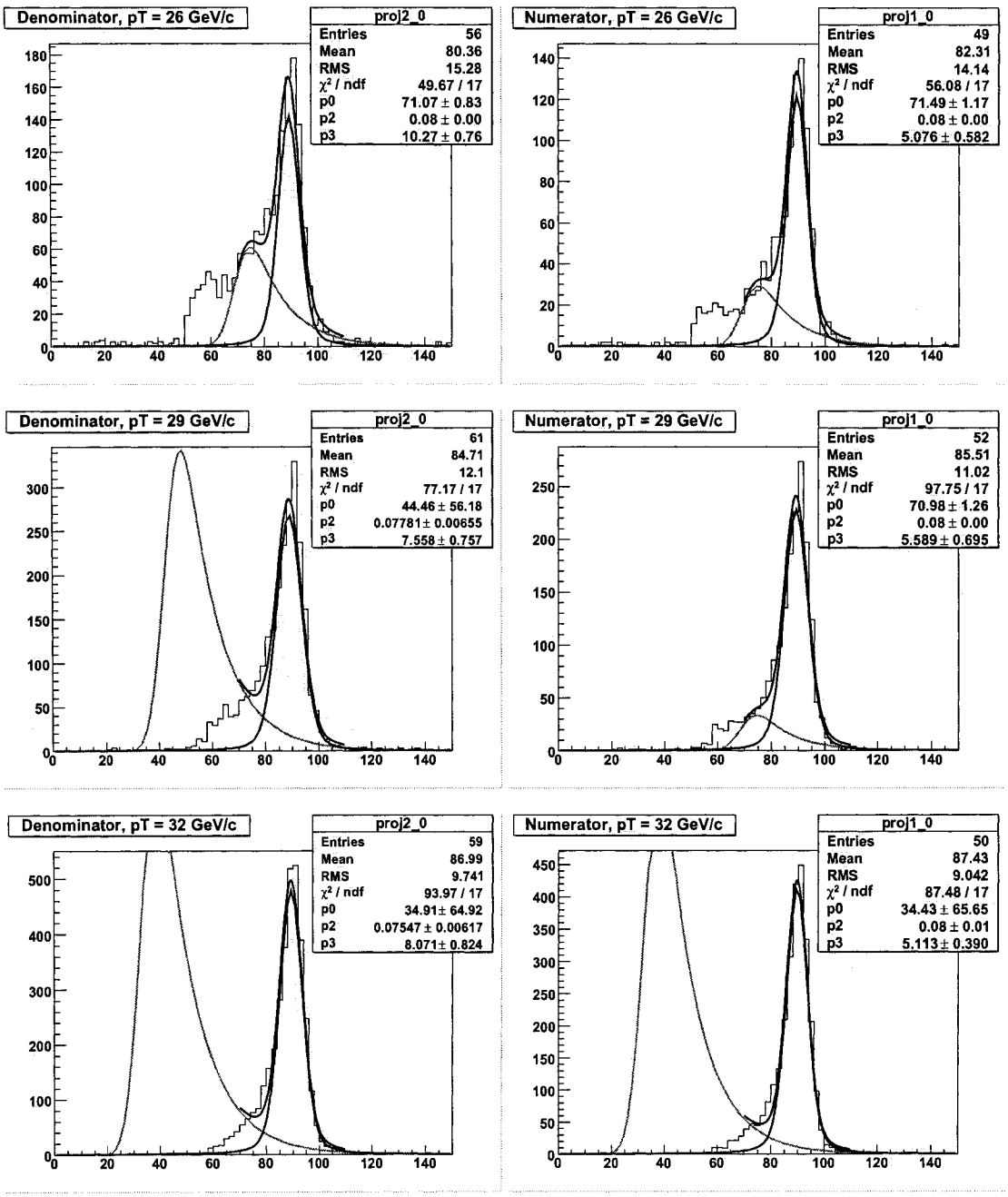

Fig. 51: Fits of 26-32 GeV/c p_T slices for CC electrons in Data.

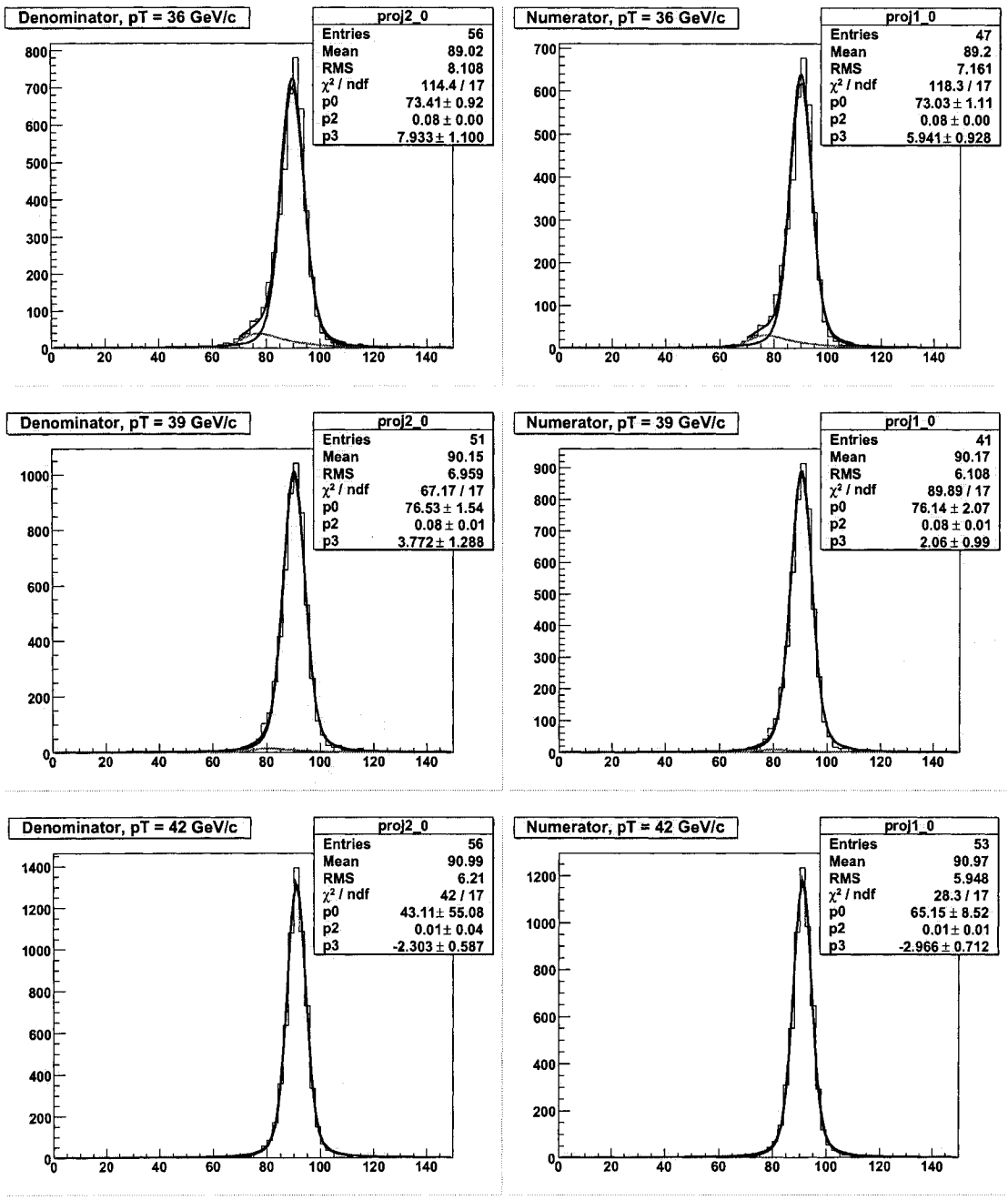

Fig. 52: Fits of 36-42 GeV/c p_T slices for CC electrons in Data.

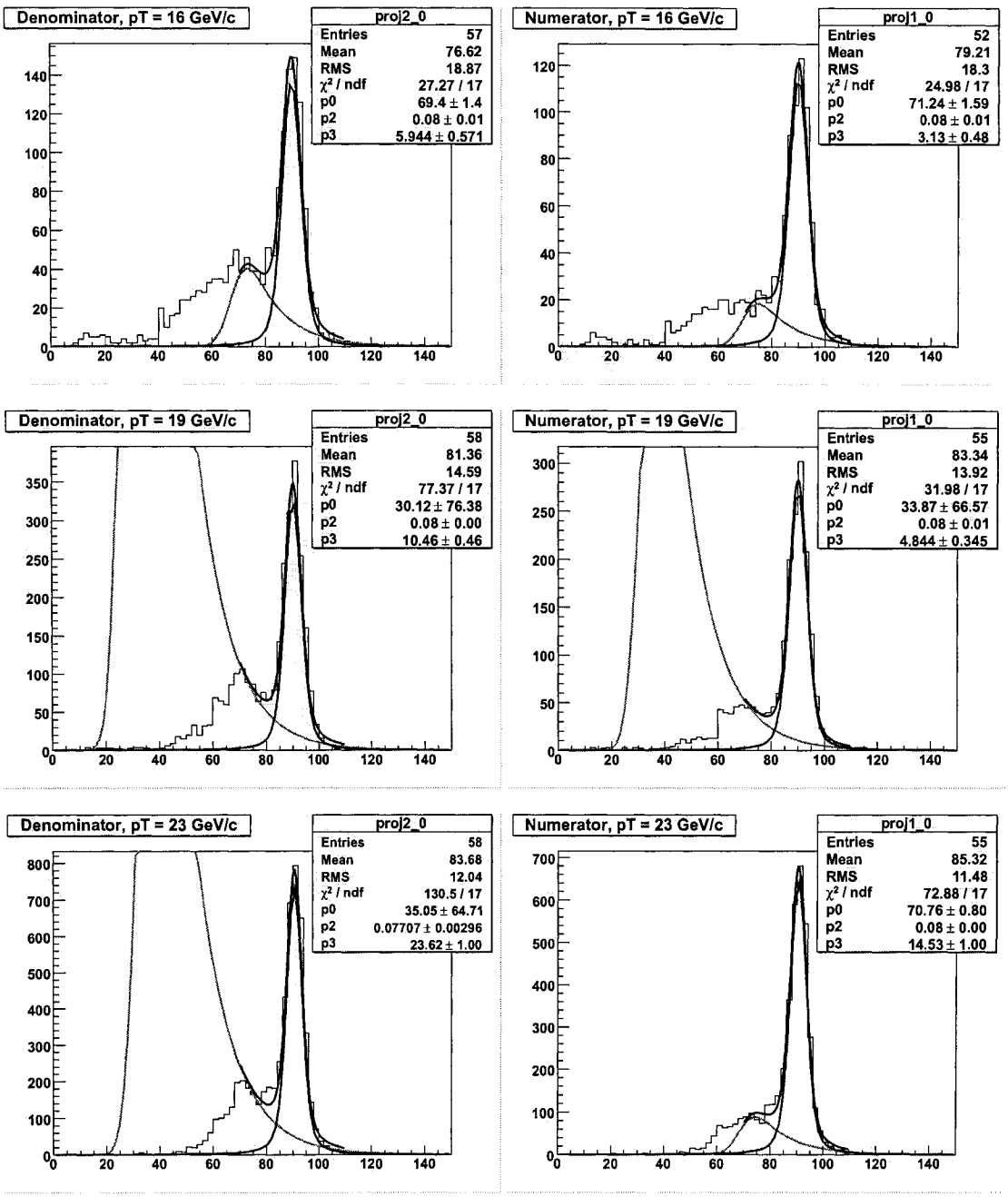

Fig. 53: Fits of 16-23 GeV/c p_T slices for CC electrons in MC.

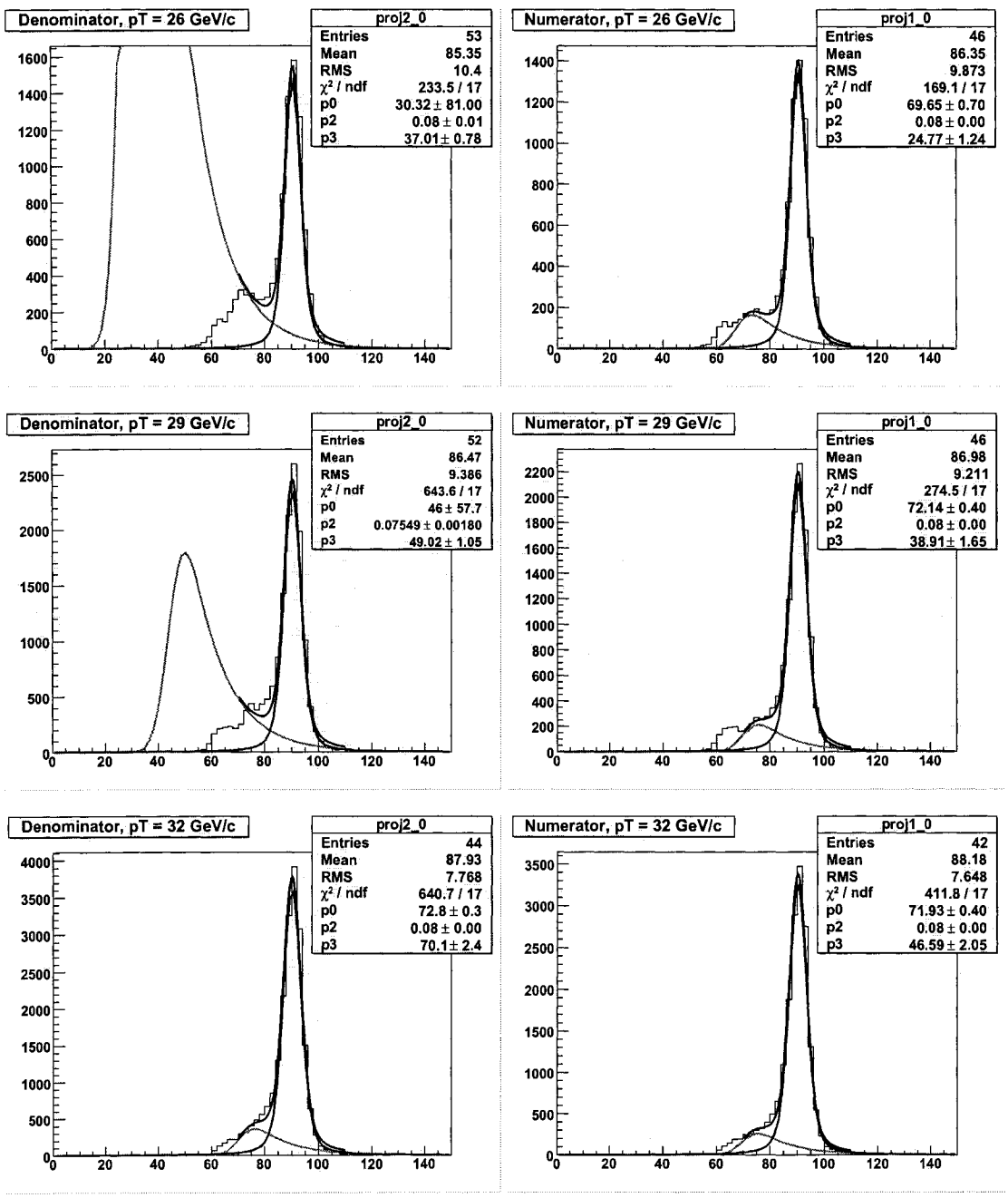

Fig. 54: Fits of 26-32 GeV/c p_T slices for CC electrons in MC.

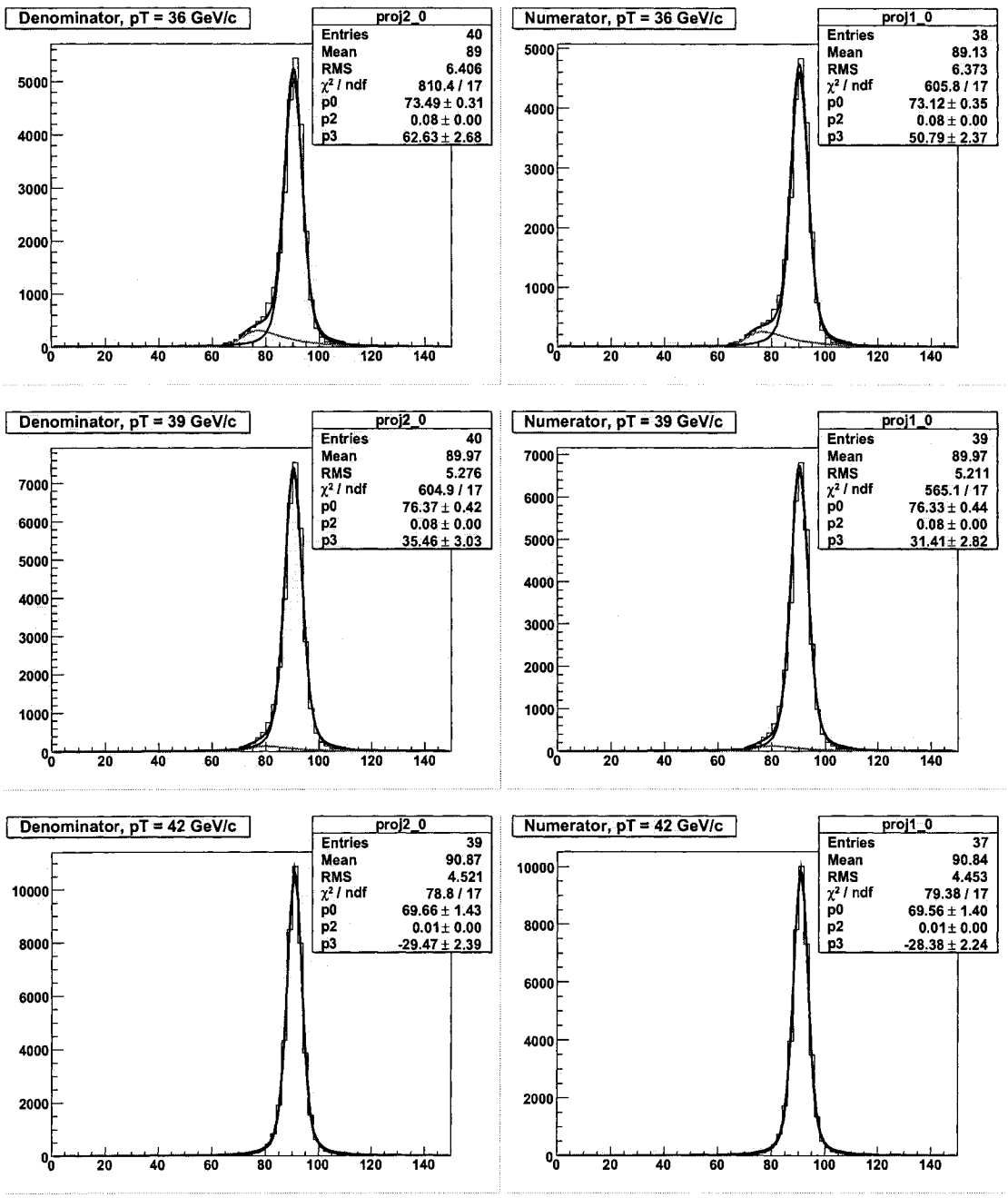

Fig. 55: Fits of 36-42 GeV/c p_T slices for CC electrons in MC.

Now we proceed with determination of the scaling factor, κ, which is defined as a ratio of two functions:

$$\kappa = \frac{F^{Data}}{F^{MC}} \tag{6.9}$$

with F's being fits of electron efficiencies with an exponential function:

$$F = 1 - exp(-(\alpha + \beta \cdot p_T)) \tag{6.10}$$

Figs. Fig. 56 illustrate fits of electron efficiencies in the CC. Note, that we performed fits after addition of the abovementioned extra 2%.

Uncertainty of the fit function due to variations in fit parameters is obtained through standar error propagation:

$$(\delta F)^2 = (\frac{\partial F}{\partial \alpha})^2 \cdot (\delta\alpha)^2 + (\frac{\partial F}{\partial \beta})^2 \cdot (\delta\beta)^2 + 2 \cdot \frac{\partial F}{\partial \alpha} \cdot \frac{\partial F}{\partial \beta} \cdot cov(\alpha, \beta) \tag{6.11}$$

Figs. Fig. 57 demonstrate uncertainty bands in the CC. Uncertainties of MC and Data fits, δF^{MC} and δF^{Data} respectively, are combined as uncertainties of independent variables:

$$\frac{\delta\kappa}{\kappa} = \sqrt{\left(\frac{\delta F^{MC}}{F^{MC}}\right)^2 + \left(\frac{\delta F^{Data}}{F^{Data}}\right)^2} \tag{6.12}$$

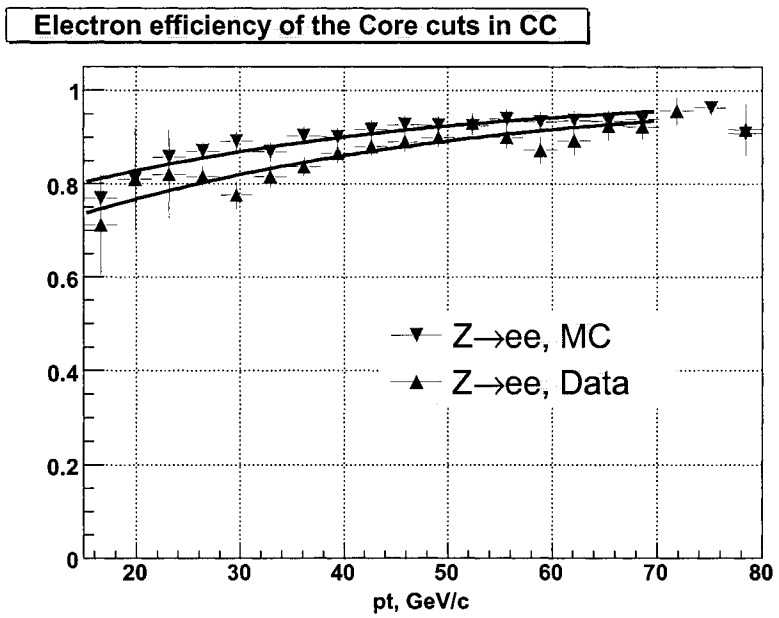

Fig. 56: Electron efficiency in CC for core cuts, Data and MC. Fitted with exponential function (Equation 6.10).

In Fig. 58 we provide Data/MC scaling factor for core set of cuts with envelop error-bands – $\kappa \pm \delta\kappa$.

Now, the following question is in order: *Is there any appreciable dependence on eta and do we need to provide* κ *as a function of both* η *and* p_T*?* The answer to this question can be found in Fig. 59. This figure illustrates ε_γ^{MC} as a function of detector eta. Note, that electrons average at approximately 30-40 GeV/c and photons – lower; therefore this figure should not be used to compare absolute efficiency scales. At any rate, we can see that the variation of the scaling factor is contained within the envelope uncertainties $\delta\kappa$ and the aswer is **no** – *It suffices to provide Data/MC scaling only as a function of* p_T.

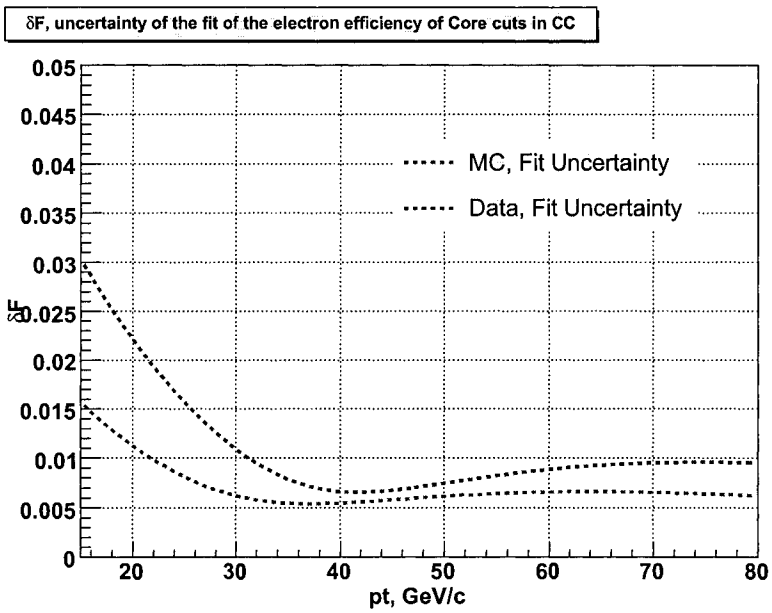

Fig. 57: Uncertainty of a fit of electron efficiency in the CC for core cuts in Data and MC. Functional form is given in Eq. (Equation 6.11).

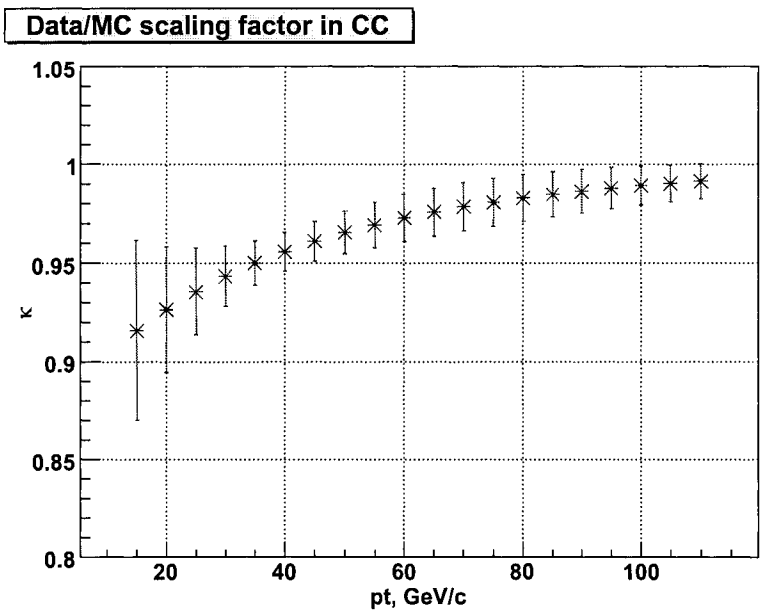

Fig. 58: Data/MC scaling factor in CC.

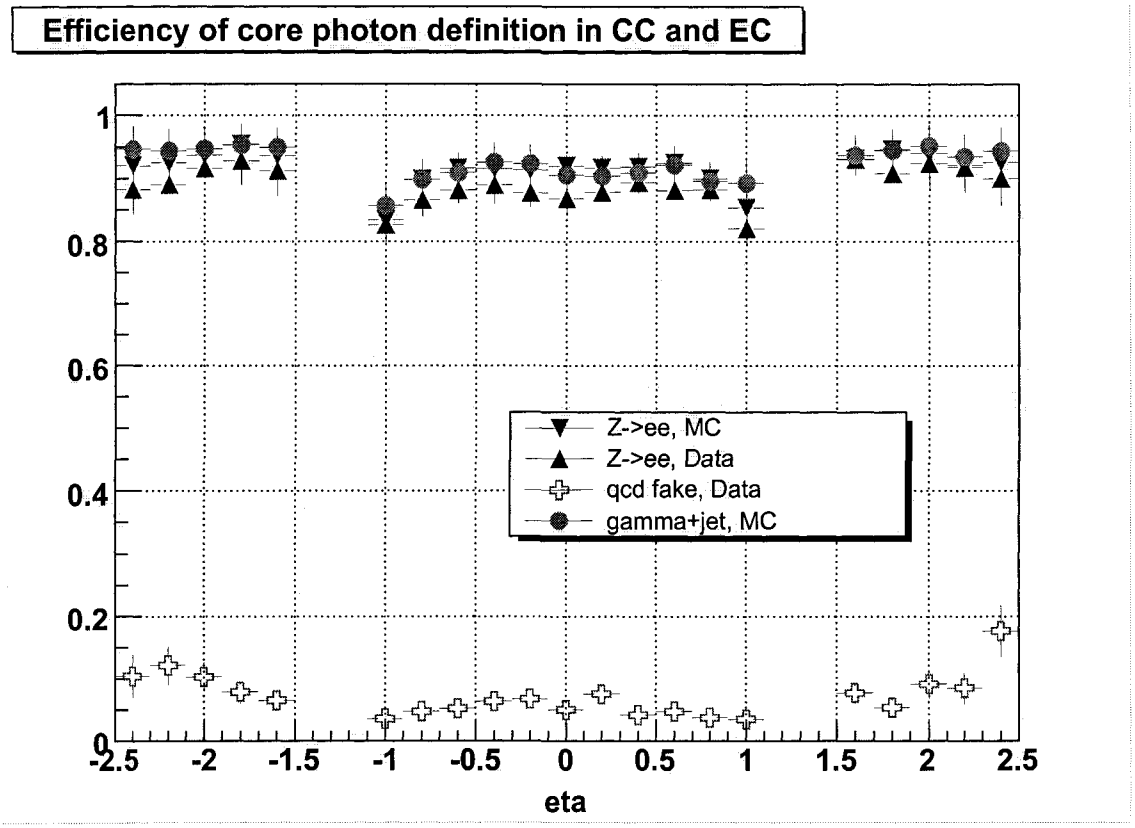

Fig. 59: Core efficiencies as functions of detector eta. Note, that whatever difference there is between electron Data and MC efficiencies it is contained within $\delta\kappa$ and therefore can be considered independent, withing errors, on eta.

For convenience we provide a numerical values of the fit parameters and the correlation coefficients between them; in CC:

$$
\begin{aligned}
F^{MC} &= 1 - e^{(1.22\pm0.017)+(0.027\pm0.000014)\cdot p_T} \\
F^{Data} &= 1 - e^{(0.95\pm0.03)+(0.026\pm0.00002)\cdot p_T} \\
cov(\alpha^{MC}, \beta^{MC}) &= -0.00045 \\
cov(\alpha^{Data}, \beta^{Data}) &= -0.00076
\end{aligned}
\tag{6.13}
$$

This information should be sufficient for all practical purposes to make Data⇄MC transition.

6.7.2 Preselection Efficiency

Preselection efficiency is a probability that an electron or a photon will form an EM cluster. Since this quantity is determined with respect to the actual number of the photons or electrons in a sample the above-mentioned tag-and-probe method should be employed with care. The best that we can do is to determine a probability to form a cluster provided an electron has left a track in the tracker and that this track forms a Z-like pair with another EM cluster in the event. It biases the sample of electrons towards those that did not undergo multiple scattering that would lead to distortion of the shower shape. However, we presume that this is not a significant effect in this detector[1]. This claim is partially backed up by MC studies.

---

[1]CMS, on the other hand, would have to devise clever algorithms to reconstruct electrons in 4T field along 2 m of trajectories through more than 2X0 of material in the tracker.

For this efficiency di-EM sample can not be used and instead we use a sample that contains at least one EM cluster and at least one track that is not associated with this cluster. Then, as a probe we use a track and compute how often this track points to the EM cluster in the calorimeter. Tag is chosen as before – tight EM cluster with a matched track. Preselection efficiency for Data and MC is shown in Fig. 60. Note that it drops at low p_T. This loss of the efficiency is caused by mis-measured photons at the vicinity of ϕ-cracks in the calorimeter. Fig. 61 illustrates behavior of *reconstruction efficiency* for electrons and photons across the ϕ-module. Requiring photons to be $\pm 10\%$ away from the boundaries brings preselection back to almost 100% values, at the expense of 20% in acceptance, mind you, and only for p_T's below 25-30 GeV/c. The benefit of ϕ-fiducial cut is quite relative and depends on the analysis. For those studies where signal is plentiful and where one can't afford to have extra few percent of uncertainty (see again Fig. 61 for Data/MC) application of this cut makes sense. However, in a majority of searches this cut turns out to be counter-productive. In this analysis, in particular, `in_phi_fiducial` cut translates into 50% loss of acceptance ($(1-0.2)^3 = 0.512$), which is clearly unacceptable.

6.7.3 Photon Reconstruction Efficiency

Photon reconstruction efficiency is a probability that a photon that has already been reconstructed as a loose EM object passes photon identification cuts (Sec. 6.6). This quantity is analysis-dependent and therefore it should be obtained from the signal MC sample. This dependence comes primarily from the hadronic objects that accompany signal photons. On Fig. 62 we demonstrate efficiency obtained from the SM $\gamma + jet$ sample and from the 2HDM $h + H^{\pm} \rightarrow 2h + W^{\pm} \rightarrow 4\gamma + 2jet$ signal sample. The former

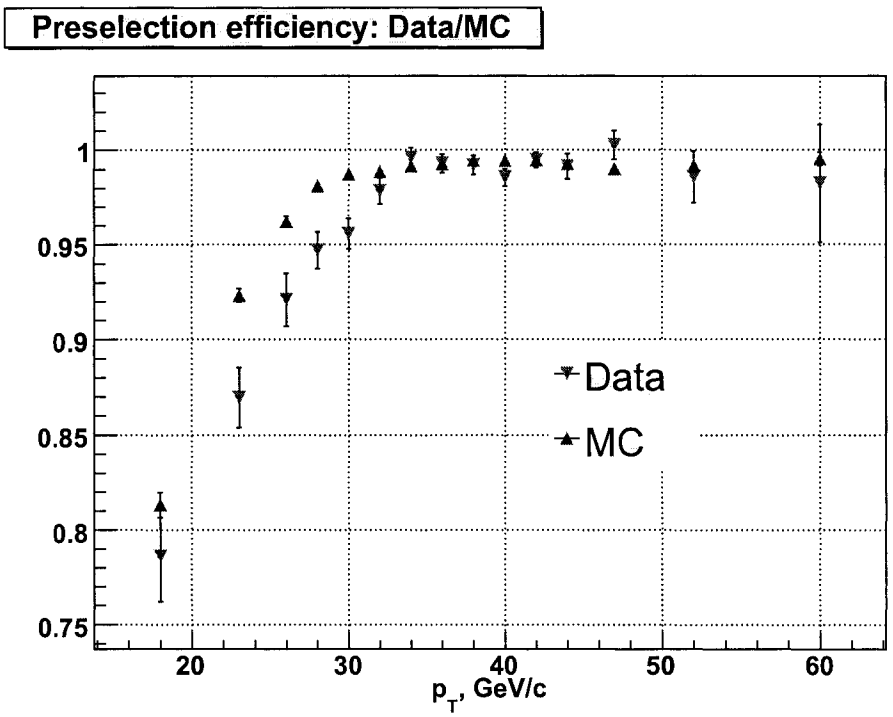

Fig. 60: Preselection efficiency.

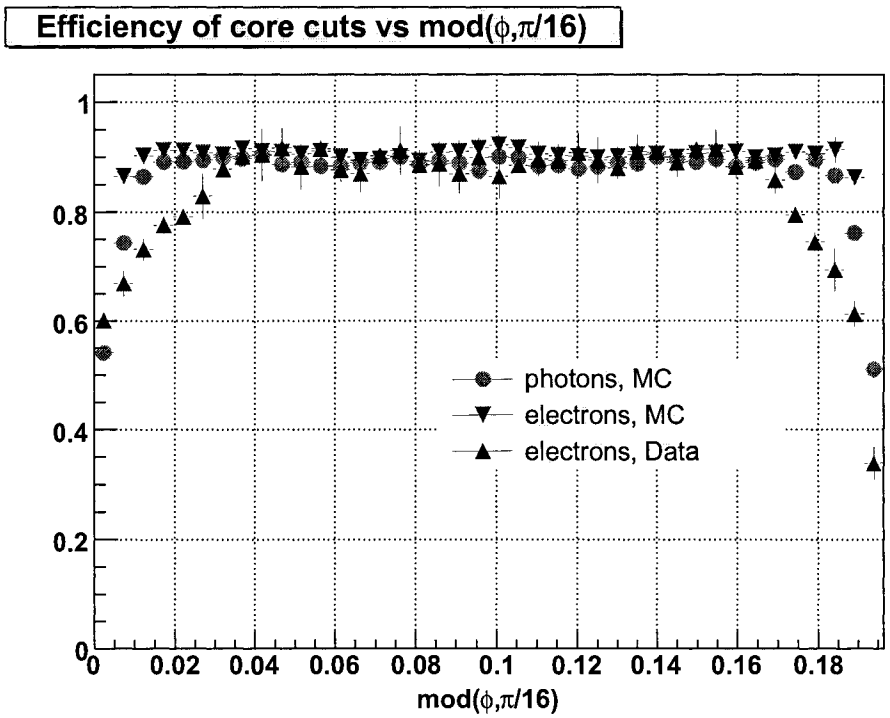

Fig. 61: Efficiency vs $mod(\phi, \pi/16)$ for core cuts.

is higher due to cuts on secondary jets and on the imbalance of total transverse energy. Result of the fit is as follows:

$$\varepsilon_\gamma = (0.93 \pm 0.048) - (-0.95 \pm 0.62)/\sqrt{p_T} - (1.4 \pm 1.9)/p_T \tag{6.14}$$

where p_T is in GeV/c.

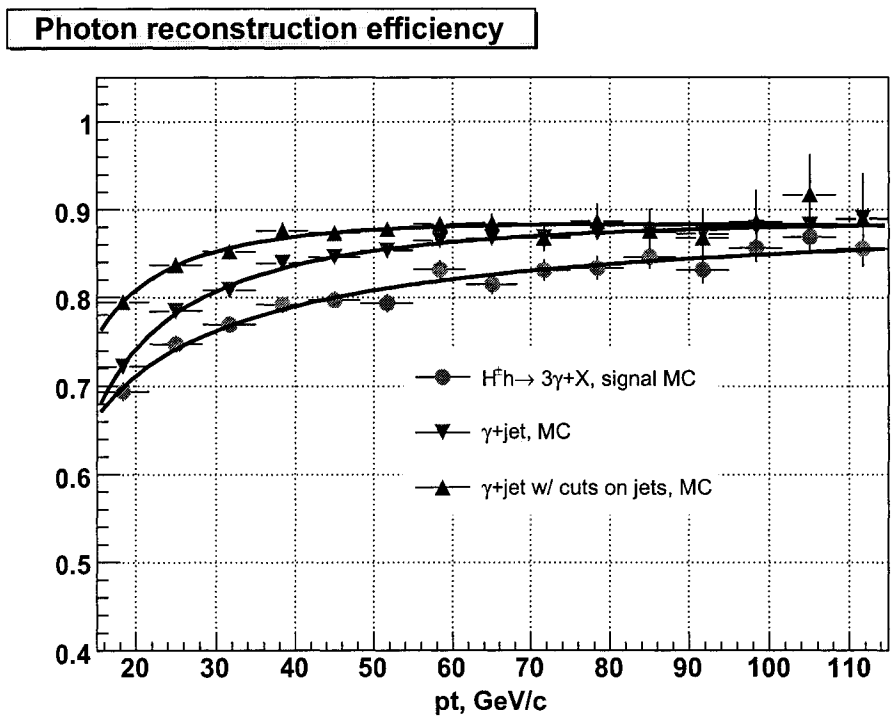

Fig. 62: Photon reconstruction efficiency.

6.7.4 Background Efficiency: $e \rightarrow \gamma$

Real electrons that come from decays of copious W and Z bosons will be identified as photons if their track is not reconstructed. Tracking inefficiency can be interpreted as $\varepsilon_{e\rightarrow\gamma}$, a probability that an electron would fake a photon. In realm of our photon identification approach this quantity is determined with respect to core cuts from the $Z \rightarrow ee$ sample. Fig. 63 illustrates this quantity as a function of electron's p_T for data and MC. We can see that there is certain degree of discrepancy between Data and MC. However, if one chooses to estimate electron background from data this discrepancy is not important as well as tightness of the cuts with respect to which this probability has been obtained. As it will be seen further electrons contribution is not a significant background source and for all practical purposes it suffice to approximate this probability with its value in Z-like p_T region[1], i.e. 25-50 Gev/c, and assign a large uncertainty. Thus, the number of observed events with electrons would enter the background with this factor (per electron):

$$\frac{\varepsilon_{e\rightarrow\gamma}}{1-\varepsilon_{e\rightarrow\gamma}}, \tag{6.15}$$

with $\varepsilon_{e\rightarrow\gamma} = 0.08 \pm 0.03$ (and 0.014 ± 0.03 with hits-on-the-road discriminant).

---

[1]Major source of energetic electrons in this study comes from W/Z and thus this approximation is a very reasonable one.

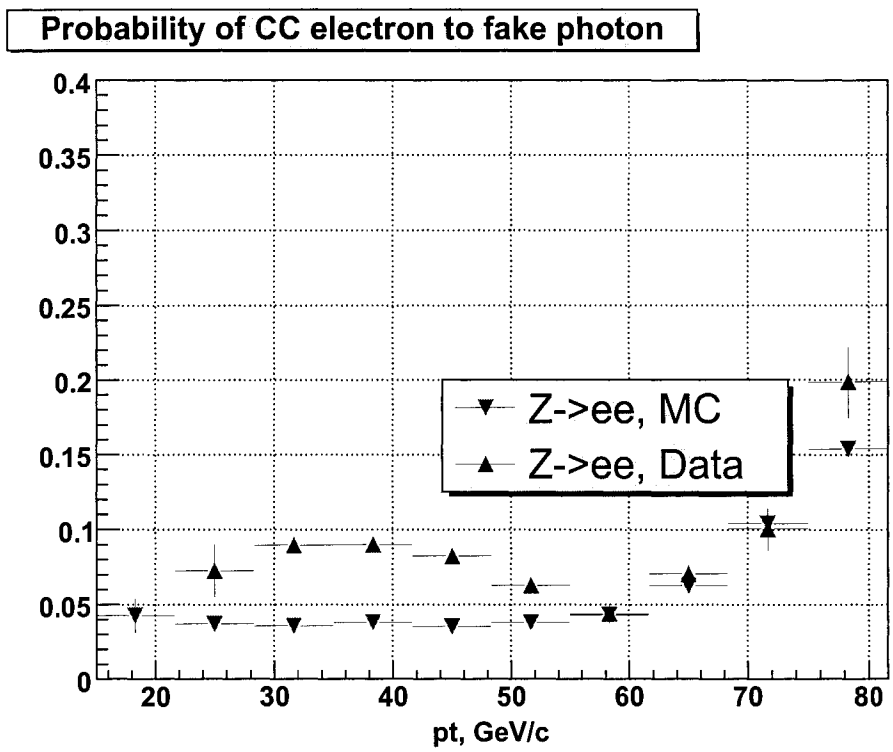

Fig. 63: Probability of an electron to loose a track (prbtrk<0.001) as a function of p_T.

6.7.5 Background Efficiency: $j \rightarrow \gamma$

Jets originate in the processes with gigantic[1] production cross sections. They contribute objects that pass photon identification criteria through two mechanisms: energetic π^0,'s ω's, and K_0^s that decay to multiple photons and "bremsstrahlung" photons that are produced during the fragmentation of a quark or a gluon. In reality it is extremely difficult to distinguish them since both are produced inside of an hadronic jet. In this study we will consider fragmentation photons as fakes.

Determination of the probability that a jet fluctuates into object that passes photon-id selection criteria should be done with care due to a significant content of direct photons. We choose to estimate this fake rate in data from di-jet events where one jet fluctuated into a fake photon and the other was registered as a good quality jet that triggered an event. This sample inevitably contains admixture of photons from also abundant γ+jet events. We use Pythia MC to determine the fraction of real photons in a sample of one photon candidate and a jet. Obtained in this way this quantity is free from potentially large systematic effects in detector simulation. However, it still carries uncertainty that comes from jet fragmentation function. It is imperative to mention that event selection in data sample was kept as close as possible to the event selection in the MC for purity estimation.

Thus, from EM loose + jet data sample we obtain a fraction of events that pass photon identification criteria. In order to separate "hadronic" photons this fraction is multiplied by a MC estimate of a fraction of hadronic photons is γ+jet sample: $1 - purity$, where $purity$ was obtained above in the Sec. 6.5. Fig. 64 demonstrates $\varepsilon_{j\rightarrow\gamma}$ as a function of p_T. The points are fitted with the exponential function:

---

[1]For example, di-jet production rate is of the order of 10^6 pb, compared to 1 pb for anticipated signal rates.

$$\varepsilon_{j\to\gamma} = (0.0016 \pm 0.0013) + (0.11 \pm 0.01) \cdot e^{-(0.039\pm0.002)\cdot p_T(GeV/c)} \tag{6.16}$$

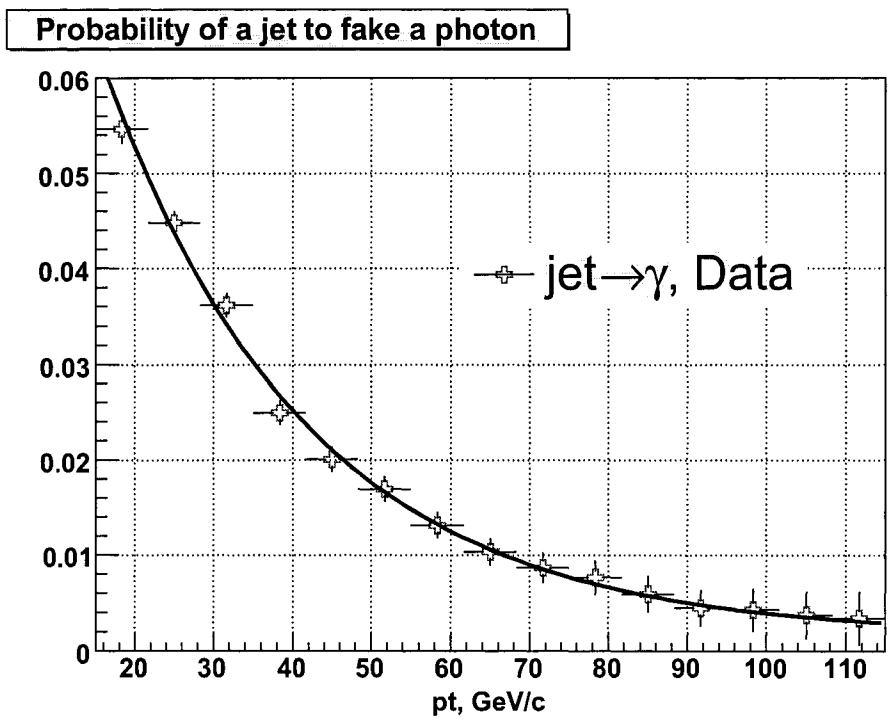

Fig. 64: Probability of a jet to fluctuate into an EM object that passes photon identification cuts.

6.8 Photon Energy Scale

Reconstructed energy of the EM objects in the DØ calorimeter depends on several parameters. These parameters are the weights at which indvidual calorimeter layers contribute to the total energy. Since these weights were fixed in such a way that the total energy reproduces the correct position of the Z peak there is inevitably some degree of uncertainty in determining their proper values. This uncertainty, and probably not the most faithful choice of the weights, results in the discrepancy between actual and reconstructed energies for p_T's away from Z peak. And this is in addtion to the intrinsic differences between showering profiles of photons, electrons, and EM-jets their energy scales will be in general different. Figs. Fig. 65 and Fig. 66 illustrate relative shifts of photon and EM-jet energies, respectively.

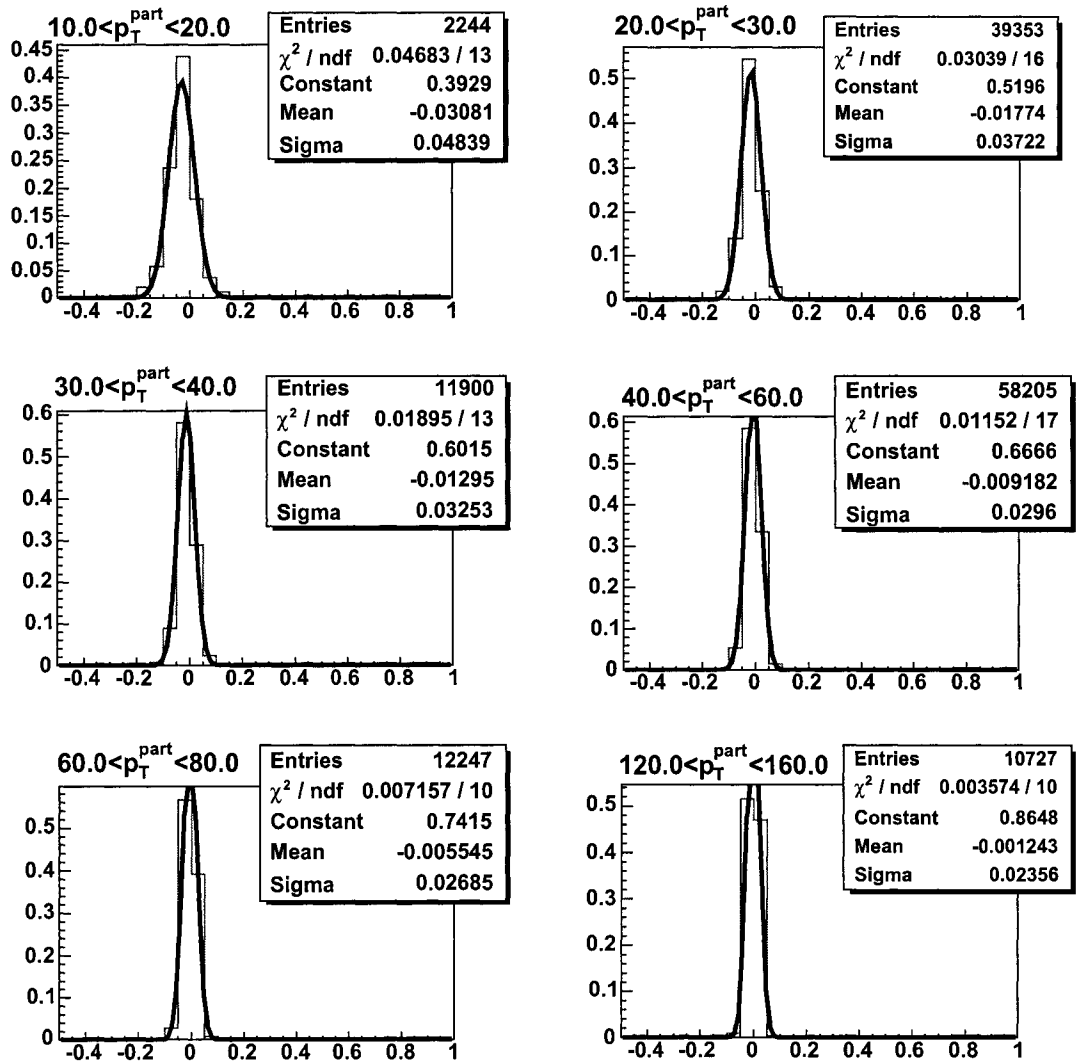

Fig. 65: Distribution of $(p_T{}^{part} - p_T{}^{reco}/p_T{}^{reco}$, the difference between generator level and reco p_T, for the direct photon MC.

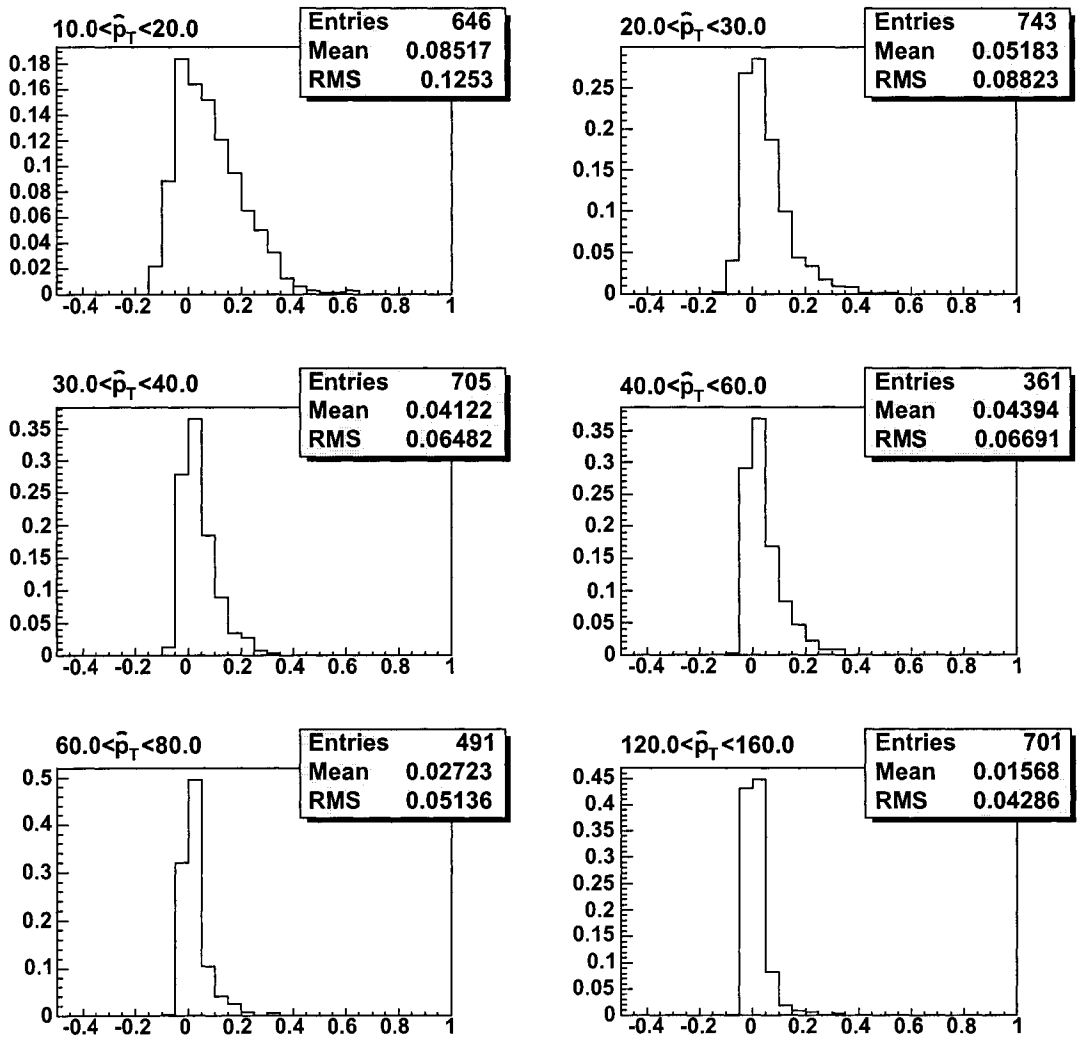

Fig. 66: Distribution of $(p_T{}^{part} - p_T{}^{reco}/p_T{}^{reco}$, the difference between generator level and reco p_T, for the EM-jet MC.

7 LUMINOSITY MEASUREMENT

Correct determination of luminosity is absolutely crucial to almost all analyses at the DØ experiment. However, without verification it can easily become a victim to easily overlooked instrumental effects. In this section we perform a measurement of the luminosity that has been delivered to the DØ detector by the Tevatron by studying a well understood physical process – production and subsensequent leptonic decays of Z bosons.

7.1 Method

Production of Z bosons at the Tevatron has been extensively studied both from theoretical [67] and experimental perspectives [68]. Decays of Z to electron-positron pairs provide a clean signature and allow an unbiased study of the reconstruction efficiencies and trigger rates, and with a known theoretical production cross section one can extract underlying luminosity of a given dataset. Strictly speaking, the result might depend on the trigger rules used to select candidate events, thus, we estimate luminosity with exactly the same combination of triggers that we use in our analysis. In order to minimize effects of trigger inefficiency and reduce systematic effects of Data/MC scaling at low p_T we require at least one electron to be above 30 GeV/c and the other one above 25 GeV/c. Both are central.

Number of observed $Z \rightarrow ee$ events is related to the delivered luminosity via the acceptance and production cross-section:

$$N_{Z\to ee} = A \cdot \sigma(q\bar{q} \to Z/\gamma^* \to e^+e^- + X) \cdot L, \tag{7.1}$$

where the acceptance is a composite quantity that consists of kinematic and topological acceptances, average trigger efficiency, electron reconstruction efficiency, and various scaling factors. We have all necessary ingredients to calculate this aggregate quantity.

For the cross-section, σ, we use a theoretical NNLO value that can be found, for example, in [67]:

$$\sigma(q\bar{q} \to Z/\gamma^* \to e^+e^- + X) = 259 \pm 8pb, \tag{7.2}$$

a theoreticl precision of 3%.

7.2 Data and MC Samples

As before, for $Z/\gamma^* \to e^+e^-$ candidate events in data we use 2EMhighpt skim, a subset of data with two energetic EM clusters. Corresponding dataset definition is `CSG_CAF_2EMhighpt_PASS3_p17.09.03`. And for MC we use Pythia $Z/\gamma^* \to e^+e^-$ events that went through the full detector simulation chain. Zero bias events have been overlayed to mimic ambient hadronic activity. Corresponding dataset definitions are `CSG_CAF-MCv1-$reqid`, where `$reqid = 24559, 23092, 23091, 23090, 24557, and 24558`.

7.3 Event Selection

The following criteria were used to select events:

- each event in the data sample is selected according to the trigger rules used in the analysis (see Sec. 8.2.1)
- each data event has to satisfy data quality requirements outlined in Sec. 8.2
- primary vertex is required to be within 60 cm of the center of the detector
- each event contains at least two central EM objects that pass **core** cuts (Sec. 6.6)[1]
- at least one EM object has $p_T > 30$ GeV/c and the other $p_T > 25$ GeV/c,
- number of Z candidate events is taken under the peak between 75 and 105 GeV/c^2.

7.4 Acceptance and Correction Factors

Fig. 67 illustrates invariant mass distribution of two electrons in MC. From this we obtain MC acceptance, i.e. fraction[2] of events that survive the above cuts.

$$A^{MC} = 0.134 \pm 0.005 \tag{7.3}$$

$$A^{MC} = A_{geom} \cdot A_{kinem} \cdot \varepsilon^{1,2}_{reco} \tag{7.4}$$

To make transition to the data it is necessary to apply corresponding correction factors:

---

[1]Due to discrepancy of the tracking efficiency between Data and MC we drop track-matching requirement. As a result di-electron invariant mass distribution acquires additional background that comes from direct diphoton events. This background can be and is fitted with the exponential function and subtracted from under the Z-peak.

[2]The denominator of this fraction is the total number of $Z \rightarrow ee$ Pythia events, thus reco efficiency here is a product of a preseletion efficiency and a core efficiency.

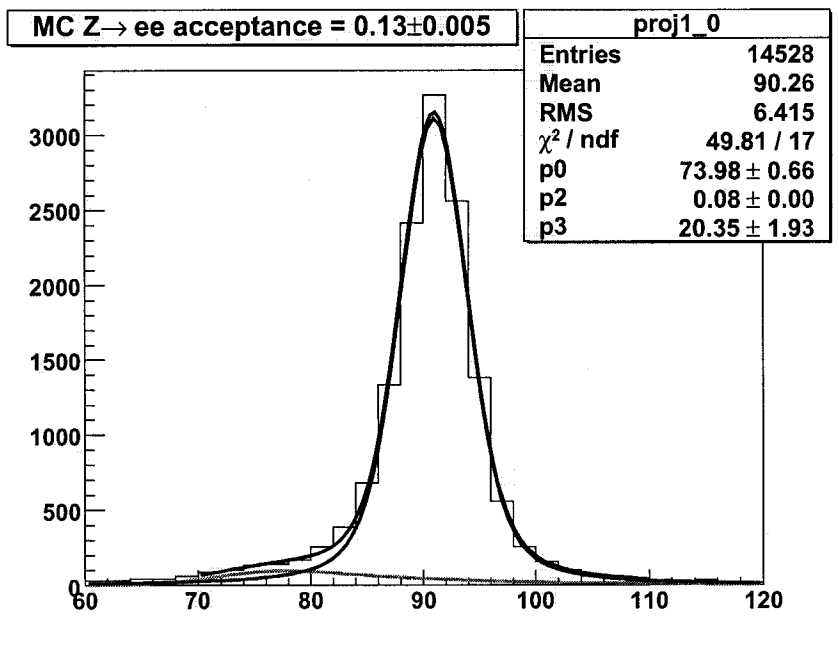

Fig. 67: Selection acceptance of $Z \rightarrow ee$ events in MC.

- $\kappa_{reco} = \kappa_{presel} \cdot \kappa_{core}$ – Data/MC reconstruction efficiency scaling (see Fig. 60 and Sec. 6.7.1). The overall Data/MC scaling factor is obtained from the MC sample by weighting each event with the corresponding product of scaling factors normalized by the total number of events that survive cuts, i,e:

$$\kappa_{reco} = \frac{\sum_i^{N_{reco}^{MC}} \kappa_{presel}^1 \cdot \kappa_{presel}^2 \cdot \kappa_{core}^1 \cdot \kappa_{core}^2}{N_{reco}^{MC}} \tag{7.5}$$

- ε_{trig} – overall trigger efficiency obtained similarly to the above:

$$\varepsilon_{trig} = 1 - \frac{\sum_i^{N_{reco}^{MC}} (1-\varepsilon^1) \cdot (1-\varepsilon^2)}{N_{reco}^{MC}} \tag{7.6}$$

here N_{reco}^{MC} is a number of $Z \rightarrow ee$ events that survive selection criteria and found under the Z-peak. It is the same number from the numerator for Equation 7.3.

Numerical values for the above factors are:

$$\kappa_{reco} = 0.93 \pm 0.02 \tag{7.7}$$

$$\varepsilon_{trig} = 0.97 \pm 0.02 \tag{7.8}$$

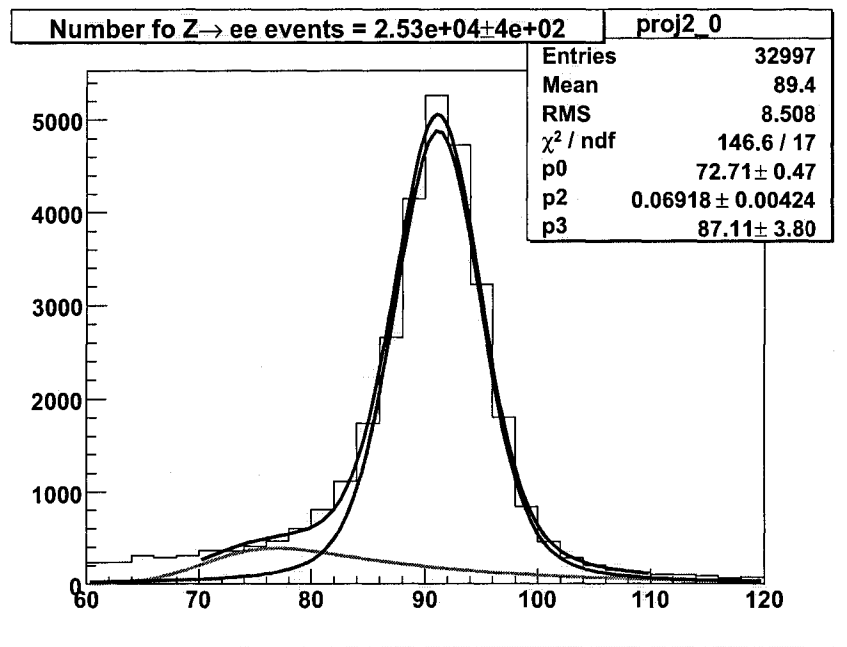

Fig. 68: Number of $Z \rightarrow ee$ events in the full dataset.

7.5 Understanding Systematics

Systematic uncertainty in this measurement comes from several sources:

- $\delta N^{Data}_{Z\to e^+e^-} = 1.6\%$ – uncertainty on the number of Z events in data. It is taken to be a fitting error.
- $\delta\kappa_{reco} = 2.1\%$ – uncertainty with Data/MC scaling and fitting of single electron efficiencies.
- $\delta\varepsilon_{trig} = 2.3\%$ – uncertainty on the trigger efficiency.
- $\delta\varepsilon_{instlumi} = 3.0\%$ – uncertainty that comes from the dependence of the various efficiencies on the instantaneous luminosity. The variation is observed to be within a few percent. We apply half of it to compensate for potentially inadequate simulation of zero bias in the MC.
- $\delta\sigma(q\bar{q} \to Z/\gamma^* \to e^+e^- + X) = 3.0\%$ – theoretical uncertainty on the NNLO calculation of the production cross section. It includes PDF uncertainty.

7.6 Results: Available Luminosity

Fig. 68 shows distribution of invariant mass of two central EM objects that pass core cuts. It corresponds to a full available dataset used in this analysis. Number of Z events, i.e. $N^{Data}_{Z\to e^+e^-}$, is calculated under the peak after the exponential background has been subtracted:

$$N^{Data}_{Z\to e^+e^-} = 25302 \pm 410 \text{events} \tag{7.9}$$

Thus, putting all factors together:

$$L = \frac{25302 \pm 410 events}{0.134 \pm 0.005 \cdot 0.93 \pm 0.02 \cdot 0.97 \pm 0.02} \oplus \delta\varepsilon_{instlumi} \oplus \delta\sigma_{theory} \tag{7.10}$$

gives us

$$L = 833 \pm 46\ pb^{-1}, \tag{7.11}$$

an experimental precision of 5.5%. Obtained luminosity number has been found to be in good agreement with the official procedures after it has underwent a substantial scrutiny and revision that resulted in the average correction factor of 1.15. Currently a big effort has been lunched to perform a maticulous study of $Z \rightarrow ee$ and $Z \rightarrow \mu\mu$ yields. Although, by the time of writing their results were not available for verification, we conclude that possible discrepancies would still reside within aggregate uncertainties of the present analysis.

8 ANALYSIS

In this chapter we describe the search for 3γ events. Such events with three energetic photons have not been observed at the DØ detector. Therefore, first we perform estimation of the backgrounds with at least one fake photon (either a jet or an electron) Sec. 8.4.1, Sec. 8.4.2. We find that that is not a dominant source of 3γ events. Then, we proceed with the estimation of the Direct Tri-Photon production (Sec. 8.4.4). We work under the assumption that the Initial State Radiation (ISR) is responsible for a third photon. We perform estimation of content of Direct Diphoton events in the data sample with two photon candidates and with the ISR rate obtained from $Z+\gamma^{isr}$ data events we obtain an estimate of the Standard Model Contribution to tri-photon events. We find a good agreement of observed events with the expected contribution of all backgrounds.

Then we devise a cut based on the imbalance of transverse momentum of the tri-photon system to extract higgs signal. This cut significantly suppresses the SM backgrounds and does not leave any observed events.

This allows us to exclude higgs masses in the regions previously unattainable either by LEP or Tevatron Run I. Results are summarized in the next chapter.

8.1 Data and MC Samples

8.1.1 Data Sample

The DØ experiment has adopted a modular approach to managing its data. After the reconstruction of raw data events are split into different subsets, called skims, according to their object content – presence of energetic EM cluster(s), muons, or hadronic jets. Split in this way the data, consisting of more than 2 billion events and several Tb's of disk space at the time of writing, became robust for an individual user.

For our purposes we start with a subset of data that was preselected based on the presence of two energetic electromagnetic clusters in the calorimeter. The corresponding skim name is 2EMhighpt and corresponding dataset definition is `CSG_CAF_2EMhighpt_PASS3_p17.09.03`[1]. As is, it contains 29.5M events and occupies almost 1Tb on disk. Due to the nature of the research in our field, before the analysis infrastructure is finalized, a certain number of iterative runs over the data are necessary. Thus, in order to further reduce[2] the size of the data we select events that contain at least 3 electromagnetic clusters with transverse momenta above 15 GeV/c. This further reduces the number of events down to 7327, small enough to be robust, yet sufficiently loose to retain patterns of most of the backgrounds.

---

[1]The names for skims and data sets are almost self-explanatory. The 2EMhighpt means "two electromagnetic objects at high transverse momenta", and the data set augments this with "reconstructed on pass 3 with fixer version p17.09.03"

[2]We are not always this lucky – reduction is not always an option and sometimes we need to devise/adopt other techniques of optimization. As was the case for Photon Identification and Jet Energy Scale Setting an approach similar to one used at SLAC was adopted. We seamlessly distributed more than one Tb of data among several servers and could reach aggregate processing rates of $3 \cdot 10^2$ million events per hour.

8.1.2 Monte Carlo Samples

Simulation of signal events in DØ detector is important for several reasons: on the one hand, it allows us to choose optimal selection criteria and calculate acceptance and on the other, it is the most reliable, if not the only, way to calculate overall event selection efficiency[1].

There exists a plethora of generators for simulation of hadron-hadron collisions. Although implementation details differ, the steps followed in all these generators are similar:

- A primary hard scattering is generated for the physics process under study,
- QCD radiative corrections to both the initial and the final state are added,
- partons are fragmented and short-lived particles are decayed (hadronization)
- experiment-specific simulation of the detector response to long lived particles in the simulated events is performed.

For the generation of the underlying signal process we used NLO calculations from the PYTHIA 6.3 [69] event generator. We use $f_i\bar{f}_j \rightarrow H^{\pm}h^0$ higgs pair-production process (`IMSUB = 297`) with a cascade higgs decay $H^{\pm} \rightarrow W^{\pm}h$ and a subsequent hadronic decay mode of the W-boson. Together with CTEQ6L1 [70] parton distribution functions PYTHIA is used for simulation of the rest of the event. We have generated 50k events for each mass point – $h = 30$ GeV/c^2 and $h = 50$ GeV/c^2, with $m_H = 150$ GeV/c^2.

---

[1] As shown, photon reconstruction efficiency does not exist by itself – it is tied up to the whole event, i.e., multiplicity of particles and hadronic activity in particular affect photon efficiency.

At the time of writing full detector reconstruction of additional mass points were not available and we used generator level MadGraphII [71] NNLO samples to verify geometrical and kinematical acceptances.

8.2 Event Selection

A cornerstone of a successful study is a reliable event selection. It hinges, in general, on the following three ingredients: choice of triggers (Sec. 8.2.1), data quality (Sec. 8.2.2), and object selection.

We use a set of triggers that select events with particle showers that deposit more than 90% of their energy in the inner region of the calorimeter. With very high probability these are electrons or photons and therefore corresponding triggers have "EM" in their names. To maximize event selection efficiency we use "OR" of several triggers. Further, we make sure that at least one trigger that fired in the event has weight "1", which dramatically simplifies verification of the luminosity estimated in Chapter 7. In addition to a certain fraction of data that was excluded due to know instrumental failures, we perform a heuristic search for regions of the detector that exhibit abnormal behavior. We map out such regions and remove them on per-event basis. This study led to discovery of certain instrumental effects that leads to the observation of "instrumental photons" in the detector.

8.2.1 Triggers

The data taking period for this study can be divided into five periods during which different lists of single EM triggers were implemented. For a definition of all triggers see Table IV They are:

- v8-10 (run $\in [160582, 174802]$),
- v11 (run$\in [174845, 178721]$),
- v12 (run $\in [178069, 194597]$),

- v13 (run $\in [194567, 208144)$.
- v14 (run $\in [207517, 211275]$).

Improvements to the Data Aqusition electronics and online/offline event reconstruction led to the evolution of triggers. As a result we have to use different trigger combinations and different triggers for different epochs. For pre-v12 dataset we use:

- EM_HI_SH or EM_HI_2EM5_SH, if both unprescaled, otherwise
- EM_HI_SH, if unprescaled, otherwise
- EM_HI, if unprescaled, otherwise
- EM_MX_SH, if unprescaled, otherwise
- EM_MX, if unprescaled.

The Level 2 trigger subsystem was not available for the entire pre-v12 dataset (all runs with run numbers ≤ 169523) in which case we do not require the Level 2 trigger condition to be satisfied.

The trigger combinations for v12 dataset are:

- E1_SHT20 or E2_SHT20 or E3_SHT20 or E1_SH30, if all unprescaled, otherwise
- E1_SHT20 or E2_SHT20 or E1_SH30, if all unprescaled, otherwise
- E1_SHT20 or E1_SH30, if both unprescaled, otherwise
- E1_SHT20 or E2_SHT20, if both unprescaled
- E1_SH30, if unprescaled
- E1_SHT20, if unprescaled.

The trigger combinations for v13 dataset are:

- E1_SHT22 or E2_SHT22 or E3_SHT22 or E1_SH30, if all unprescaled, otherwise
- E1_SHT22 or E2_SHT22 or E1_SH30, if all unprescaled, otherwise
- E1_SHT22 or E1_SH30, if both unprescaled, otherwise
- E1_SH30, if unprescaled.

The trigger combinations for v14 dataset are:

- E1_ISH30 or E2_ISHT22 or E1_SH35 or E1_SHT25 or E3_ISH30 or E3_ISHT22 or E3_SH35 or E3_SHT25, if all unprescaled, otherwise
- E1_ISH30 or E2_ISHT22 or E1_SH35 or E1_SHT25, if all unprescaled.

Individual selection efficiencies of the trigger combinations used for this analysis were estimated using the tag-and-probe method. The combined trigger efficiency from several single-paricle triggers is

$$\varepsilon_{trig}^{overal} = 1 - \prod_{i=1,2,3} \left(1 - \varepsilon_{trig}^{i}\right) \tag{8.1}$$

where ε_{trig}^{i} is single-particle trigger efficiency. Thus, per event trigger efficiency was found to be

$$\varepsilon_{trig}^{overal} = 0.98 \pm 0.02. \tag{8.2}$$

for the physics event sample used in this thesis.

Trigger	L1	L2	L3
EM_HI_SH	CEM(1,10)	EM(1,12)	ELE_LOOSE_SH_T(1,20)
EM_HI_2EM5_SH	CEM(2,5)	EM(1,12)	ELE_LOOSE_SH_T(1,20)
EM_HI	CEM(1,10)	EM(1,12)	ELE_LOOSE(1,30)
EM_MX_SH	CEM(1,15)	none	ELE_LOOSE_SH_T(1,20)
EM_MX	CEM(1,15)	none	ELE_LOOSE(1,30)
E1_SHT20	CEM(1,11)	none	ELE_NLV_SHT(1,20)
E2_SHT20	CEM(2,6)	none	ELE_NLV_SHT(1,20)
E3_SHT20	CEM(1,9)CEM(2,3)	none	ELE_NLV_SHT(1,20)
E1_SH30	CEM(1,11)	none	ELE_NLV_SH(1,30)
E1_SHT22	CEM(1,11)	none	ELE_NLV_SHT(1,22)
E2_SHT22	CEM(2,6)	none	ELE_NLV_SHT(1,22)
E3_SHT22	CEM(1,9)CEM(2,3)	none	ELE_NLV_SHT(1,22)

L1 Triggers

CEM(1,10)	one EM trigger tower with $E_T > 10$ GeV
CEM(2,5)	two EM trigger towers with $E_T > 5$ GeV
CEM(1,15)	one EM trigger tower with $E_T > 15$ GeV
CEM(1,11)	one EM trigger tower with $E_T > 11$ GeV
CEM(2,6)	two EM trigger towers with $E_T > 6$ GeV
CEM(1,9)CEM(2,3)	one EM trigger tower with $E_T > 9$ GeV, another EM trigger tower with $E_T > 3$ GeV

L2 Triggers

EM(1,12)	one EM candidate with $E_T > 12$ GeV (not present for runs below 169524)

L3 Triggers

ELE_LOOSE_SH_T(1,20)	one electron with $\|\eta\| < 3.0$ and $E_T > 20$ GeV passing loose requirements including shower shape cuts
ELE_LOOSE(1,30)	one electron with $\|\eta\| < 3.0$ and $E_T > 30$ GeV passing loose requirements
ELE_NLV_SHT(1,20)	one electron with $\|\eta\| < 3.6$ and $E_T > 20$ GeV passing tight shower shape cuts
ELE_NLV_SH(1,30)	one electron with $\|\eta\| < 3.6$ and $E_T > 30$ GeV passing loose shower shape cuts

Table IV: Single EM triggers used to select events with electron candidates.

8.2.2 Data Quality

Data flagged as unusable [1] by data-quality experts are excluded from the analysis. CFT, calorimeter, and luminosity subsystems of the detector are required to be fully operational. Yet, despite this we discovered an excess of photon-like objects that was not consistent with our background expectations. We placed these events under scrutiny but did not observe any noticeable patterns in the distributions of the selection variables that would have allowed us to single out suspicious objects.

A general approach for the identification of problematic regions in the detector is a task which is anything but trivial. A lot of effort has been spent to assure the high quality of DØ data, yet certain instrumental effects, disguised as real physical objects, still pass quality safeguards. Photons, for example, as opposed to all other objects (except neutrino), identified primarily by their traces in the calorimeter, are the most vulnerable to such instrumental backgrounds. As a result, many analyses, and particularly the present one, that contain photon(s) in the final state acquire backgrounds that are difficult to model or estimate.

A certain class of instrumental effects, regardless of their nature, can be eliminated as long as they have the following properties:

- localized in the EM calorimeter
- persistent in time

---

[1] Corresponding quality flags in the framework: instlum>0, coherent_noise, empty_crate, ring_of_fire, noon_noise, badcalrun, badlbn, bad_earlyrun, useless_calrun.

- and/or contribution of the average amount of energy deposited in these regions substantially differs from the neighbors.

Here, we describe a search for regions of the EM Calorimeter whose occupancy or average energy *significantly* differs from the expected values.

Method

We start with the assumption that problematic regions of the calorimeter are localized in eta and phi coordinates[1] and are run-dependent. For our study we use a dataset that contains at least one EM object. For each EM object in the event we fill two three-dimensional histograms:

- `occupancy3d->Fill(phi[iem], eta[iem], run)`
- `energy3d->Fill(phi[iem], eta[iem], run, e[iem])`

where `iem` is an index of the EM particle in the event. Binning was chosen as follows:

- *phi* $\in [0, 2\pi]$, `nbins = 32`
- *eta* $\in [0 - 2.52.5]$, `nbins = 50`
- *run* $\in [152817, 220000]$, `nbins = 200`

Note that, in order to have average energy contributed by the cell `(iphi,ieta)`, every bin of `energy3d` histogram should be normalized by the total number of events contributing to the corresponding cell.

---

[1] As determined from the third layer of the EM Calorimeter.

Now we need to choose a discriminant. The simplest choice of such a discriminant would be a degree of deviation of a given cell with respect to its nearest neighbors, e.g. $S_i = 2 \cdot n_i/(n_{i-1} + n_{i+1})$. Unfortunately, such a choice, although seemingly robust, fails to describe the effect in the vicinity of the cell with very high/low occupancy.

A better choice is to consider the deviation of the occupancy in a given cell from the average taken in all *other* cells[1] divided by the covariance in these cells. Due to the eta dependence of occupancy, e.g. Fig. 69, we perform the comparison only with the cells in the same `ieta` bin. Thus, the significance of the $i^{th}(i = (iphi, ieta, irun))$ bin can be defined as:

$$S_i = \frac{n_i - \langle n_i \rangle_{\bar{i}}}{\sqrt{\langle n_i^2 \rangle_{\bar{i}} - \langle n_i \rangle_{\bar{i}}^2}} \tag{8.3}$$

with :

- n_i = `occupancy3d(or energy 3d)-> GetBinContent(iphi, ieta, irun)`
- $\langle n_i \rangle_{\bar{i}} = \frac{\sum_{j \neq i}^{nphi} n_j}{nphi-1}$
- $\langle n_i^2 \rangle_{\bar{i}} = \frac{\sum_{j \neq i}^{nphi} n_j^2}{nphi-1}$

Values obtained in Equation 8.3 are used to fill a three-dimensional significance histogram – a map with questionable regions. Each event is checked against entries of this map and objects that fall into region with large significance are removed.

---

[1]To emphasize – we exclude cell under consideration in the calculation of the average and the covariance.

Data Sample

For this study we use all the data collected by the DØ experiment during 2003-2006. This period fully contains the dataset used in this analysis. The EMinclusive skim is the most complete subset of DØ EM-data since it contains events with at least one electromagnetic object with $p_T > 12$ GeV/c. Also, exactly the same data quality flags are used as for the analysis.

Results

Fig. 69 illustrates the occupancy for a sample run range. We see that there are two regions in the calorimeter with abnormally high occupancies. The corresponding significance map, shown in Fig. 70 clearly picks up these two regions. This map is used in almost every analysis at DØ that involves photons.

This study led to the discovery of a previously overlooked hardware glitch in the calorimeter readout. It initiated the creation of a dedicated module which is run in the Control Room, thus allowing us to detect this problem in the real time. Very recently another problem of a similar nature has been spotted.

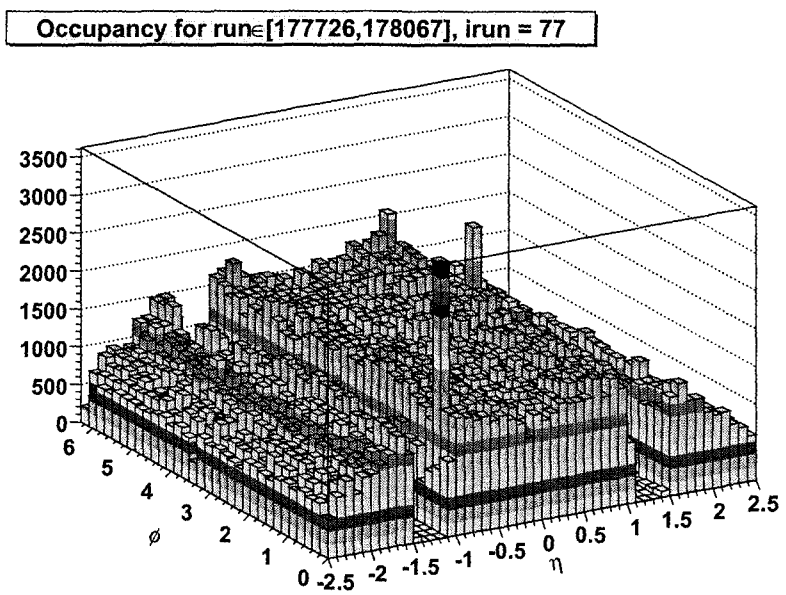

Fig. 69: Occupancy of EM calorimeter for run range [177726-178067]. This range is an example of the occurence of detector noise that was not flagged by the conventional quality safeguards.

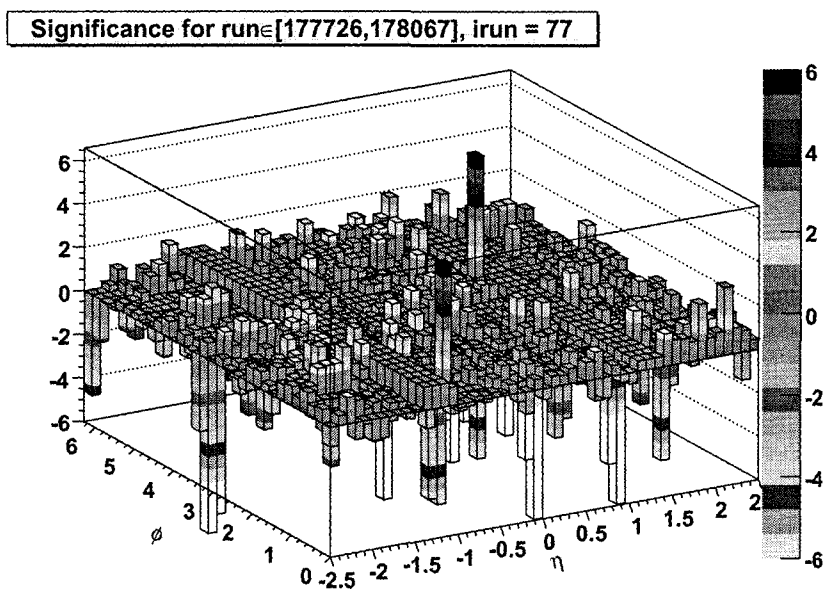

Fig. 70: Distribution of significance of the calorimeter noise for a sample run range [177726-178067] where there are two hot regions.

8.2.3 Kinematical Selection

Once the quality of the data has been assured we proceed with the event selection:

- $|z_{vtx}| < 60$ cm (if Primary Vertex is found),
- at least three photons with the following cuts:
  - $iso < 0.07$,
  - $emfr > 0.97$,
  - $IsoHC[0.05, 0.4] < 2.0$ GeV/c,
  - $sigphi < 14$ cm^2,
  - $prbtrk < 0.001$,
  - $|\eta| < 1.1$.
- p_T-ordered cuts: ${p_T}^1 > 30$ GeV/c, ${p_T}^2 > 20$ GeV/c, ${p_T}^3 > 15$ GeV/c.

The last bullet is motivated by the distribution of p_T-ordered momenta of photons in the signal MC (see Fig. 71). The background, obtained from a 3EM subskim clusters lower in p_T (see Fig. 72).

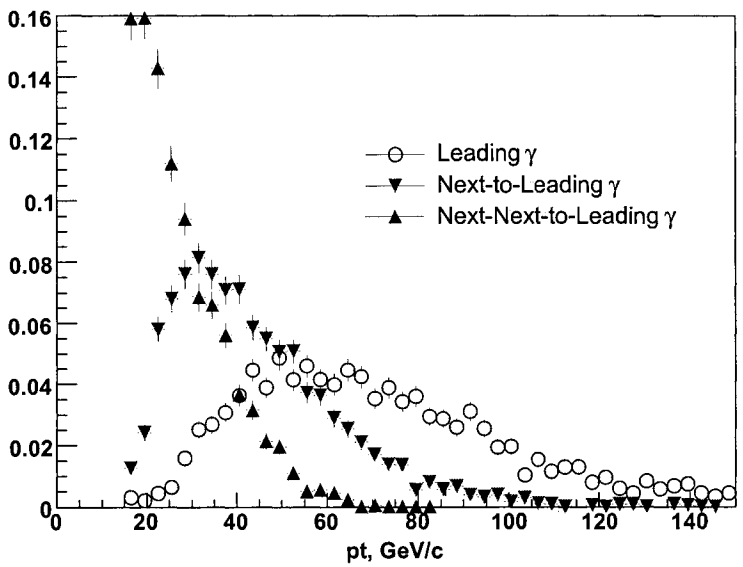

(a) $m_f = 30$ GeV/c^2, $H^{\pm} = 150$ GeV/c^2

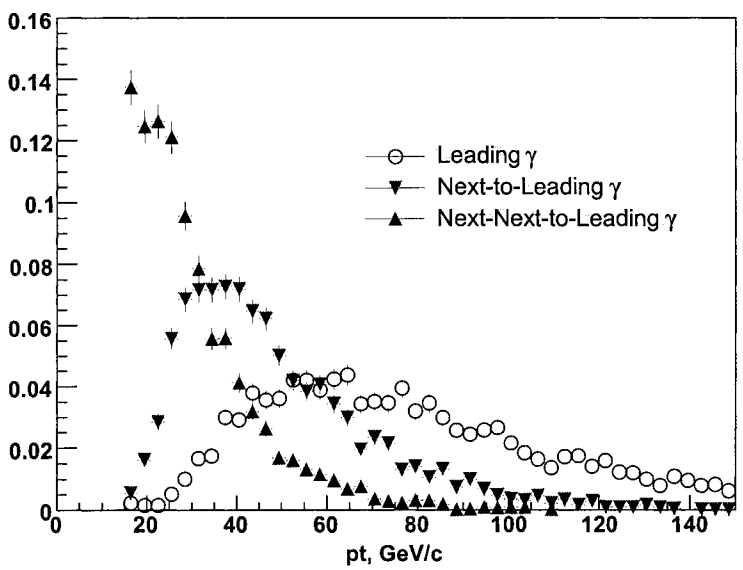

(b) $m_f = 50$ GeV/c^2, $H^{\pm} = 150$ GeV/c^2

Fig. 71: Spectrum of p_T-ordered signal photons for two higgs masses. Distributions are normalized to the total number of events.

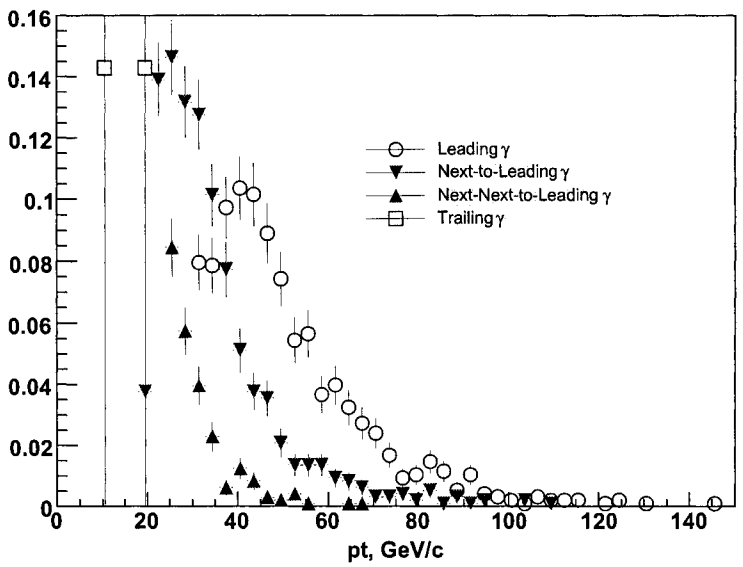

Fig. 72: p_T-ordered spectrum EM object in 3EM data sample. Distributions are normalized by the number of entries.

run	event	$\not\!\!E_T$	z_{vtx}	$m^{inv}_{\gamma^1,\gamma^2,\gamma^3}$	$m^{inv}_{\gamma^1,\gamma^2}$	$m^{inv}_{\gamma^1,\gamma^3}$	$m^{inv}_{\gamma^2,\gamma^3}$
210428	8543039	3.11	-7.94	94.9	66.7	65.5	16
202853	31140462	0.594	1.7	129	106	66.9	28.2
195238	12030738	10.7	-34	75.3	51.4	48.2	26.6
174646	8281777	11.9	4.63	293	236	165	54.2
168149	4004796	5.09	4.45	101	83.5	56.2	13.1

Table V: Observed $3\gamma + X$ events.

8.3 Observed Events

We observe 5 events with three photons. These events are listed in Table V and their Event Displays are given in App. A.

At this point we proceed with the evaluation various backgrounds that might be contributing to these final states. The main idea behind background estimation is that various contributions can be obtained from a better defined state provided the corresponding efficiency is know. An example is a 3γ contribution from $p\bar{p} \rightarrow WZ \rightarrow eee$ final state can be estimated by weighting observed number of $3e$ events with a probability of an electron to loose track cubed: $n^{3\gamma}_{WZ} = n^{eee}_{WZ} \cdot f^3_{e\rightarrow\gamma}$.

8.4 Backgrounds

Several Standard Model processes can result in the three-photon final state. We split them into three categories:

- EW – containing W or Z boson in association with photon(s),
- QCD – processes of the form $\{jjj\}$, $\{\gamma jj\}$, and $\{\gamma\gamma j\}$,
- Direct Tri-Photon (DTP) processes.

We derive all backgrounds from data. An exception is the DTP background for which we use MC to crosscheck the ISR rate.

8.4.1 EW

The first source of $3\gamma+X$ background events considered comes from the processes that have a real vector boson (W or/and Z) whose tracks were not reconstructed due to tracking inefficiency. These processes are:

- $Z+\gamma, Z+j$,
- $W+\gamma\gamma, W+\gamma j$, and $W+jj$
- $W+Z$

An estimate of the contribution from $Z\gamma$ is done from events with different number of electrons and photons – $\{e,e,\gamma\}$, $\{e,\gamma,\gamma,\}$, and $\{e,e,e,\}$. We observe 131 events with two reconstructed electrons and one photon. Fig. 73 illustrates the distribution of invariant mass of two electrons (m_{ee}) plotted vs three-body invariant mass ($m_{ee\gamma}$). Note that there is a significant fraction of events with three-body invariant

mass ($m_{ee\gamma}$) peaking around the Z mass. These events correspond to a process known as a Final State Radiation (FSR) – emission of a photon from an electron leg of the $q\bar{q} \to Z/\gamma^* \to ee$ diagram.

This process contributes events when both tracks are lost. Probability for an electron to lose a track was obtained above and thus for $Z\gamma$ contribution we have:

$$\begin{aligned} n_{Z\gamma}^{3\gamma} &= N_{Z\gamma} \cdot f_{e\to\gamma}^2 \\ &= 131 \cdot (0.014)^2 \\ &= 0.026 \text{ events} \end{aligned} \tag{8.4}$$

Identification of other EW backgrounds is a bit more involved since they don't have a resonant production on which to make a selection. We choose the following route – contribution of events with a W is estimated from $\{e\gamma\gamma\}$ events, having accounted for all other contributions to this final state.

We observe 7 events with two photons and one electron (Table VI). They can come from $Z\gamma$ processes with only one lost track:

$$\begin{aligned} n_{Z\gamma}^{e\gamma\gamma} &= N_{Z\gamma} \cdot 2 \cdot f_{e\to\gamma} \\ &= 131 \cdot 2 \cdot (0.014) \\ &= 3.7 \text{ events} \end{aligned} \tag{8.5}$$

Therefore, an upper estimate on the number of events with a W and two photons (real or fake) is $7 - 3.7 = 3.3$ events. Thus, their contribution will be even less and comparable to $n_{Z\gamma}^{3\gamma}$:

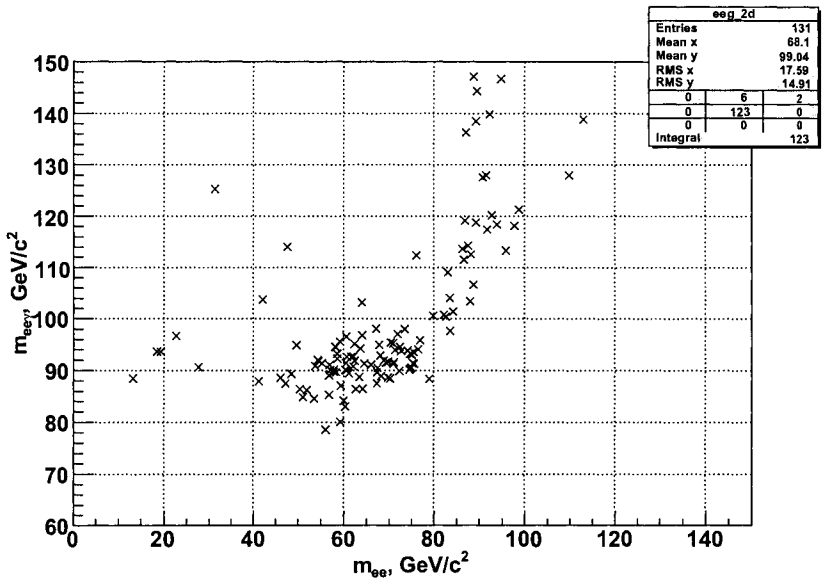

Fig. 73: Distribution of invariant mass of two electrons vs three-body invariant mass for $Z\gamma \to ee$ events in data. Note, that majority of events clusters around $m_{ee\gamma} \approx m_Z$. These events correspond to the ISR process.

run	event	$\not{E}_T$	z_{vtx}	$m^{inv}_{\gamma^1,\gamma^2,e}$	$m^{inv}_{\gamma^1,\gamma^2}$	$m^{inv}_{\gamma^1,e}$	$m^{inv}_{\gamma^2,e}$
188157	12627700	4.74	-29.5	99.1	30.3	78	53
206098	61236329	9.83	-40.2	121	15.1	94.7	73.4
202496	55167474	10.1	-12.8	142	108	88.1	28.3
187800	82968527	66.4	31.2	121	88.6	70.2	44.3
208803	31528660	2.16	-8.33	67	42.3	43.6	28.3
206430	31184398	4.55	-24	253	67.9	228	86
178853	31896103	9.33	0.605	72.6	11.3	53.6	47.6

Table VI: Observed $2\gamma + e + X$ events.

$$n^{3\gamma}_{W\gamma\gamma} = 3.3 \cdot 0.014 = 0.046 \text{ events.} \tag{8.6}$$

Similarly for the WZ contribution. We observe 10 events with three electrons (Table VII). Almost all of them can be attributed to $Z\gamma$ where a photon has undergone conversion ($f_{\gamma\to e} \approx 0.06$): $N^{3e}_{Z\gamma} = 131 \cdot 0.06/(1-0.06) \approx 8.4$ events. Thus, the contribution of WZ processes is $O(10^{-6})$ and ignored thereafter.

Therefore, the overall contribution from EW backgrounds to the 3γ sample is

$$n^{3\gamma}_{EW} = 0.072 \pm 0.036 \text{ events.} \tag{8.7}$$

8.4.2 QCD

By QCD background we mean contributions to the $3\gamma + X$ final state that come from direct (or fragmentation) photons and/or EM-like jets, denoted by j. If we know the signal and background efficiencies, i.e. probabilities of a photon and a jet to pass photon-id cuts ($\varepsilon_s \equiv \varepsilon_\gamma$ and $\varepsilon_b \equiv f_{j\to}$, respectively) we can estimate contributions from the four possible combinations of jets and photons: $\{j,j,j\}$, $\{j,j,\gamma\}$, $\{j,\gamma,\gamma\}$, and $\{\gamma,\gamma,\gamma\}$. The last component can, in principle, contain the higgs signal. Number of 3γ events that were produced in the collisions can be obtained by solving four linear equations:

$$\begin{pmatrix} n_{ppp} \\ n_{fpp} \\ n_{ffp} \\ n_{fff} \end{pmatrix} = \hat{\mathbf{E}} \times \begin{pmatrix} N_{sss} \\ N_{bss} \\ N_{bbs} \\ N_{bbb} \end{pmatrix} \tag{8.8}$$

where $\vec{n}$ the observed events (pass cuts is p, fail[1] cuts is f), and $\vec{N}$ denotes produced events with "s" for signal and "b" for background. The 4×4 matrix $\hat{\mathbf{E}}$ is defined as:

$$\hat{\mathbf{E}} = \begin{pmatrix} \varepsilon_s^3 & \varepsilon_s^2\varepsilon_b & \varepsilon_s\varepsilon_b^2 & \varepsilon_b^3 \\ 3(1-\varepsilon_s)\varepsilon_s^2 & \varepsilon_s^2(1-\varepsilon_b)+2(1-\varepsilon_s)\varepsilon_s\varepsilon_b & \varepsilon_b^2(1-\varepsilon_s)+2(1-\varepsilon_b)\varepsilon_b\varepsilon_s & 3(1-\varepsilon_b)\varepsilon_b^2 \\ 3(1-\varepsilon_s)^2\varepsilon_s & \varepsilon_b(1-\varepsilon_s)^2+2(1-\varepsilon_s)(1-\varepsilon_b)\varepsilon_s & \varepsilon_s(1-\varepsilon_b)^2+2(1-\varepsilon_b)(1-\varepsilon_s)\varepsilon_b & 3(1-\varepsilon_b)^2\varepsilon_b \\ (1-\varepsilon_s)^3 & (1-\varepsilon_s)^2(1-\varepsilon_b) & (1-\varepsilon_s)(1-\varepsilon_b)^2 & (1-\varepsilon_b)^3 \end{pmatrix} \tag{8.9}$$

For simplicity we do not take into account p_T-dependence of the efficiencies and instead use their values at 25 GeV/c, which approximately corresponds to the p_T average in the event sample. Thus, using Data/MC scaling we obtain for the probability in Data that a photon will be selected as a photon:

---

[1]In order to remove electrons from W's and Z's we left the track veto cut on f and recomputed efficiencies.

$$\begin{aligned} \varepsilon_{\gamma}^{Data} &= \kappa \cdot \varepsilon_{\gamma}^{MC} \\ &= (0.93 \pm 0.04) \cdot (0.81 \pm 0.03) \\ &= 0.75 \pm 0.05 \end{aligned} \tag{8.10}$$

and for an EM-jet to be selected as a photon:

$$\varepsilon_{j}^{Data} = 0.043 \pm 0.004 \tag{8.11}$$

Thus, substituting numerical values of efficiencies from Equation 8.11 and Equation 8.10 in Equation 8.9 we obtain:

$$\hat{\mathbf{E}} = \begin{pmatrix} 0.422 & 0.0236 & 0.00132 & 0.000074 \\ 0.422 & 0.555 & 0.0608 & 0.00507 \\ 0.141 & 0.362 & 0.708 & 0.116 \\ 0.0156 & 0.0599 & 0.229 & 0.879 \end{pmatrix} \tag{8.12}$$

with the determinant equal to 0.13.

The following numbers of events are observed:

$$\begin{pmatrix} n_{ppp} \\ n_{fpp} \\ n_{ffp} \\ n_{fff} \end{pmatrix} = \begin{pmatrix} 5 \\ 27 \\ 160 \\ 246 \end{pmatrix} \tag{8.13}$$

and therefore the solution of Equation 8.8 gives us the number of events that were produced in the collisions:

$$\begin{pmatrix} N_{sss} \\ N_{bss} \\ N_{bbs} \\ N_{bbb} \end{pmatrix} = \begin{pmatrix} 10.1 \\ 19.5 \\ 176 \\ 232 \end{pmatrix} \tag{8.14}$$

Thus, the QCD contribution from $\{j,j,j\}$, $\{j,j,\gamma\}$, and $\{j,\gamma,\gamma\}$ processes, is estimated to be

$$n_{QCD}^{3\gamma} = 0.71 \pm 0.15 \text{ events.} \tag{8.15}$$

Number of events with three real photons from DTP cannot be obtained from the solution of this equation since it, in principle, contains other processes that enter those 5 observed events. In order to

determine them we need to first remove other backgrounds and verify that the QCD contribution would not change.

We assumed that the fake rate has a constant value taken at the averge of the distribution of p_T of all EM loose objects in the original 3EM sample. To assess variation due to possibility that most background events would favor to cluster at lower p_T we raise the fake rate (Equation 8.11) from 0.042 to 0.070, which brings expected QCD events up to 0.94 events.

8.4.3 Instrumental Backgrounds

Besides QCD and EW backgrounds studied above there are other potential sources of 3γ final state:

- three hot towers,
- high occupancy in the tracker, that can severely affect tracking,
- "ghost" SMT event – hits that belong to previous collision,
- wrong primary vertex.

Hot towers that are lit most of the time during the run have been removed in our study. However those hot towers whose appearence is sporadic are almost indistinguishable from photons. Luckily one class of hot towers that makes it through all defense barriers is given away by ADC information in the first layers. Such information is not available in the CAF trees but can be obtained from the thumbnails. We examined individual events in final samples with low statistics – $\{e,e,e\}$, $\{e,\gamma,\gamma\}$, and $\{\gamma,\gamma\gamma\}$, and did not find any bad towers.

High occupancy in the tracker would lead to a failure to properly reconstruct tracks. For each interesting event we extract hit and track occupancies, then we compare the track reconstruction efficiency

in $Z \rightarrow ee$ events with similar occupancies. Corresponding events do not have abnormally high occupancies.

It was discovered that a certain number of events contains SMT hits that belong to a previous collision. Such behavior is not correlated with the run number and goes away after DAQ shifter issues SCLinit. These events can be identified by SMT experts. We checked our events on this matter and did not find any signs of this abnormality.

In cases when an event contains two or more deep inelastic collisions track isolation suffers from a wrongly identified primary vertex leading to clean photons while in reality they might be EW or QCD background. One can partially secure himself from such events by CPS-EM pointing by using the spacial distribution of EM cluster to point at the (x,y,z) origin and then estimate the z of the collision. We check whether events have at least one CPS-matched EM cluster that points within ± 2 cm of the primary vertex. We do observe that the pointed vertex is within its resolution from the primary vertex. However, this does not eliminate events where objects came from different vertices – it would require each object to have a matched CPS cluster, which, in its turn, would introduce an additional hit in acceptance – an unacceptable factor of $\approx (0.8)^3 = 0.5$.

8.4.4 Direct 3γ (DTP)

The above study indicates that around 80% of our tri-photon events come from real-photon events. They might be an irreducible DTP background or ... a long sought-after signal.

We approach the estimation of DTP background in the following way. We scale the number of di-photon events observed in data with a rate at which one would expect to observe a third photon in Direct-Diphoton-Production (DDP) processes provided by Pythia[1]:

$$N^{3\gamma}_{DTP} = \frac{N_{\gamma\gamma\gamma}(MC)}{N\gamma\gamma(MC)} \cdot N^{\gamma\gamma}(Data) \otimes \rho \tag{8.16}$$

This task is not trivial and deserves a separate full-fledged paper. However, a certain fraction of DDP calculations overlaps with the present study, thus allowing us to carry on with this background.

One of the major difficulties in the calculation of DDP cross section is to separate di-photon signal from fake QCD backgrounds. The quantity of interest is ρ, purity, – the fraction of di-photon events in the sample that consists of $\{\gamma,\gamma\}$, $\{\gamma, j\}$, and $\{j, j\}$ processes.

Similarly to the above we employ an efficiency matrix approach. This time, however, we compose a 3×3 efficiency matrix and relate contributions from $\{\gamma,\gamma\}$, $\{\gamma, j\}$, and $\{j, j\}$ processes to the $n_{i,j}$ numbers of observed two-body events. Here, indices i and j can be p or f, and as before, $p(f)$ indicates – "passed(failed) photon-id cuts":

---

[1]This effectively chooses to consider ISR photons. ISR contribution is expected to be large (if not the largest). Thus, this assumption provides a conservative estimate of the background.

$$\begin{pmatrix} n_{pp} \\ n_{fp} \\ n_{ff} \end{pmatrix} = \hat{\mathbf{E}} \times \begin{pmatrix} N_{ss} \\ N_{bs} \\ N_{bb} \end{pmatrix} \tag{8.17}$$

with the efficiency matrix

$$\hat{\mathbf{E}} = \begin{pmatrix} \varepsilon_s^2 & \varepsilon_s\varepsilon_b & \varepsilon_b^2 \\ 2(1-\varepsilon_s)\varepsilon_s & \varepsilon_s(1-\varepsilon_b)+(1-\varepsilon_s)\varepsilon_b & 2(1-\varepsilon_b)\varepsilon_b \\ (1-\varepsilon_s)^2 & (1-\varepsilon_s)(1-\varepsilon_b) & (1-\varepsilon_b)^2 \end{pmatrix} \tag{8.18}$$

Fig. 74 illustrates distributions of invariant mass of $\{\gamma,\gamma\}$, $\{\gamma,j\}$, $\{j,j\}$, $\{e,e\}$, $\{\gamma,j\}$, and $\{e,\gamma\}$ pairs. Thus, we write down the observed number of events that pass/fail photon-id cuts:

$$\begin{pmatrix} n_{pp} \\ n_{pf} \\ n_{ff} \end{pmatrix} = \begin{pmatrix} 3.5 \cdot 10^3 \\ 37.3 \cdot 10^3 \\ 108.1 \cdot 10^3 \end{pmatrix} \tag{8.19}$$

Before we proceed with solving Equation 8.17, we make an estimate of the contribution of events that contain real electrons, since they, in principle, can contribute to the events in Equation 8.19.

One of the most abundant sources of real electrons are W bosons. When a W is produced in association with a jet or a photon it contributes events to the $\{\gamma,\gamma\}$ or $\{\gamma,j\}$ configurations when its electron loses its track. With fraction of momentum carried away by a neutrino, full identification of W is impossible. Hence, we reverse the problem and first estimate the QCD background to the $\{e,j\}$ final state where a jet faked an electron. This can be done with the assumption that the $\{j,j\}$ sample fully consists of real jets. The probability of a jet to fake an electron has been computed before:

$$f_{j\to e} = 0.010 \pm 0.005 \tag{8.20}$$

and therefore, the QCD contribution to $\{e,j\}$ final state is as follows:

$$\begin{aligned} n_{QCD}^{ej} &= 2 \cdot f_{j\to e} \cdot n_{jj} \\ &= 2.2 \cdot 10^3 \end{aligned} \tag{8.21}$$

This number should be subtracted from the total number of number of $\{e,j\}$ events: $6.7 \cdot 10^3 = 9.5 \cdot 10^3 - 2.8 \cdot 10^3$ (see Fig. 74), where the number of $Z \to ee$ with one poorly reconstructed electron has been subtracted.

There is another source of $\{e,j\}$ events, they are $\{\gamma,j\}$ events where a photon underwent conversion and has been reconstructed as an electron. In order to estimate the contribution of such events recall that the corresponding rate is

$$f_{\gamma \to e} = 0.07 \pm 0.04 \tag{8.22}$$

Here the large size of the uncertainty reflects the distribution of unaccounted material in the detector and has been deliberately overestimated.

With the conversion rate and the number of $\{\gamma, j\}$ events we can estimate its contribution to $\{e, j\}$:

$$\begin{aligned} n^{ej}_{\gamma j} &= f_{\gamma \to e} \cdot n_{\gamma e} \\ &= 0.07 \cdot 37.3 \cdot 10^3 \\ &= 2.6 \cdot 10^3 \end{aligned} \tag{8.23}$$

The rest of $\{e, j\}$ events is attributed to $W + j$:

$$n^{ej}_{W+j} = 4.1 \cdot 10^3 \tag{8.24}$$

And consequently its contribution to $\{\gamma, j\}$ is estimated to be negligible:

$$\begin{aligned} n^{\gamma j}_{W+j} = f_{e \to j} \cdot n^{ej}_{Wj} = \quad & 0.02 \cdot 4.1 \cdot 10^3 \\ = 82 & \end{aligned} \tag{8.25}$$

The contribution of $W+X$ to $\{\gamma,\gamma\}$ is also expected to be negligible in comparison with the total di-photon count. Similarly the contribution of the Z boson can also be neglected (see corresponding histogram in Fig. 74 for the visual crosscheck).

Thus, we can proceed to Equation 8.17. The solution is then

$$\begin{pmatrix} N_{ss} \\ N_{bs} \\ N_{bb} \end{pmatrix} = \begin{pmatrix} 3.7 \cdot 10^3 \\ 37.4 \cdot 10^3 \\ 107.8 \cdot 10^3 \end{pmatrix} \tag{8.26}$$

with the individual contributions

$$n^{2\gamma}_{\gamma+j} = 0.2 \cdot 10^3, \tag{8.27}$$

$$n^{2\gamma}_{j+j} = 1.2 \cdot 10^3, \tag{8.28}$$

$$n^{2\gamma}_{DDP} = 2.1 \cdot 10^3. \tag{8.29}$$

And thus the relevant fractions for the purity are

$$\begin{aligned} \rho &= \frac{n^{2\gamma}_{DDP}}{n^{2\gamma}_{DDP} + n^{2\gamma}_{QCD}} \\ &= 0.61 \pm 0.12 \end{aligned} \tag{8.30}$$

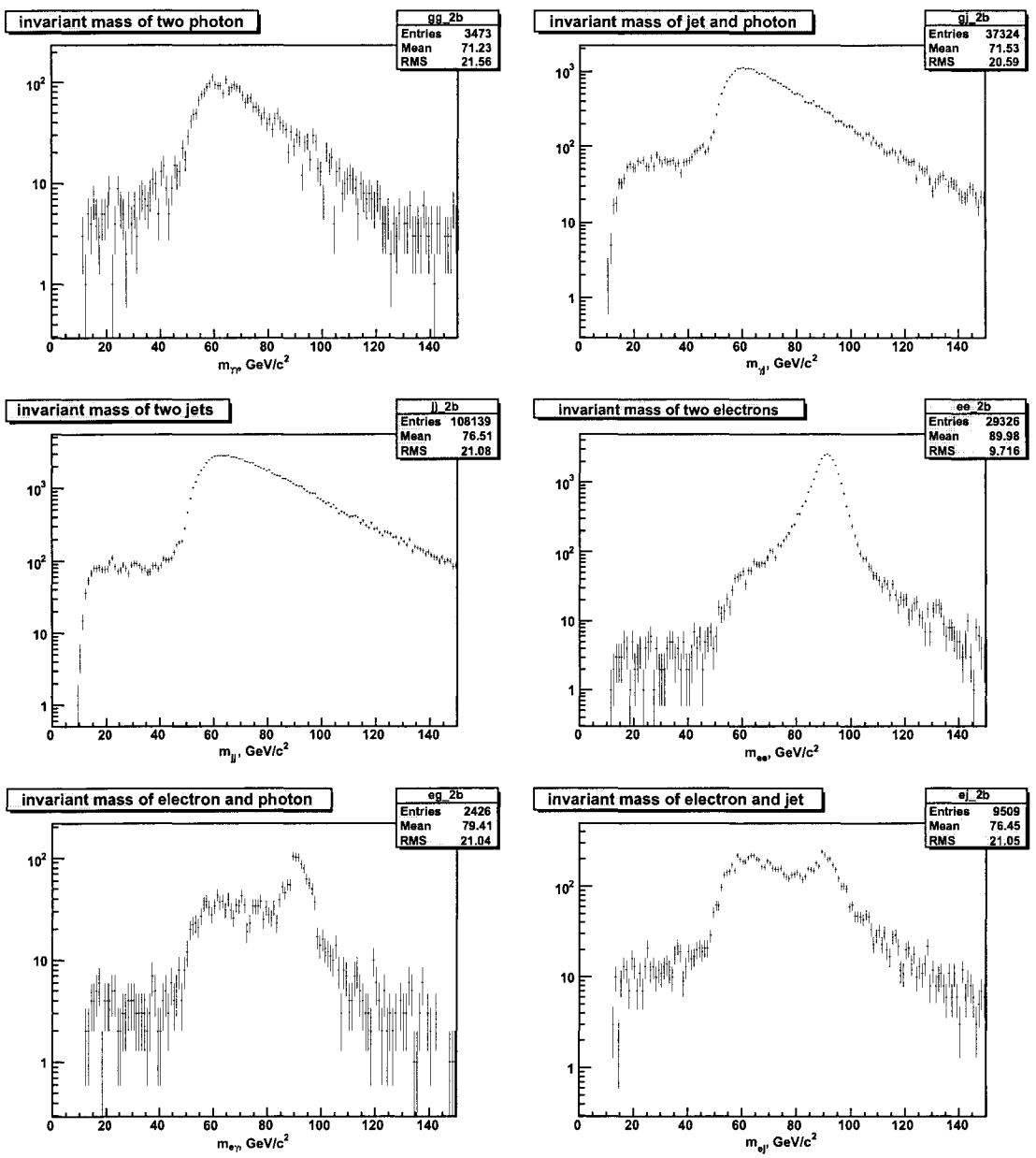

Fig. 74: Distributions of invariant mass of $\{\gamma,\gamma\}$, $\{\gamma,j\}$, $\{j,j\}$, $\{e,e\}$, $\{\gamma,j\}$, and $\{e,\gamma\}$ pairs. Entries are used for the calculation of the DTP contribution.

$$\frac{n_{\gamma+j}^{2\gamma}}{n_{j+j}^{2\gamma}} = 0.16 \pm 0.03 \tag{8.31}$$

where the systematic uncertainty has been estimated to be 20%. Note, that the results in Equation 8.30 and Equation 8.31 are in rather good agreement with previous DDP studies [72].

Now, we can proceed with the estimation of DTP. As stated above, we assume that the third photon comes from the ISR. Data permits us to study this process through $Z+\gamma$ final state. As opposed to the FSR where the three-body mass is clustered around the Z-peak, ISR process has the di-electron invariant mass around the Z. Fig. 75 illustrates the distribution of m_{ee} in $Z+\gamma$ events for which events in the $|m_{ee\gamma} - 92.4| < 10$ GeV/c^2 window have been removed. There are 28 events whose di-electron invariant mass is within the 10 GeV/c^2 window around Z. The corresponding ISR rate is

$$\begin{aligned} \frac{n_{Z+\gamma}^{ISR}}{n_Z^{total}} &= \frac{28}{2.7 \cdot 10^3} \\ &= (1.0 \pm 0.2) \cdot 10^{-3} \end{aligned} \tag{8.32}$$

Independently, we obtain a similar rate from the di-photon MC. We have generated $5.1 \cdot 10^4$ DDP events with Pythia event generator and reconstructed them with the full-chain DØ simulation software. Having selected events with two central EM clusters with ${p_T}^1 > 30$ GeV/c and ${p_T}^2 > 20$ GeV/c and $|z_{vtx}| < 60$cm we are left with $5.6 \cdot 10^3$ events. We did not apply any additional quality cuts on two

run	event	$\not\!\!E_T$	z_{vtx}	$m^{inv}_{e^1,e^2,e^3}$	$m^{inv}_{e^1,e^2}$	$m^{inv}_{e^1,3}$	$m^{inv}_{e^2,e^3}$
193803	79898361	4.34	10.3	90.6	60.2	64.8	19.6
208909	21464961	17.1	-50	90.7	41.5	62.2	51.3
190057	13016387	6.08	5.69	167	146	75	29.2
167886	24252142	10.8	4.48	195	159	92	67.5
202950	8230763	12.2	10	82.6	61.9	48.3	25.8
204682	33801453	2.97	15.9	86.5	66.9	54	9.33
203407	50912462	6.41	-9.76	143	106	95.6	16.8
168992	3522948	2.25	-0.522	87.5	63.7	52.5	29.2
205281	17365200	19.7	17.9	102	78.3	39.8	52.4
192295	64599759	5.33	6.85	97.8	72.1	53.7	38.7

Table VII: Observed $3e+X$ events.

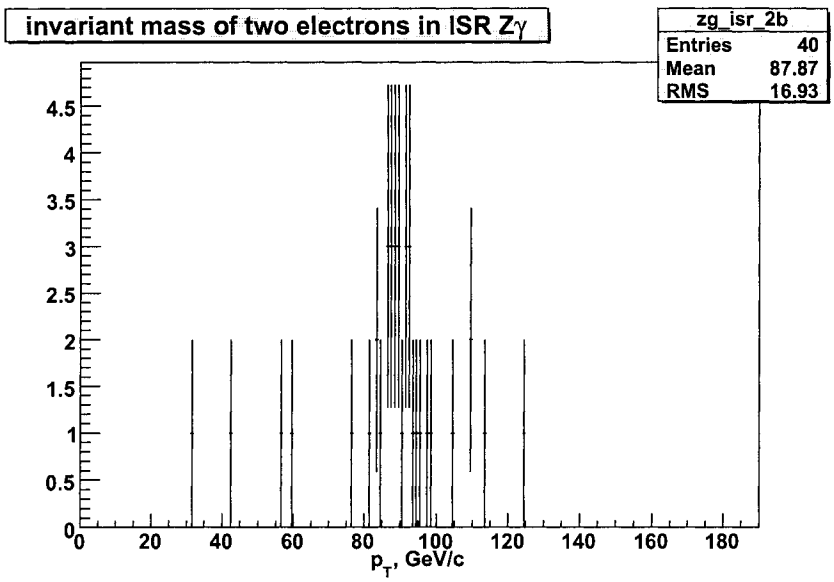

Fig. 75: Distributions of di-electron invariant mass in $Z+\gamma$ events for which FSR has been removed by the $|m_{ee\gamma} - 92.4| < 10$ GeV/c^2 cut.

leading photons, otherwise we would run out of statistics. Although, we do apply standard photon selection on the third photon. At the end we are left with 7 tri-photon events. The corresponding ratio is

$$\begin{aligned} \frac{n_{DTP}^{3\gamma}}{n_{DDP}^{total}} &= \frac{7}{5.6 \cdot 10^3} \\ &= (1.3 \pm 0.4) \cdot 10^{-3} \end{aligned} \tag{8.33}$$

Hence, combining the number of the DDP events (Equation 8.29) with the ISR rate (Equation 8.33) we obtain the DTP contribution

$$n_{DTP}^{3\gamma} = 2.73 \pm 0.55 \text{ events.} \tag{8.34}$$

Thus the total background to $3\gamma + X$ final state is estimated from the sum of $n_{DTP}^{3\gamma} = 2.73 \pm 0.55$ and $n_{QCD}^{3\gamma} = 0.71 \pm 0.15$ to be

$$n_{SM}^{3\gamma+X} = 3.5 \pm 0.6 \text{ events.} \tag{8.35}$$

Fig. 78 demonstrates the distribution of di-photon invariant mass in data and from expected backgrounds. Note that each event contributes three entries (three possible photon-photon combinations), e.g. for data there are 15 entries, although we observe 5 events. The overall agreement is rather good and we can see that the data follow the shape of the background. Yet, there is an excess of ≈ 1.5 events as well as one event with very large invariant mass in the region where the background is virtually zero.

In the next section we devise another quantity found to be a very powerful discriminant for separation of the signal from background.

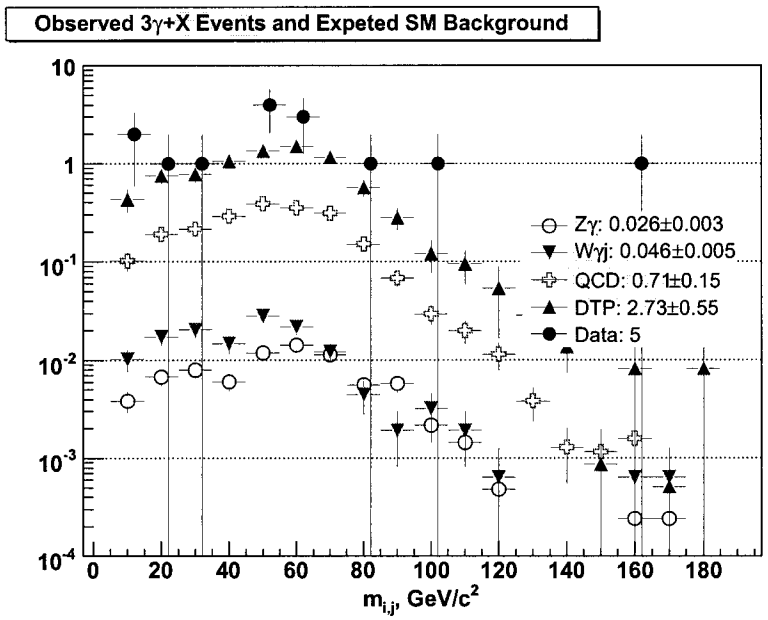

Fig. 76: Distribution of two-body invariant mass for $3\gamma+X$ events observed in data and expected SM background. Note that each event contributed three entries – $m_{1,2}$, $m_{1,3}$, and $m_{2,3}$.

8.5 Further Background Suppression

Let us recall that the underlying signal event has four photons and two jets or a lepton from a W. Each object is quite energetic carrying on average 10-20 GeV/c in the transverse direction. Thus a

system of only three photons would be very unbalanced in p_T, with the recoil particle(s) carrying away the rest of the collision energy. Background events, on the other hand are expected to be quite balanced in p_T. The boost, or total transfer momentum, of 3-body system can be written as

$$H_T \equiv \sqrt{\left(\sum_{i=1}^{3} p_x^i\right)^2 + \left(\sum_{i=1}^{3} p_y^i\right)^2}. \tag{8.36}$$

where the sum goes over objects that pass id and geometrical requirements, which implies that any 4-particle event with one of the particles failing selection cuts will have H_T that reflects p_T boost of 3-body system. Quantitatively the rate of the imbalanced events is proportional to the content of 4-jet events in 3-jet sample which is proportional to $\alpha_s \approx 0.2$. However we are interested in the 4-jet fraction that is observed in experiment. Recent DØ results [73] indicate that

$$\frac{\sigma^{\text{obs}}(p\bar{p} \to 4j)}{\sigma^{\text{obs}}(p\bar{p} \to 3j)} = 6^{+1.6}_{-1.4} \cdot 10^{-3} \tag{8.37}$$

This number will be higher due to lower momenta thresholds we use in our analysis and allowing jet to be fail either of the cuts, However, the order of magnitude estimation gives this fraction $O(10^{-2})$.

Fig. 8.5(a) illustrates distribution of boost of three photons in the signal MC. We can see that 25 GeV/c cut has very high efficiency of $\approx 90\%$. For the background, on the other hand, shown in 8.5, this will cut $\approx 85\%$ of the events.

Thus, we choose to cut on $H_T = 25$ GeV/c. Efficiencies for this cut are

$$\varepsilon^{\text{signal}}_{H_T>25} = 0.92 \pm 0.01 \tag{8.38}$$

$$\varepsilon^{\text{bkg}}_{H_T>25} = 0.15 \pm 0.01 \tag{8.39}$$

After this cut the expected background becomes

$$n^{3\gamma+X}_{SM} = 0.5 \pm 0.2 \text{ events.} \tag{8.40}$$

The number of data events that pass this same cut is zero.

8.6 A Glance Forward

Continuing our *"no stone left unturned"* approach we turn our attention to the topologies where one of the photons is allowed to be in the forward region. We observe 8 events with some of their properties listed in Table VIII. Some of these events are beautiful and clean events, and note that only two events survive H_T cut and contribute to the masses around 60 GeV/c^2 and, in principle, can be a part of the signal. In this work we do not proceed with background estimation for such configurations.

It is interesting to point out one event. This is event, number 4406285 in run 206504, is peculiar because of its extremely large invariant mass ≈ 0.43 TeV. This event is perfectly balanced, both in overall energy deposited in the calorimeter and in the the boost of the 3γ system. The background rate at this part of the spectrum is exceedingly small. In the future we will subject this event to scrutiny on the subject of instrumental effects and cosmic muons and repeat this search with more statistics.

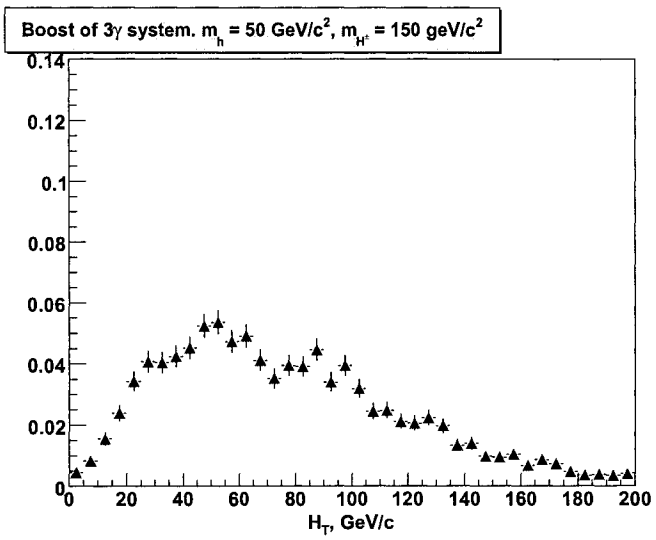

(a)

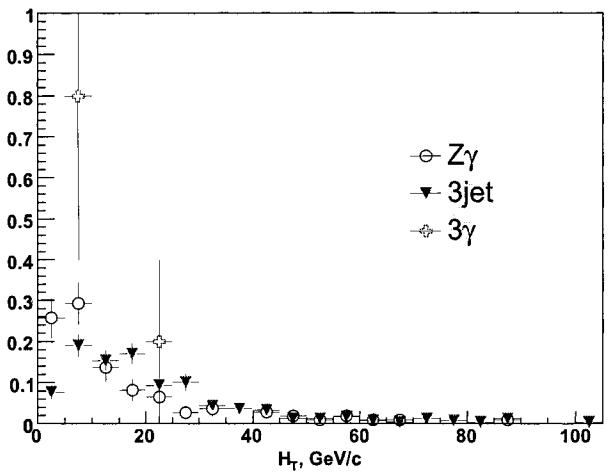

(b)

Fig. 77: Distribution of boost of 3γ system for the signal MC (a) and distribution of the boost of 3-body system for typical backgrounds – $3j$, $Z\gamma$ (b), and for the observed events. Entries are normalized to one. A cut $H_T > 25$ GeV/c is found to be 90% efficient for the signal while reducing the background almost 7-fold(15%).

8.7 Overall Signal Acceptance

In order to proceed toward a conclusive statement about our observation we need to know the signal the fraction of events that survives selection criteria – an acceptance. For this purpose we turn to the signal MC sample.We define acceptance, A^{MC}, as a ratio of number of events that pass selection requirements[1] to the total number of generated evens:

$$A^{MC} = \frac{N_{pass}}{N_{total}} \tag{8.41}$$

In our analysis we consider only a scenario with a fixed value of the mass of $H^{\pm}$ (150 GeV/c^2). Table IX illustrates overall acceptance before the H_T cut. Its value depends of position in the table – horizontal row corresponds to the number of photons in the event in the End Cap Calorimeter (EC) and the column – number of photons in the Central Calorimeter (CC). For example, we are interested in topologies with up to three photons in CC, and thus we have to add all combinations that lead to 3γ configuration: $0.18 + 0.04 + 0.2$. After application of the cut on transverse boost of the system we get final per event MC acceptance

$$A^{MC} = 0.19 \pm 0.03 \tag{8.42}$$

---

[1] In the acceptance we incorporate efficiencies of photon-id, p_T-ordered cut, primary vertex cut, and H_T cut. Trigger efficiency and Data/MC scaling factors applied separately.

Acceptance is flat over a large range of m_h (30-100 GeV/c^2) rising slowly at higher values and dropping at low masses (<20 GeV/c^2) due to a very small opening angle between photons. We incorporate this effect into the uncertainty that reflects a 13% rise of the geometrical acceptance over the range of masses of interest. Addition of 2+1 configuration would increase the acceptance by 0.05%

$$A^{MC}(2_{CC}+1_{EC}) = 0.24 \pm 0.04. \tag{8.43}$$

Overall signal acceptance can be written as

$$A = \kappa \cdot \varepsilon_{trig} \cdot A^{MC} \tag{8.44}$$

with κ being the average Data/MC scaling factor

$$\kappa = \frac{\sum_i^{N^{MC}} \kappa(p_{T1}) 1 \cdot \kappa(p_{T2}) \cdot \kappa(p_{T3})}{N^{MC}} \tag{8.45}$$

where $\kappa(p_T)$ is a product of scaling factors for preselection (Fig. 58) and core efficiencies (Fig. 60) weighted by the $\{p_{T1}, p_{T2}, p_{T3}\}$ distribution of the signal MC. It is equal to

run	event	$\not\!\!E_T$	z_{vtx}	H_T	$m^{inv}_{\gamma^1,\gamma^2,\gamma^3}$	$m^{inv}_{\gamma^1,\gamma^2}$	$m^{inv}_{\gamma^1,\gamma^3}$	$m^{inv}_{\gamma^2,\gamma^3}$
206504	4406285	3.71	7.15	16.7	425	208	352	115
189667	30724433	0.875	-48.6	7.44	109	56.9	82.1	43.5
208733	32043806	7.71	-9.74	9.74	194	74.8	105	146
203410	84821974	21.6	-0.0784	9.84	103	82.1	35.6	51.8
189368	79717130	29.3	-14.7	136	279	255	92.9	65.8
209226	47829010	21.9	4.3	14.8	99.9	68.5	51.2	51.7
192781	24371933	7.54	-11	5.13	135	74.8	57.5	96.9
195054	27312492	23.3	10.2	68.2	257	230	56.4	101

Table VIII: Observed $3\gamma + X$ events with one forward photon. Corresponding event displays can be found in Appendix D.

EC\CC	0	1	2	3	4
4	0.00	–	–	–	–
3	0.00	0.00	–	–	–
2	0.01	0.01	0.01	–	–
1	0.04	0.08	0.06	0.02	–
0	0.06	0.21	0.30	0.18	0.04

Table IX: Signal acceptance vs occupancy of the event in central (CC) and forward (EC) regions of the calorimeter for a benchmark point $m_h = 50$ GeV/c^2, $m_{H^\pm} = 150$ GeV/c^2.

$$\kappa = 0.86 \pm 0.06 \tag{8.46}$$

Thus, for the overall signal acceptance we have

$$A = 0.16 \pm 0.03 \tag{8.47}$$

We ignored correlation effects between systematic uncertainties, e.g. when two photons are in the same p_T bin then the individual uncertainties should be treated as correlated. We estimated the magnitude of the effect by changing p_T binning which was found to be small in comparison with the overall uncertainty.

At this point we are ready to make a conclusion about out observations.

8.8 Limit Setting

Nearly all searches sooner or later come to a question of inference. Inference, or equivalently, testing of a consistency of prior experience or a validity of a new reasoning in view of observed data is a non-trivial and often there is some degree of ambiguity. As a result there exist several approaches.

In searches for physics beyond the standard model, like the present study, establishing proper statistical procedures is paramount and should be used consistently by the whole field. About a decade ago the Particle Data Group (PDG) attempted to clarify the situation and came up with the "PDG Prescription" on setting limits in astro-particle experiments. Over the years this prescription evolved, and

currently several methods are discussed by the PDG as the most robust: the Bayesian method [74] and two variations of the Frequentist method based on the ratio of likelihoods – the Feldman-Cousins and CL_s [75] methods. Each of the methods has its own advantages and drawbacks. Fortunately, despite different philosophy and sometimes different definition of confidence intervals, these methods agree in the regime where the observed number of events agrees well with the background. However, in the case of significant downward background fluctuations that might lead to the exclusion of the background only hypothesis, serious differences arise.

The CL_s approach adopted by DØ is free from this problem. We employ this method to calculate a confidence level for this Higgs search. Since the expected signal and background are small enough to require the use of the Poisson statistics, this method perfectly fits this analysis. The confidence levels are computed by comparing the observed data configuration to the signal expectations for two hypotheses: the background hypothesis where only the Standard Model background processes contribute to the accepted event rate and the signal+background hypothesis where the Higgs signal adds to the background. The likelihood ratio of the Poisson probabilities of the two hypothesis is then defined as

$$Q = \frac{P_{Poisson}(data \mid signal + background)}{P_{Poisson}(data \mid background)} \tag{8.48}$$

To test the consistency of the data with the signal+background hypothesis, the confidence level is defined as CL_s

$$1 - CL_{s+b} = P(Q \leq Q_{obs} \mid signal + background) \tag{8.49}$$

i.e. the fraction of experiments in a large ensemble of signal+background experiments which would produce results less signal-like than the observed data. By definition a signal+background hypothesis is excluded at 95% confidence level if $CL_{s+b} < 0.05$.

The calculated limit depends on the signal and background detection efficiency, the integrated luminosity and the number of candidates selected from the data events. The effects of the systematic uncertainties of the signal and background as well as the uncertainty of the integrated luminosity are incorporated. Although we ignore correlation between some of the uncertainties, e.g. acceptance contains that same Data/MC scaling as the one used for the luminosity calculations. Table X summarizes all ingredients necessary for limit setting. The number of signal, i.e. higgs, events expected in this data set with 0.83 fb $^{-1}$ of luminosity is

$$N_{sig} = A \cdot \sigma_{higgs} \cdot L \tag{8.50}$$

In the limit of zero background events, the Poisson probability to get zero data events N_{sig} are expected is 5%

$$P(0|N_{sig}) = 0.05 \tag{8.51}$$

or

$$\frac{(A \cdot \sigma_{higgs} \cdot L)^0 \cdot \exp -A \cdot \sigma_{higgs} \cdot L}{0!} = 0.05 \tag{8.52}$$

yields

$$A \cdot \sigma_{higgs} \cdot L \approx 3 events \tag{8.53}$$

or

$$\sigma_{higgs} \approx 24 \text{ fb} \tag{8.54}$$

The official software implementation of the the upper limit seeting for cross section from Equation 8.49 is officially available [76] and has been used to obtain the following result on the maximum possible higgs production cross section allowed by this experiment at the 95% confidence level:

$$\sigma_{CL_s}^{95\%} = 25.3 fb. \tag{8.55}$$

As we can see it agrees well with back-of-envelope results in Equation 8.54.

Although an inclusion of 2CC+1EC configuration would bring this limit down to 14 fb we leave it to the next iteration of the analysis. This limit is already cutting deep into the region of 2HDM and HTM that has not been previously excluded. Fig. 78 demonstrates the production cross section for several benchmark points overlaid with the obtained upper limit. A region to the left of the mass at which the exclusion curve intersects the theoretical production cross section corresponds to the excluded region. The benchmark exclusion is as follows:

- $m_{CL_s}^{95\%} = 66$ GeV/c^2 for $m_{H^\pm} \leq 100$ GeV/c^2, $\tan\beta = 3$
- $m_{CL_s}^{95\%} = 44$ GeV/c^2 for $m_{H^\pm} \leq 150$ GeV/c^2, $\tan\beta = 3$
- $m_{CL_s}^{95\%} = 80$ GeV/c^2 for $m_{H^\pm} \leq 100$ GeV/c^2, $\tan\beta = 30$
- $m_{CL_s}^{95\%} = 50$ GeV/c^2 for $m_{H^\pm} \leq 150$ GeV/c^2, $\tan\beta = 30$

Fig. 78 represents the first exclusion results of the fermiophobic Higgs boson in a class of Two Higgs Doublets and Triplet Higgs Models.

	value	uncertainty
N_{obs}	0	-
N_{bkg}	0.50	0.20
L_{int}	0.83 fb^{-1}	0.04
A_{sig}	0.16	0.03

Table X: Summary of quantities used in the calculation of the upper cross-section limit.

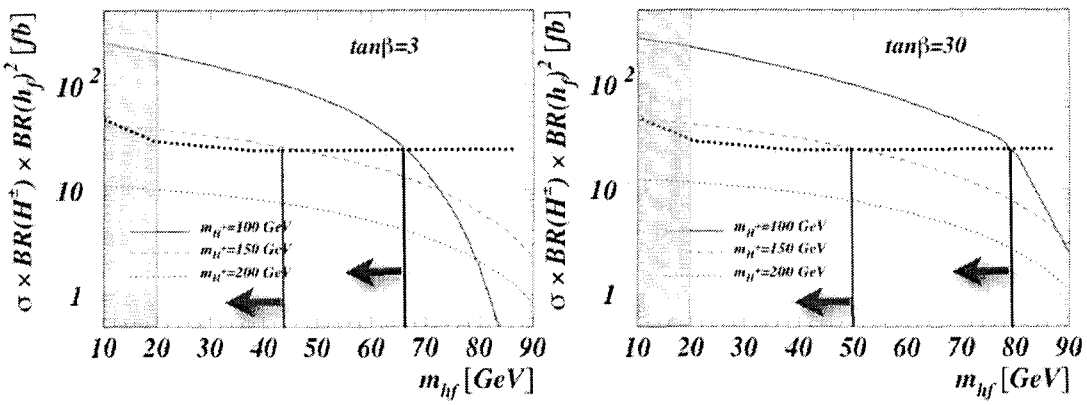

Fig. 78: Exclusion regions for four benchmark points. Results obtained from the 95% CL cross-section limit ($25.3fb$) on the $\sigma(q\bar{q} \to H^{\pm}h \to 3\gamma + X)$ processes. Regions to the left from the vertical lines correspond to the excluded Higgs masses, e.g. $m^{95\%}_{CL_s} = 80$ GeV/c^2 for $m_{H^{\pm}} \leq 100$ GeV/c^2, $\tan\beta = 30$.

9 SUMMARY

In this thesis we describe a search for a fermiophobic Higgs boson in $3\gamma + X$ events. The study has been performed on 0.83 fb^{-1} of data collected with the DØ detector that resides at one of the interaction regions of the Tevatron collider, the world's highest energy accelerator. This study was motivated by a fairly recent phenomenological paper [33] where it was noticed that in certain class of models (2HDM Type I and THM) the multi-photon final states like this one become detectable at the luminosity that has been collected by the DØ experiment by 2006. The mechanism that permits such final state becomes available when the conventional higgs production mechanism (higgs strahlung) are suppressed. This leads to the fact that Higgs boson with mass ($m_{h_f} < 90$ GeV/c^2) lower than the current limit has not been excluded.

We have observed zero events with expected 0.5 ± 0.2 events. Background contribution and overall normalization constant, luminosity, were estimated exclusively from the data. It was observed that before the signal-oriented cut on the momentum imbalance the dominant background contribution comes from Direct Tri-Photon production. Five events were observed with 2.73 ± 0.55 and 0.78 ± 0.15 expected from Direct Tri-Photon Process and processes with at least one fake photon, respectively. Estimation of DTP contribution was done under the assumption that one of the photons comes from Initial State Radiation. This leads to the underestimation of the DTP contribution. However, we observed consistency of the ISR rate obtained from MC with the one obtained from $Z\gamma$ events in data. Even

with the conservative assumption that DTP background is underestimated by as much as 40%, the DTP contribution becomes insignificant after the application of the H_T cut.

Having observed zero events we set 95% CL upper limit on the production cross section of fermiophobic Higgs boson in the considered scenaria which is equal to 25.3 fb^{-1} and constitutes to the best result todate.

With the combined 6-8 fb^{-1} expected from both Tevatron experiments in the next few years, a large fraction of such fermiophobic higgs boson phase space will be covered. And if no signal is observed, the LHC will be able to exclude most of the remaining phase space.

APPENDICES

Appendix A

EVENT DISPLAY OF $3\gamma + X$ EVENTS

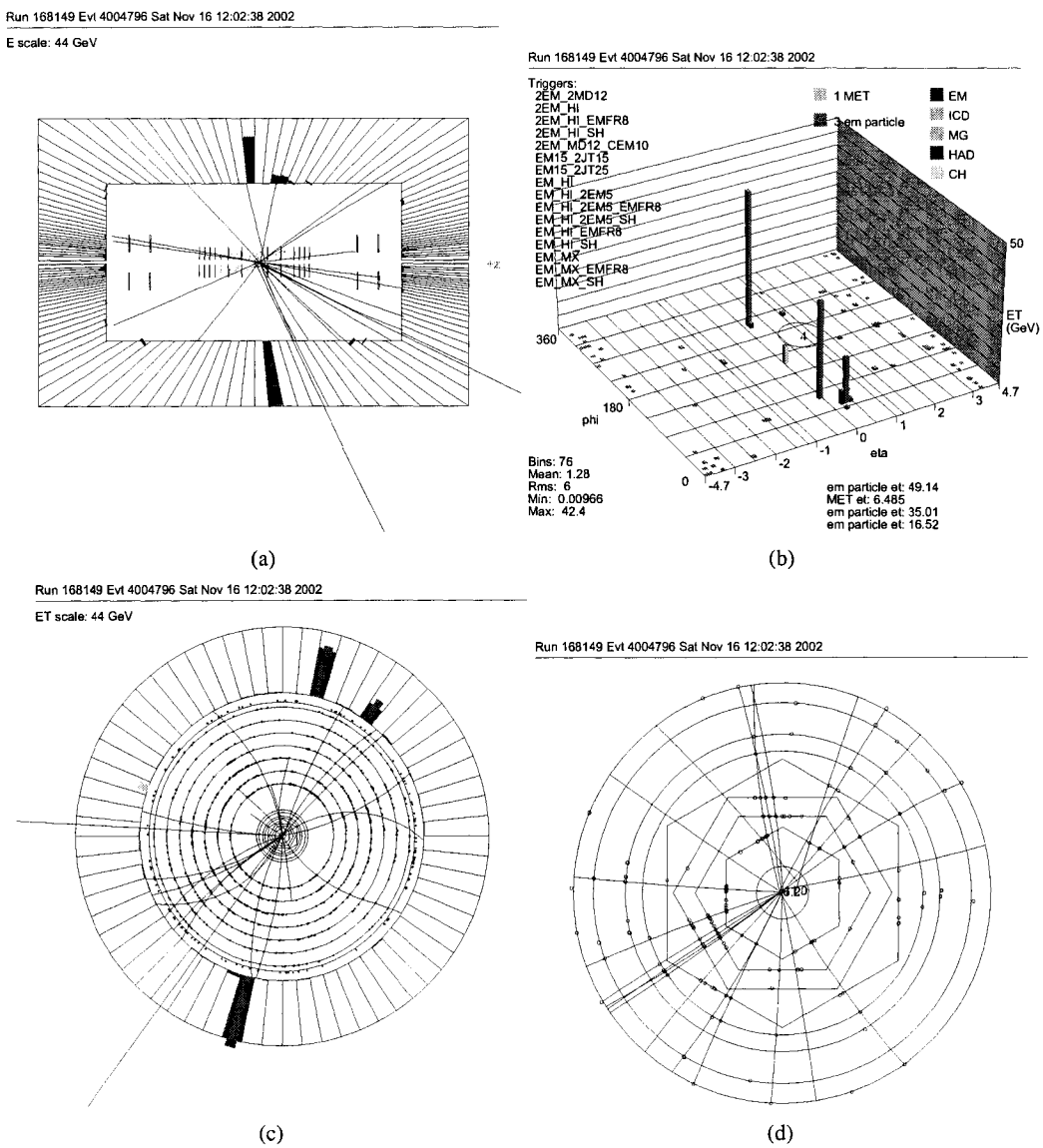

Fig. 79: Event display of 3γ event with (run:event) = (168149:4004796).

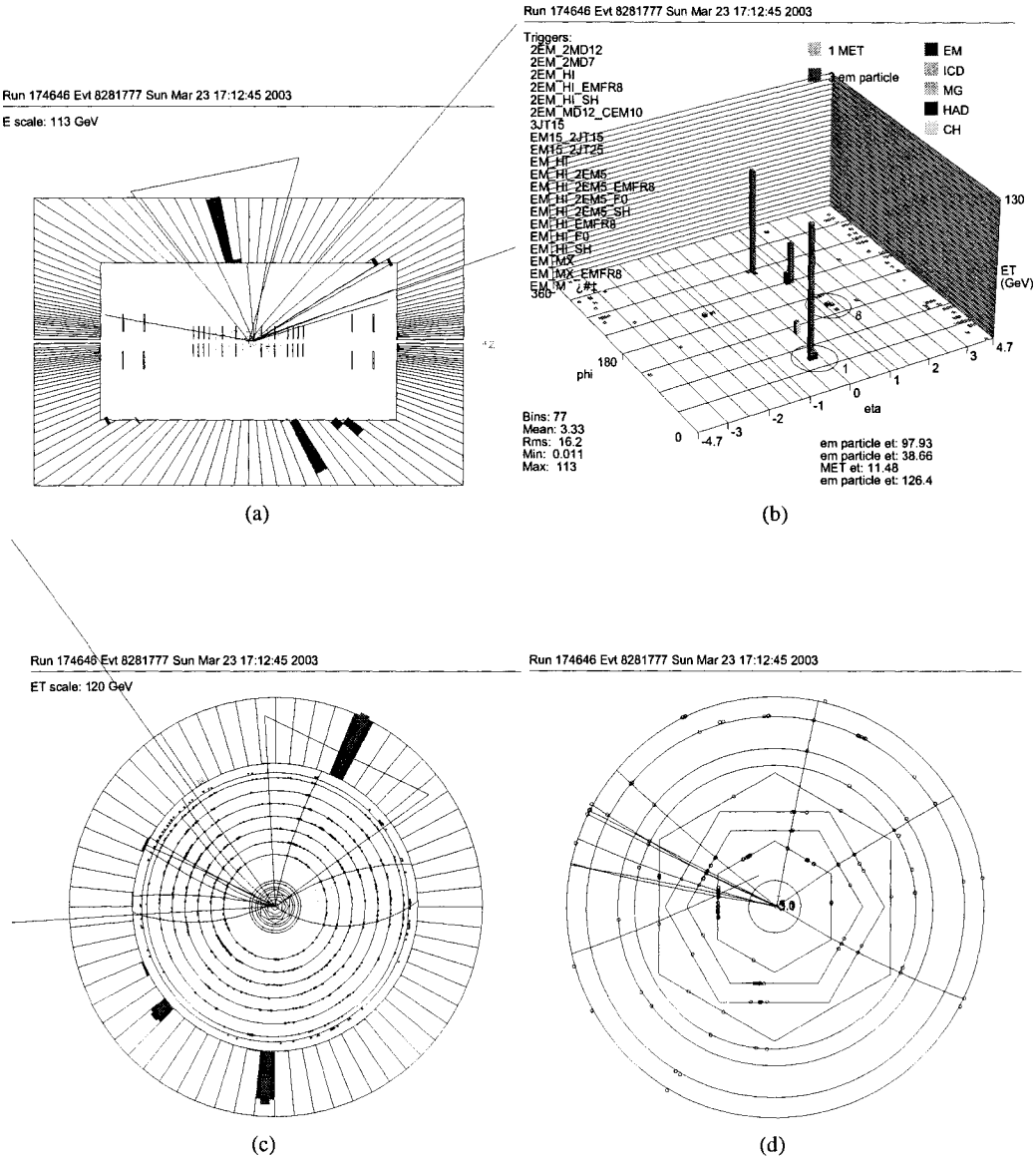

Fig. 80: Event display of 3γ event with (run:event) = (174646:8281777).

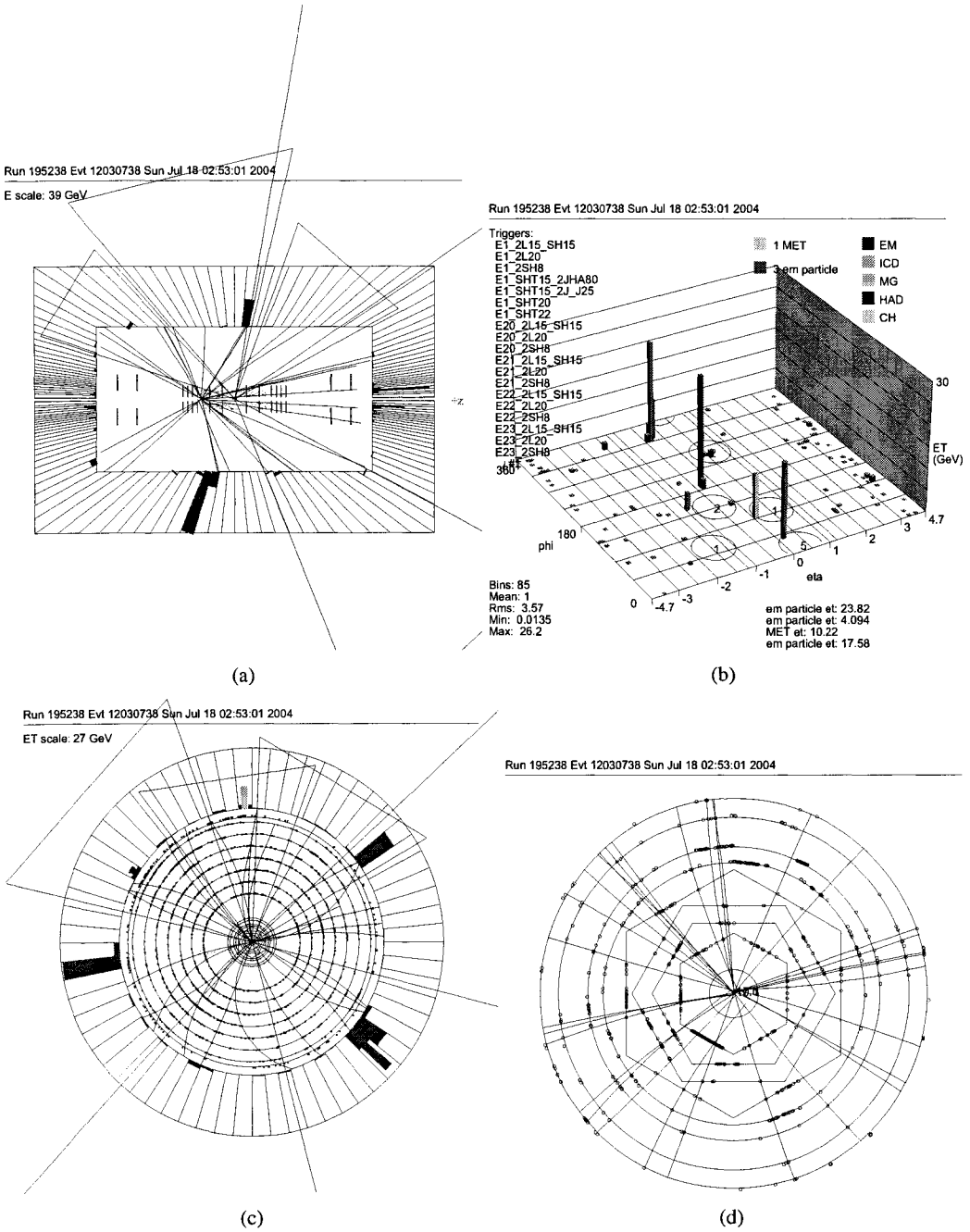

Fig. 81: Event display of 3γ event with (run:event) = (195238:12030738).

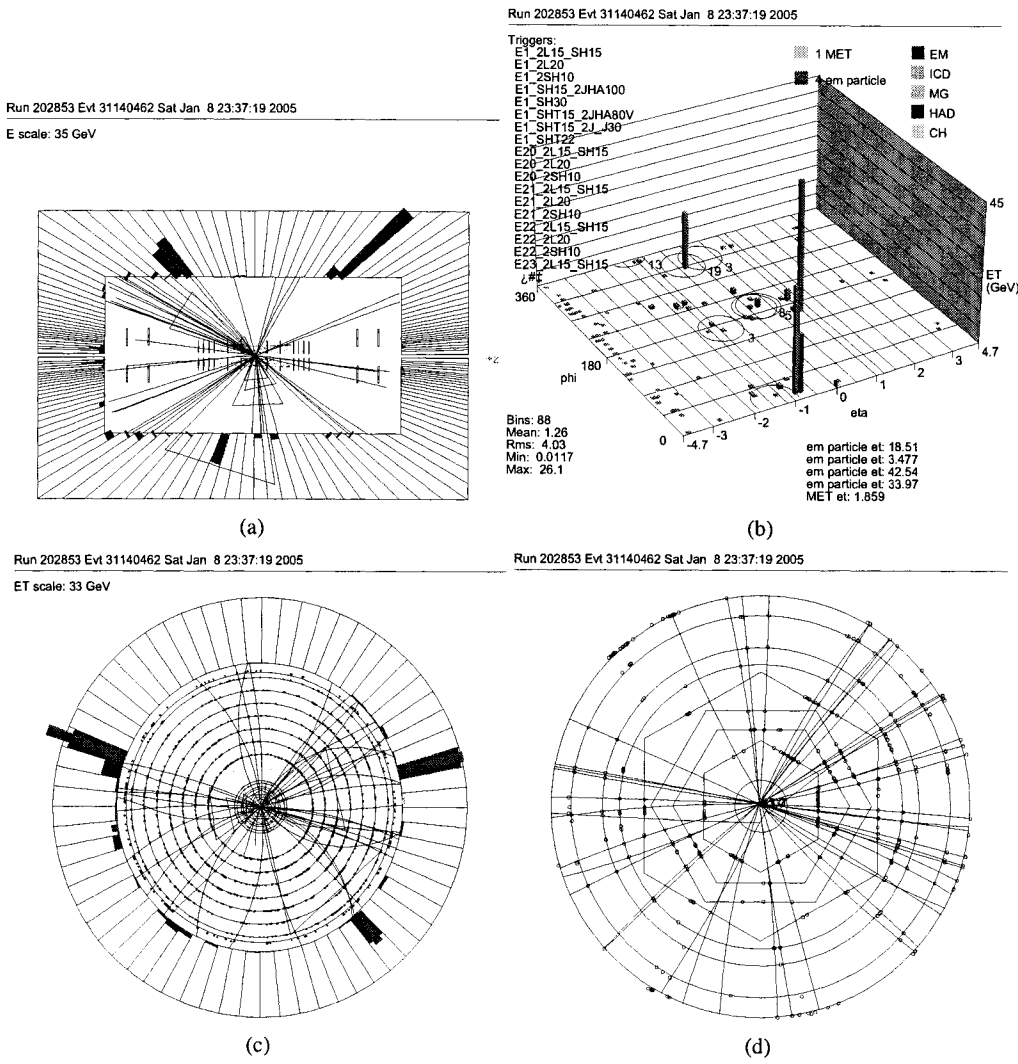

Fig. 82: Event display of 3γ event with (run:event) = (202853:31140462).

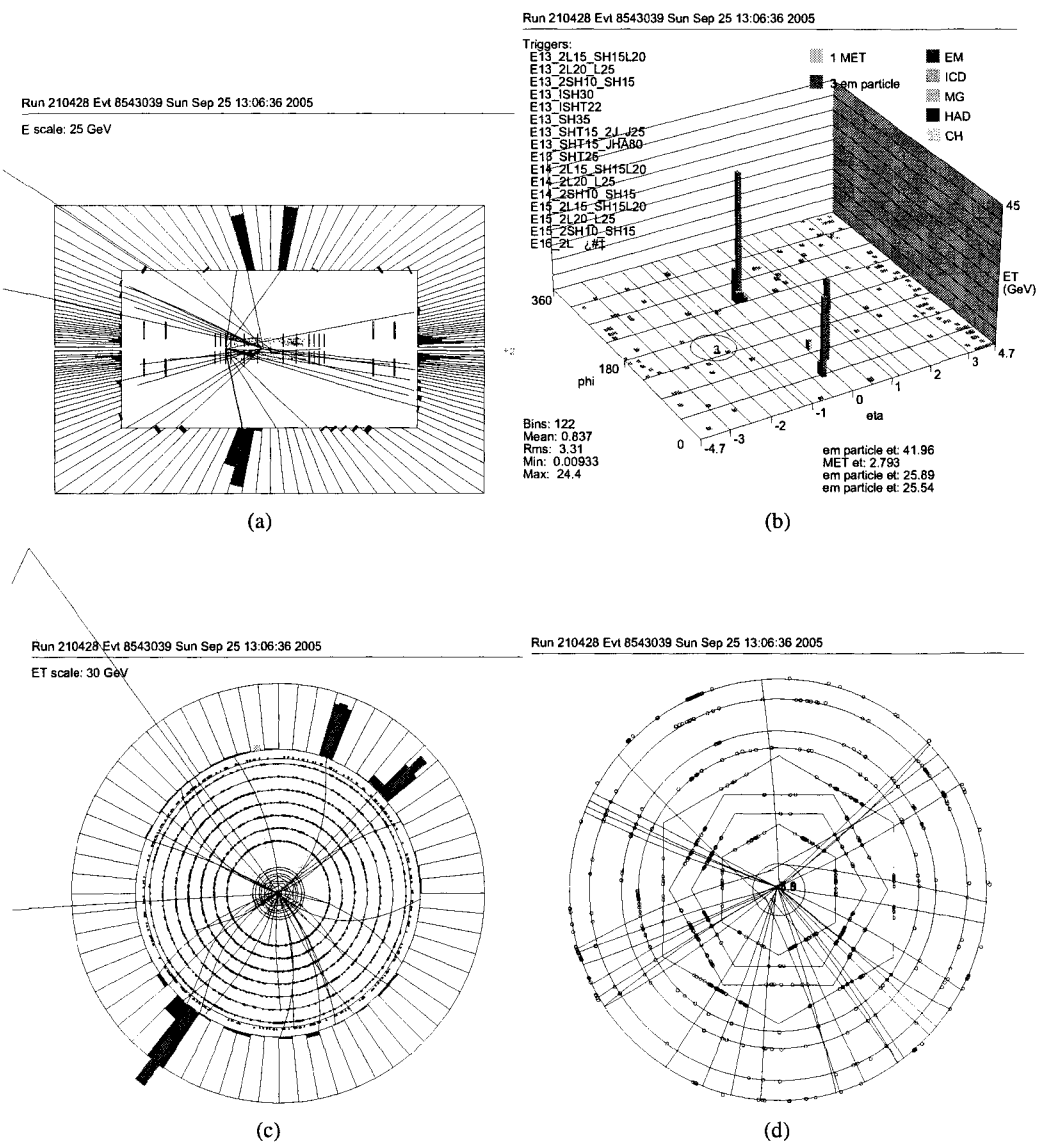

Fig. 83: Event display of 3γ event with (run:event) = (210428:8543039).

Appendix B

EVENT DISPLAY OF $2\gamma + E + X$ EVENTS

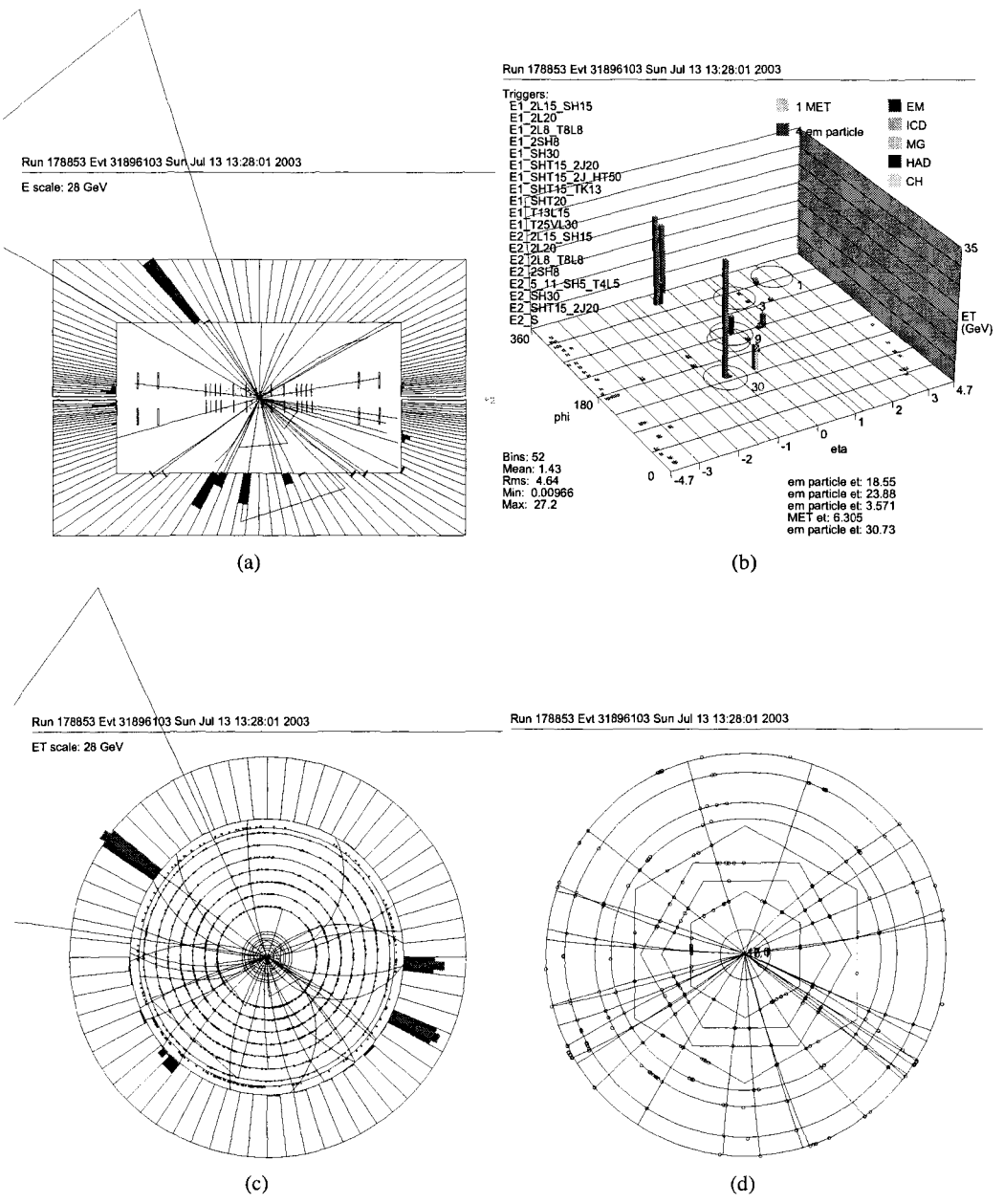

Fig. 84: Event display of $2\gamma + e + X$ event with (run:event) = (178853:31896103).

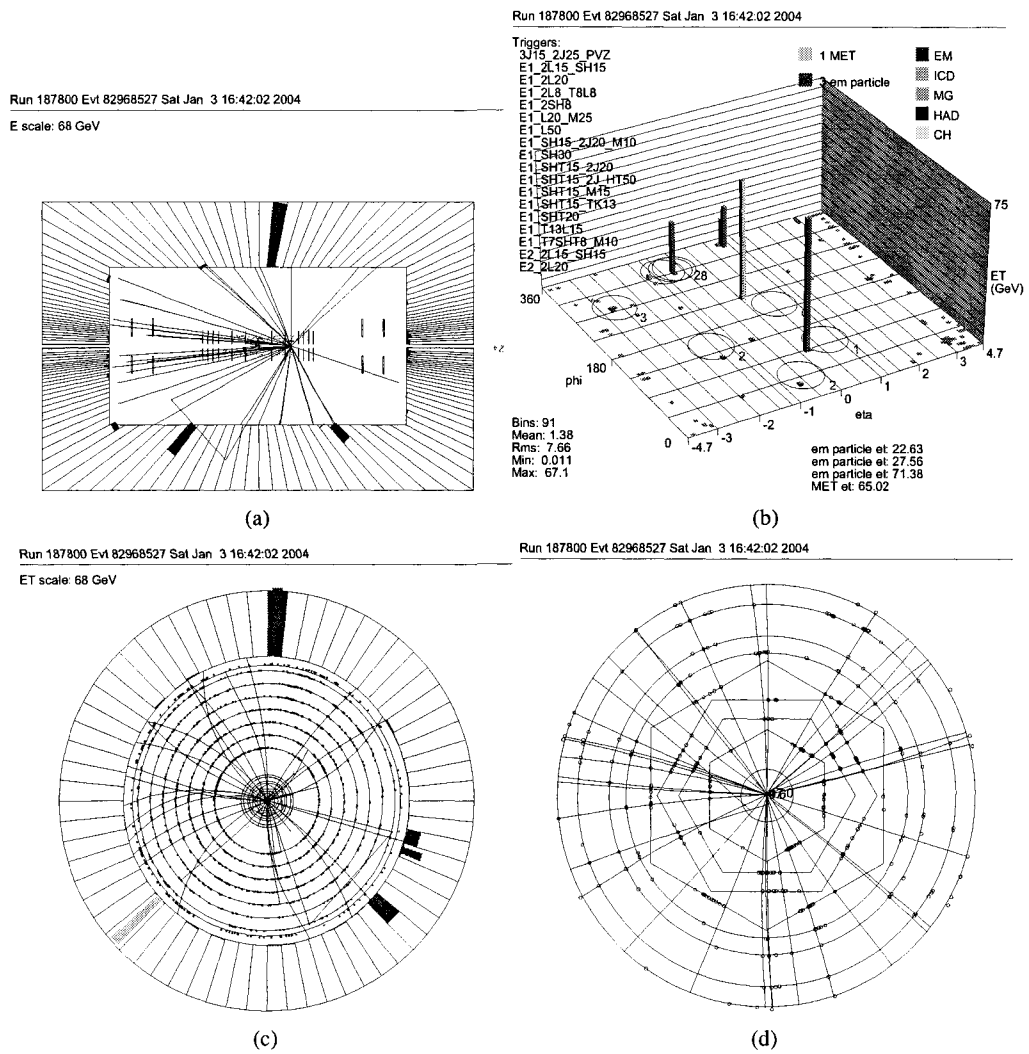

Fig. 85: Event display of $2\gamma + e + X$ event with (run:event) = (187800:82968527).

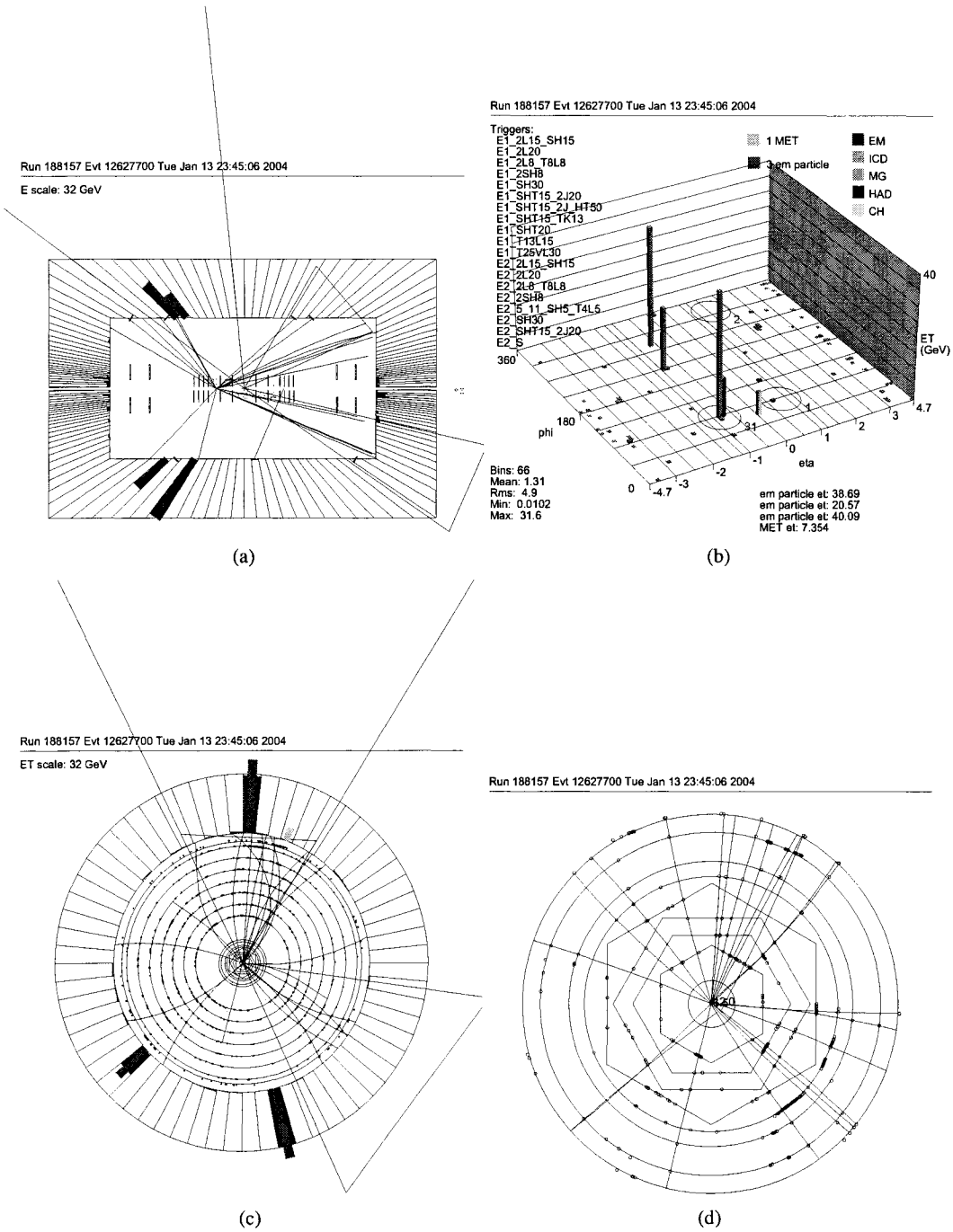

Fig. 86: Event display of $2\gamma + e + X$ event with (run:event) = (188157:12627700).

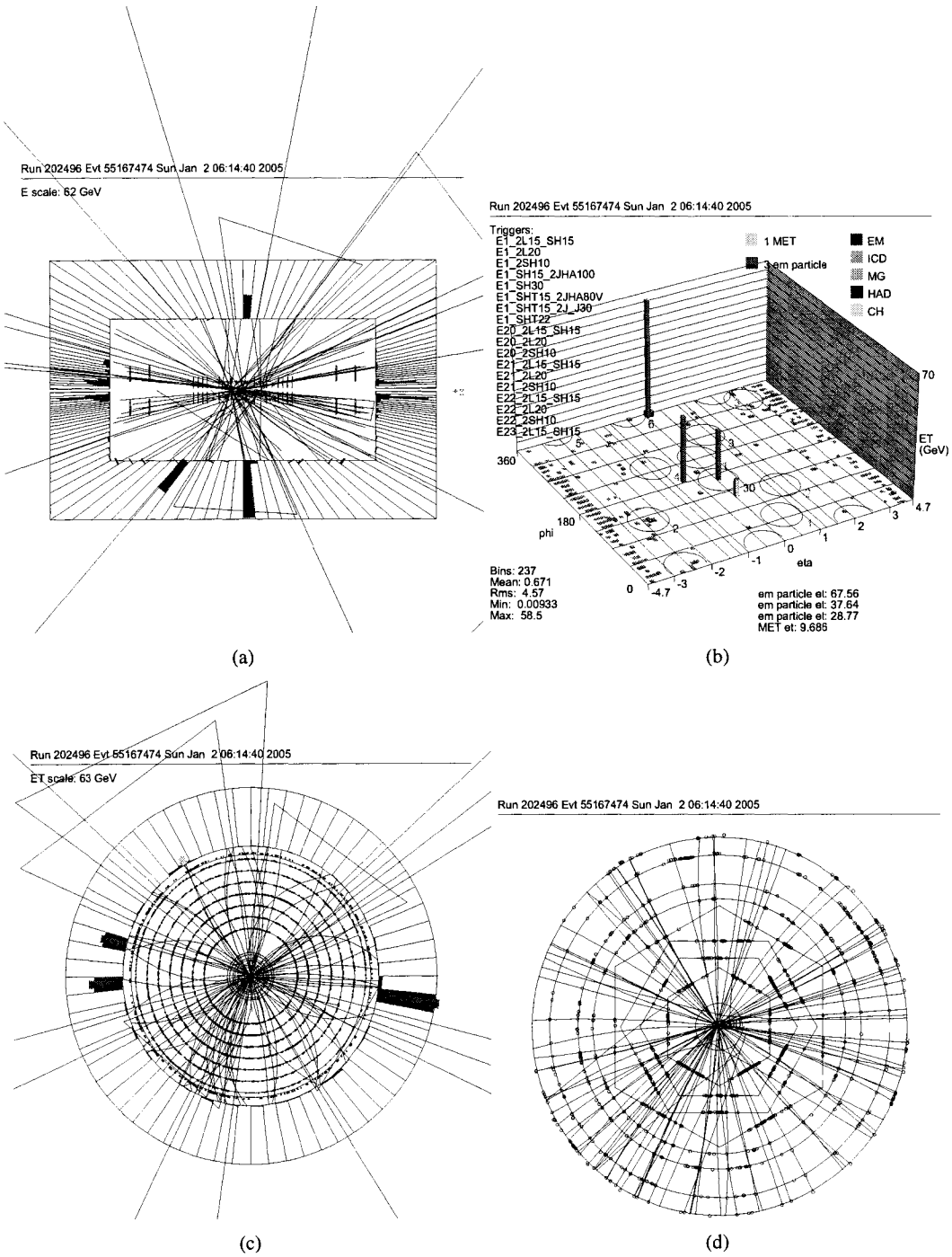

Fig. 87: Event display of $2\gamma + e + X$ event with (run:event) = (202496:55167474).

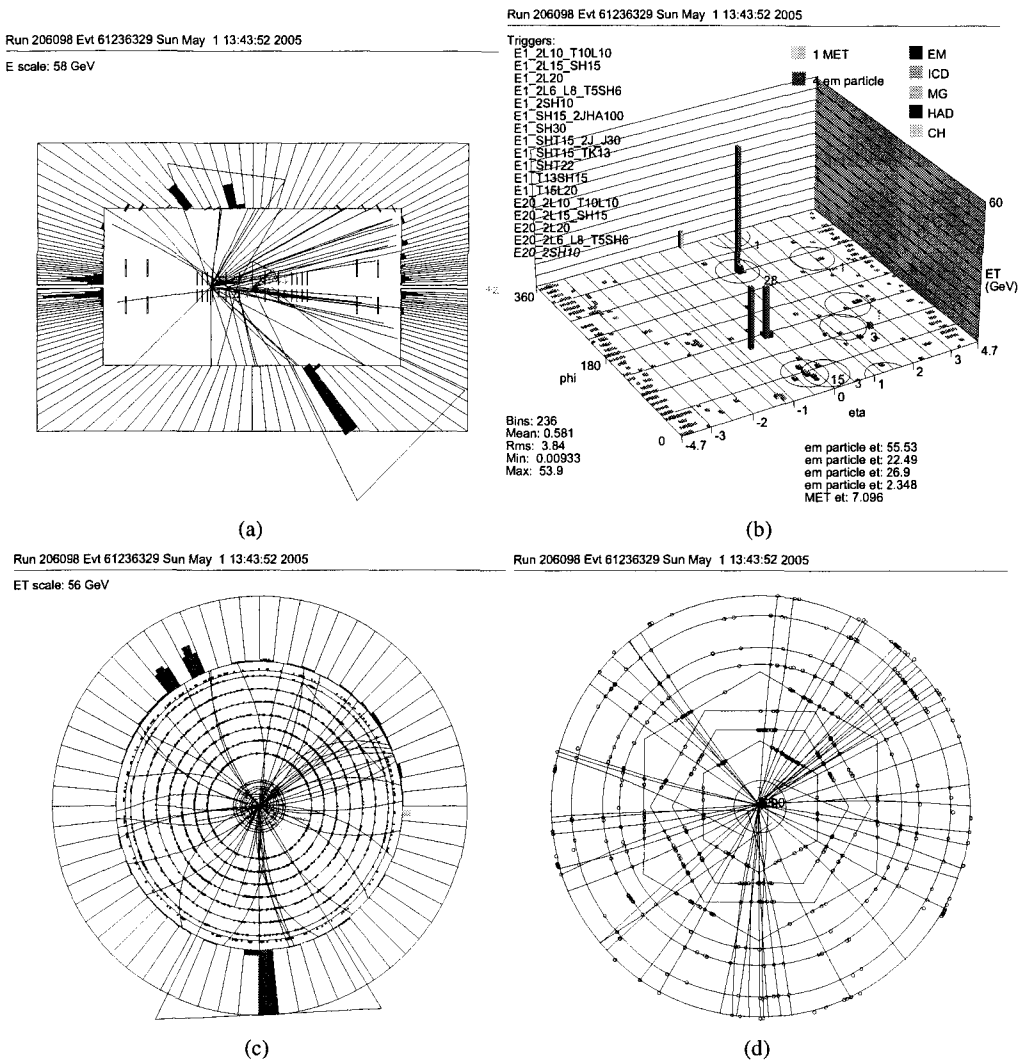

Fig. 88: Event display of $2\gamma + e + X$ event with (run:event) = (206098:61236329).

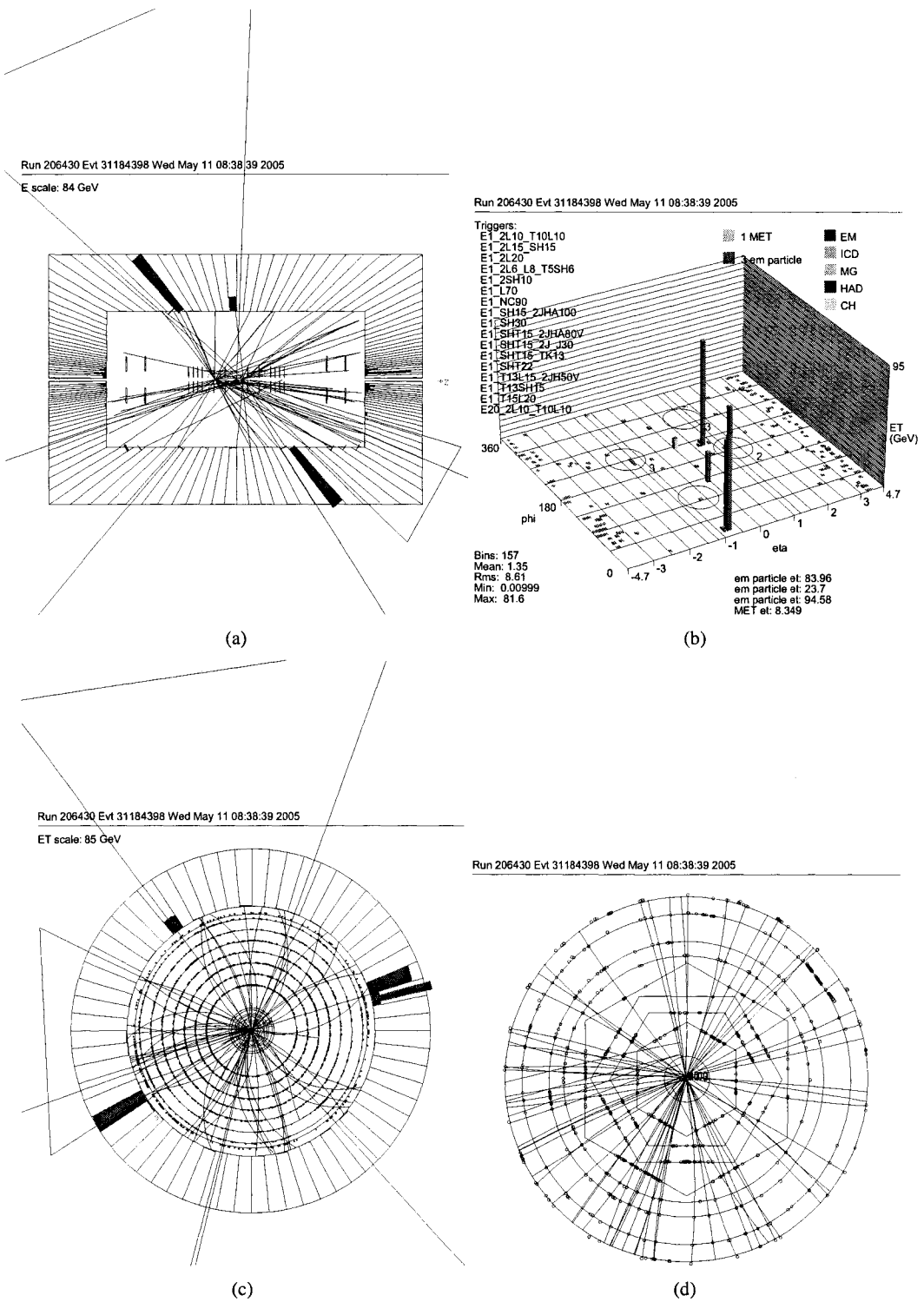

Fig. 89: Event display of $2\gamma + e + X$ event with (run:event) = (206430:31184398).

Appendix C

EVENT DISPLAY OF $3E+X$ EVENTS

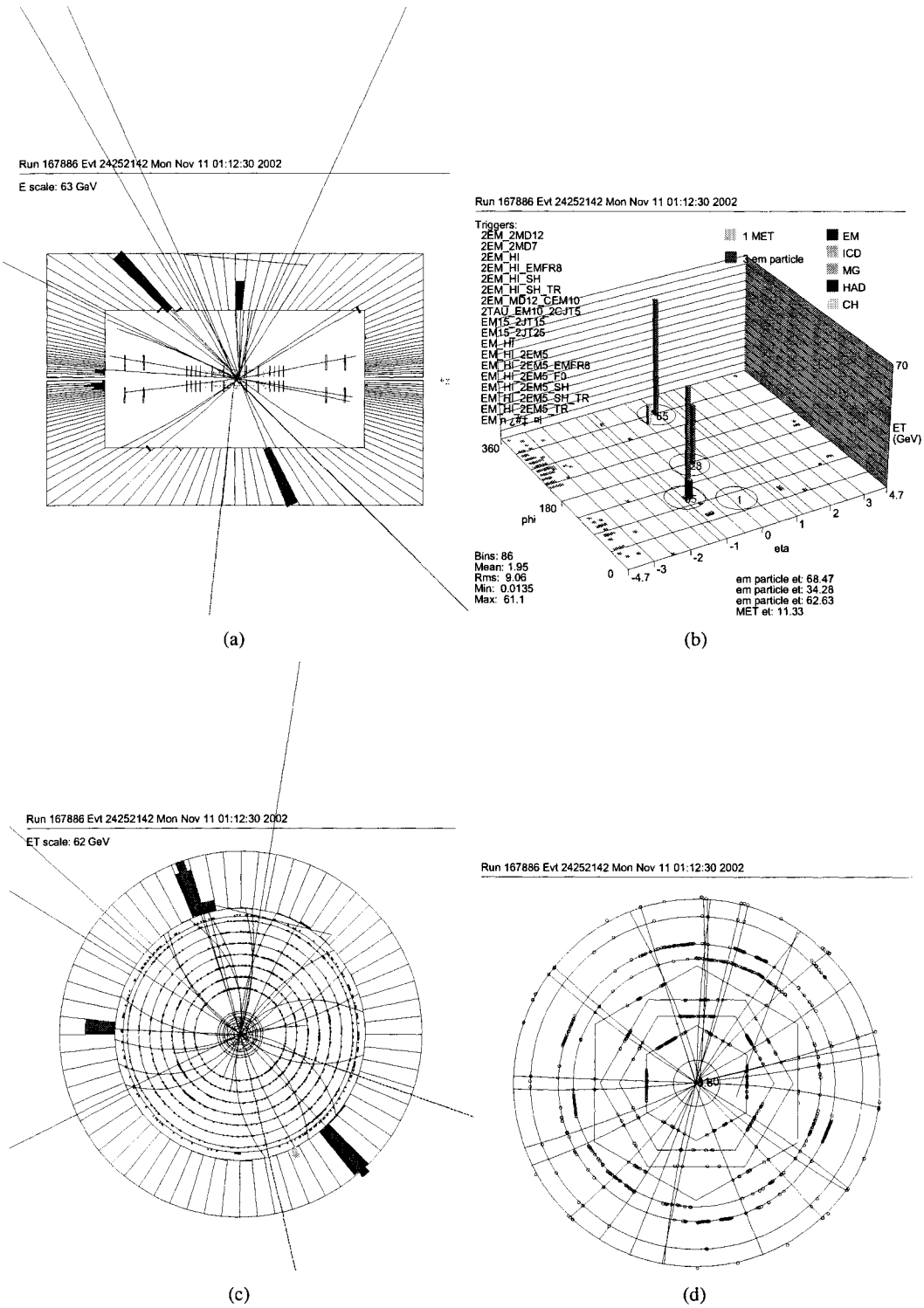

Fig. 90: Event display of $3e + X$ event with (run:event) = (167886:24252142).

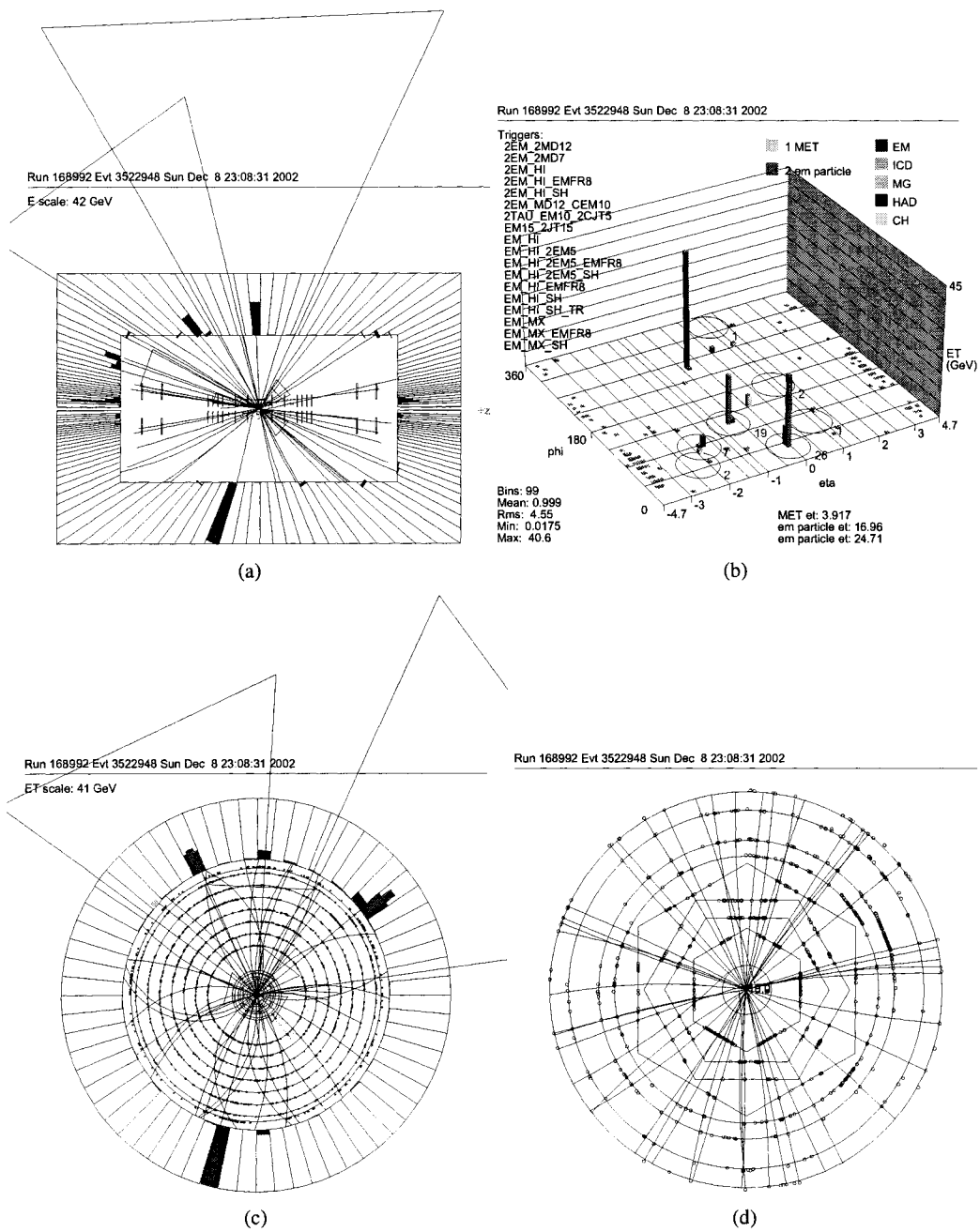

Fig. 91: Event display of $3e + X$ event with (run:event) = (168992:3522948).

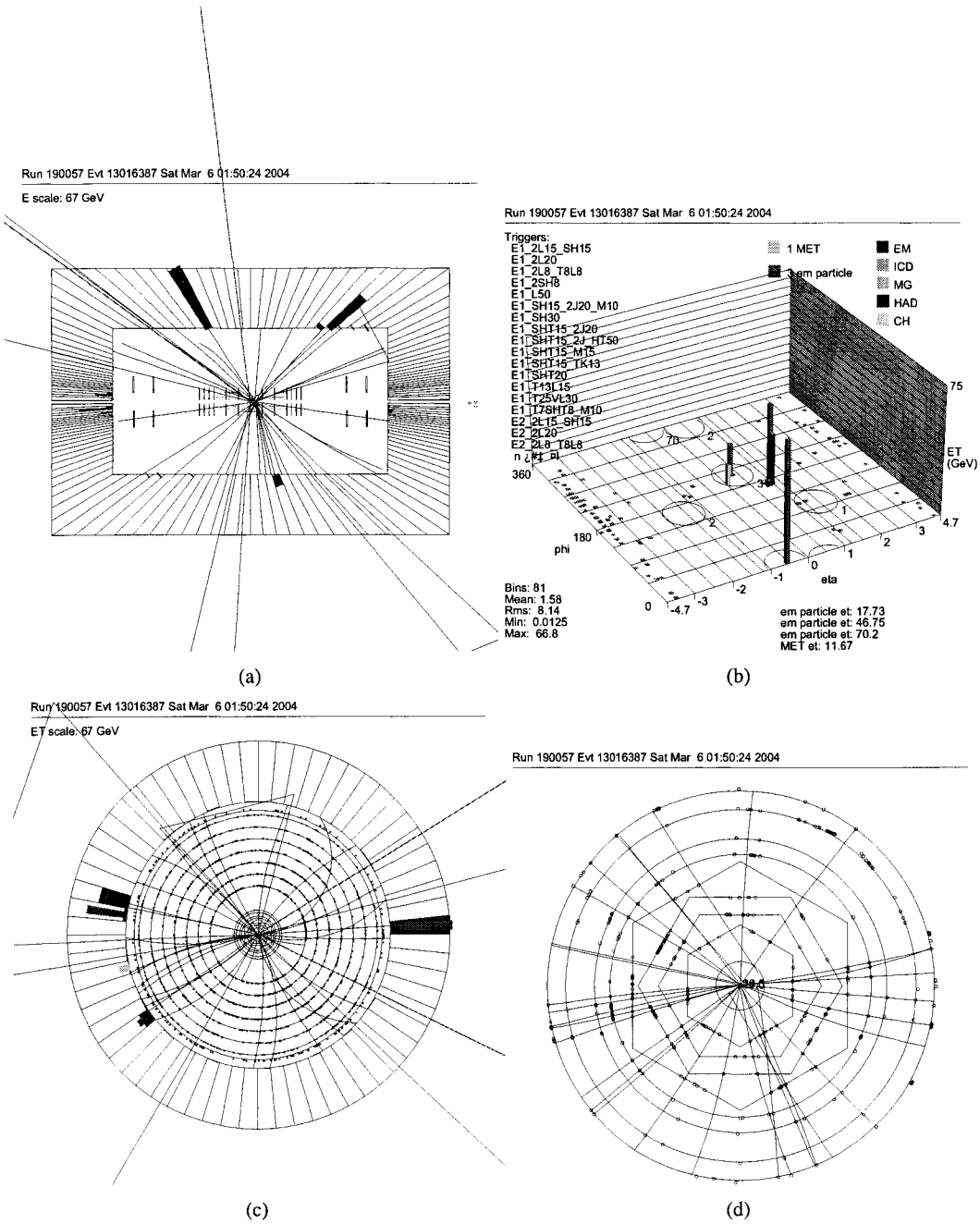

Fig. 92: Event display of $3e+X$ event with (run:event) = (190057:13016387).

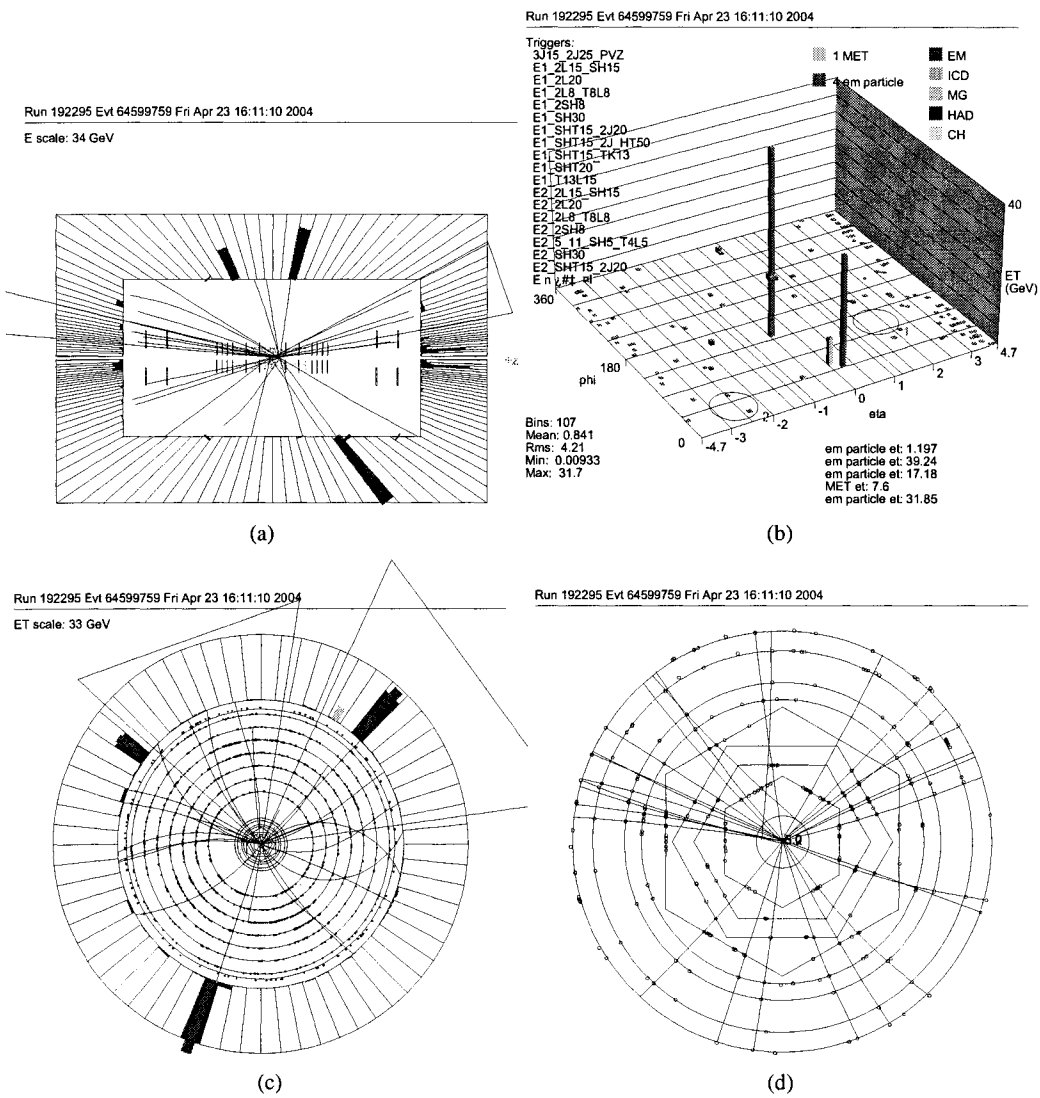

Fig. 93: Event display of $3e + X$ event with (run:event) = (192295:64599759).

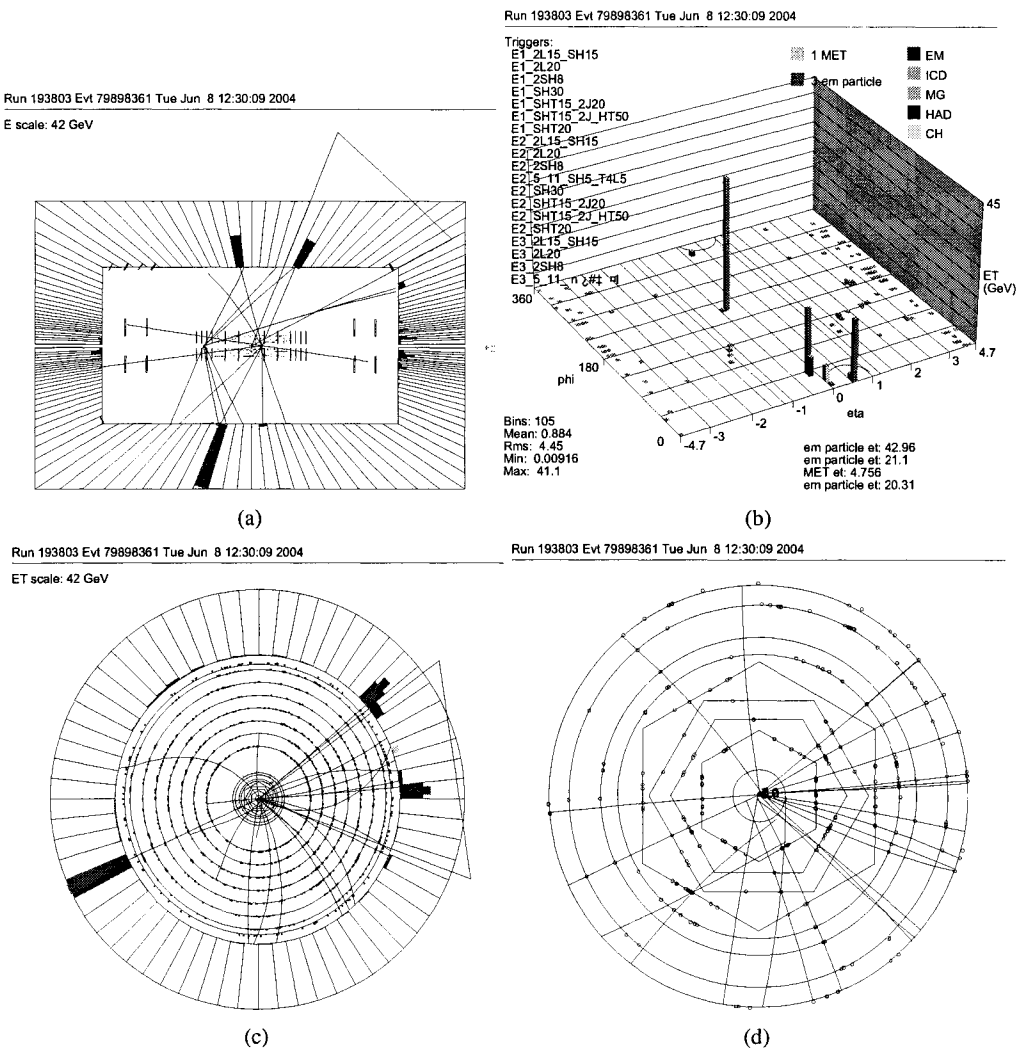

Fig. 94: Event display of $3e + X$ event with (run:event) = (193803:79898361).

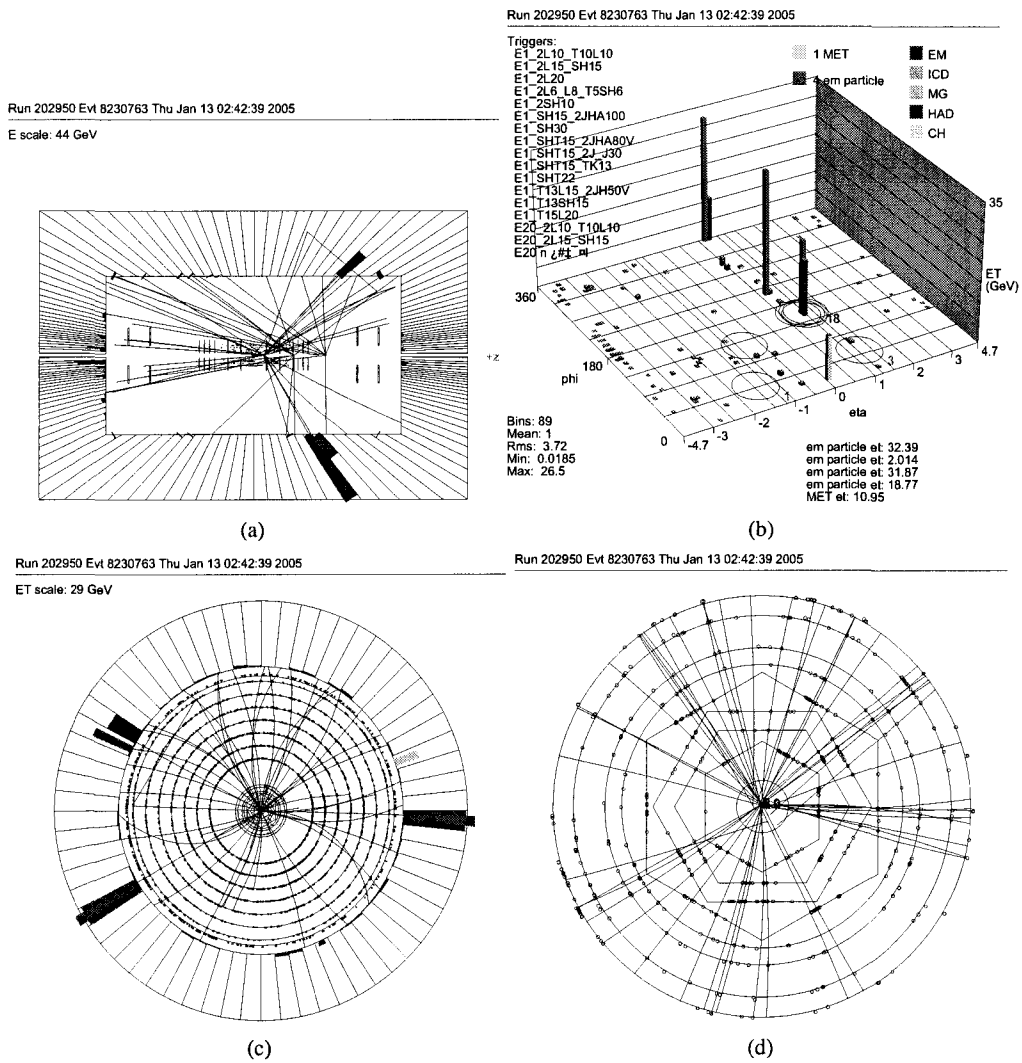

Fig. 95: Event display of $3e + X$ event with (run:event) = (202950:8230763).

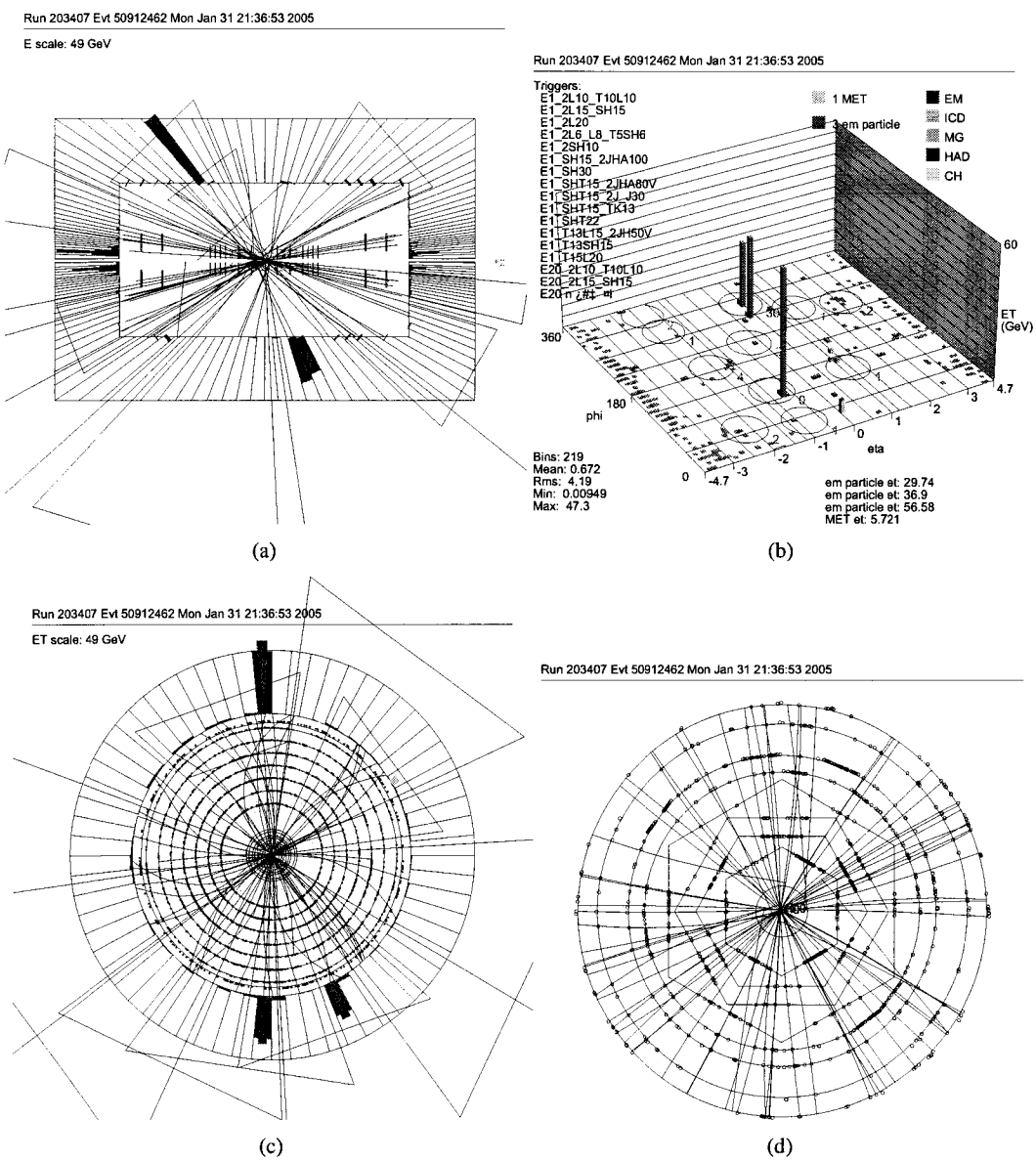

Fig. 96: Event display of $3e+X$ event with (run:event) = (203407:50912462).

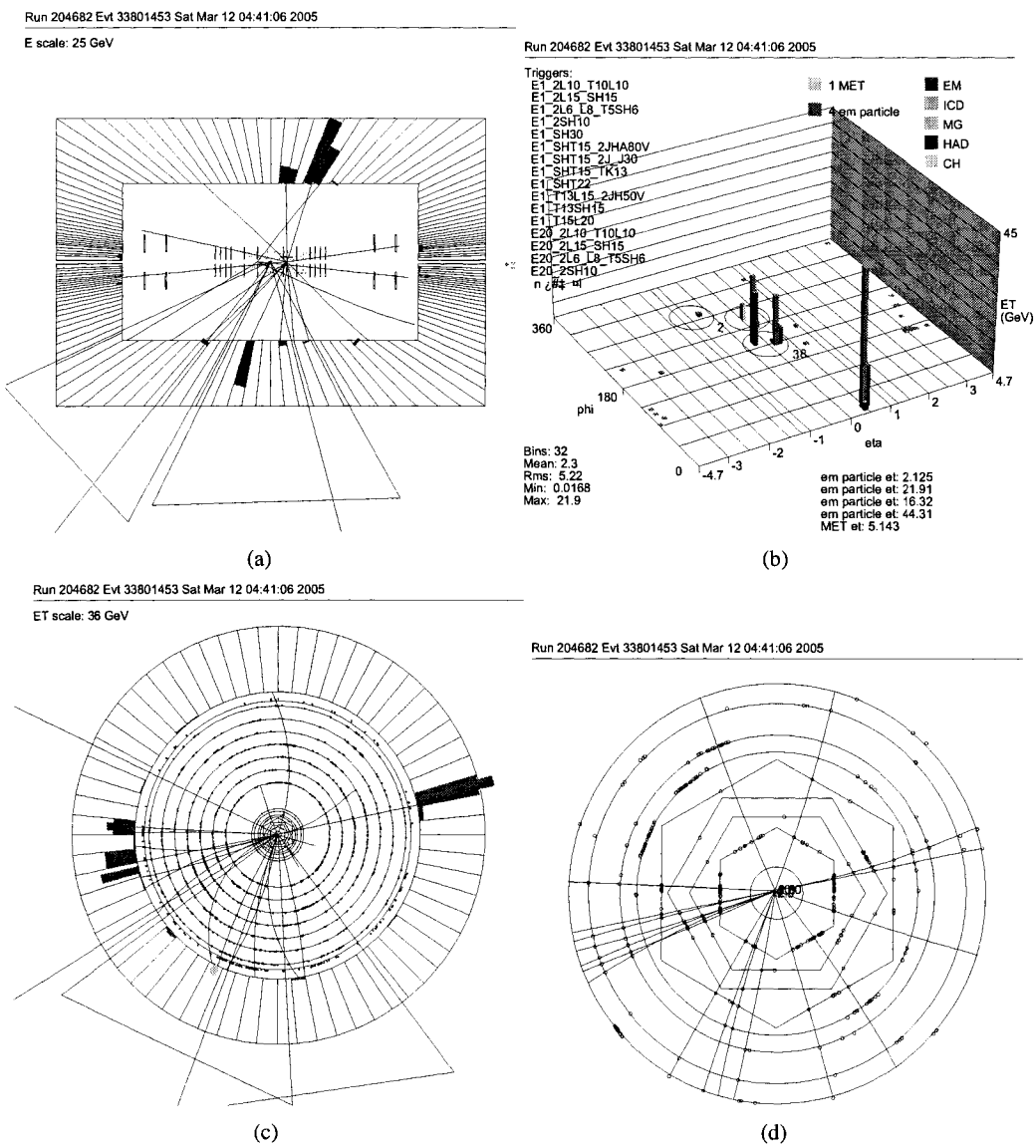

Fig. 97: Event display of $3e + X$ event with (run:event) = (204682:33801453).

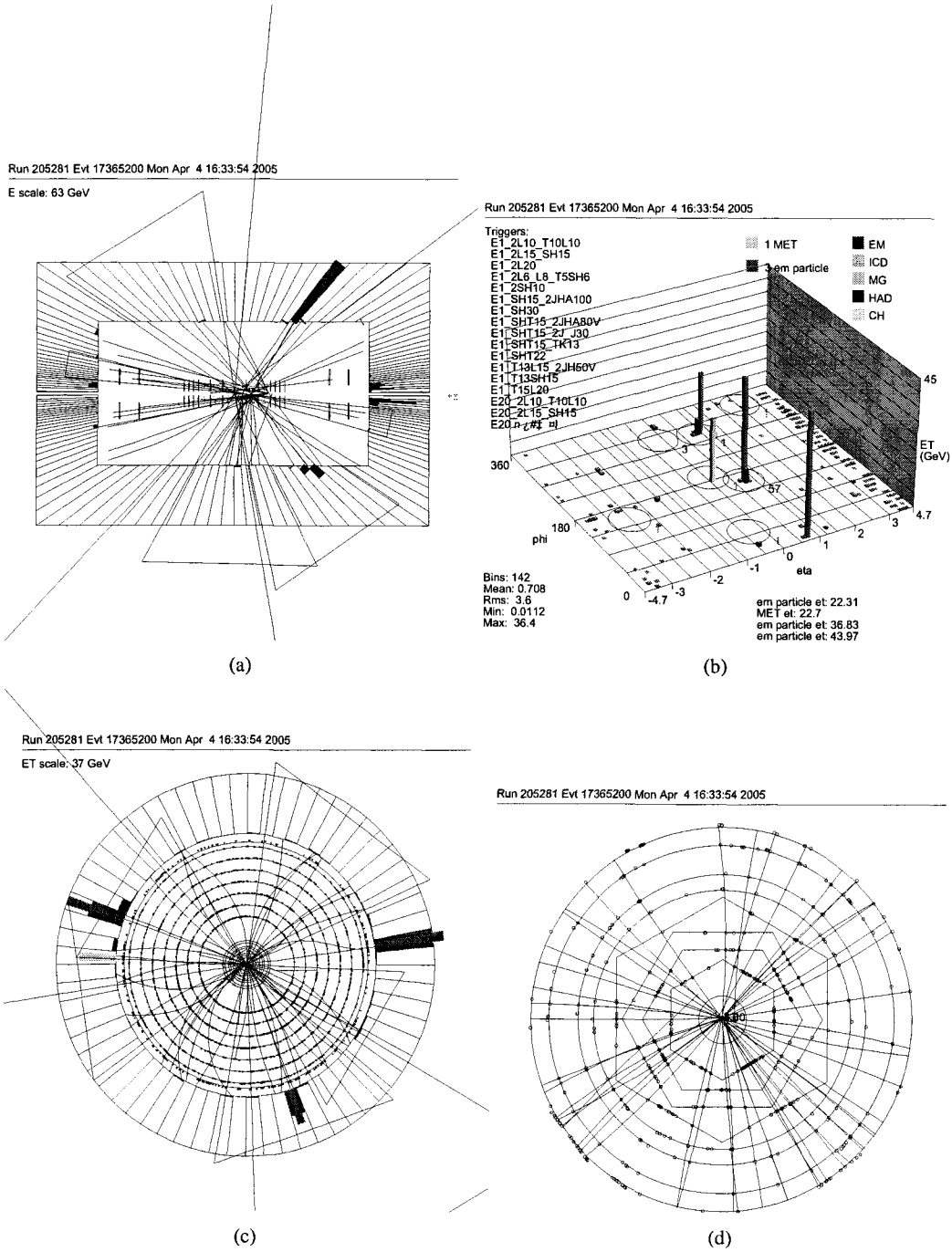

Fig. 98: Event display of $3e+X$ event with (run:event) = (205281:17365200).

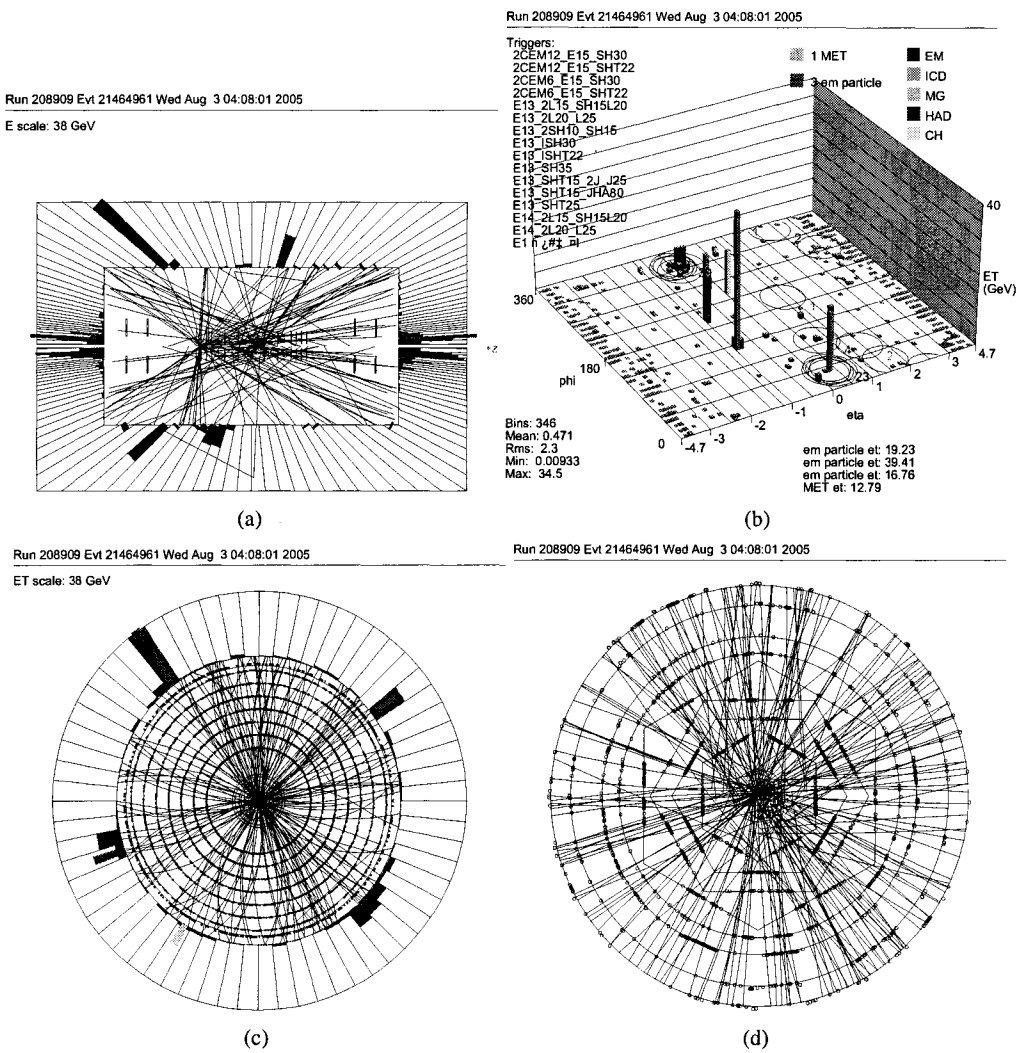

Fig. 99: Event display of $3e + X$ event with (run:event) = (208909:21464961).

Appendix D

EVENT DISPLAY OF $3\gamma + X$ EVENTS WITH ONE FORWARD PHOTON

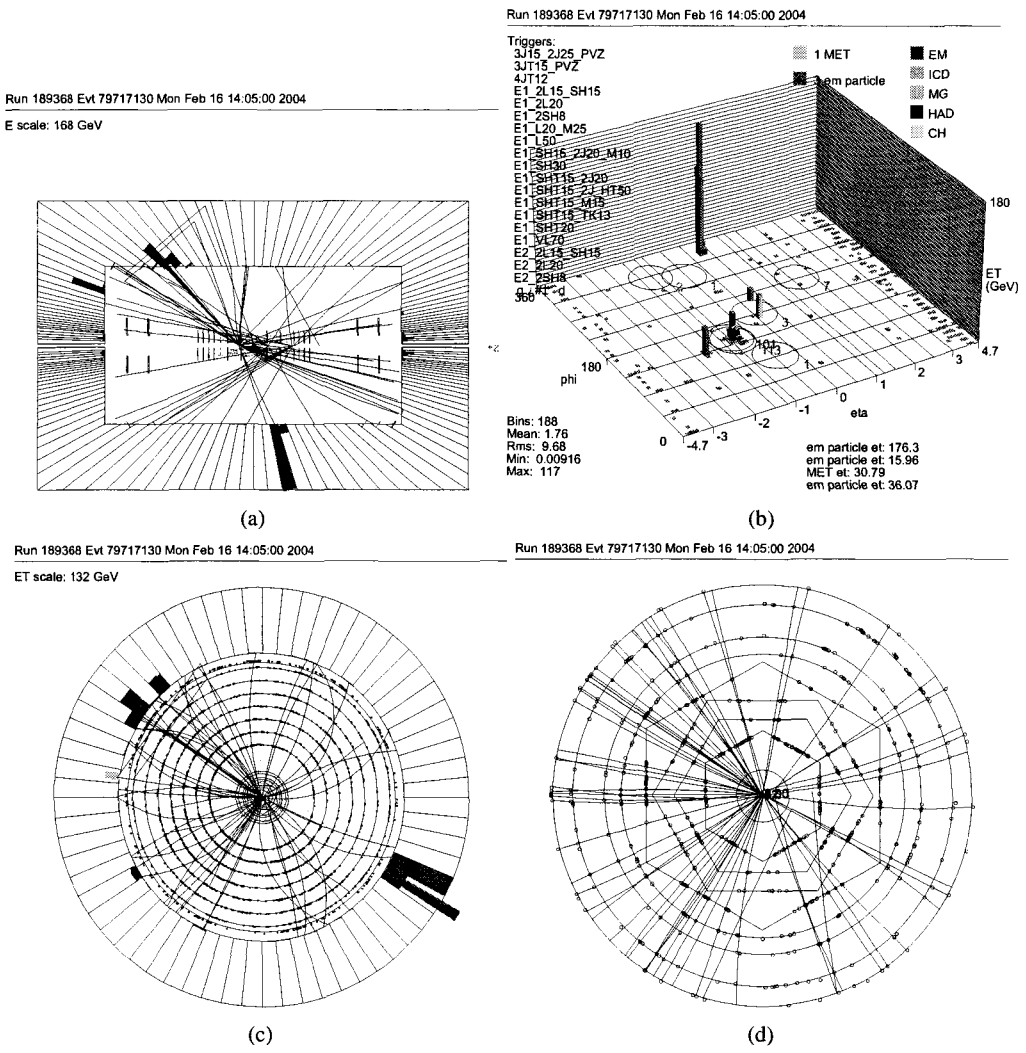

Fig. 100: Event display of $3\gamma + X$ event with 2CC+1EC topolology with (run:event) = (189368:79717130).

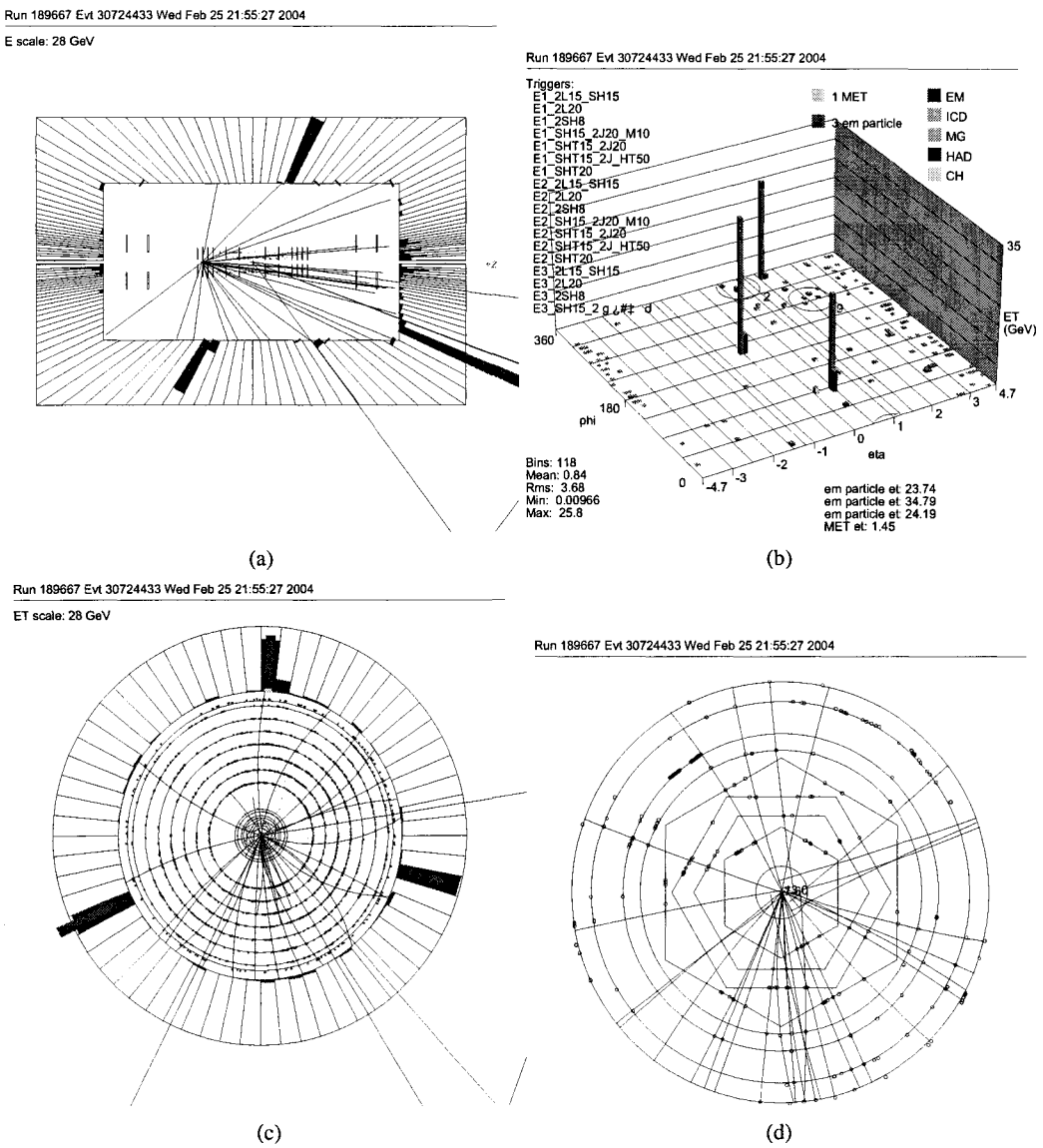

Fig. 101: Event display of $3\gamma + X$ event with 2CC+1EC topolology with (run:event) = (189667:30724433).

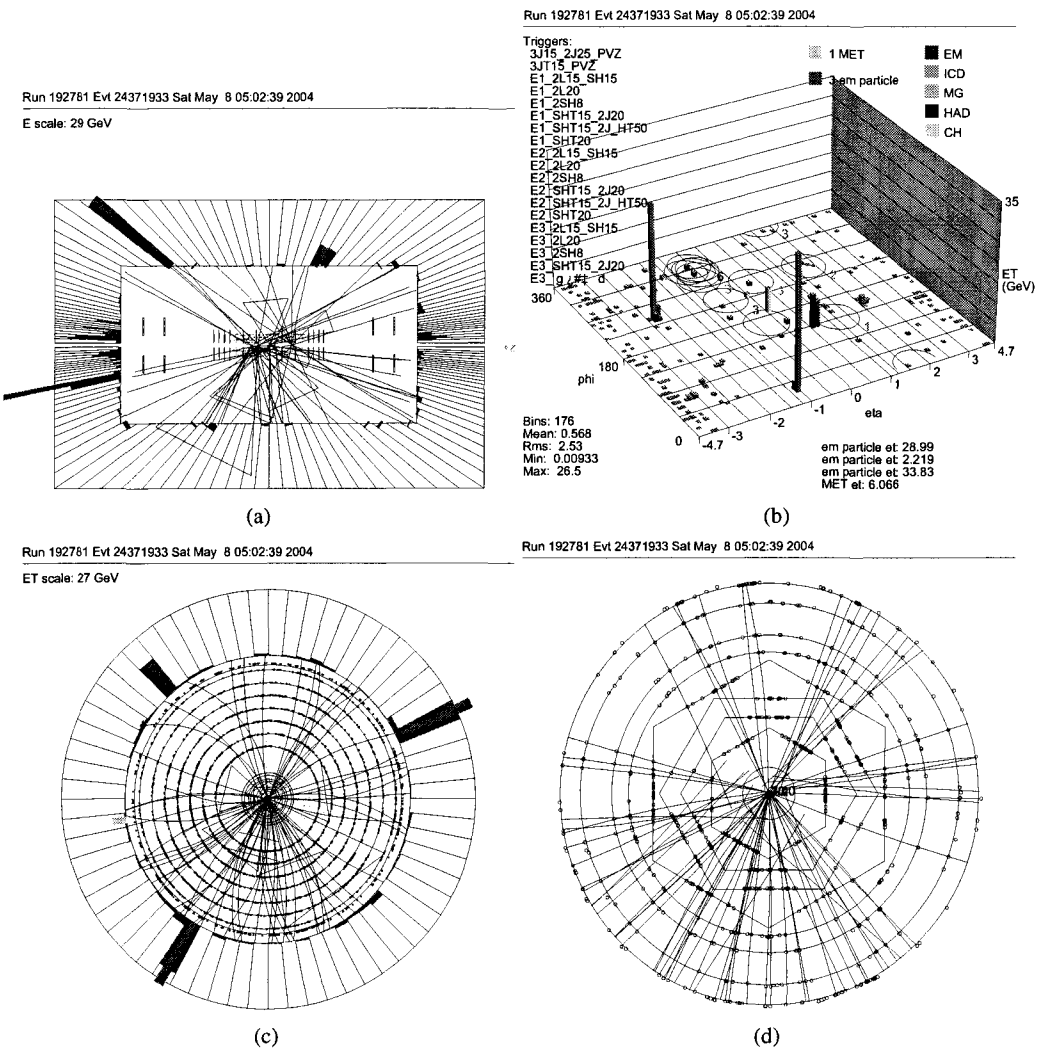

Fig. 102: Event display of $3\gamma + X$ event with 2CC+1EC topolology with (run:event) = (192781:24371933).

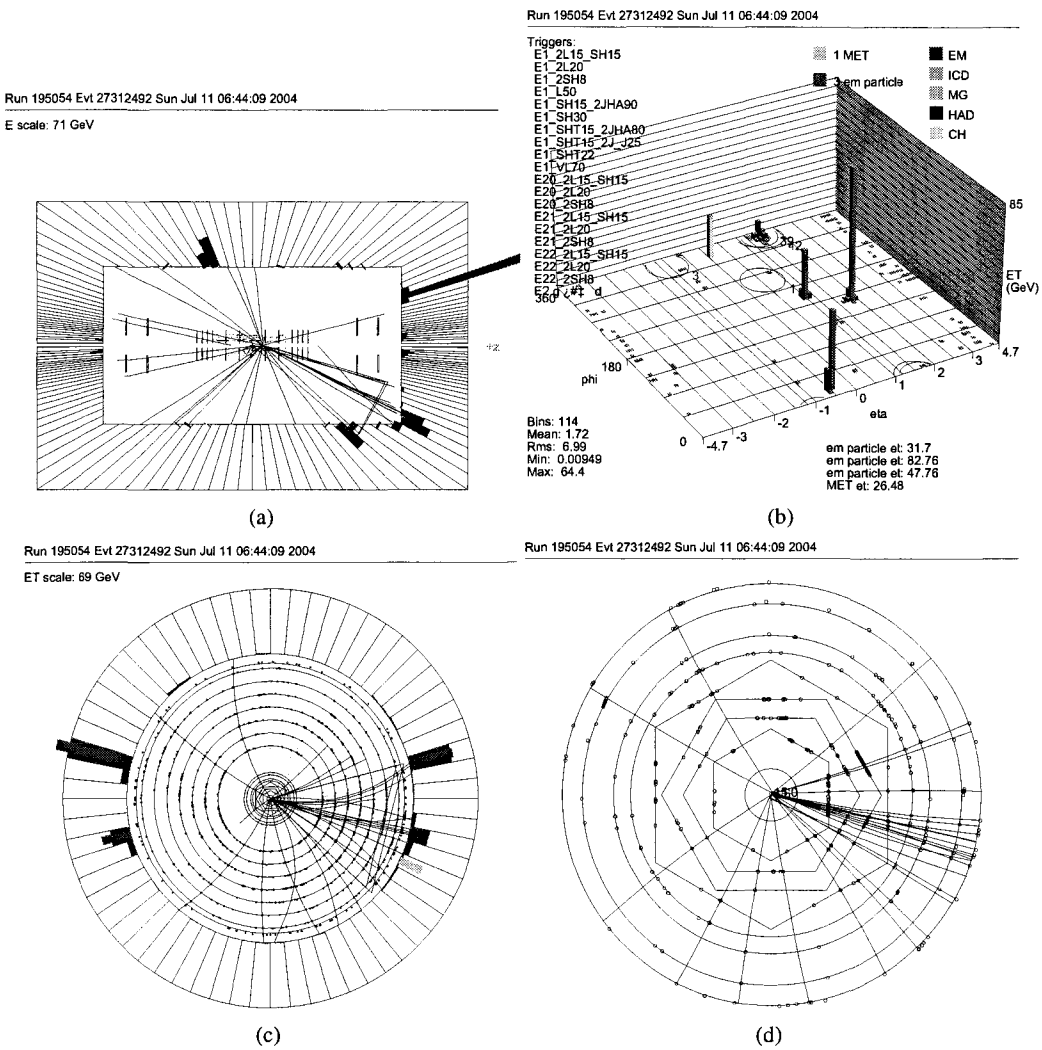

Fig. 103: Event display of $3\gamma + X$ event with 2CC+1EC topolology with (run:event) = (195054:27312492).

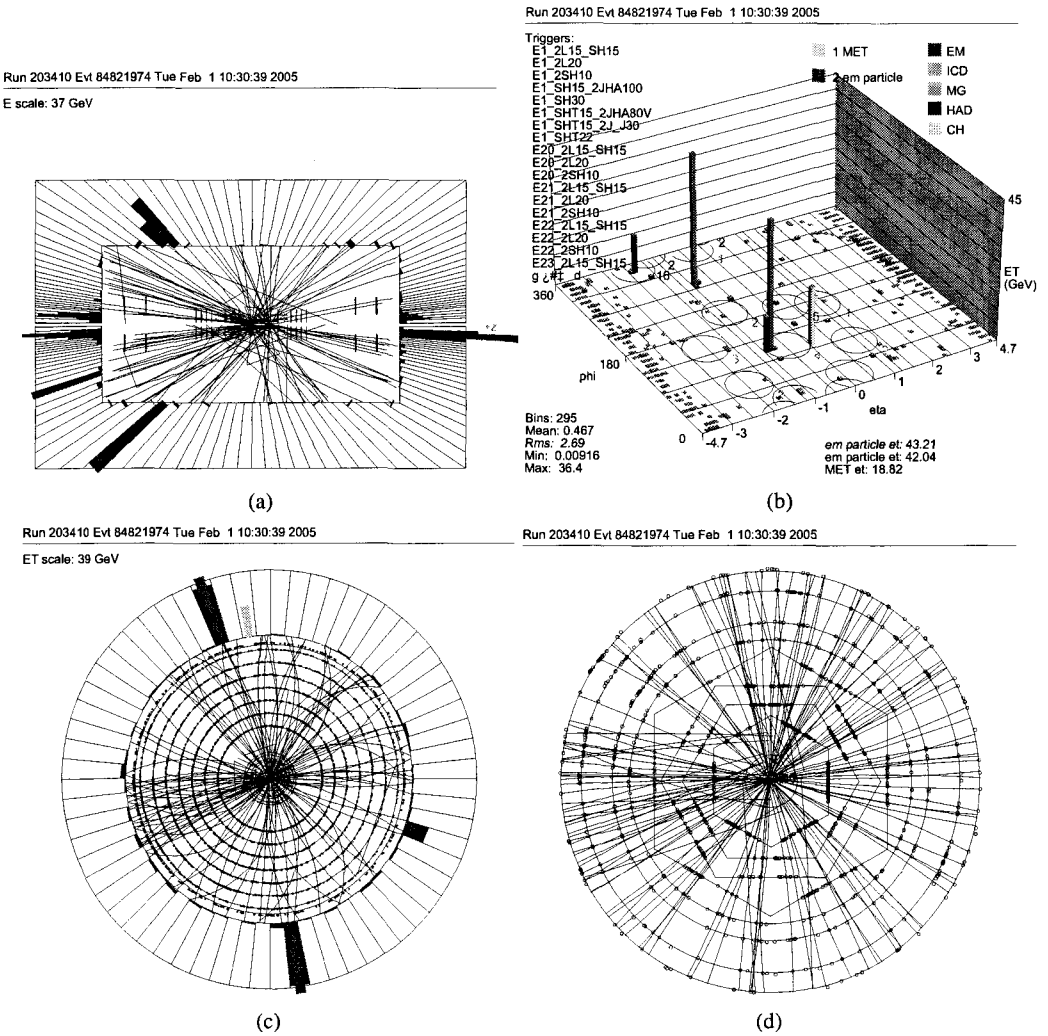

Fig. 104: Event display of $3\gamma + X$ event with 2CC+1EC topolology with (run:event) = (203410:84821974).

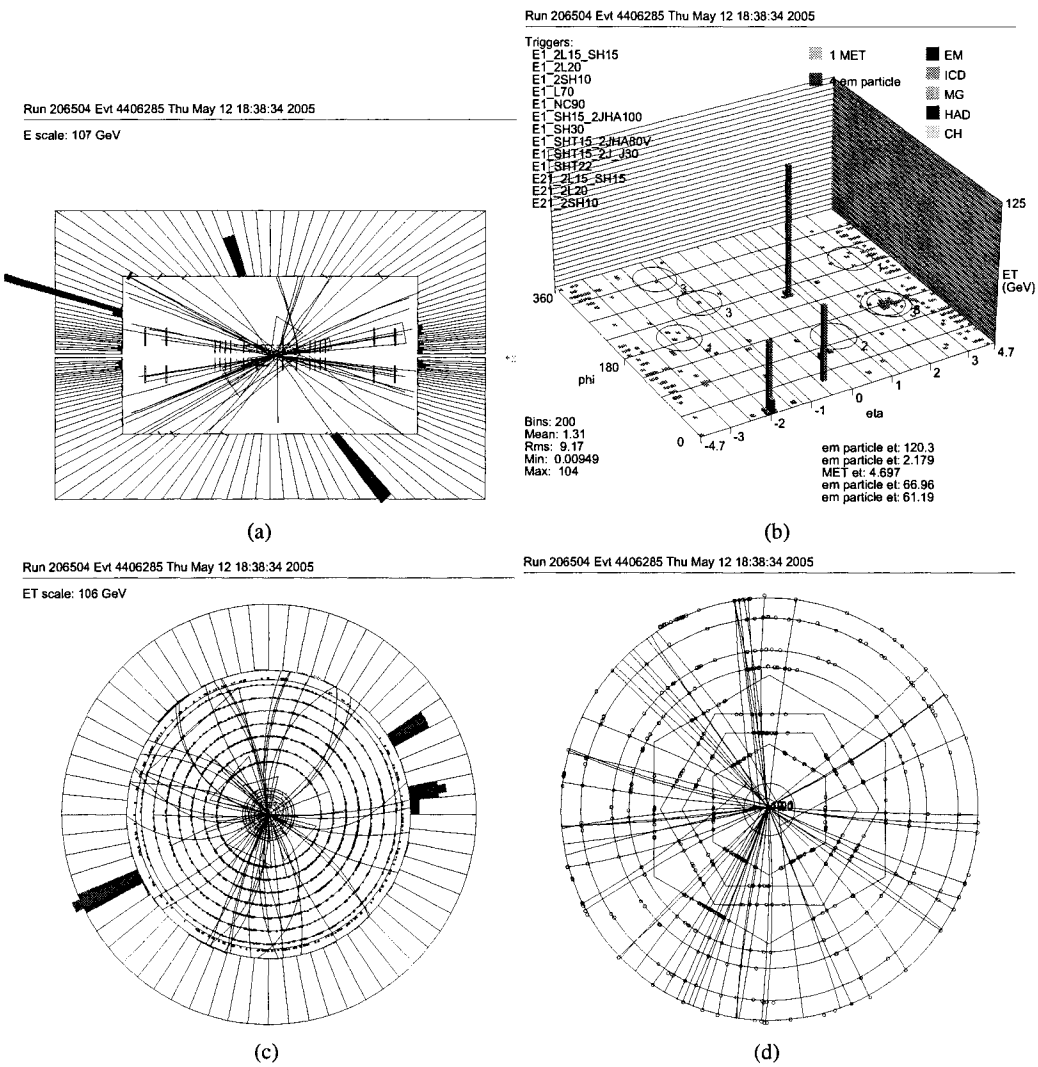

Fig. 105: Event display of $3\gamma + X$ event with 2CC+1EC topolology with (run:event) = (206504:4406285).

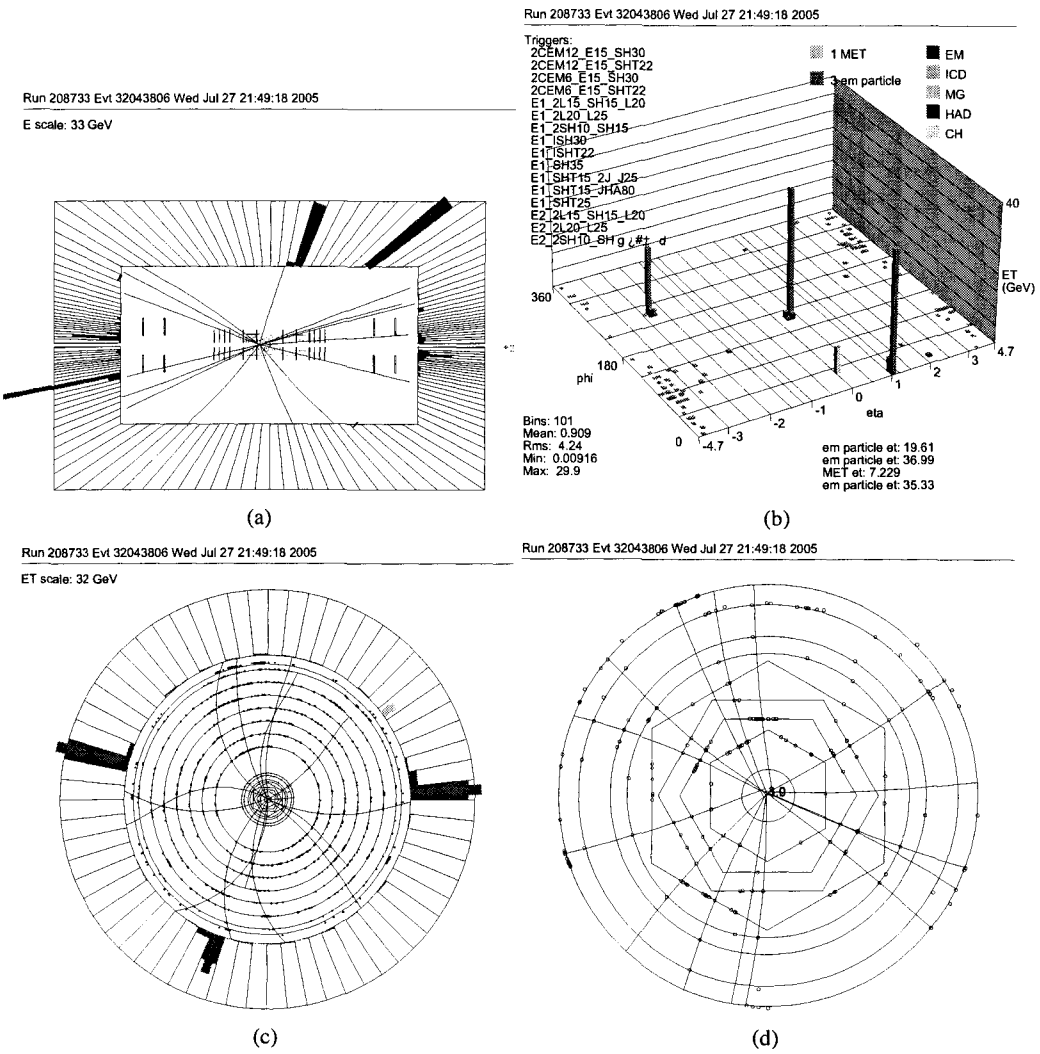

Fig. 106: Event display of $3\gamma + X$ event with 2CC+1EC topolology with (run:event) = (208733:32043806).

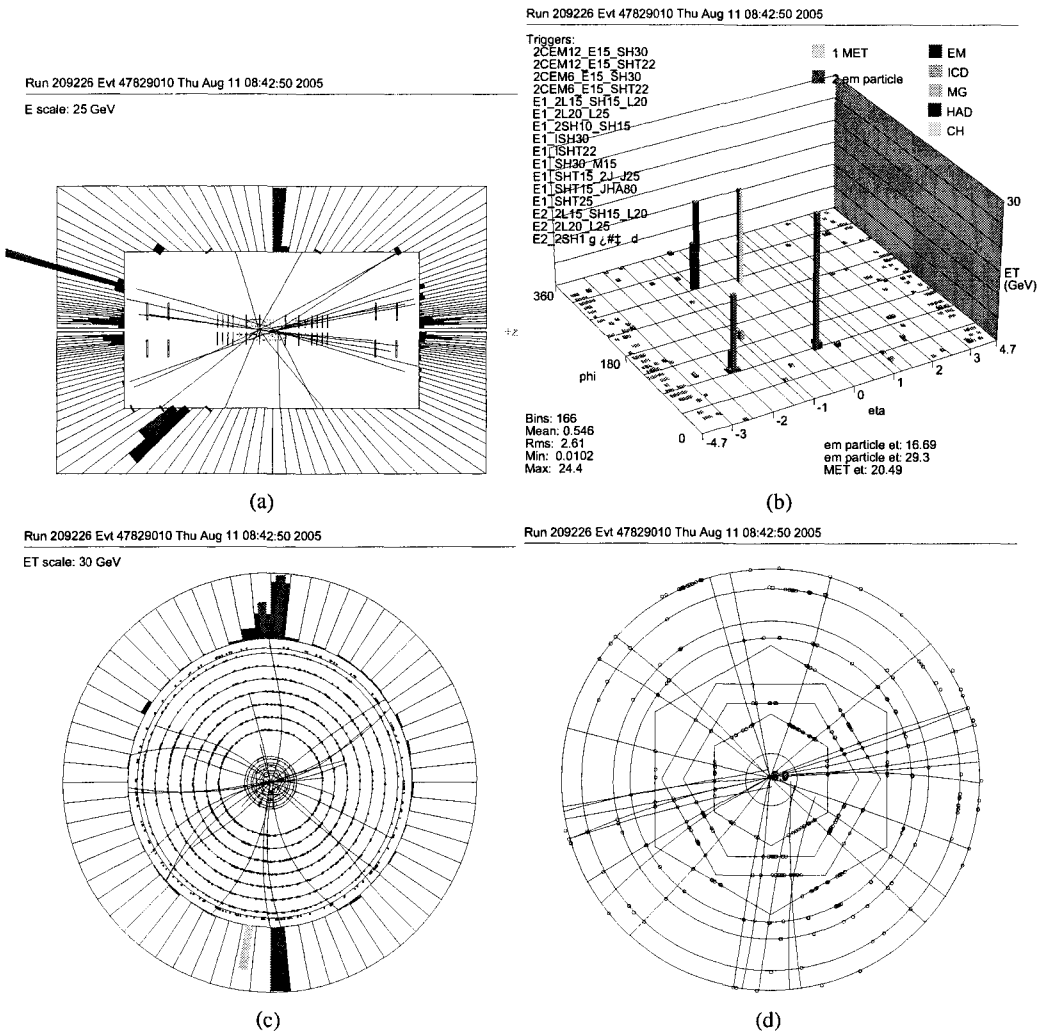

Fig. 107: Event display of $3\gamma + X$ event with 2CC+1EC topolology with (run:event) = (209226:47829010).

CITED LITERATURE

1. V.D. Barger, J.L. Hewett, and R.J. Phillips, Phys. Rev D **41**, 3421 (1990).

2. M. Veltman, "*Facts and Mysteries in Elementary Particle Physics*", World Scientific (2003).

3. D. Griffiths, "*Introduction to Elementary Particles*", John Wiley & Sons (1987).

4. F. Halzen and A. Martin, "*Quarks and Leptons*", John Wiley & Sons (1984).

5. C. Quigg, "*Gauge Theories of the Strong, Weak, and Electromagnetic Interactions*", Westview Press (1983).

6. R. Ellis *et al.*, "*QCD and Collider Physics*", Cambridge University Press (1996).

7. H. Prosper and M. Danilov,"*Techniques and Concepts of High-Energy Physics XII*", NATO Science Series (2003).

8. S. Eidelman *et al.*, "*Review of Particle Physics*", Phys. Lett. B, **592:1** (2004).

9. E. Gross *et al.*, Z. Phys. **C63**, 417 (1994); Erratum: *ibid.*, **C66**, 32 (1995).

10. A. Djouadi, M. Spira, and P.M. Zerwas, Z. Phys. **C70**, 675 (1996).

11. ALEPH, DELPHI, L3 and OPAL Collaborations, Phys. Lett. B **565**, 61(2003)

12. N. Cabibbo *et al.*, Nucl. Phys. **B158**, 295 (1979); T. Hambye and K. Riesselmann, Phys. Rev. **D55**, 7255 (1997); G. Isidori et al., Nucl. Phys. **B609**, 387 (2001).

13. B.W. Lee *et al.*, Phys. Rev. Lett. **38** (1977) 883; M. Quiros, *Constraints on the Higgs boson properties from the effective potential*, hep- ph/9703412; A. Ghinculov and T. Binoth, Acta Phys. Polon. **B30** (1999) 99.

14. L. Maiani, G. Parisi and R. Petronzio, Nucl. Phys. **B136** (1979) 115; N. Cabibbo et al., Nucl. Phys. **B158** (1979) 295; R. Dashen and H. Neunberger, Phys. Rev. Lett. **50** (1983) 1897; D.J.E. Callaway, Nucl. Phys. **B233** (1984) 189; M.A. Beg et al., Phys. Rev. Lett. **52** (1984) 883; M. Lindner, Z. Phys. **C31** (1986) 295.

15. G. Altarelli and G. Isidori, Phys. Lett. **B337** (1994) 141; J.A. Casas, J.R. Espinosa and M. Quiros, Phys. Lett. **B342** (1995) 171, Phys. Lett. **B383** (1996) 374; B. Grzadkowski and M. Lindner, Phys. Lett. **B178** (1986) 81; T. Hambye and K. Riesselmann, Phys. Rev. **D55** (1997) 7255.

16. N. Varelas, SM Higgs Searches at the Tevatron, HEP- EPS Conference, Lisbon, July 21-27, 2005.

17. V. Bueschr and K. Jakobs, *Higgs Searches at Hadron Colliders*, hep-ph/0504099

18. H. E. Haber, G. L. Kane, and T. Sterling, Nucl. Phys. **B161**, 493 (1979); J. F. Gunion, R. Vega, and J. Wudka, Phys. Rev. D **42**, 1673 (1990); J. L. Basdevant, E. L. Berger, D. Dicus, C. Kao, and S. Willenbrock, Phys. Lett. B **313**, 40(1993); V. Barger, N. G. Deshpande, J. L. Hewett, and T. G. Rizzo, separate Higgs, Report No. OITS-499, hep-ph/9211234; P. Bamert and Z. Kunszt, Phys. Lett. B **306**, 335 (1993); A. G. Akeroyd, 368, 89 (1996) ; M. C. Gonzalez-Garcia, S. M. Lietti, and S. F. Novaes, Phys. Rev. D **57**, 7045 (1998); A. Barroso, L. Brucher, and R. Santos, Phys. Rev. D **60**, 035005 (1999); L. Brucher and R. Santos, Eur. Phys. J. C 12, **87** (2000).

19. B. Dobrescu, Phys. Rev. D (to be published), Report No. FERMILAB-PUB-99/234-T, hep-ph/9908391; B. Dobrescu, G.Landsberg, and K. Matchev, FERMILAB-PUB-99/324-T.

20. L. Hall and C. Kolda, Phys. Lett. B **459**, 213 (1999); H. Cheng, B. A. Dobrescu, and C. T. Hill, Electroweak symmetry breaking and extra dimensions, Report No. FERMILAB-PUB-99/358-T, hep-ph/9912343.

21. M. Carena, S. Mrenna, and C. E. Wagner, Phys. Rev. D **60**, 075010 (1999).

22. S. Mrenna, talk given at PASCOS99, Lake Tahoe, California, 1999.

23. A. Djouadi, M. Spira, and P. M. Zerwas, Phys. Lett. B **311**, 255 (1993); A. Stange, W. Marciano, and S. Willenbrock, Phys. Rev. D **49**, 1354 (1994); M. A. Diaz and T. J. Weiler, Decays of a fermiophobic Higgs, Report No. VAND-TH-94-1, hep-ph/9401259; K. Melnikov, M. Spira, and O. Yakovlev, Z. Phys. C **64**, 401 (1994) ; S. Moretti and W. J. Stirling, Phys. Lett. B 347, 291 (1995); Y. Liao and X. Li, 396, 225 (1997); M. Steinhauser, ÒCorrections to the decay of an intermediate-mass Higgs boson into two photons, Report No. MPI-PHT-96-130, hep-ph/9612395; A. Djouadi, ÒDecays of the Higgs bosons, Report No. PM-97-51, hep-ph/9712334.

24. G. Abbiendi *et al.* [OPAL Collaboration], Phys. Lett. B **544**, 44(2002)

25. P. Abreu *et al.* [DELPHI Collaboration], Phys. Lett. B **507**, 89(2001); Eur. Phys. J. C **35**, 313, (2004)

26. A .Heister *et al.* [ALEPH Collaboration], Phys. Lett. B **544**, 16(2002)

27. P. Achard *et al.* [L3 Collaboration], Phys. Lett. B **534**, 28(2002); Phys. Lett. B **568**, 191 (2003)

28. B. Abbott et al. [Dŕ Collaboration], Phys. Rev. Lett. 82, 2244 (1999)

29. T. Affolder et al. [CDF Collaboration], Phys. Rev. D 64, 092002 (2001)

30. S. Mrenna and J. Wells, Phys. Rev. D 63, 015006 (2001)

31. G. Landsberg and K. T. Matchev, Phys. Rev. D 62, 035004 (2000)

32. A. Melnitchouk [D0 Collaboration], Int. J. Mod. Phys. A 20, 3305 (2005)

33. A. G. Akeroyd and M. A. Diaz, Phys. Rev. D 67, 095007 (2003)

34. A. G. Akeroyd, M. A. Diaz and F. J. Pacheco, Phys. Rev. D 70, 075002 (2004)

35. A. G. Akeroyd, A. Alves, M. A. Diaz and O. Eboli, arXiv:heph/0512077 (2005)

36. J. Thompson, Introduction to Colliding Beams at Fermilab, FERMILAB-TM-1909 (1994).

37. General Reference Documents for Accelerators. 2002.
http://www-numi.fnal.gov/workgrps/protonwg/accel_reference.html.

38. Accelerator Concepts Rookie Books. 2003.
http://www-bdnew.fnal.gov/operations/rookie_books/rbooks.html.

39. Edmunds, D.: Run IIa Tevatron Beam Structure.
http://www.pa.msu.edu/hep/d0/ftp/l1/framework/drawings/run_iia_beam_structure.ps.

40. Edwards, T. et al., Determination of the Effective Inelastic p anti-p Cross Section for the DØ Run II Luminosity Measurement, FERMILAB-TM-2278-E (2004).

41. Begel, M. *et al.*, "*D0 Luminosity in Run 2: Delivered*", DØ Note 3970 (2002).

42. T. Ferbel, A Brief Description of the D0 Detector in Run II (2004). http://www-d0.fnal.gov/Run2Physics/WWW/templates/detector.tex.

43. Abachi, S. *et al.*, "*The D0 Detector*", Nucl. Instrum. Methods Phys. Res. A **338:185** (1994).

44. D0 Collaboration: D0 Silicon Tracker Technical Design Report. 1994. http://d0server1.fnal.gov/projects/silicon/www/tdr_final.ps.

45. D0 Collaboration: The D0 Upgrade: Central Tracker Technical Design Report. 1999. http://d0server1.fnal.gov/users/stefan/www/CFT_TDR/CFT_TDR.ps.

46. Adams, M. et al.: Design Report of the Central Preshower Detector for the D0 Upgrade. 1996. http://d0server1.fnal.gov/users/qianj/CPS/doc/dn3104.pdf.

47. Gordeev, A. et al., "*Technical Design Report of the Forward Preshower Detector for the DØ Upgrade*", DØ Note 3445 (1998).

48. S. Snyder, "*Measurement of the Top Quark Mass at DØ* ", Stony Brook University (1995).

49. B. Baldin *et al.*, "*Technical Design Report of the Central Muon System*", DØ Note 3365 (1997).

50. G. Alexeev *et al.*, "*Technical Design Report of the D0 Forward Muon Tracking Detector Based on Mini-Drift Tubes*", DØ Note 3366 (1997).

51. D0 Collaboration: d0reco. 2004. http://wwwd0.fnal.gov/Run2Physics/WWW/algorithm.htm.

52. Borisov, G.: Ordering a Chaos... or Technical Details of AA Tracking. 2004. http://www-d0.fnal.gov/global_tracking/talks/20030228/talk-adm-030228.ps.

53. A. Khanov, "*Histogramming Method for Finding Tracks*", DØ Note 3778 (2000).

54. O. Atramentov, Y. Maravin, "*Utilizing CFT and SMT hits count for photon and electron reconstruction*", DØ Note (2004)

55. A. Schwartzman and M. Narain, "*Probabilistic Primary Vertex Selection*", DØ Note 4042 (2002).

56. G. Bernardi, B. Olivier, B. Knuteson, M.Strovink, "*NADA: A New Event by Event Hot Cell Killer*", DØ Note 3687 (1999); Gregorio Bernardi Sophie Trincaz-Duvoid, "*Improvement of the NADA Algorithm: Hot Cell Killing in D0 Run II Data*", DØ Note 4057 (2002)

57. O. Atramentov, "*Search for Warm Regions in the EM Calorimeter in 2003-2006 p17 Data*", DØ Note 5080(2006)

58. O. Atramentov *et al*, "*Photon Identification in P17 Data*", DØ Note 4976(2006)

59. A. Askew and S. Mattingly, "*Measurement of Anomalous Coupling Limits in Wγ Events*", DØ Note 4686 (2005).

60. A. Askew and D. Duggan, "*CPS Variables for Photon Identification*", DØ Note 4949 (2005).

61. Landsberg, G.: Ph.D Thesis, SUNY at Stony Brook, 1994

62. Genik, R.: Ph.D Thesis, Michigan State University, 1998

63. Private communication with Jon Hays.

64. CPS cluster is matched to an EM ob ject if the highest energy CPS cluster, in dR=0.05 from EM object, is within 5σ of CPS-EM matching resolution. See DØ Note 4411.

65. O.Atramentov, D.Bandurin, Y.Maravin, "*Photon energy scale for jet energy scale setting*", DØ Note 4974 (2005)

66. J.Hays, J.Mitrevski, C.Schwanenberger, "*The Program Package em_cer*", DØ Note 5070 (2006)

67. S. I. Alekhin: The NNLO predictions for the rates of the W / Z production in (anti)-p p collisions arXiv:hep-ph/0307219 (2003).

68. DØ Collaboration: "*Measurement of $Z \rightarrow ee$ and $W \rightarrow e\nu$ Production Cross Sections with $|\eta| < 2.3$*", DØ Note 4403 (2004).

69. Sjoestrand, T. et al.: PYTHIA 6.3 Physics and Manual, hep-ph/0308153 (2003).

70. CTEQ: CTEQ6 Parton Distributions, hep-ph/0512167 (2005).

71. Maltoni, F.: Madevent: Automatic Event Generation with MADGRAPH, hep-ph/0208156 (2002).

72. Y. Liu, "*Measurement of the Cross Section for Production of Prompt Diphoton in p-pbar collisions at sqrt(s) = 1.96 TeV*", PhD. Thesis, Geneva U. (2004).

73. L. Wilke and T. Hebbeker, "Measurement of Multijet Production", DØ Note 4694 (2005).

74. R.T. Cox, Am. J. Phys. **14**, 1 (1946); H. Jeffreys, "*Theory of Pobability*", 3rd edition, Oxford University Press (1961); E.T. Jaynes and L. Bretthorst, "*Probability Theory, the Logic of Science*", Oxford, 2003; A. O'Hagan, "*Kendall's Advanced Theory of Statistics, Volume 2B: Bayesian Inference*", Oxford (1994).

75. T. Junk, Nucl. Instrum. Meth. A **434**, 435 (1999); A.L. Read, CERN Yellow Report 2000-005.

76. The online version of the algorithm described in DØ Note 3476 is located at: http://www-clued0.fnal.gov/ hobbs/limit_calc/limit_calc.html